

# SPECTROSCOPIC CHARACTERIZATION OF SUPEROXIDE REDUCTASES

by

MICHAEL DEAN CLAY

(Under the Direction of MICHAEL K. JOHNSON)

## ABSTRACT

A new pathway of reactive oxygen species detoxification in anaerobic and microaerophilic microorganisms has recently been discovered. The enzyme at the center of this pathway, superoxide reductase (SOR), catalyzes the reduction rather than the disproportionation of superoxide. Two distinct forms of SOR containing 1Fe and 2Fe have been structurally characterized by X-ray crystallography. Both contain a novel superoxide-reducing mononuclear non-heme iron active-site, while 2Fe-SORs contain an additional desulforedoxin-type non-heme iron site.

The research in this dissertation focuses on understanding the structural and electronic determinants of enzymatic superoxide reduction through detailed spectroscopic characterization of the unique mononuclear non-heme iron active-site in wild-type and variant forms of the 1Fe-SOR in *Pyrococcus furiosus* and the 2Fe-SOR in *Desulfovibrio vulgaris*, using the combination of absorption, CD, magnetic circular dichroism, electron paramagnetic resonance, resonance Raman and FTIR. The results confirm a common SOR active-site in both 1Fe- and 2Fe-SORs and emphasize the importance of utilizing a high-spin iron center with axial cysteinyl ligation for mediating electron transfer, reductive superoxide binding, and effecting release of the product peroxide.

INDEX WORDS: Superoxide Reductase, Magnetic Circular Dichroism, Electron Paramagnetic Resonance, Resonance Raman, Charge Transfer, Desulfoferrodoxin, Neelaredoxin

SPECTROSCOPIC CHARACTERIZATION OF SUPEROXIDE REDUCTASES

by

MICHAEL DEAN CLAY

B.S., University of Michigan, Flint, 1997

A Dissertation Submitted to the Graduate Faculty of The University of Georgia in Partial  
Fulfillment of the Requirements for the Degree

DOCTOR OF PHILOSOPHY

ATHENS, GEORGIA

2002

© 2002

Michael Dean Clay

All Rights Reserved

SPECTROSCOPIC CHARACTERIZATION OF SUPEROXIDE REDUCTASES

by

MICHAEL DEAN CLAY

Major Professor: Michael K. Johnson

Committee: Michael W. W. Adams  
Donald M. Kurtz, Jr.  
Robert A. Scott  
Robert S. Phillips

Electronic Version Approved:

Maureen Grasso  
Dean of the Graduate School  
The University of Georgia  
December 2002

I would like to thank and dedicate this work to my family; Mom, Kathleen, Dad, Rosie, Grandpa and Grandma Milan, and Grandpa and Grandma Clark, for all of their support, encouragement and love.

## ACKNOWLEDGEMENTS

I wish to express my deepest gratitude to my major Professor, Dr. Michael K. Johnson, for his guidance, support, and loyalty during the course of my studies.

I thank my reading and examining committee, Dr. Donald M. Kurtz, Jr., Dr. Robert A. Scott, Dr. Michael W. W. Adams, and Dr. Robert S. Phillips, for their effort, insightful discussion and fruitful collaborations.

I thank Dr. Eugene Studier and Dr. David O’Keeffe for teaching me about research, and for helping me to choose the right graduate school, and Dr. Robert Kren for introducing and teaching me the many facets of inorganic chemistry.

I thank Dr. Glenn Martin and Dr. Lars Beholtz, my boss’ at Selective Technologies, for teaching me to be a chemist, for showing me how to prosper in an industrial environment, and most of all for their unwavering support.

I thank my Johnson lab mentors, Dr. Jeffrey N. Agar and Dr. Ish K. Dhawan, for their guidance in and out of lab. I also thank the rest of my friends in the Johnson, Kurtz and Adams lab for their assistance, friendship and support.

I thank my roommates, Nate, Chris, Jeff, Scott and Archer, for putting up with me through thick and thin and making Athens fun.

I thank Jennifer Powell for helping me understand the importance of school, which has allowed me to pursue my dreams.

Last, but not least, I want to thank the UGA chemistry night crew for making those long lab nights not so lonely.

## TABLE OF CONTENTS

	Page
ACKNOWLEDGEMENTS .....	v
LIST OF TABLES .....	ix
LIST OF FIGURES .....	x
CHAPTER	
1 Introduction & Literature Review.....	1
Background .....	1
Reactive Oxygen Species .....	2
Aerobic ROS Detoxification .....	6
Anaerobic ROS Detoxification .....	17
Summary of Presented Work .....	26
References .....	28
2 Spectroscopic Studies of <i>Pyrococcus furiosus</i> Superoxide Reductase:	
Implications for Active Site Structures and the Catalytic Mechanism .....	62
Abstract .....	63
Introduction .....	66
Experimental Section .....	68
Results and Analysis .....	72
Discussion .....	95
Acknowledgments .....	107

	References .....	108
3	Resonance Raman characterization of the mononuclear iron active-site vibrations and putative electron transport pathways in <i>Pyrococcus furiosus</i> superoxide reductase .....	154
	Textual Footnotes .....	155
	Abstract .....	156
	Introduction .....	158
	Materials and Methods .....	159
	Results .....	161
	Discussion .....	168
	References .....	178
4	Nitric Oxide Binding at the Mononuclear Active Site of Reduced <i>Pyrococcus furiosus</i> Superoxide Reductase: Implications for the Structural and Electronic Determinants of Enzymatic Superoxide Reduction .....	211
	Textual Footnotes .....	212
	Abstract .....	213
	Introduction .....	214
	Materials and Methods .....	216
	Results .....	217
	Discussion .....	223
	Acknowledgments .....	229
	References .....	230

5	Spectroscopic Characterization of the 2Fe-Superoxide Reductase from <i>Desulfovibrio vulgaris</i> .....	250
	Textual Footnotes .....	251
	Abstract .....	252
	Introduction .....	253
	Materials and Methods .....	255
	Results and Analysis .....	258
	Discussion .....	268
	Acknowledgments .....	273
	References .....	274

## LIST OF TABLES

	Page
Table 1.1: Purified and Characterized 1Fe- and 2Fe-SORs.....	37
Table 1.2: Summary of 1Fe- and 2Fe-SOR Rate Constants .....	39
Table 2.1: Excited state electronic assignments for recombinant <i>P. furiosus</i> SOR.....	112
Table 2.2: Near-IR excited state transition energies and ligand field splittings for high-spin Fe <sup>2+</sup> center reduced recombinant <i>P. furiosus</i> SOR.....	114
Table 2.3: EXAFS of air-oxidized and dithionite-reduced <i>P. furiosus</i> SOR.....	115
Table 3.1: Assignment of the resonance Raman spectrum of oxidized wild-type <i>P. furiosus</i> SOR .....	182
Table 5.1: Assignment of the resonance Raman spectrum of oxidized C13S <i>D. vulgaris</i> 2Fe-SOR .....	278

## LIST OF FIGURES

	Page
Figure 1.1: Dioxygen-based redox chemistry .....	41
Figure 1.2: Biological superoxide generation, effects and detoxification .....	43
Figure 1.3: SOR gene organization and possible ROS detoxification operon.....	45
Figure 1.4: Proposed anaerobic ROS detoxification pathway in <i>Pyrococcus furiosus</i> .....	47
Figure 1.5: Proposed <i>in vivo</i> superoxide generation, effects and detoxification in a typical <i>Pyrococcus furiosus</i> cell.....	49
Figure 1.6: Sequence alignments of SOR homologues .....	51
Figure 1.7: <i>Pyrococcus furiosus</i> 1Fe-SOR crystal structure.....	53
Figure 1.8: Oxidized and reduced active-site structures in <i>P. furiosus</i> 1Fe-SOR .....	55
Figure 1.9: <i>Desulfovibrio desulfuricans</i> 2Fe-SOR crystal structure.....	57
Figure 1.10: X-ray crystal structure of Center I and II from <i>Desulfovibrio</i> <i>desulfuricans</i> 2Fe-SOR.....	59
Figure 1.11: Proposed mechanism for SOR .....	61
Figure 2.1: X-band EPR spectra of recombinant <i>P. furiosus</i> SOR.....	117
Figure 2.2: Temperature dependence of the EPR spectrum of recombinant <i>P. furiosus</i> SOR in 50 mM HEPES buffer, pH 7.5 .....	119
Figure 2.3: Dye-mediated EPR redox titration of recombinant <i>P. furiosus</i> SOR.....	121
Figure 2.4: Temperature dependence of the EPR spectrum of recombinant <i>P. furiosus</i> SOR exchanged into 50 mM CHES buffer, pH 10.0 .....	123

Figure 2.5: UV-visible absorption spectra of recombinant <i>P. furiosus</i> SOR.....	125
Figure 2.6: UV-visible VTMCD spectra of recombinant <i>P. furiosus</i> SOR.....	127
Figure 2.7: VHVT MCD saturation magnetization data for recombinant <i>P. furiosus</i> SOR at pH 7.5 .....	129
Figure 2.8: Schematic orbital energy level diagram and depiction of the (Cys)S(p) → Fe <sup>3+</sup> (d) charge transfer transitions .....	131
Figure 2.9: Comparison of the UV-visible absorption, CD and VTMCD spectra of cyanide-bound recombinant <i>P. furiosus</i> SOR .....	133
Figure 2.10: UV absorption and VTMCD spectra of ascorbate-reduced recombinant <i>P. furiosus</i> SOR .....	135
Figure 2.11: Near-IR absorption, CD and VTMCD spectra of ascorbate-reduced recombinant <i>P. furiosus</i> SOR .....	137
Figure 2.12: Near-IR VTMCD spectra of ascorbate-reduced recombinant <i>P. furiosus</i> SOR in the presence of azide.....	139
Figure 2.13: Near-IR CD and VTMCD spectra of ascorbate-reduced recombinant <i>P. furiosus</i> SOR in the presence of cyanide.....	141
Figure 2.14: Schematic orbital energy level diagram for the square-pyramidal Fe <sup>2+</sup> center in reduced SOR .....	143
Figure 2.15: VHVT MCD saturation magnetization data for ascorbate-reduced recombinant <i>P. furiosus</i> SOR collected at 12400 cm <sup>-1</sup> .....	145
Figure 2.16: Iron K near-edge spectra of recombinant <i>P. furiosus</i> SOR.....	147
Figure 2.17: EXAFS oscillations and Fourier transforms of air-oxidized and dithionite-reduced <i>P. furiosus</i> SOR.....	149

Figure S2.1: Redox titration of <i>P. furiosus</i> SOR at pH 7.0 as monitored by UV-visible absorption at 660 nm.....	151
Figure S2.2: Effect of pH on the visible absorption maximum of <i>P. furiosus</i> SOR.....	153
Figure 3.1: Visible absorption spectrum and resonance Raman excitation profile for the 323-cm <sup>-1</sup> vibrational mode of wild-type <i>P. furiosus</i> SOR .....	184
Figure 3.2: Resonance Raman spectra of natural abundance (NA) and <sup>34</sup> S globally labeled wild-type <i>P. furiosus</i> SOR .....	186
Figure 3.3: Resonance Raman spectra of natural abundance (NA) and <sup>15</sup> N globally labeled wild-type <i>P. furiosus</i> SOR .....	188
Figure 3.4: Resonance Raman spectra of natural abundance (NA) and <sup>54</sup> Fe globally labeled wild-type <i>P. furiosus</i> SOR .....	190
Figure 3.5: Resonance Raman spectrum of wild-type <i>P. furiosus</i> SOR in the high frequency region, 800-2000 cm <sup>-1</sup> .....	192
Figure 3.6: Resonance Raman spectra of natural abundance (NA) and <sup>15</sup> N globally labeled wild-type <i>P. furiosus</i> SOR in the Fe-N(His) stretching region.....	194
Figure 3.7: Comparison of the resonance Raman spectra of wild-type <i>P. furiosus</i> SOR at pH 7.5 and 10.5 with the E14A variant at pH 7.5 .....	196
Figure 3.8: Top and side view of the <i>P. furiosus</i> SOR active site showing the near-planar arrangement of the Fe-S-C <sub>β</sub> -C <sub>α</sub> -N unit .....	198
Figure S3.1: Visible absorption spectra of wild-type <i>P. furiosus</i> SOR at pH 7.5 and 10.5 and of the E14A variant at pH 7.5 .....	200
Figure S3.2: Resonance Raman spectra of wild-type <i>P. furiosus</i> SOR at pH 7.5 and 10.5 and of the E14A variant at pH 7.5 using 568-nm excitation .....	202

Figure S3.3: Resonance Raman spectra of wild-type <i>P. furiosus</i> SOR at pH 7.5 in H <sub>2</sub> <sup>16</sup> O and H <sub>2</sub> <sup>18</sup> O 50 mM HEPES buffers using 647-nm excitation .....	204
Figure S3.4: Resonance Raman spectra of wild-type <i>P. furiosus</i> SOR at pH 10.5 in H <sub>2</sub> <sup>16</sup> O and H <sub>2</sub> <sup>18</sup> O 50 mM CAPS buffer with 647-nm excitation.....	206
Figure S3.5: Resonance Raman spectra of E14A <i>P. furiosus</i> SOR at pH 7.5 in H <sub>2</sub> <sup>16</sup> O and H <sub>2</sub> <sup>18</sup> O 50 mM HEPES buffers using 647-nm excitation.....	208
Figure S3.6: Resonance Raman spectra of natural abundance (NA) and <sup>15</sup> N globally labeled wild-type <i>P. furiosus</i> SOR at pH 10.5 .....	210
Figure 4.1: Proposed catalytic mechanism of SOR .....	235
Figure 4.2: X-band EPR of the NO adduct of ascorbate-reduced <i>P. furiosus</i> SOR .....	237
Figure 4.3: UV-visible absorption and MCD spectra of the NO adduct of ascorbate- reduced <i>P. furiosus</i> SOR .....	239
Figure 4.4: Resonance Raman spectra of the <sup>14</sup> NO and <sup>15</sup> NO adducts of ascorbate- reduced <i>P. furiosus</i> SOR .....	241
Figure 4.5: Resonance Raman spectra of NO adduct of natural abundance (NA) and <sup>34</sup> S globally labeled ascorbate-reduced <i>P. furiosus</i> SOR .....	243
Figure 4.6: Schematic orbital depiction of the (Cys)S–Fe–NO unit.....	245
Figure S4.1: VTVH MCD saturation magnetization data for the NO adduct of <i>P. furiosus</i> SOR at 21050 cm <sup>-1</sup> (475 nm).....	247
Figure S4.2: FTIR spectra of the <sup>14</sup> NO and <sup>15</sup> NO adducts of ascorbate-reduced <i>P. furiosus</i> SOR .....	249
Figure 5.1: X-band EPR spectra of <i>D. vulgaris</i> 2Fe-SOR.....	280
Figure 5.2: UV-visible absorption spectra of wild-type <i>D. vulgaris</i> 2Fe-SOR .....	282

Figure 5.3: UV-visible VTMCD spectra of wild-type <i>D. vulgaris</i> 2Fe-SOR.....	284
Figure 5.4: Near-IR VTMCD spectra of wild-type <i>D. vulgaris</i> 2Fe-SOR .....	286
Figure 5.5: UV-visible absorption and VTMCD spectra of hexachloroiridate-oxidized C13S <i>D. vulgaris</i> 2Fe-SOR.....	288
Figure 5.6: UV absorption and VTMCD spectra of ascorbate-reduced C13S <i>D. vulgaris</i> 2Fe-SOR.....	290
Figure 5.7: Near-IR absorption, CD, and VTMCD spectra of ascorbate-reduced C13S <i>D. vulgaris</i> 2Fe-SOR.....	292
Figure 5.9: Low-energy resonance Raman spectrum of oxidized C13S <i>D. vulgaris</i> 2Fe-SOR from 180 – 800 cm <sup>-1</sup> .....	294
Figure 5.9: High-energy resonance Raman spectrum of oxidized C13S <i>D. vulgaris</i> 2Fe-SOR from 800 – 2000 cm <sup>-1</sup> .....	296

## CHAPTER 1

### INTRODUCTION & LITERATURE REVIEW

#### Background

The detoxification of reactive oxygen species (ROS) such as superoxide ( $O_2^-$ ), hydrogen peroxide ( $H_2O_2$ ) and hydroxyl radical ( $OH^\bullet$ ) is of vital concern to many, if not all, living organisms. Over the millennia, organisms have evolved to survive under different degrees of oxidative stress (1). Specifically, aerobic and anaerobic organisms have each developed their own unique pathway to dispose of potentially hazardous ROS. Though the initial discovery of ROS detoxification among aerobes three decades ago was quite controversial at the time, the summation of evidence over the years in support of such a pathway has established the existence and importance of aerobic ROS detoxification (2;3). More recently, controversy has also surrounded the recent discovery of a distinct ROS detoxification pathway in anaerobic organisms (4;5). This novel pathway has been proposed to enzymatically dispose of superoxide and hydrogen peroxide by way of reduction rather than disproportionation (6;7). The importance of this pathway, in regards to anaerobes, relies on the premise that poisonous dioxygen is not produced during the detoxification of superoxide or hydrogen peroxide. The enzyme at the center of this pathway is superoxide reductase (SOR) and is responsible for the reduction and protonation of superoxide to yield hydrogen peroxide (4;7). The research in this thesis focuses on determining the enzymatic mechanism of superoxide reduction by detecting the effects of pH and redox variation, exogenous ligand binding and

mutagenesis on the SOR iron active site through a wide array of spectroscopic techniques. The combination of these techniques provides a detailed electronic structure of the SOR active site that correlates to function and reactivity along the reaction coordinate.

### **Reactive Oxygen Species**

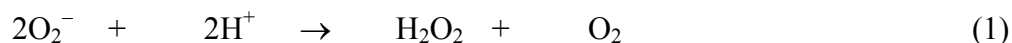
The *in vivo* generation of reactive oxygen species (ROS), such as superoxide ( $O_2^-$ ), hydrogen peroxide ( $H_2O_2$ ), and hydroxyl radical ( $OH^\bullet$ ), plays an important role in governing cellular function (3;8;9). Due to their very nature, these species must be tightly regulated, whether generation is intentional or not. In order to control these toxic agents, organisms have evolved with unique pathways for generating and detoxifying ROS. Prior to discussing these pathways, the nature of these ROS will be discussed.

**Superoxide.** Superoxide, the one electron reduction product of dioxygen, is the most prominent of the ROS (3;8-10). This is primarily true, not because of its reactivity, but rather due to superoxide being the precursor to more reactive ROS, such as hydrogen peroxide and especially the hydroxyl radical. The prefix “super” refers to an older nomenclature that dealt with the stoichiometry of  $KO_2$ , which is different from other oxides (10). Now, unfortunately, this prefix is often assumed to describe the powerful redox or radical qualities of superoxide. Depending on the environment, superoxide can act as a relatively powerful oxidant ( $E_o = + 940$  mV vs NHE, pH 7), as well as a mild reductant ( $E_o = - 160$  mV vs NHE, pH 7), see Figure 1.1 (11). However, its radical nature is often overemphasized, due to its limited reactivity with polyunsaturated lipids and DNA (10).

**Biological generation.** Unlike dioxygen, the charged nature of the superoxide ion, pKa of 4.8, tends to prevent it from traversing membranes (8;9). Therefore, the diffusion of superoxide into a cell seems unlikely. However, dioxygen, which is freely diffusible across membranes, appears to be the direct precursor of superoxide within the cell. The most prominent site of unintentional superoxide generation *in vivo* arises from the incomplete, one electron, reduction of dioxygen in the respiratory chain of aerobic prokaryotes and eukaryotes, see Figure 1.2 (3;8). Specifically, ubisemiquinone in complex III and NADH dehydrogenase (complex I) are believed to be the key points of one electron reduction of dioxygen within the electron transport chain in eukaryotes (12). Other redox agents that can reduce dioxygen to superoxide include enzymes with reduced cofactors (e. g. flavin-containing oxidoreductases), univalent redox components (e. g. ascorbate, thiols and catecholamines), as well as by external factors such as photochemical reactions and some redox dyes (8). Paradoxically, superoxide is intentionally produced for protection as well as cellular signaling and regulation. For example, humans have an immunological response in which phagocytes, such as neutrophils and eosinophils, generate a bolus of superoxide by the enzyme NADPH oxidase for the specific purpose of destroying invading microorganisms (3).

**Deleterious effects.** Although there are advantages to superoxide generation, the disadvantages are of much greater concern with respect to proper cellular function. The understanding of superoxide's deleterious effects may help explain the onset of certain diseases, the aging process, and possibly cell death. Once superoxide has been generated within the cell, it tends to remain compartmentalized (*vide supra*), which may limit its destructive nature. Superoxide has been known to inactivate various enzymes such as

catalase, glutathione peroxidase, as well as [4Fe-4S]-containing dehydratases, such as aconitase, see Figure 1.2 (8;9;12). Though these enzymes are inactivated by superoxide, it is relatively unreactive with polyunsaturated lipids and DNA, even if increased superoxide production results in their damage (8;9). This result helped uncover a more pressing danger of intracellular superoxide generation, Fenton chemistry (13). This particular type of chemistry involves the natural disproportionation of superoxide to dioxygen and hydrogen peroxide and a transition metal catalyst to generate dioxygen, hydroxide, and most importantly the hydroxyl radical, as shown in reactions 1, 2 and 3.



The hydroxyl radical is an extraordinarily powerful oxidant and will undergo radical chemistry damaging lipids, carbohydrates, proteins, nucleic acids, metal centers and other cellular components (1;9;10). Thus, rather than superoxide, it is the ROS that are subsequently produced, and particularly the reactive hydroxyl radical and metal-peroxide adducts that generate most of the dioxygen-derived damage in biological systems (10;12;14). However, Fridovich argues that because superoxide is more selective in its reactivity than the hydroxyl radical, superoxide is potentially more damaging (1). This may be true if one considers the hydroxyl radical reacting within a very small radius of generation, whereas superoxide can diffuse a considerable distance, thus increasing its radius of attack, before reacting with its target.

Though Fenton-derived hydroxyl radical generation *in vivo* appears plausible, critics have raised important points that undermine the idea of *in vivo* Fenton chemistry.

The three major criticisms of *in vivo* Fenton chemistry are that free metal catalysts are unavailable due to strict metal regulation, Fenton reaction rate constants are too slow, and the natural disproportionation of superoxide is too fast to react with transition metal catalysts, even if they are available (13). In response to these criticisms, superoxide has been shown to inactivate iron-sulfur cluster proteins, thus releasing free iron in solution for Fenton chemistry to occur (vide supra). Also, Fenton reaction rate constants suggest that hydroxyl radicals may be formed at a rate of 50 per cell per second, which still could have disastrous cellular consequences. In addition, the natural disproportionation of superoxide is relatively fast, occurring with a rate constant of  $4 \times 10^5 \text{ M}^{-1} \text{ sec}^{-1}$ , at pH 7.4 (8). However, the half-life of superoxide disproportionation, without catalyst, is inversely proportional to superoxide concentration multiplied by the rate constant. Therefore, since superoxide is estimated to have an intracellular concentration of approximately  $1-9 \times 10^{-10} \text{ M}$ , the half-life for disproportionation is 1-7 hours.

Whether Fenton chemistry is involved or not, this matter of semantics should not cloud the point that an increase in ROS, whether direct or indirect, has a negative impact on proper cellular function (1;9). Moreover, human cellular damage by ROS has been highly studied and implicated in a wide range of human diseases such as: inflammatory diseases (arthritis (15), vasculitis (16), glomerulonephritis (17) and more), ischemic diseases (heart disease (18), stroke (19) and more), neurologic diseases (multiple sclerosis (20), Alzheimer's (21), Parkinson's (22), amyotrophic lateral sclerosis (ALS) (23), muscular dystrophy (24) and others), acquired immunodeficiency syndrome (AIDS) (25), gastric ulcers (26), hypertension (27), alcoholism (28), smoking-related diseases (29) and many more (3;12). In addition to these diseases, the process of aging has also

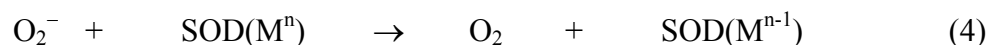
been linked to ROS oxidative damage (30). In lieu of the damaging effects of ROS, evolutionary pressure has selected for the survival of organisms that have developed various defense mechanisms against the destructive force of ROS.

### **Aerobic ROS Detoxification**

**History.** The first indication of a superoxide defense mechanism was reported by McCord and Fridovich in 1969 when they discovered the enzyme superoxide dismutase (SOD) (2). Yet, at the time, the precedence for biological superoxide generation was just as unknown and controversial as the enzyme itself. Before 1968, superoxide was considered a chemical curiosity that formed salts from reacting dioxygen with potassium, rubidium, or cesium (10). However, two reports of biological superoxide generation were identified in 1968 and 1969. The first report, by McCord and Fridovich, established that xanthine oxidase could reduce dioxygen to superoxide, which could subsequently reduce cytochrome *c* (31). This reaction was considered highly unusual, at the time, but their data supported the conclusions. The second report, by Bray and coworkers, established more conclusively the generation of superoxide from xanthine oxidase by electron paramagnetic resonance (EPR) (32). McCord and Fridovich were then able to isolate and purify a copper protein from bovine erythrocytes that inhibited the reduction of cytochrome *c* by superoxide (2). They concluded that this copper protein, of previous unknown function, must have been eliminating superoxide by enzymatic disproportionation or dismutation, see reaction 1, thus causing the inhibition in cytochrome *c* reduction. This happened to be the case and hence the discovery of a new class of enzyme, superoxide dismutase (SOD). Yet, this powerful discovery drew many critics as to the actual role of this protein. Many believed that the SOD activity was

actually an artifact of adventitious redox chemistry, not uncommon amongst *in vitro* reactions. These critics were slowly silenced over the years as significant discoveries supported SOD activity. First, SOD was measured to catalyze the dismutation of superoxide at diffusion-limited rates (*vide infra*) (33;34). SOD's are ubiquitous among aerobic organisms and are also inducible upon oxidative stress (35-37). The most convincing support of SOD activity was derived from genetic studies. In 1986, seventeen years after the discovery of SOD, Carlioz and Touati were able to construct mutant *Escherichia coli* lacking both *sodA* and *sodB* genes, coding for Mn-SOD and Fe-SOD, respectively (38). The mutant *E. coli* grew poorly on minimal medium in the presence of oxygen, only when both genes were absent. However, most importantly, this phenotype could be fully complemented by insertion of plasmids containing the evolutionarily unrelated eukaryotic CuZn or Mn superoxide dismutase genes (38;39). This ultimately supported the hypothesis that superoxide dismutation is the *in vivo* function of these proteins.

**Aerobic Enzymatic Defenses Against Superoxide.** Since the SOD function is firmly established, the next step is to focus more closely on the properties of the different types of SODs. Currently, there are a total of four types of SOD enzymes, which include CuZn-, Fe-, Mn- and the most recently discovered Ni-SOD. Each SOD performs the same basic metal (M) catalyzed disproportionation of superoxide, as shown in the elementary steps in reaction 4 and 5, as well as the overall reaction in reaction 6 (1).



It is important to note that SODs in general are found in almost all organisms exposed to oxygen, and therefore are expected to be essential for aerobic life (38).

**CuZn-SOD.** The first type of SOD discovered was the CuZn-SOD (superoxide: superoxide oxidoreductase, EC 1.15.1.1) (2). This type of SOD is found in the cytosols of eukaryotic cells, in the periplasms of gram-negative bacteria, in the plastids of plants and in the extracellular spaces of mammals (1). These SODs are subdivided based on cellular placement. The cytosolic CuZn-SODs consist of an overall homodimeric structure, while the extracellular forms are homotetrameric, with each monomer composed of eight antiparallel  $\beta$  strands which form a flattened cylinder, also known as an immunoglobulin-like  $\beta$ -barrel fold (structurally similar to SORs) (40). These monomers also contain tetrahedrally ligated Cu and Zn atoms that are connected by nitrogens of a bridging imidazolate (Im). This unique bridge is the only example thus far of an imidazole bridging two metals and is thought to play a vital role in the “ping-pong” mechanism of superoxide disproportionation, as shown in reaction 7, 8 and 9 (1;41).



The proposed mechanism involves superoxide binding to  $\text{Cu}^{2+}$  to generate  $\text{Cu}^{1+}$  and dioxygen. Next, the imidazolate dissociates from the  $\text{Cu}^{1+}$  and is protonated. The Zn is thought to play a structural role in stabilizing the imidazolate. Finally, another superoxide binds to  $\text{Cu}^{1+}$ , becomes reduced and protonated to yield hydrogen peroxide, thus returning the CuZn active-site back to its original oxidized, imidazolate-bridged conformation. This mechanism is thought to proceed by a Cu-mediated inner-sphere

oxidation and reduction of superoxide, a Cu-oxygen/peroxide intermediate has yet to be detected. Additionally, a number of pulse radiolytic kinetic studies supported the diffusion-limited disproportionation of superoxide by CuZn-SODs with rate constants of  $2 \times 10^9 \text{ M}^{-1}\text{s}^{-1}$ , 5000 times faster than the uncatalyzed disproportionation of superoxide (42).

**Mn-SOD.** In 1970, a year after the CuZn-SOD discovery, Fridovich and coworkers were able to isolate a Mn-SOD (43). The Mn-SOD, like the CuZn-SOD, was found to exist in dimeric and tetrameric forms. However, the primary amino acid sequence was notably unrelated to the CuZn form. The *E. coli* Mn-SOD is dimeric and its synthesis is induced upon oxidative stress. The homotetrameric form has a related primary sequence, but is found in the mitochondrial matrix of eukaryotes (1).

Crystallographic characterization indicates that each monomer consists of one Mn ion coordinated by three histidyl nitrogens, one glutamate oxygen and a bound hydroxide or water in a trigonal bipyramidal arrangement (44). The mechanism, though not as complicated as the CuZn form, involves a similar “ping-pong” mechanism of superoxide dismutation, by which superoxide first binds and reduces the  $\text{Mn}^{3+}$  by one electron, thus producing  $\text{Mn}^{2+}$  and dioxygen (41;44). This reduction causes the bound hydroxide to gain a proton, become water and thus facilitate subsequent superoxide binding, reduction and protonation to hydrogen peroxide. This latter reaction leaves the oxidized  $\text{Mn}^{3+}$  in its original trigonal bipyramidal resting state with coordinated hydroxide. The proposed mechanism, much like the CuZn-SOD mechanism, assumes inner-sphere binding of the superoxide to the Mn, even though a Mn-oxygen/peroxide intermediate has also not been isolated. Pulse radiolytic studies have determined a slightly slower, relative to the CuZn-

SOD, rate constant of  $5.6 \times 10^7 \text{ M}^{-1}\text{s}^{-1}$  for the Mn-SOD catalyzed disproportionation of superoxide (45).

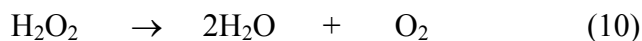
**Fe-SOD.** The Fe-SOD, discovered by Fridovich and coworkers in 1973, is extremely homologous structurally and mechanistically to the Mn-SOD, as well as having similar cellular localization (41;44;46). Pulse radiolytic studies have also determined a similar diffusion-limited rate constant of  $3 \times 10^8 \text{ M}^{-1}\text{s}^{-1}$  for the Fe-SOD catalyzed disproportionation of superoxide (47). However, the Fe-SOD is constitutively expressed under both anaerobic and aerobic conditions, whereas the Mn-SOD is induced upon oxidative stress (36). Some organisms, such as *Propionibacterium shermanii* and *Bacteroides fragilis*, produce a cambialistic SOD, which is able to function with either Fe or Mn in the active site (48;49). These organisms insert Fe into the cambialistic SOD under anaerobic conditions and Mn under aerobic conditions (1).

**Ni-SOD.** Although the CuZn-, Mn- and Fe-SOD were all discovered in the early 1970's, it was not until 1996 that Kang and coworkers discovered the Ni-SOD in *Streptomyces seoulensis* (50). Preliminary biochemistry, spectroscopy and kinetic studies have recently added to the understanding of this new class of SOD. The Ni-SOD amino acid sequence indicates no homology with any of the currently known SOD sequences (51). The *S. seoulensis* Ni-SOD is a homotetramer, with a possible stoichiometry of one or two Ni ions per 13.4 kDa monomer (52). The Ni-SOD activity was determined by pulse radiolysis, and a value of  $k_{\text{cat}} = 1.3 \times 10^9 \text{ M}^{-1}\text{s}^{-1}$  per Ni was obtained (52;53). Electron paramagnetic resonance (EPR) and X-ray absorption spectroscopies (XAS) suggest a  $\text{Ni}^{2/3+}$  redox couple, as well as the identification of nitrogen and sulfur ligation. Though much has been accomplished with this new Ni-SOD, more research needs to be

focused on determining the overall and active-site structures, especially concerning the Ni stoichiometry, as well as avenues of expression and cellular localization.

**Aerobic Enzymatic Defenses Against Hydrogen Peroxide.** One of the deleterious effects of superoxide is to produce the even more oxidative and reactive species, hydrogen peroxide. Therefore, biological organisms must also maintain a strict line of defense against hydrogen peroxide as well. This line of defense consists of two main types of enzymes, catalases and peroxidases.

**Catalases.** Unlike the relatively recent discovery of SOD, catalase was first characterized and named in 1900 as a result of its ability to evolve molecular oxygen (54). Catalases are a class of enzymes that detoxify hydrogen peroxide by catalyzing their disproportionation, reaction 10 (55;56).

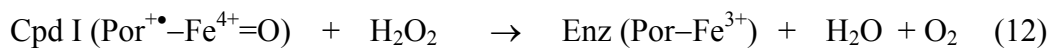


There are two main types of catalases; a large group with heme active sites and a much smaller group with a dimanganese active site (1).

The heme catalases constitute a wide array of subgroups with different heme types (heme *b*, heme *d*), monomer sizes (55 – 84 kDa) and quaternary structures (mostly tetramers, with some dimers, hexamers and heterotrimers), which span all kingdoms of life (55). Despite these differences, the core region that comprises the heme active site has a  $\beta$ -barrel fold motif, much like CuZn-SODs and SORs. The most studied of these catalases are those expressed by *E. coli*, which contain two types of heme catalases, hydroperoxidase I and II (HP-I and II) (1). HP-I is associated with the cytoplasmic membrane and the periplasm and has the unusual ability to act as a peroxidase in addition to its catalase activity. HP-II is expressed in the cytosol and does not possess any

peroxidase activity. Mammalian catalases are homotetramers with each monomer containing a tightly bound NADPH in addition to its heme active site, in which the iron is axially ligated by a deprotonated phenolic oxygen atom of a tyrosine (1;57). This unusual heme ligation is unique to catalases. Much like HP-I, mammalian catalases also have the ability to act as peroxidases, but only to small molecules, such as methanol, ethanol, nitrite and formate (55).

Though the exact mechanism of heme catalases varies, in general, there are two distinct stages in the reaction pathway, summarized in reaction 11 and 12 (56).



The first stage involves hydrogen peroxide oxidizing the enzyme (Enz) heme to an oxyferryl species in which one oxidation equivalent is removed from the iron and one from the porphyrin (Por) ring to generate a porphyrin cation radical, compound I (Cpd I), and the product water, reaction 11. The second stage involves another hydrogen peroxide reducing compound I to regenerate the resting state enzyme, water and oxygen, reaction 12 (55;56).

The disproportionation of hydrogen peroxide by catalases is extremely rapid. In the case of mammalian catalases, first order rates between  $2 \times 10^6 \text{ sec}^{-1}$  and  $1 \times 10^7 \text{ sec}^{-1}$  have been observed. This correlates to each heme active site dismutating between 2 and 10 million molecules of hydrogen peroxide per second (55), under saturating hydrogen peroxide, but the  $K_m$  is very high ( $\sim 10 \text{ mM}$ ).

The non-heme manganese catalases have only been detected in microaerophilic bacteria, such as *Lactobacillus plantarum*, *Thermoleophilum album* and *Thermus*

*thermophilus*. The crystal structure of the *L. plantarum* enzyme reveals a hexameric overall structure with each monomer consisting of a 4-helix bundle that holds the dimanganese active site, similar to many non-heme diiron proteins (58). Though not fully understood, the mechanism of hydrogen peroxide disproportionation catalyzed by Mn-catalase is thought to involve cycling between the reduced  $[\text{Mn}^{2+}\text{Mn}^{2+}]$  and oxidized  $[\text{Mn}^{3+}\text{Mn}^{3+}]$  states during turnover (59). Lastly, *L. plantarum* cannot synthesize heme. However, if heme is present in the medium, then the organism will produce a heme-containing catalase. When heme is not available *L. plantarum* will then produce the Mn-containing catalase. This observation illustrates the importance of *L. plantarum* maintaining a catalase, whether heme or Mn.

**Peroxidases.** Peroxidases are an extremely diverse class of enzymes that reduce various peroxides, as shown as a simple example in reaction 13 (1).



The diversity is mainly based on structural and functional differences that directly relate to the purpose for reducing the peroxide. Some peroxidases reduce hydrogen peroxide for direct detoxification, whereas others use hydrogen peroxide or alkyl peroxide to catalyze the oxidation of various organic and inorganic substrates, xenobiotics (vide infra) (57). Since peroxidases are so diverse in structure, function and origin, there are many ways to categorize them. One way is to divide the peroxidase family into three main groups based on active-site structure, which includes heme peroxidases (e. g. cytochrome *c* peroxidase), non-heme metal peroxidases (e. g. vanadium peroxidases) and non-heme non-metal peroxidases (e. g. NADH peroxidase, glutathione peroxidase and peroxiredoxins).

The heme peroxidases probably have the most diverse function of the three groups. These peroxidases have the ability to catalyze four main peroxidase reactions, as shown in reactions 14, 15, 16 and 17, where A = substrate and X = halide (57;60).



Depending on the active site, each peroxidase may have the ability to perform one or more of these reactions. In brief, reactions 14 – 17 can be considered to have two functional roles. One role is the detoxification of hydrogen peroxide by reduction, with the other role involving the oxidation of some substrate (61). The latter role, whether primary or not, is what differentiates the various peroxidases. For example, both horseradish and spinach peroxidase are representative of reaction 14 and are specifically thought to oxidatively couple phenolic monomers for the biosynthesis of lignin in cell walls during growth, as well as cellular healing (61). The human peroxidases, myeloperoxidase (MPO), eosinophil peroxidase (EPO) and lactoperoxidase (LPO) are termed haloperoxidases for their ability to utilize reaction 15 to produce hypohalous acids (e. g. hypochlorous and hypobromous acid) as antimicrobial agents (60). Moreover, human thyroid peroxidase (TPO) utilizes iodide and hydrogen peroxide to catalyze the iodination of tyrosine through reaction 16, thus forming the hormones triiodothyronine (T<sub>3</sub>) and thyroxine (T<sub>4</sub>) responsible for stimulating metabolism (60;62). In regards to reaction 17, both cytochrome *c* peroxidase (CCP) and prostaglandin endoperoxidase synthase (PGHS) catalyze the reduction of alkyl peroxides to alcohols (60;62). CCP

facilitates the oxidation of cytochrome c through the use of hydrogen peroxide and alkyl peroxides, whereas PGHS reduces the alkyl peroxide prostaglandin G<sub>2</sub> (PGG<sub>2</sub>) to the active alcohol prostaglandin H<sub>2</sub> (PGH<sub>2</sub>) (63). Interestingly, aspirin primarily targets PGHS by inhibiting the production of PGH<sub>2</sub>.

Though the heme peroxidase reactions are different, they appear to share a common mechanism involving the generation of compound I (Por<sup>+•</sup>-Fe<sup>4+</sup>=O), similar to the heme catalase mechanism. However, subsequent steps involve oxidation of the substrate to form compound II (Por-Fe<sup>4+</sup>=O), which can oxidize another substrate, yield water and return the enzyme back to its resting state (Por-Fe<sup>3+</sup>) (60;63;64).

There are also peroxidases that do not contain a heme moiety but do contain a metal, most notably, the vanadium peroxidases (65). This group, though once considered rare, has been increasingly discovered in marine algae, lichens, fungi, bacteria, and higher plants (66). Of the vanadium-containing peroxidases isolated thus far, all have expressed haloperoxidase activity, as shown in reaction 15. They also offer a much different catalytic mechanism and higher stability compared to their heme counterparts. Despite low sequence similarities, the vanadium peroxidases are classified as all-helical proteins and share the four-helix bundle motif as well as a highly conserved vanadate-binding motif (67). The proposed mechanism involves a vanadate (VO<sub>4</sub><sup>3-</sup>), in which the vanadium is ligated by one histidyl nitrogen and four terminal oxygens in a trigonal bipyramidal arrangement. The vanadate is proposed to act as a Lewis acid and bind hydrogen peroxide side-on, displacing two oxygen atoms as water and hydroxide. A halide then attacks the vanadium-peroxo oxygen, which oxidizes the halide and subsequently breaks the peroxo O-O bond, forming a vanadium-O-Hal complex. The

last step involves breaking the vanadium–OHal bond by water protonation, thus generating a hypohalous acid (HOHal) and the resting state vanadate complex (67).

The last group of peroxidases does not contain a heme group or a transition metal ion to carry out their peroxidase activity. These peroxidases are extremely diverse and have active sites that may include one or more of the following: one or two cysteines, flavin adenine dinucleotide (FAD), selenocysteine and glutathione. These active-sites give rise to three basic types of non-heme non-metal peroxidases which are, FAD-dependent peroxidases, glutathione peroxidases and peroxiredoxins (68), most of which carry out the reduction of both hydrogen peroxide and alkyl peroxide to water and alcohol, respectively, as shown in reactions 14 and 17.

The FAD-dependent peroxidases include examples such as nicotinamide adenine dinucleotide (NADH) peroxidase and NADH oxidase. Both of these proteins contain one FAD and gain their reducing equivalents from NADH. However, NADH peroxidase reduces hydrogen peroxide to water using one redox active cysteine residue, while NADH oxidase reduces dioxygen to water using two redox active cysteines (68).

There is also the glutathione peroxidase that contains the unique selenocysteine residue. The reducing equivalents for this peroxidase come from the cofactor glutathione, which upon oxidation forms a disulfide with another glutathione. This disulfide is reduced by the enzyme glutathione reductase, thus replenishing reduced glutathione for the peroxidase (69).

The last group consists of the thiol-specific antioxidant family known as the peroxiredoxins. This novel family of peroxidases contains one or two redox active

cysteine residues, and obtains their reducing equivalents from such proteins as thioredoxin and other redox disulfide sources (70).

Though these three groups of peroxidases have little sequence and structural similarity as well as different redox sources, all of them have at least one or two cysteines or selenocysteine. The proposed mechanism for non-heme non-metal peroxidase catalyzed hydrogen peroxide or alkyl peroxide reduction involves the sulfur (or selenium) of a cysteine residue (Cys-S-H) attacking and reducing the peroxide and subsequently forming a sulfenic acid intermediate (Cys-S-OH). This intermediate is then reduced back to its original thiol form to complete the cycle (68;71). In addition to peroxide detoxification, peroxiredoxins are also thought to play vital roles in redox regulation and signaling.

#### **Anaerobic ROS Detoxification.**

Since an introduction to aerobic ROS detoxification has been addressed, attention will now be placed on the relatively recent discovery of anaerobic ROS detoxification, with a specific focus on superoxide reductase.

**History.** In 1990, LeGall and coworkers were able to isolate a new type of non-heme iron protein from *Desulfovibrio desulfuricans* (ATCC 27774) and *Desulfovibrio vulgaris* (strain Hildenborough) (72). This new 14-kDa protein of unknown function was named desulfoferrodoxin (Dfx) due to its spectroscopic properties being close to that of the rubredoxin-like protein, desulfiredoxin (Dx). At the time, Dfx was suggested to be a rubredoxin oxidoreductase (Rbo), yet this would not be established till later. Initial spectroscopic characterization supported the identity of two different iron coordinations per monomer (72;73). One iron, now termed center I, was believed to have a

coordination similar to desulforedoxin, a tetrahedrally coordinated iron of cysteinyl ligation, and the second iron, center II, of unknown coordination. Further analysis by Johnson and coworkers provided the initial evidence of cysteinyl ligation to the second iron site through the use of resonance Raman spectroscopy (74). Then, in 1997, a crystal structure of *D. desulfuricans* Dfx at 1.9-Å resolution confirmed an overall dimeric structure with each monomer containing a desulforedoxin domain and a second iron site of novel coordination. This new iron site was coordinated by four histidyl-nitrogens (3εN and 1δN) in a planar arrangement and an axially ligated cysteinate-sulfur to yield an overall square pyramidal geometry (75). Despite all of the spectroscopic and crystallographic characterization, Dfx was still a protein of relatively unknown function. However, around the same time, Touati and coworkers had discovered that the *rbo* gene from *Desulfoarculus baarsii* or *D. vulgaris* could be inserted and expressed in mutant *sodA sodB E. coli* and fully complement the phenotypic defects of this mutant (76). This meant that Rbo/Dfx could substitute for Mn-SOD and Fe-SOD and thus implied that Rbo/Dfx had SOD activity. Nevertheless, Touati's studies reported that the classical SOD assay did not show activity for the isolated Dfx. However, later studies by Fridovich showed that Rbo/Dfx expression lowered intracellular superoxide in the *E. coli sodA sodB* (obtained from Touati) and was therefore suggested, although not proven, to scavenge superoxide by reduction (77). Also, in 1994, LeGall and coworkers were able to isolate another non-heme iron protein, this time from the sulfate-reducing bacterium *Desulfovibrio gigas* (78). This novel blue 14-kDa protein of unknown function was named neelaredoxin (Nlr), from Sanskrit *neela* meaning blue and *redoxin* referring to the redox cycling of the iron center. It was also noted that Nlr had a high sequence

homology and analogous spectroscopic properties to the C-terminal domain of Dfx. Then, in 1999, LeGall and coworkers reported superoxide dismutase activities for both Nlr and Dfx (79;80). However, the very same year, Adams and coworkers established that *Pyrococcus furiosus* Nlr was really a superoxide reductase (SOR), rather than a dismutase, supporting Fridovich's proposal (6). Shortly after, Touati, Niviere and coworkers also established the superoxide reductase activity in *D. baarsii* Rbo/Dfx (7). Thus, these groups confirmed the *in vitro* enzymatic reduction of superoxide as well as initiated the debate of *in vivo* reduction versus dismutation activity of both Nlr and Rbo/Dfx.

**Anaerobic Defense Against Superoxide: Superoxide Reductase (SOR).** The enzymatic reduction of superoxide, as opposed to dismutation, involves two key differences. First, dismutation involves superoxide as the lone electron source, whereas, in reduction the electron source is not superoxide but some other electron carrier (vide infra) (e. g. rubredoxin and NAD(P)H) (6;81). The other important difference is that the products of dismutation are dioxygen and hydrogen peroxide, while the product of reduction is only hydrogen peroxide, as shown in equation 18 and 19.



**SOR Gene Organization and ROS Detoxification Scheme.** Since aerobic organisms are under constant threat of ROS, it was initially not surprising to find SODs predominantly located in aerobes and absent in many anaerobes. This distribution pattern was originally rationalized on the basis of anaerobic organisms not requiring a ROS defense mechanism as a result of living in an anaerobic environment. However, Adams

and coworkers argued that anaerobes could be transiently exposed to dioxygen and would subsequently not only need a ROS defense pathway, but more importantly one that would not generate dioxygen (6). Therefore, since Nlr and Rbo/Dfx were initially isolated from anaerobic and microaerophilic microorganisms, the SOR activities of both proteins helped support this novel anaerobic ROS detoxification scheme.

Among the currently sequenced genomes, recognizable SORs are present only in anaerobic and microaerophilic archaea and bacteria. Figure 1.3 provides representative anaerobes with *sor* genes as well as gives a description of the genes associated with the *sor* gene (82). Originally, *sor* was thought to be part of a universal anaerobic ROS detoxification operon, involving the genes encoding rubredoxin (*rub*) and rubrerythrin (*rbr*) in addition to *sor*, as shown in *P. furiosus*, see Figure 1.3. However, some organisms may contain a combination of the two or just *sor* or *rbr*. Due to this inconsistency, these three gene products may or may not work together as previously thought. Regardless of the existence of a specific operon, rubredoxin, a small 7-kDa mononuclear non-heme iron protein, had been shown *in vitro* to reduce the SOR from *P. furiosus* and *D. vulgaris* (6;81). Additionally, in *P. furiosus*, NAD(P)H could reduce rubredoxin by way of an NADPH:rubredoxin oxidoreductase (NROR,  $K_m = 5 \mu\text{M}$  (NADPH) and  $10 \mu\text{M}$  (rubredoxin)) (83). Such considerations have led to a proposal for a simple anaerobic ROS detoxification pathway, see Figure 1.4. This involves the reduction of dioxygen to superoxide, which is subsequently reduced and protonated to yield hydrogen peroxide in a reaction catalyzed by SOR. The reducing equivalents are supplied by NAD(P)H, by way of NADPH:rubredoxin oxidoreductase and rubredoxin. The step involving hydrogen peroxide reduction to water is currently speculative in *P.*

*furiosus*, but may involve rubrerythrin or genes which have homology with various peroxiredoxins and NAD(P)H (per)oxidase (4;6). This novel pathway is also diagrammatically depicted in a simple *P. furiosus* cell, Figure 1.5, to show an overall reaction scheme of superoxide generation, deleterious effects and detoxification. First, only small uncharged molecules, such as dioxygen, may freely diffuse across the cell membrane. Once inside, dioxygen can become reduced to superoxide by a variety of redox agents and enzymes, as previously mentioned. If not properly disposed, superoxide can attack many cellular components and render them inactive. This is of particular concern to proteins with Fe-S clusters. Superoxide is known to attack and oxidize Fe-S clusters, which ultimately releases free Fe into solution (12;84). Though the inactivation of Fe-S clusters is detrimental by itself, the release of free Fe into solution presents a much greater threat, due to Fenton chemistry. To alleviate these deleterious effects, SOR eliminates superoxide by catalyzing its reduction and protonation to hydrogen peroxide. Though not confirmed in *P. furiosus*, hydrogen peroxide is likely to be reduced to water by some peroxidase, represented by X.

**Types of SOR.** SORs are divided into three main groups based on protein sequence alignments from currently sequenced genomes, as shown in Figure 1.6 (85). The SORs of group 1, G1, contain two basic domains. The N-terminal domain is highly homologous to a small mononuclear non-heme iron protein called desulfiredoxin (Dx), whereas, the C-terminal domain is highly homologous to neelaredoxin (Nlr). In common with group 1, group 2, G2, also has two domains. However, while having homology with the C-terminal Nlr domain, the N-terminal domain bears no homology to Dx. The last group, G3, only contains the Nlr domain as well as two insert regions. Oddly enough, all

three types contain roughly the same number of amino acids ( $\sim 124 \pm 2$ ). In accord with the sequence prediction, purified samples of G2 and G3 enzymes were found to contain one iron per monomer and hence have been termed 1Fe-SORs, whereas purified samples of G1 enzymes contain two irons per monomer and have been termed 2Fe-SORs.

Insight into the SOR active-site structure was provided from the detailed x-ray crystallographic and preliminary spectroscopic analyses of the 1Fe-SOR from *P. furiosus* (86), Figures 1.7 and 1.8, and the 2Fe-SOR from *D. desulfuricans* (72;74;75), Figures 1.9 and 1.10. Initial enzymology and spectroscopic analysis has also helped characterize the 1Fe-SOR from *Desulfovibrio gigas* (78;80), *Treponema pallidum* (87;88), and *Archaeoglobus fulgidus* (89), as well as the 2Fe-SOR from *Desulfovibrio vulgaris* (73;85;90), and *Desulfoarculus baarsii* (7). Table 1.1 summarizes the structural and redox properties of the currently purified 1Fe- and 2Fe-SORs.

The *P. furiosus* 1Fe-SOR crystal structure, shown in Figure 1.7, was determined to a resolution of 1.7 and 2.0 Å for the oxidized and reduced forms, respectively (86). The overall structure consists of a homotetramer, with each monomer adopting an immunoglobulin-like  $\beta$ -barrel fold that coordinates a mononuclear non-heme iron center. This novel iron site, as seen in Figure 1.8, is coordinated by four histidyl nitrogens (3 $\epsilon$  and 1 $\delta$ ) in a planar arrangement, and one axially ligated cysteinate sulfur. Unfortunately, the crystal structure displayed heterogeneity in terms of a sixth ligand. In two of the subunits of the oxidized structure, a monodentate glutamate carboxylate served as the ligand to form an overall six-coordinate, octahedral geometry. In the remaining two subunits, the sixth coordination site is either vacant or occupied by solvent molecules, see Figure 1.8a. The iron centers in all four subunits of the reduced structure exhibit square

pyramidal pentacoordination, with loss of glutamate ligation and subsequent movement of a lysine  $\epsilon$ -amino group 6.0 Å above the open iron site, see Figure 1.8b. However, the reduced protein also exhibited low iron occupancy, which made metal-ligand distances unreliable in this state. The crystallographic heterogeneity in both the oxidized and reduced forms of *P. furiosus* 1Fe-SOR therefore needed to be addressed by spectroscopic studies in solution.

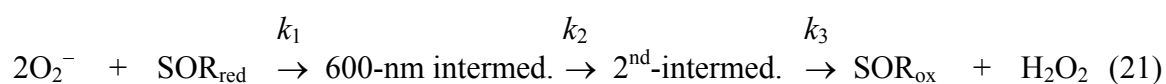
The *D. desulfuricans* 2Fe-SOR crystal structure, shown in Figure 1.9, was determined to a resolution of 1.9 Å in what was presumed to be the oxidized form (75). The overall structure of the 2Fe-SOR is a homodimer, with each monomer containing two domains and one iron atom within each domain. Each monomer is joined together by H-bonding as well as one calcium ion. The N-terminal domain I coordinates a single iron atom, termed center I, through four highly conserved cysteinate sulfurs in a distorted tetrahedral geometry, similar to Dx. The C-terminal domain II, similar to the *P. furiosus* 1Fe-SOR, adopts an immunoglobulin-like  $\beta$ -barrel fold that coordinates a mononuclear non-heme iron center, termed center II. The center II iron is coordinated in a square pyramidal arrangement very close to that of the reduced 1Fe-SOR. While glutamate coordination was not present in the *D. desulfuricans* 2Fe-SOR crystal structure, lysine 47  $\epsilon$ -amino group was located 7.4 Å above the open iron site, strikingly similar to the reduced *P. furiosus* 1Fe-SOR structure. However, a clear picture of the oxidized and reduced active-site structures for both 1Fe- and 2Fe-SORs has yet to be deduced from crystallography. This is one of the objectives addressed in this dissertation.

**SOR Reaction Kinetics, Spectroscopy and Overall Mechanism.** While the crystal structure and preliminary spectroscopy of both 1Fe- and 2Fe-SORs have yielded a great deal of structural insight, there still remain many questions concerning iron coordination and the mechanism of enzymatic superoxide reduction. There have been two main approaches to address these questions, namely pulse-radiolytic kinetic techniques and detailed spectroscopic studies, each involving wild-type and site-specific active-site variants. Both approaches over the past three years have complemented each other to yield a proposed pathway of SOR mediated superoxide reduction, see Figure 1.11 (4;91;92). Since this thesis presents spectroscopic data in support of the proposed pathway, a summary of the recent pulse-radiolytic kinetic results is presented below.

Since the reduction of superoxide by SOR occurs at a nearly diffusion-controlled rate, one way to monitor this reaction is through the combination of pulse radiolysis and ultra-fast absorption techniques. Pulse radiolysis is a technique that generates high-energy electrons, in this case, for the ultimate reduction of dioxygen to superoxide. This process is used to generate a controlled amount of superoxide in a sample cuvette that also contains SOR. The generation and decay of superoxide as well as any SOR (hydro)peroxy-ferric intermediates is monitored by ultra-fast absorption spectroscopy. Finally, kinetic fits are applied to the generation and decay of each species for the purpose of determining kinetic order and constants ( $k$ ) as well as some thermodynamic properties associated with the reaction.

In brief, pulse radiolytic kinetic results on 1Fe- and 2Fe-SORs have led to the identification of at least one chromophoric intermediate with a visible absorption band centered near 600 nm (89;90;92;93) and possibly another with a visible absorption band

centered at 550 nm (94;95). Table 1.2 summarizes the various 1Fe- and 2Fe-SOR pulse-radiolytic kinetic results from the organisms *D. vulgaris* (90;92), *D. baarsii* (95), *T. pallidum* (94) and *A. fulgidus* (89;93). The kinetic constants, presented in Table 1.2, for *D. vulgaris* and *A. fulgidus* correspond to reaction 20, whereas the constants for *T. pallidum* and *D. baarsii* correspond to reaction 21.



Though absorption spectroscopy provides little detail regarding the exact identity of these intermediates, the kinetics can still support the proposed mechanism in Figure 1.11. Most SORs have a nearly diffusion-controlled formation of the ~600-nm intermediate, with a bimolecular rate constant  $k_1 \sim 1 \times 10^9 \text{ M}^{-1}\text{s}^{-1}$ , which corresponds to step 2 in Figure 1.11. However, the kinetics of steps 3 and 4 are currently debated. The respective 1Fe- and 2Fe-SORs from *A. fulgidus* and *D. vulgaris* support a decay of the ~600-nm intermediate with a first order rate constant  $k_2$  which is  $20,000 \text{ s}^{-1}$  and  $84 \text{ s}^{-1}$  respectively (92;93). The results for these two SORs provide no clear evidence for a second intermediate, and therefore it is unclear whether  $k_2$  corresponds to a combination or separation of steps 3 and 4. However, the 1Fe-SOR from *T. pallidum* supports a  $k_2$  which is  $4800 \text{ s}^{-1}$  and is thought to correspond to step 3 (94). The 2Fe-SOR from *D. baarsii* appears to support a  $k_2$  which is  $500 \text{ s}^{-1}$  and  $k_3$  which is  $25 \text{ s}^{-1}$  and it is thought that these constants respectively correspond to steps 3 and 4 (95).

## Summary of Presented Work

The research in this dissertation focuses on resolving the crystallographic heterogeneity of the iron active-site in both 1Fe- and 2Fe-SORs, as well as understanding the enzymatic mechanism of superoxide reduction by detecting the effects of pH and redox variation, exogenous ligand binding and mutagenesis on the SOR iron active site through a wide array of spectroscopic techniques. The combination of these techniques provides a detailed electronic and geometric structure of the SOR iron active site that correlates to function and reactivity along the reaction coordinate.

Chapter 2 is a detailed spectroscopic investigation of *P. furiosus* 1Fe-SOR as a function of pH and exogenous ligand binding. The results indicate that (Cys)S – Fe  $\pi$  bonding is important in providing a strong trans influence in both oxidized and reduced SOR. Also, near-IR absorption, CD and VTMCDC results confirmed that reduced SOR has a square pyramidal ferrous site with an open binding site trans to the cysteinyl sulfur. Lastly, the binding of azide and cyanide to the reduced SOR iron site supported an inner-sphere mechanism for superoxide reduction.

Chapter 3 is an assessment of the vibrational characteristics of the (Cys)S–Fe unit of *P. furiosus* 1Fe-SOR using resonance Raman spectroscopy. Through the use of isotopically labeled SOR, vibrations associated with the (Cys)S – Fe unit were identified. The strong resonant enhancement of these vibrations suggested that the cysteinyl sulfur ligation is important for providing a superexchange pathway for electron transfer, thereby promoting reductive binding of substrate and effecting product release.

Chapter 4 addresses the use of NO as a substrate analog to superoxide in order to probe the electronic determinates of enzymatic superoxide reduction. EPR, absorption,

VTMCD, resonance Raman and FTIR spectroscopies provide evidence for the reductive binding of NO to the reduced iron active-site in *P. furiosus* 1Fe-SOR. The results indicate that the trans cysteinyl sulfur and the iron spin state play important roles in mediating electron transfer and effecting product release.

Chapter 5 provides a detailed spectroscopic analysis of *D. vulgaris* 2Fe-SOR as well as a comparison to *P. furiosus* 1Fe-SOR. The results reveal spectroscopic differences between the oxidized SOR active-sites that are best interpreted in terms of minor changes in the conformation of the Fe–S(Cys) unit and may be important in mediating electron transfer to the unique iron active site. However, the electronic properties of the oxidized and reduced active sites in 1Fe- and 2Fe-SORs are shown to be very similar, reinforcing the importance of the trans cysteinyl sulfur and high-spin state iron to mediate superoxide reduction and effect peroxide release. The binding of ferrocyanide to the SOR iron active site is also addressed.

## References

1. Fridovich, I. (1998) *J. Exp. Biol.* 201, 1203-1209.
2. McCord, J. M. and Fridovich, I. (1969) *J. Biol. Chem.* 244, 6049-6055.
3. McCord, J. M. (2000) *Am. J. Med.* 108, 652-659.
4. Adams, M. W. W., Jenney, Jr. F. E., Clay, M. D., and Johnson, M. K. (2002) *J. Biol. Inorg. Chem.* 7, 647-652.
5. Abreu, I. A., Xavier, A. V., LeGall, J., Cabelli, D. E., and Teixeira, M. (2002) *J. Biol. Inorg. Chem.* 7, 668-674.
6. Jenney, F. E., Verhagen, M. F. J. M., Cui, X., and Adams, M. W. W. (1999) *Science* 286, 306-309.
7. Lombard, M., Fontecave, M., Touati, D., and Nivière, V. (2000) *J. Biol. Chem.* 275, 115-121.
8. Auchere, F. and Rusnak, F. (2002) *J. Biol. Inorg. Chem.* 7, 664-667.
9. Fridovich, I. (1997) *J. Biol. Chem.* 272, 18515-18517.
10. Sawyer, D. T. and Valentine, J. S. (1981) *Acc. Chem. Res.* 14, 393-400.
11. Pierre, J. L. and Fontecave, M. (1999) *BioMetals* 12, 195-199.
12. Valentine, J. S., Wertz, D. L., Lyons, T. J., Liou, L.-L. G. J. J., and Gralla, E. B. (1998) *Curr. Opin. Chem. Biol.* 2, 253-262.
13. Stohs, S. J. and Bagchi, D. (1995) *Free Radic. Biol. Med.* 18, 321-336.
14. Sawyer, D. T. and Gibian, M. J. (1979) *Tetrahedron* 35, 1471-1481.

15. Vaille, A., Jadot, G., and Elizagaray, A. (1990) *Biochem. Pharmacol.* 39, 275-282.
16. Warren, J. S., Yabroff, K. R., Mandel, D. M., and Johnson, K. J. (1990) *Free Radic. Biol. Med.* 8, 163-172.
17. Shah, S. V. (1995) *Annu. Rev. Physiol.* 57, 245-262.
18. Omar, B. A. and McCord, J. M. (1991) *J. Mol. Cell. Cardiol.* 23, 149-159.
19. Baker, K., Marcus, C. B., Huffman, K., Kruk, H., Malfroy, B., and Doctrow, S. R. (1998) *J. Pharmacol. Exp. Ther.* 284, 215-221.
20. Toshniwal, P. K. and Zarling, E. J. (1992) *Neurochem. Res.* 17, 205-207.
21. Lyras, L., Cairns, N. J., Jenner, A., Jenner, P., and Halliwell, B. (1997) *J. Neurochem.* 68, 2061-2069.
22. Cohen, G. (1984) *Neurotoxicology* 5, 77-82.
23. Aguirre, T., Matthijs, G., Robberecht, W., Tilkin, P., and Cassiman, J. J. (1999) *Eur. J. Hum. Genet.* 7, 599-602.
24. Ragusa, R. J., Chow, C. K., and Porter, J. D. (1997) *Neuromuscul. Disord.* 7, 379-386.
25. Flores, S. C., Marecki, J. C., Harper, K. P., Bose, S. K., Nelson, S. K., and McCord, J. M. (1993) *Proc. Natl. Acad. Sci. U. S. A.* 90, 7632-7636.
26. Davies, G. R., Simmonds, N. J., Stevens, T. R. J., Grandison, A., Blake, D. R., and Rampton, D. S. (1992) *Gut.* 33, 1467-1472.
27. Kerr, S., Brosnan, M. J., McIntyre, M., Reid, J. L., Dominiczak, A. F., and Hamilton, C. A. (1999) *Hypertension* 33, 1353-1358.

28. Dianzani, M. U. (1985) *Alcohol Alcohol.* 20, 161-173.
29. Asami, S., Manabe, H., Miyake, J., and et al. (1997) *Carcinogenesis* 18, 1763-1766.
30. Harman, D. (1956) *J. Gerontol.* 2, 298-300.
31. McCord, J. M. and Fridovich, I. (1968) *J. Biol. Chem.* 243, 5753-5760.
32. Knowles, P. F., Gibson, J. F., Pick, F. M., Brick, F., and Bray, R. C. (1969) *Biochem. J.* 111, 53-58.
33. Imlay, J. A. (2002) *J. Biol. Inorg. Chem.* 7, 659-663.
34. Fielden, E. M., Roberts, P. B., Bray, R. C., Lowe, D. J., Mautner, G. N., Rotilio, G., and Calabrese, L. (1971) *Biochem. J.* 139, 49-60.
35. McCord, J. M., Keele, Jr. B. B., and Fridovich, I. (1971) *Proc. Natl. Acad. Sci. U. S. A.* 68, 1024-1027.
36. Hassan, H. M. and Fridovich, I. (1977) *J. Biol. Chem.* 252, 7667-7672.
37. Gregory, E. M. and Fridovich, I. (1973) *J. Bacteriol.* 114, 543-548.
38. Carlioz, A. and Touati, D. (1986) *EMBO J.* 5, 623-630.
39. Natvig, D. O., Imlay, K., Touati, D., and Hallewell, R. A. (1987) *J. Biol. Chem.* 262, 14697-14701.
40. Tainer, J. A., Getzoff, E. D., Beem, K. M., Richardson, J. S., and Richardson, D. C. (1982) *J. Mol. Biol.* 160, 181-217.
41. Holm, R. H., Kennepohl, P., and Solomon, E. I. (1996) *Chem. Rev.* 96, 2239-2314.

42. Klug, D., Rabani, J., and Fridovich, I. (1972) *J. Biol. Chem.* 247, 4839-4842.
43. Keele, Jr. B. B., McCord, J. M., and Fridovich, I. (1970) *J. Biol. Chem.* 245, 6176-6181.
44. Lah, M. S., Dixon, M. M., Pattridge, K. A., Stallings, W. C., Fee, J. A., and Ludwig, M. L. (1995) *Biochemistry* 34, 1646-1660.
45. McAdam, M. E., Fox, R. A., Lavelle, F., and Fielden, E. M. (1977) *Biochem. J* 165, 71.
46. Yost, Jr. F. J. and Fridovich, I. (1973) *J. Biol. Chem.* 248, 4905-4908.
47. Fee, J. A., McClune, G. J., O'Neill, P., and Fielden, E. M. (1981) *Biochem. Biophys. Res. Commun.* 100, 377.
48. Meier, B., Barra, D., Bossa, F., Calabrese, L., and Rotilio, G. (1982) *J. Biol. Chem.* 257, 13977-13980.
49. Gregory, E. M. and Dapper, C. H. (1983) *Archs. Biochem. Biophys.* 220, 293-300.
50. Youn, H.-D., Kim, E.-J., Roe, J.-H., Hah, Y. C., and Kang, S.-O. (1996) *Biochem. J.* 318, 889-896.
51. Kim, E.-J., Chung, H.-J., Suh, B., Hah, Y. C., and Roe, J.-H. (1998) *Mol. Microbiol.* 27, 187-195.
52. Choudhury, S. B., Lee, J.-W., Davidson, G., Yim, Y.-I., Bose, K., Sharma, M. L., Kang, S.-O., Cabelli, D. E., and Maroney, M. J. (1999) *Biochemistry* 38, 3744-3752.
53. Maroney, M. J. (1999) *Curr. Opin. Chem. Biol.* 3, 188-199.

54. Loew, O. (1900) *U. S. Dept. of Agri. Repts.* 65, 5.
55. Nicholls, P., Fita, I., and Loewen, P. C. (2001) *Adv. Inorg. Chem.* 51, 51-106.
56. Switala, J. and Loewen, P. C. (2002) *Archs. Biochem. Biophys.* 401, 145-154.
57. Lippard, S. J. and Berg, J. M. (1994) *Principles of Bioinorganic Chemistry* University Science Books, Mill Valley, CA.
58. Barynin, V. V., Whittaker, M. M., Antonyuk, S. V., Lamzin, V. S., Harrison, P. M., Artymiuk, P. J., and Whittaker, J. W. (2001) *Structure* 9, 725-738.
59. Waldo, G. S. and Penner-Hahn, J. E. (1995) *Biochemistry* 34, 1507-1512.
60. O'Brian, P. J. (2000) *Chem. Biol. Interact.* 129, 113-139.
61. Veitch, N. C. and Smith, A. T. (2001) *Adv. Inorg. Chem.* 51, 107-162.
62. Voet, D. and Voet, J. G. (1995) *Biochemistry* Wiley, New York.
63. Miller, M. A. (1996) *Biochemistry* 35, 15791-15799.
64. Banci, L. (1997) *J. Biotech.* 53, 253-263.
65. Vollenbroek, E. G. M., Simons, L. H., van Schijndel, J. W. P. M., Barnett, P., Balzar, M., Dekker, H., van der Linden, C., and Wever, R. (1995) *Biochem. Soc. Trans.* 23, 267-271.
66. Hemrika, W., Renirie, R., Dekker, H. L., Barnett, P., and Wever, R. (1997) *Proc. Natl. Acad. Sci. U. S. A.* 94, 2145-2149.
67. Weyand, M., Hecht, H.-J., Kieb, M., Liaud, M.-F., Vilter, H., and Schomburg, D. (1999) *J. Mol. Biol.* 293, 595-611.

68. Claiborne, A., Yeh, J. I., Conn Mallett, T., Luba, J., Crane, I. E. J., Charrier, V., and Parsonage, D. (1999) *Biochemistry* 38, 15407-15416.
69. Arthur, J. R. (2000) *Cell. Mol. Life Sci.* 57, 1825-1835.
70. Rhee, S. G., Kang, S. W., Chang, T.-S., Jeong, W., and Kim, K. (2001) *IUBMB Life* 52, 35-41.
71. Nunn, C. M., Djordjevic, S., Hillas, P. J., Nishida, C. R., and Ortiz de Montellano, P. R. (2002) *J. Biol. Chem.* 277, 20033-20040.
72. Moura, I., Tavares, P., Moura, J. J. G., Ravi, N., Huynh, B. H., Liu, M.-Y., and LeGall, J. (1990) *J. Biol. Chem.* 265, 21596-21602.
73. Verhagen, M. F. J. M., Voorhorst, W. G. B., Kolkman, J. A., Wolbert, R. B. G., and Hagen, W. R. (1993) *FEBS Lett.* 336, 13-18.
74. Tavares, P., Ravi, N., Moura, J. J. G., LeGall, J., Huang, Y.-H., Crouse, B. R., Johnson, M. K., Huynh, B. H., and Moura, I. (1994) *J. Biol. Chem.* 269, 10504-10510.
75. Coelho, A. V., Matias, P., Fülöp, V., Thompson, A., Gonzalez, A., and Carrondo, M. A. (1997) *J. Biol. Inorg. Chem.* 2, 680-689.
76. Pianzolla, M. J., Soubes, M., and Touati, D. (1996) *J. Bacteriol.* 178, 6736-6742.
77. Liochev, S. I. and Fridovich, I. (1997) *J. Biol. Chem.* 272, 25573-25575.
78. Chen, L., Sharma, P., LeGall, J., Mariano, A. M., Teixeira, M., and Xavier, A. V. (1994) *Eur. J. Biochem.* 226, 613-618.
79. Romão, C. V., Liu, M.-Y., LeGall, J., Gomes, C. M., Braga, V., Pacheco, I., Xavier, A. V., and Teixeira, M. (1999) *Eur. J. Biochem.* 261, 438-443.

80. Silva, G., Oliveira, S., Gomes, C. M., Pacheco, I., Liu, M.-Y., Xavier, A. V., Teixeira, M., LeGall, J., and Rodrigues-Pousada, C. (1999) *Eur. J. Biochem.* 259, 235-243.
81. Coulter, E. D. and Kurtz, D. M., Jr. (2001) *Arch. Biochem. Biophys.* 394, 76-86.
82. Lumpio, H. L., Shenvi, N. V., Summers, A. O., Voordouw, G., and Kurtz, Jr. D. M. (2001) *J. Bacteriol.* 183, 101-108.
83. Ma, K. and Adams, M. W. W. (1999) *J. Bacteriol.* 181, 5530-5533.
84. Kurtz, Jr. D. M. and Coulter, E. D. (2001) *Chemtracts* 14, 407-435.
85. Ascenso, C., Rusnak, F. M., Cabrito, I., Lima, M. J., Naylor, S., Moura, I., and Moura, J. J. G. (2000) *J. Biol. Inorg. Chem.* 5, 720-729.
86. Yeh, A. P., Hu, Y., Jenney, F. E., Adams, M. W. W., and Rees, D. C. (2000) *Biochemistry* 39, 2499-2508.
87. Jovanovi'c, T., Ascenso, C., Hazlett, K. R. O., Sikkink, R., Krebs, C., Litwiller, L. M., Benson, L. M., Moura, I., Moura, J. J. G., Radolf, J. D., Huynh, B. H., Naylor, S., and Rusnak, F. M. (2000) *J. Biol. Chem.* 275, 28439-28448.
88. Lombard, M., Touati, D., Fontecave, M., and Nivière, V. (2000) *J. Biol. Chem.* 275, 27021-27026.
89. Abreu, I. A., Saraiva, L. M., Carita, J., Huber, H., Stetter, K. O., Cabelli, D. E., and Teixeira, M. (2000) *Mol. Microbiol.* 38, 322-334.
90. Coulter, E. D., Emerson, J. P., Kurtz, D. M., Jr., and Cabelli, D. E. (2000) *J. Am. Chem. Soc.* 122, 11555-11556.
91. Coulter, E. D. and Kurtz, Jr. D. M. (2002) *J. Biol. Inorg. Chem.* 7, 653-658.

92. Emerson, J. P., Coulter, E. D., Cabelli, D. E., Phillips, R. S., and Kurtz, Jr. D. M. (2002) *Biochemistry* 41, 4348-4357.
93. Abreu, I. A., Saraiva, L. M., Soares, C. M., Teixeira, M., and Cabelli, D. E. (2001) *J. Biol. Chem.* 276, 38995-39001.
94. Nivière, V., Lombard, M., Fontecave, M., and Houée-Levin, C. (2001) *FEBS Lett.* 497, 171-173.
95. Lombard, M., Houée-Levin, C., Touati, D., Fontecave, M., and Nivière, V. (2001) *Biochemistry* 40, 5032-5040.

Table 1.1 Properties of purified 1Fe- and 2Fe-SORs.

SOR Type	Oligomer	Fe / Monomer	Fe Coordination	Midpoint Potential (mV)	Organism	References
1Fe-SOR	Homotetramer (~ 14 kDa monomer)	1	[Fe(NHis) <sub>4</sub> (SCys)]	+250 +190 +250 ~ +200	<i>Pyrococcus furiosus</i> <i>Desulfovibrio gigas</i> <i>Archaeoglobus fulgidus</i> <i>Treponema pallidum</i>	(6;87) (78) (91;95) (89;90)
2Fe-SOR	Homodimer (~ 14 kDa monomer)	2	CI: [Fe(SCys) <sub>4</sub> ] CII: [Fe(NHis) <sub>4</sub> (SCys)]	CI = +4; CII = +240 CI = +2; CII = +90 CI = -2; CII = +247 N.A.	<i>Desulfovibrio desulfuricans</i> <i>Desulfovibrio vulgaris</i> <i>D. vulgaris truncated</i> <i>Desulfoarculus baarsii</i>	(72) (72;73) (85) (7)

Table 1.2 Summary of 1Fe- and 2Fe-SOR rate constants. The rate constants ( $k_1$ ,  $k_2$  and  $k_3$ ) refer to reactions 20 and 21. Modified from (5). n.p., not presented; (-), not observed.

<b>SOR Type and Organism</b>	<b><math>k_1</math> (M<sup>-1</sup>s<sup>-1</sup>)</b>	<b><math>k_2</math> (s<sup>-1</sup>)</b>	<b><math>k_3</math> (s<sup>-1</sup>)</b>	<b>References</b>
WT 2Fe-SOR, <i>D. vulgaris</i>	1.4 x 10 <sup>9</sup>	84	(-)	(92;94)
E47A 2Fe-SOR, <i>D. vulgaris</i>	2.2 x 10 <sup>9</sup>	65	(-)	(92;94)
K48A 2Fe-SOR, <i>D. vulgaris</i>	2.1 x 10 <sup>8</sup>	25	(-)	(94)
WT 2Fe-SOR, <i>D. baarsii</i>	1.1 x 10 <sup>9</sup>	500	25	(97)
E47A 2Fe-SOR, <i>D. baarsii</i>	1.2 x 10 <sup>9</sup>	440	20	(97)
K48I 2Fe-SOR, <i>D. baarsii</i>	3.8 x 10 <sup>7</sup>	300	n.p.	(97)
WT 1Fe-SOR, <i>T. pallidum</i>	6.0 x 10 <sup>8</sup>	4800	n.p.	(96)
WT 1Fe-SOR, <i>A. fulgidus</i>	1.5 x 10 <sup>9</sup>	2 x 10 <sup>4</sup>	(-)	(91;95)
E12Q 1Fe-SOR, <i>A. fulgidus</i>	1.5 x 10 <sup>9</sup>	2 x 10 <sup>4</sup>	(-)	(95)
E12V 1Fe-SOR, <i>A. fulgidus</i>	4.0 x 10 <sup>8</sup>	2 x 10 <sup>4</sup>	(-)	(95)

Figure 1.1 Dioxygen-based redox chemistry at pH 7 (mV/NHE). Adapted from (11).

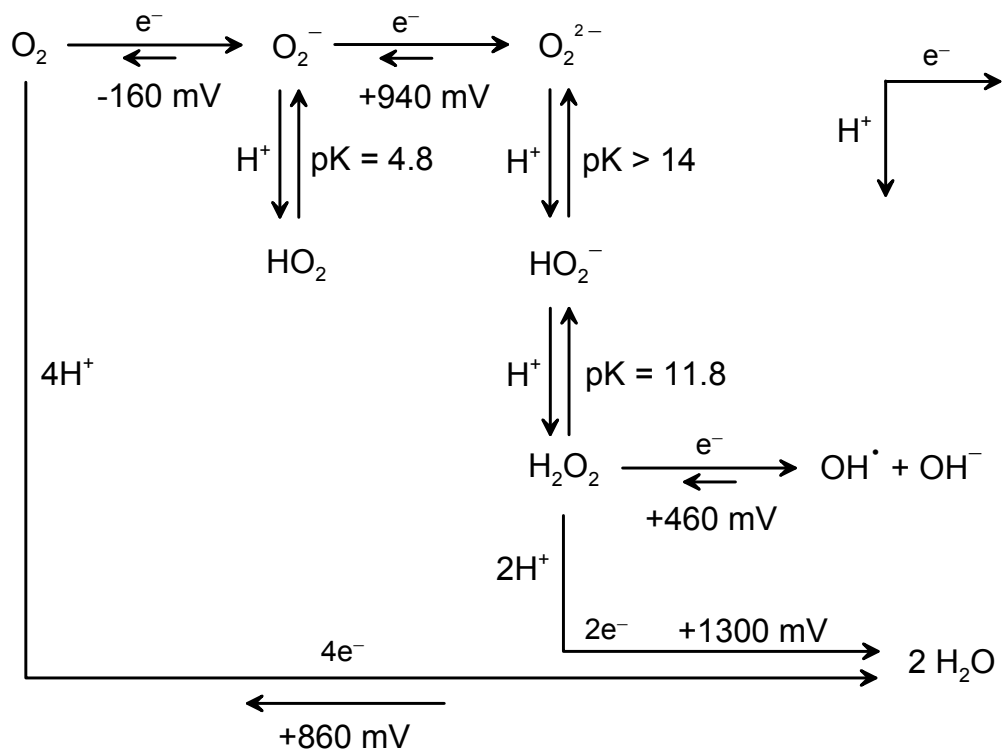


Figure 1.2 Biological superoxide generation, effects and detoxification. Modified from (8).

## Generation

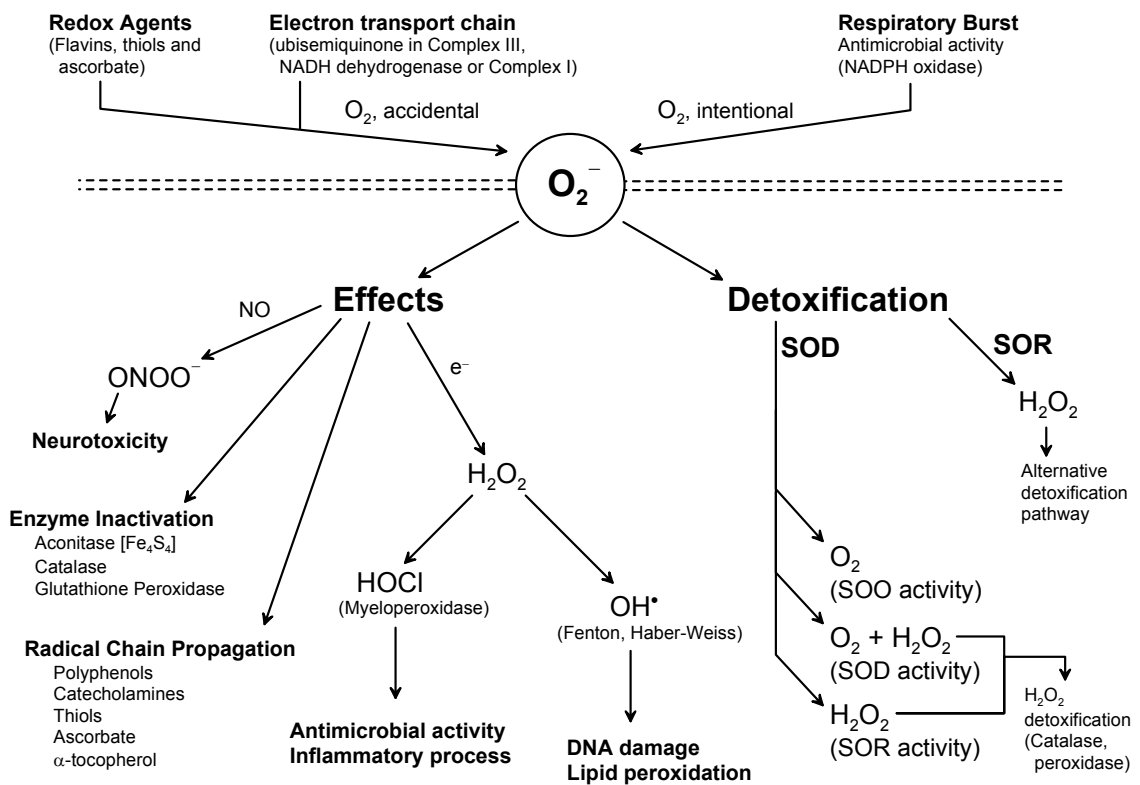


Figure 1.3 SOR gene organization and possible ROS detoxification operon in selected archaea and bacteria. Modified from (82).

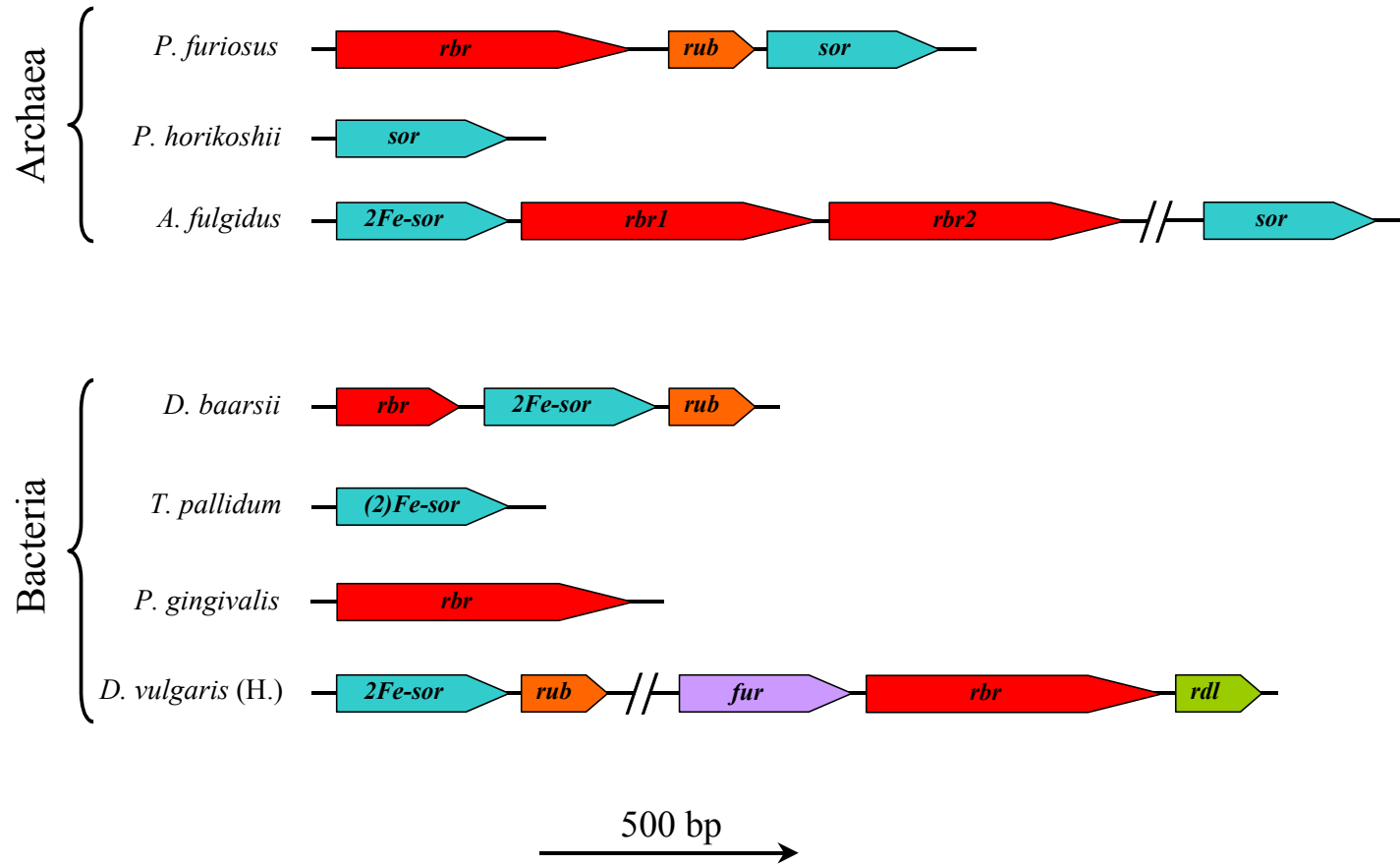


Figure 1.4 Proposed anaerobic ROS detoxification pathway in *Pyrococcus furiosus*.  
Modified from (4; 6).

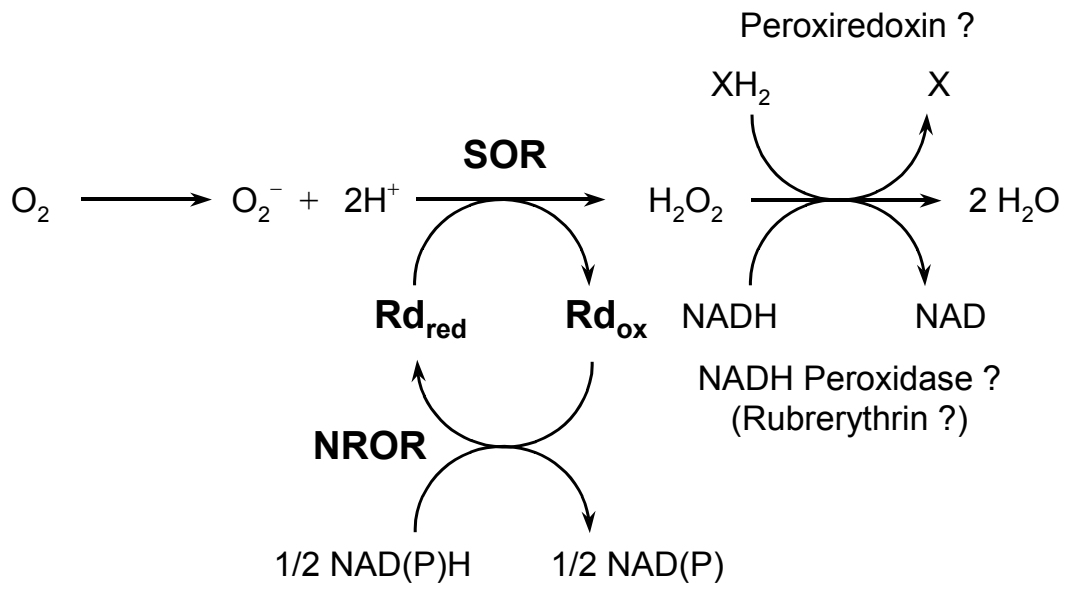


Figure 1.5 Proposed *in vivo* superoxide generation, effects and detoxification in a typical *Pyrococcus furiosus* cell. Modified from (82).

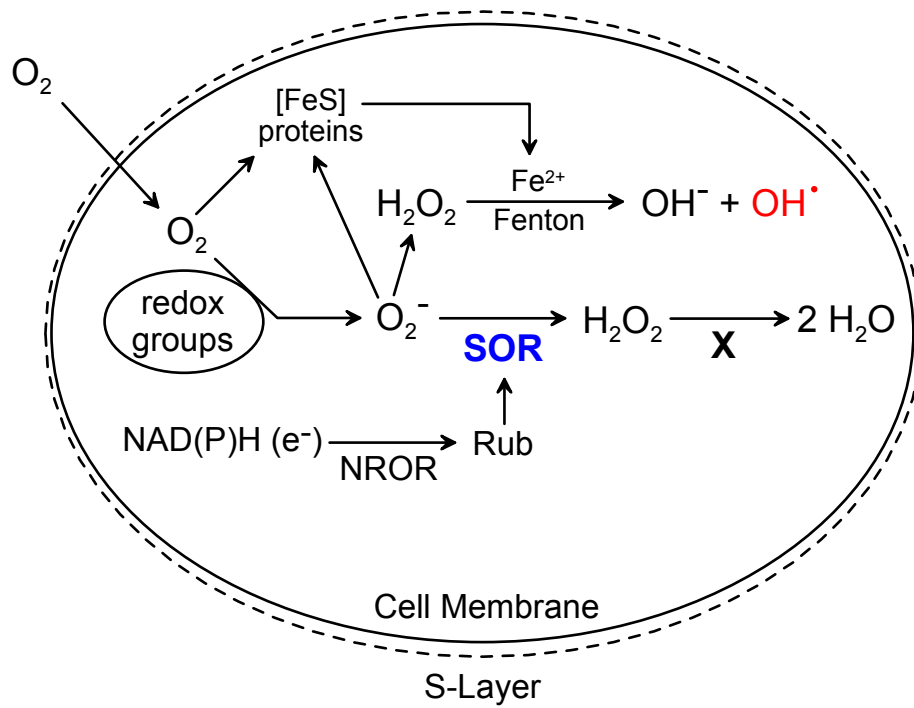


Figure 1.6 Sequence alignments of SOR homologues. The arrows refer to conserved iron binding residues. Dfx, desulfoferrodoxin; Dx, desulforedoxin; Nlr, Neelaredoxin; *A.f.*, *Archaeoglobus fulgidus*; *C.a.*, *Clostridium acetobutylicum*; *D.b.*, *Desulfoarculus baarsii*; *D.d.*, *Desulfovibrio desulfuricans* (ATCC 27774); *D.g.*, *Desulfovibrio gigas*; *D.v.* (H), *Desulfovibrio vulgaris* (Hildenborough); *D.v.* (M), *Desulfovibrio vulgaris* (Miyazaki); *M.t.*, *Methanobacterium thermoautotrophicum*; *M.j.*, *Methanococcus jannaschii*; *P.f.*, *Pyrococcus furiosus*; *P.h.*, *Pyrococcus horikoshii*; *P.a.*, *Pyrococcus abyssi*; *T.m.*, *Thermotoga maritima*; *T.p.*, *Treponema pallidum*. Modified from (85).

		↓ ↓	↓ ↓ ↓	↓	↓	↓
G1	<i>D.g. Dx</i>	MANEGDVYKCELCGQVVKVL-EEGGGTLVCCGEDMVKQ-----				
	<i>D.v. (H) Dfx</i>	MPNQYEIYKCIHCGNIVEVL-HAGGGDLVCCGEPMKLMKEGTS DGAKEKHVPVIE-----KTANGYKVTV--GS-VAHPMEEKHWIEW				
	<i>D.v. (M) Dfx</i>	. PNMLEVYKCVHCGNIVEVM-HAGGGDLVCCGEPMKFMKEGTS DGAKEKHVPVIE-----KTATGYKVKV--GS-VAHPMEEETHWIEW				
	<i>D.d Dfx</i>	. PKHLEVYKCTHCGNIVEVL-HGGGAELVCCGEPMKHMVEGSTDGAMEKHVPVIE-----KVDGGYL IKV--GS-VPHPMEEKHWIEW				
	<i>D.b. Dfx</i>	MPERLQVYKCEVCGNIVEVL-NGGIGELVCCNQDMKLMSENTVDAAKEKHVPVIE-----KIDGGYKVKV--GA-VAHPMEEKHYIQW				
	<i>M.t. Dfx</i>	MTETNQIFRCNVCGNIVEVL-NPGAGQLVCCNQPMELLVARRTDVGPEKHVPVVE-----ETGTGIRVKV--GE-VPHPMEEENHHIQW				
	<i>A.f. Dfx</i>	MTEVMQVYKCMVCGNIVEVV-HAGRGQLVCCGQPMKLMEVKTDEGKEKHVPVIE-----REGNKVYVKV--GS-VAHPMEEQHYIEW				
G2	<i>C.a.</i>	MNNDLSIYVSKNSGTAVLLL-QGNGTDLTCGSEPAKIVANTTDAAQEKHVPHIT-----KNGNNIDVSV--GS-VEHPMTPEHFIEW				
	<i>T.p.</i>	MGRELSFFLQKESAGFFLGMDAPAGSSVACGSEVLRAPVGTVDAAKEKHIPVVE---V-HGHEVKVKV--GS-VAHPMTPEHYIAW				
G3	<i>D.g. Nlr</i>	-----MKMCDMEQ-TADWKTEKHVPAIECDDAVAADAFFPVTVSLGKEIAHPNTEHHIRW				
	<i>T.m. Nlr/SOR</i>	-----MKLSDFIK-TEDFKKEKHVPVIEAPEKVKKDEKVQIVVTVGKEIPHPNTEHHIRW				
	<i>A.f. Nlr/SOR</i>	-----MELFQTADWKKEKHVPVIEVLAEGGVVEVKVSV--GKEIPHPNTEHHIAW				
	<i>P.f. SOR</i>	-----MISETIRSGDWKGEKHVPVIEYER-EGELVKVKVQV--GKEIPHPNTEHHIRY				
	<i>P.h. Nlr/SOR</i>	-----MVKFAAKWCAKSLVHHKAKVIGMLKETIRSGDWKGEKHVPVIEY-EREGDLVKVEVSV--GKEIPHPNTEHHIAW				
	<i>P.a. Nlr/SOR</i>	-----MVGMLKDTIKSGDWKGEKHVPVIEY-EKEGDLVKVEVSV--GKEIPHPNTEHHIAW				
	<i>M.j. Nlr/SOR</i>	-----MTHYCGINRMKE-GTDF EKKHTPFIECKDRVKANDYFEVKISTG--IPHPMEDNHF IHW				

		↓ ↓
<i>D.g. Dx</i>	-----	
<i>D.v. (H) Dfx</i>	IELVAD--GV-----SYKKFLK-----PGDAP-EAEFCIK-ADK-----VV-AREYCNLHGHWKAEA	}
<i>D.v. (M) Dfx</i>	IELIAD--GR-----SYTRFLK-----PGDAP-EAEFCIQ-ATE-----VS-AREYCNLHGHWKA	
<i>D.d Dfx</i>	IELLAD--GR-----SYTKFLK-----PGDAP-EAFFAID-ASK-----VT-AREYCNLHGHWKAEN	
<i>D.b. Dfx</i>	IELLAD--DK-----CYTQFLK-----PGQAP-EAVFLIE-AAK-----VV-AREYCNHGHWKAEN	
<i>M.t. Dfx</i>	IEVIA--GDM-----VYRKDLN-----PGDNP-EAEFPVEMASDFM---V---RIYCNHGLWY	
<i>A.f. Dfx</i>	IEVIDD--GC-----VHRKQLK-----PGDEPK-AEFTV-M-SDR-----VS-ARAYCNHGLWQSG	
<i>C.a.</i>	IILV---SGDRLEMA---KLT-----PDMKP-RAQFHNVTSGT-----V-YA--YCNLHSLWKADI	
<i>T.p.</i>	VCLK-TRKG-IQL-----KEL-----PVDGAPEVTFALTADDQ-----VLEAYEFCNLHGVWSGK	
<i>D.g. Nlr</i>	IRCYFKPEGDKFSEYVGSFEFTAHGECAGPNEGPVYTNHTVTFQLKIKTPGVLVASSFCNIHGLWES SKAVALK	
<i>T.m. Nlr/SOR</i>	IKVFFQPDGDPYVYEVGRYEFNAHGESVQGPNIGAVYTEPTVTTVVKLNRS GTIIALS YCNHGLWES SQKITVEE	
<i>A.f. Nlr/SOR</i>	IELVFQPEGSKFPYVVGRAEFAAHGASVDGPNTSGVYTDPAVAFKAEKSGKLTAFS YCNHGLWGMGEA	
<i>P.f. SOR</i>	IELYFLPEGENFVYQVGRVEFTAHGESVNGPNTSDVYTEPIAYFVLKTKKKGKLYALS YCNHGLWENE	
<i>P.h. Nlr/SOR</i>	IELYFHPEGGQFPILVGRVEFTNHSD---PLTEP---RAVFF-FKTSKKGKLYALS YCNHGLWENEVQLE	
<i>P.a. Nlr/SOR</i>	IELYFHPEDGQFPILVGRVAFTSH---DDPLTEP---RAVFF-FKTKKKGKLYALS YCNHGLWENEVQLE	
<i>M.j. Nlr/SOR</i>	IELY---MGDLYLARV---DFT-----QFMKP-EVKLMVKAPSKHEKFI LRALMRCNLHGVWEYEKILLE	

Figure 1.7 *Pyrococcus furiosus* 1Fe-SOR crystal structure (86). Each color represents a different monomer. The silver spheres represent iron atoms.

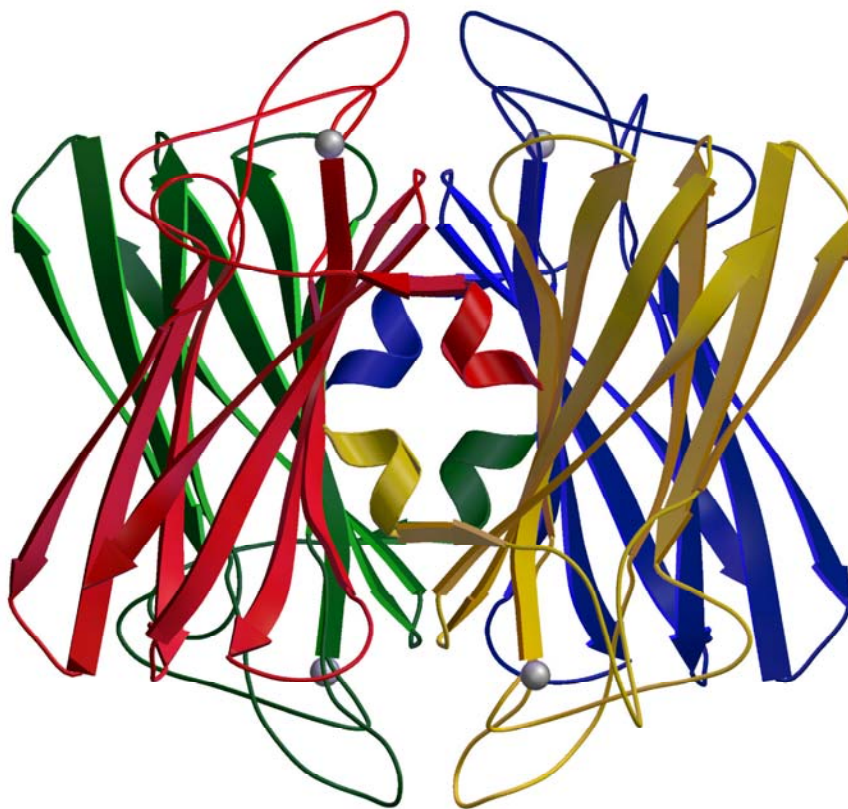
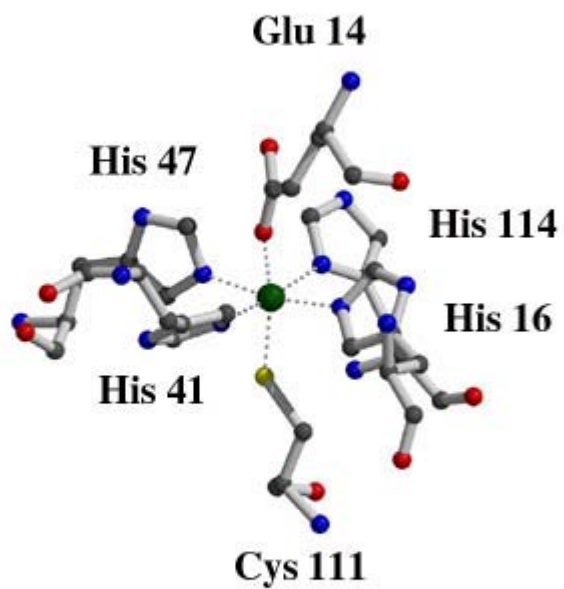


Figure 1.8 X-ray crystal structure of oxidized (a) and reduced (b) iron active-site in *P. furiosus* 1Fe-SOR. Modified from (86).

(a)



(b)

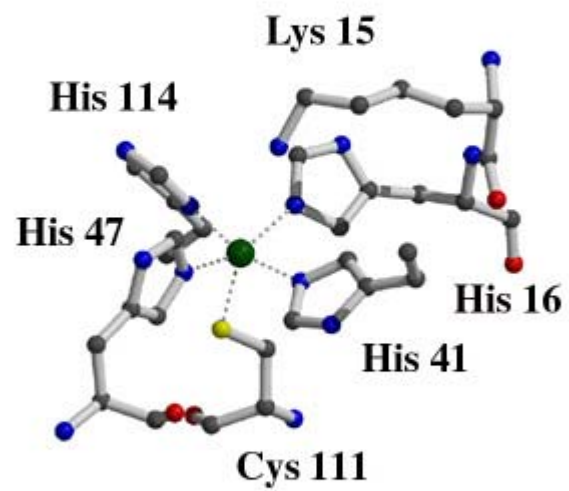


Figure 1.9 *Desulfovibrio desulfuricans* (ATCC 27774) 2Fe-SOR crystal structure (75). Each color represents a different monomer. The silver spheres represent iron atoms and the purple sphere represents calcium ion .

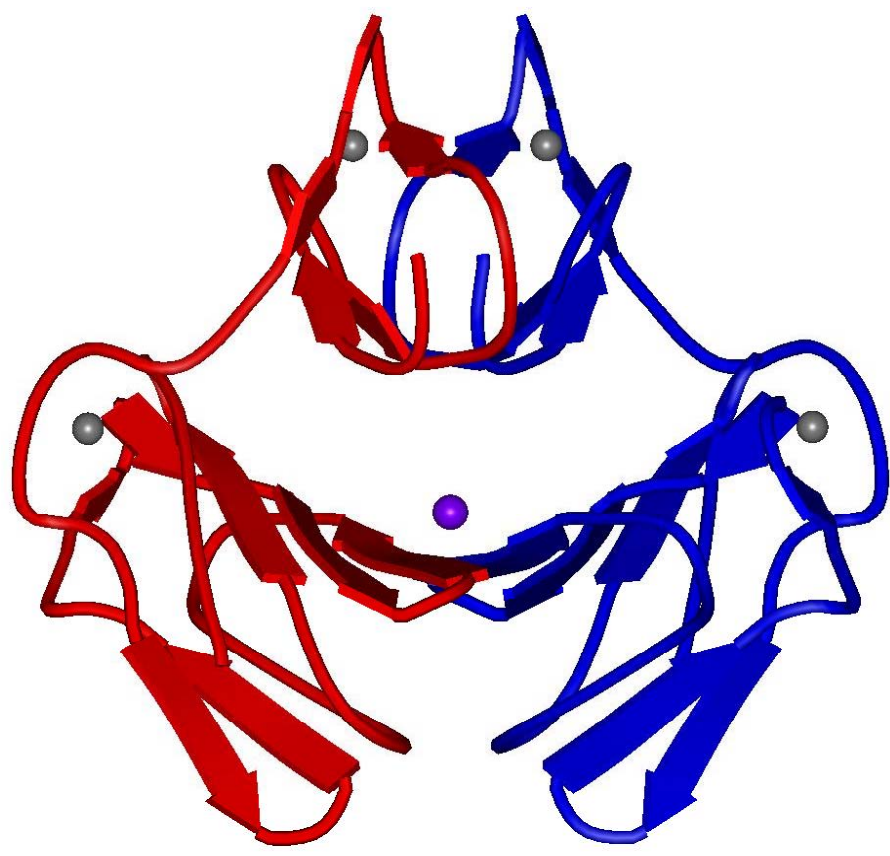
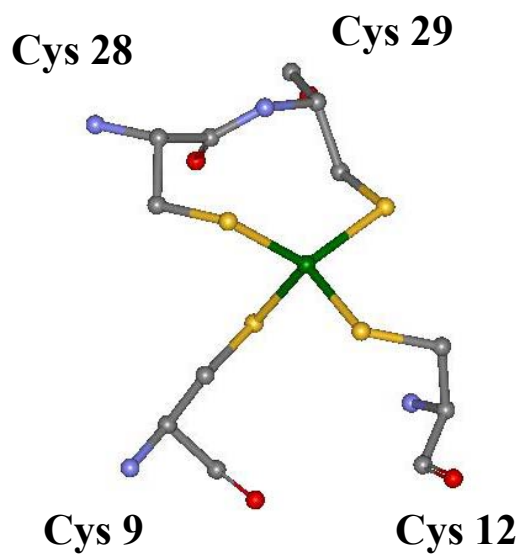


Figure 1.10 Desulforedoxin-like site (a) and SOR active-site (b) of 2Fe-SOR from *Desulfovibrio desulfuricans* (ATCC 27774) (75).

(a)



(b)

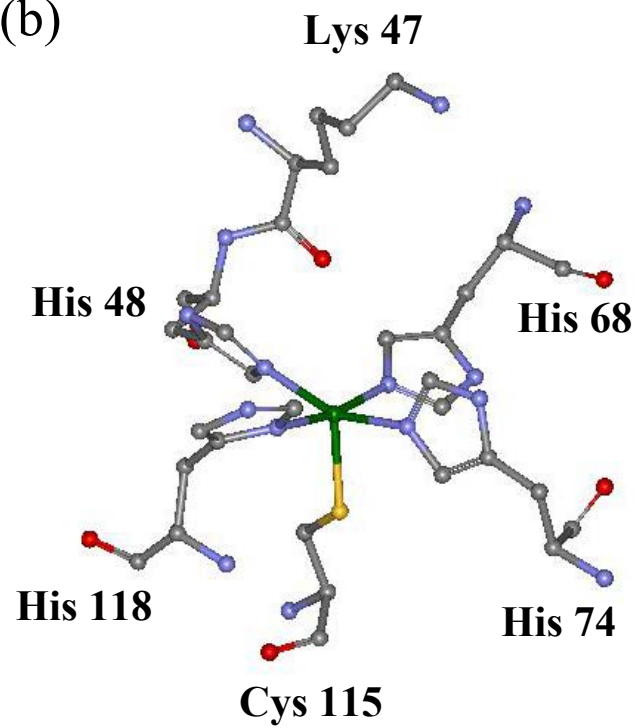
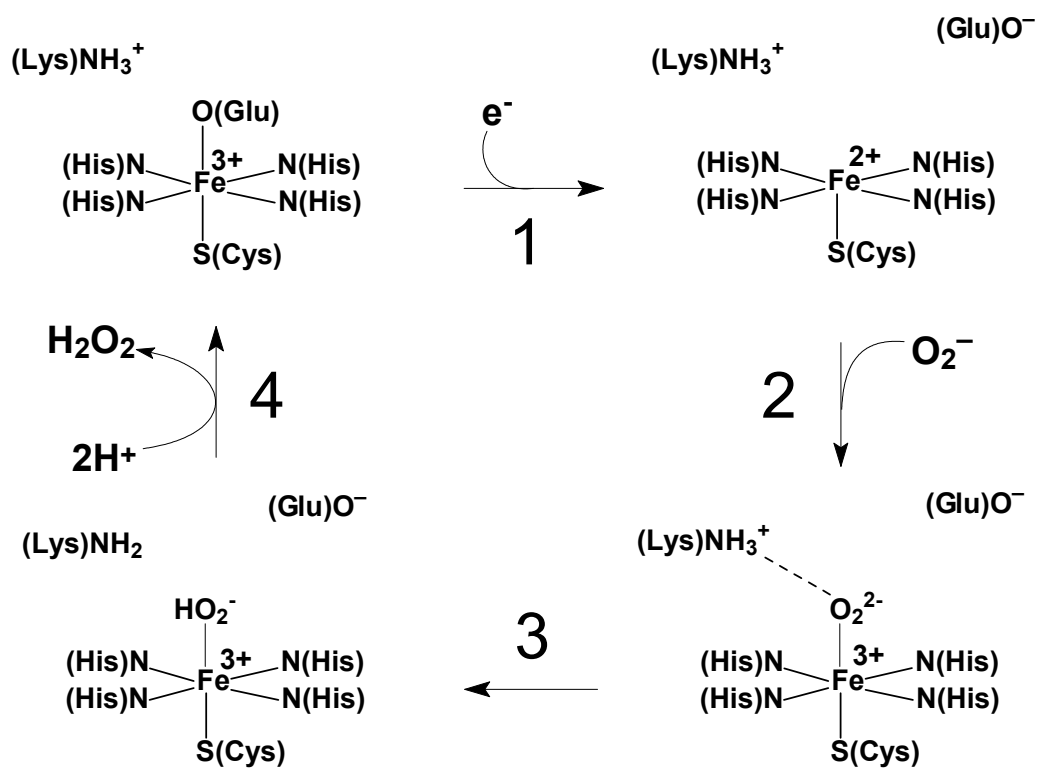


Figure 1.11 Proposed mechanism for SOR (4; 93; 94).



**CHAPTER 2**

**SPECTROSCOPIC STUDIES OF *PYROCOCCUS FURIOSUS***

**SUPEROXIDE REDUCTASE: IMPLICATIONS FOR ACTIVE SITE**

**STRUCTURES AND THE CATALYTIC MECHANISM<sup>1</sup>**

---

<sup>1</sup> Clay, Michael D.,<sup>‡</sup> Francis E. Jenney, Jr.,<sup>§</sup> Peter L. Hagedoorn,<sup>‡,†</sup> Graham N. George,<sup>¶</sup> Michael W. W. Adams,<sup>§</sup> and Michael K. Johnson<sup>‡</sup> (2002) *J. Am. Chem. Soc.* **124**, 788-805. Departments of <sup>‡</sup>Chemistry and <sup>§</sup>Biochemistry & Molecular Biology, and the <sup>‡,§</sup>Center for Metalloenzyme Studies, University of Georgia, Athens, GA 30602; <sup>†</sup>Department of Biotechnology, Technical University of Delft, The Netherlands; and <sup>¶</sup>Stanford Synchrotron Radiation Laboratory, SLAC, Stanford University, PO Box 4349, MS 69, Stanford, CA 94309

## Abstract

The combination of UV/visible/NIR absorption, CD and variable temperature magnetic circular dichroism (VTMCD), EPR and X-ray absorption (XAS) spectroscopies has been used to investigate the electronic and structural properties of the oxidized and reduced forms of *Pyrococcus furiosus* rubredoxin:superoxide oxidoreductase (SOR) as a function of pH and exogenous ligand binding. XAS shows that the mononuclear ferric center in the oxidized enzyme is very susceptible to photo-reduction in the X-ray beam. This observation facilitates interpretation of ground and excited state electronic properties and the EXAFS results for the oxidized enzyme in terms of the published X-ray crystallographic data (Yeh, A. P.; Hu, Y.; Jenney, F. E.; Adams, M. W. W.; Rees, D. C. *Biochemistry* **2000**, *39*, 2499-2508). In the oxidized state, the mononuclear ferric active site has octahedral coordination with four equatorial histidyl ligands and axial cysteinate and monodentate glutamate ligands. Fe-EXAFS are best fit by one Fe-S at 2.36 Å and five Fe-N/O at an average distance of 2.12 Å. The EPR-determined spin Hamiltonian parameters for the high-spin ( $S = 5/2$ ) ferric site in the resting enzyme,  $D = -0.50 \pm 0.05 \text{ cm}^{-1}$  and  $E/D = 0.06$ , are consistent with tetragonally compressed octahedral coordination geometry. UV-visible absorption and VTMCD studies facilitate resolution and assignment of  $\pi\text{His} \rightarrow \text{Fe}^{3+}(\text{t}_{2\text{g}})$  and  $(\text{Cys})\text{S}(\text{p}) \rightarrow \text{Fe}^{3+}(\text{t}_{2\text{g}})$  charge transfer transitions and the polarizations deduced from MCD saturation magnetization studies indicate that the zero-field splitting (compression) axis corresponds to one of the axes with *trans*-histidyl ligands. EPR and VTMCD studies provide evidence of azide, ferrocyanide, hydroxide, and cyanide binding via displacement of the glutamate ligand. For azide, ferrocyanide, and hydroxide, ligand binding occurs with retention of the high-spin ( $S =$

$5/2$ ) ground state ( $E/D = 0.27$  and  $D < 0$  for azide and ferrocyanide;  $E/D = 0.25$  and  $D = +1.1 \pm 0.2 \text{ cm}^{-1}$  for hydroxide), whereas cyanide binding results in a low-spin ( $S = 1/2$ ) species ( $g = 2.29, 2.25, 1.94$ ). The ground-state and charge-transfer/ligand-field excited-state properties of the low-spin cyanide-bound derivative are shown to be consistent with a tetragonally elongated octahedral coordination with the elongation axis corresponding to an axis with *trans*-histidyl ligands. In the reduced state, the ferrous site of SOR is shown to have square pyramidal coordination geometry in frozen solution with four equatorial histidines and one axial cysteine on the basis of XAS and UV and NIR VTMCD studies. Fe-EXAFS are best fit by one Fe-S at 2.37 Å and four Fe-N/O at an average distance of 2.15 Å. VTMCD reveals a high-spin ( $S = 2$ ) ferrous site with (Cys)S(p)  $\rightarrow$  Fe<sup>2+</sup> charge-transfer transitions in the UV region and  $^5T_{2g} \rightarrow ^5E_g$  ligand-field transitions in the NIR region at 12400 cm<sup>-1</sup> and < 5000 cm<sup>-1</sup>. The ligand-field bands indicate square pyramidal coordination geometry with  $10Dq < 8700 \text{ cm}^{-1}$  and a large excited-state splitting,  $\Delta^5E_g > 7400 \text{ cm}^{-1}$ . Analysis of MCD saturation magnetization data leads to ground state zero-field splitting parameters for the  $S = 2$  ground state,  $D \sim +10 \text{ cm}^{-1}$  and  $E/D \sim 0.1$ , and complete assessment of ferrous d-orbital splitting. Azide binds weakly at the vacant coordination site of reduced SOR to give a coordination geometry intermediate between octahedral and square pyramidal with  $10Dq = 9700 \text{ cm}^{-1}$  and  $\Delta^5E_g = 4800 \text{ cm}^{-1}$ . Cyanide binding results in an octahedral ferrous site with  $10Dq = 10900 \text{ cm}^{-1}$  and  $\Delta^5E_g = 1750 \text{ cm}^{-1}$ . The ability to bind exogenous ligands to both the ferrous and ferric sites of SOR is consistent with an inner sphere catalytic mechanism involving superoxide binding at the ferrous site to yield a ferric-(hydro)peroxo intermediate. The structural and electronic properties of the SOR active site are discussed in relation to the

role and bonding of the axial cysteine residue and the recent proposals for the catalytic mechanism.

## Introduction

Over the last two years, evidence has emerged for a novel mechanism of oxygen detoxification in anaerobic and microaerophilic microorganisms involving an enzyme that preferentially catalyzes superoxide reduction rather than superoxide dismutation.<sup>1-5</sup> Rubredoxin:superoxide oxidoreductase (SOR) is proposed to catalyze the reduction of superoxide to hydrogen peroxide utilizing electrons from NADPH, by way of NADPH: rubredoxin oxidoreductase and rubredoxin.<sup>2</sup> In anaerobic or microaerophilic organisms, SOR may offer a selective advantage over superoxide dismutase (SOD) for removing superoxide, by eliminating the concomitant generation of O<sub>2</sub>.<sup>2</sup>

Thus far, three distinct types of enzymes with superoxide reductase activity have been characterized. The initial evidence for an enzyme with superoxide reductase activity came from the hyperthermophilic anaerobe *Pyrococcus furiosus*.<sup>2</sup> The superoxide reductase activity was associated with a heterotetramer composed of 14.3 kDa subunits, each containing a single non-heme iron. This protein was shown to be homologous (50% identity) with neelaredoxin from *Desulfovibrio (D.) gigas*; a spectroscopically characterized non-heme iron protein,<sup>6</sup> that had previously been reported to have significant SOD activity.<sup>7</sup> The structures of oxidized and reduced forms of *P. furiosus* SOR have been determined at 1.7- and 2.0-Å resolution, respectively,<sup>8</sup> and the protein fold and iron center were found to be very similar to a homologous domain in *D. desulfuricans* desulfoferrodoxin (Dfx).<sup>9</sup> Desulfoferrodoxins have been purified and characterized from many sulfate-reducing bacteria and are known to be modular non-heme iron proteins comprising a rubredoxin-like desulfoferrodoxin domain and a

neelaredoxin-like domain.<sup>10-12</sup> While initial studies of *D. desulfuricans* Dfx indicated SOD activity<sup>13</sup>, more recent studies of *Desulfoarculus (Ds.) baarsii* and *D. vulgaris* Dfx have provide strong evidence that this protein also functions as a superoxide reductase.<sup>3,14</sup> Most recently, an enzyme with superoxide reductase activity has been purified and characterized from *Treponema pallidum*, a microaerophilic bacterium responsible for venereal syphilis, that lacks the classical antioxidant enzymes found in aerobic organisms.<sup>4,5</sup> *T. pallidum* SOR has strong sequence homology to Dfx, but lacks three of the cysteine residues that ligate the rubredoxin-like iron center in the desulforedoxin domain.

The X-ray structures *P. furiosus* SOR and *D. desulfuricans* Dfx reveal a novel SOR active site involving a mononuclear iron coordinated by the imidazole nitrogens of four histidines (three  $\epsilon$ N and one  $\delta$ N) in a planar arrangement, with a cysteinyl sulfur occupying one axial position.<sup>8,9</sup> There is currently no clear consensus concerning a sixth ligand in the oxidized state. In two of the four subunits of *P. furiosus* SOR, a conserved glutamate carboxylate serves as an axial ligand to form a six-coordinate, octahedral environment.<sup>8</sup> In the other two subunits of *P. furiosus* SOR,<sup>8</sup> and in *D. desulfuricans* Dfx,<sup>9</sup> the sixth coordination site is either vacant or occupied by a solvent molecule. A similar five-coordinate square-pyramidal iron site is present in reduced *P. furiosus* SOR.<sup>8</sup> Hence, the possibility of partial or complete reduction during crystallization and/or photoreduction in the X-ray beam may provide an explanation of the apparent variability in the oxidized active-site structure.<sup>8</sup>

*P. furiosus* SOR is anomalous among metalloenzymes in that X-ray structure determination has preceded detailed spectroscopic analysis. In order to address the

active-site geometric and electronic structure in solution and the origin of the heterogeneity apparent in the oxidized crystals structure, we report here the results of EPR, UV/visible/near-IR absorption, CD, and variable-field/variable-temperature magnetic circular dichroism (VHVT MCD), and X-ray absorption (XAS) studies of the oxidized and reduced forms of native and recombinant forms of *P. furiosus* SOR, as a function of pH and the binding of exogenous ligands. The results provide the first detailed assessment of the ground and excited state properties of the mononuclear Fe active site of SOR in both the oxidized and reduced states and provide evidence for binding of cyanide and azide at the active site in both oxidation states. In addition, the spectroscopic results address the origin of the conflicting reports concerning the ground state properties of the high-spin Fe<sup>3+</sup> center in oxidized SOR and Dfx samples,<sup>3-6,10-12,15</sup> and provide assessment of metrical data for Fe-ligand distances in solution. The exogenous ligand binding properties and the spectroscopically determined Fe<sup>3+</sup> and Fe<sup>2+</sup> coordination geometries and excited state properties are discussed in relation to the role and bonding of the axial cysteine residue and the recent proposals for the catalytic mechanism.<sup>14,16,17</sup>

## Experimental Section

**Cloning of the *P. furiosus sor* gene.** All standard molecular biology techniques were performed using the published protocols.<sup>18</sup> *Pyrococcus furiosus* cells (DSM 3638) were grown and cell free extracts were prepared as previously described.<sup>19</sup> The gene encoding *P. furiosus* SOR (*sor*) was cloned into the expression vector pET3a (Novagen, Madison, WI) and designated pPfNd1. *E. coli* strain BL21(DE3) was used for expression

of recombinant *P. furiosus* SOR, and was grown in a 100 L fermenter at 37 °C stirred at 170 rpm under aerobic conditions in M9 minimal medium<sup>20</sup> supplemented with 0.4% glycerol as carbon source, 100 µM FeSO<sub>4</sub>, 0.05% thiamine, 1x vitamins<sup>21</sup> and 200 µg/ml ampicillin in a 100 L fermenter. Cultures were then grown to A<sub>600</sub> ~ 0.7, and induced with 1 mM IPTG for 4 hrs.

**Purification of recombinant *P. furiosus* SOR.** Frozen *E. coli* cells (116 g) were thawed (1 g per 3 mL) in 50 mM Tris-HCl buffer pH 8.5 containing 1 mM EDTA, 0.5 mg/mL lysozyme, 100 mM NaCl and 1 mM phenylmethylsulfonyl fluoride. The cells were broken at 4 °C by sonication and the extract was heated until the solution temperature reached 70 °C, and then chilled on ice for 2 hrs. After centrifugation (25,000 x g, 45 min, 4 °C) the supernatant (460 mL, 920 mg protein) was applied, diluted by 75% with buffer, to a column of Q Sepharose FastFlow equilibrated with 50 mM Tris-HCl pH 8.5. A linear gradient from 0 – 75 mM NaCl was applied followed by a linear gradient from 75 – 500 mM NaCl. Fractions containing SOR eluted as 190 - 250 mM NaCl was applied. These were concentrated by ultrafiltration, ammonium sulfate was added to a final concentration of 1 M, and this sample was applied to a column of Phenyl Sepharose equilibrated in 20 mM MOPS pH 7.0 containing 1 M (NH<sub>4</sub>)<sub>2</sub>SO<sub>4</sub>. SOR was block eluted with 20 mM MOPS pH 7.0, concentrated and desalted by ultrafiltration. The final yield was 131 mg of SOR from 116 g *E. coli* cells wet weight.

**Biochemical techniques and sample preparation.** Protein concentrations were measured using the Biuret method after trichloroacetic acid (TCA) precipitation,<sup>21</sup> except that samples were heated at 50 °C for 30 min after TCA addition. The superoxide reductase activity of SOR, and its apparent SOD activity were measured as previously

described.<sup>2</sup> Superoxide reductase activity was measured as the difference in the rate of cytochrome *c* reduction with and without SOR. One unit of activity catalyzes the reduction of one  $\mu\text{mol}$  of superoxide  $\text{min}^{-1}$ , which is equivalent to one  $\mu\text{mol}$  of cytochrome oxidized  $\text{min}^{-1}$ . Calculations of the superoxide reductase activity of SOR assume negligible SOD activity.<sup>2</sup> Iron reconstitution of native *P. furiosus* SOR was performed in sealed vials under argon. The conditions were: 50 mM Tris-HCl pH 8.0, 0.5 mM protein, 100 mM dithiothreitol, 10 mM  $\text{Fe}(\text{NH}_4)_2\text{SO}_4$ , for 30 min at 25 °C followed by 30 min at 80 °C. The samples were then desalted using a Sephadex G25 column in 50 mM Tris-HCl pH 8, and concentrated by ultrafiltration.

Buffer exchange prior to spectroscopic measurements was carried out by ultrafiltration and the buffering media used for individual samples are indicated in the figure legends. Stock solutions of potassium cyanide or sodium azide were freshly prepared in the same buffers as the samples. Reduction of SOR was carried out under anaerobic conditions by addition of a 10-fold stoichiometric excess of dithionite or ascorbate. Excess reductant was removed by ultrafiltration prior to addition of azide or cyanide and subsequent spectroscopic studies. All reduced samples were handled in a Vacuum Atmospheres glove box ( $< 1 \text{ ppm O}_2$ ).

**Spectroscopic methods.** XAS measurements were carried out at the Stanford Synchrotron Radiation Laboratory with the SPEAR storage ring containing 60-100 mA at 3.0 GeV. Data were collected on beamline 7-3 using a Si(220) double crystal monochromator, with an upstream vertical aperture of 1 mm, and a wiggler field of 1.8 T. Harmonic rejection was accomplished by detuning one monochromator crystal to approximately 50% off peak, and no specular optics were present in the beamline. The

incident X-ray intensity was monitored using a nitrogen-filled ionization chamber and X-ray absorption was measured as the X-ray Fe K $\alpha$  fluorescence excitation spectrum using an array of thirteen germanium intrinsic detectors.<sup>22</sup> During data collection, samples were maintained at a temperature of approximately 10 K, using an Oxford Instruments liquid helium flow cryostat. For each sample eight to ten 35-min scans were accumulated, and the absorption of an iron metal foil was measured simultaneously by transmittance. For the oxidized enzyme the sample position was adjusted after each scan in order to illuminate a fresh part of the sample, and prevent photoreduction. The X-ray energy was calibrated with reference to the lowest energy inflection point of the foil, which was assumed to be 7111.3 eV. The extended X-ray absorption fine structure (EXAFS) oscillations  $\chi(k)$  were quantitatively analyzed by curve-fitting the weighted k-space data using the EXAFSPAK suite of computer programs,<sup>23</sup> employing *ab-initio* theoretical phase and amplitude functions generated with the program FEFF version 8.2.<sup>24</sup> No smoothing, Fourier filtering or related manipulations were performed upon the data.

Absorption spectra were recorded on Shimadzu UV301PC spectrophotometer. VHVT MCD measurements were recorded on samples containing 55% (v/v) glycerol or d<sub>3</sub>-glycerol using a Jasco J-715 (180-1000 nm) or J-730 (700-2000 nm) spectropolarimeter mated to an Oxford Instruments Spectromag 4000 (0-7 T) split-coil superconducting magnet. The experimental protocols for measuring MCD spectra of oxygen-sensitive samples over the temperature range 1.5-300 K with magnetic fields up to 7 T have been described elsewhere.<sup>25</sup> VHVT MCD saturation magnetization data for the high-spin ( $S = 5/2$ ) Fe<sup>3+</sup> and high-spin ( $S = 2$ ) Fe<sup>2+</sup> species were analyzed according to the published procedures,<sup>26,27</sup> using software kindly supplied by Professor Edward I.

Solomon. X-band (~9.6 GHz) EPR spectra were recorded on a Bruker ESP-300E EPR spectrometer with a dual mode ER-4116 cavity and equipped with an Oxford Instruments ESR-9 flow cryostat (4.2-300 K). Frequencies were measured with a Hewlett Packard 5350B frequency counter and the field was calibrated with a Bruker ER 035M gaussmeter. EPR spin quantitations based on the total area under the absorption envelope or the area under the low-field “absorption-shaped” feature in the first-derivative spectrum were carried out using the procedures developed by Aasa and Vänngård.<sup>28</sup> Simulations of  $S = 1/2$  signals were carried out using the Simfonia software package (Bruker Instruments).

EPR redox titrations were performed at ambient temperature (25-27 °C) in the glove box under anaerobic conditions using 300  $\mu\text{M}$  SOR in a 100-mM HEPES buffer, pH 7.5. Mediator dyes were added, each to a concentration of ca. 60  $\mu\text{M}$ , in order to cover the desired range of redox potentials, i.e. 1,4-benzoquinone, 1,2-naphthoquinone, thionine, methylene blue, duroquinone and 1,2-naphthoquinone-4-sulfonate. Samples were first oxidized with a minimal excess of potassium ferricyanide followed by reductive titration with ascorbate. After equilibration at the desired potential, a 0.2-mL aliquot was transferred to a calibrated EPR tube and immediately frozen in liquid nitrogen. Potentials were measured using a platinum working electrode and a saturated Ag/AgCl reference electrode. All redox potentials are reported relative to NHE.

## Results and analysis

**EPR.** X-band EPR was not effective in probing the ground state properties of the  $\text{Fe}^{2+}$  center in ascorbate-reduced *P. furiosus* SOR. No resonances indicative of an integer

spin species were observed over the temperature range 4.2-100 K in either parallel or perpendicular mode. The ground state properties of the  $\text{Fe}^{3+}$  center in oxidized *P. furiosus* SOR were investigated by EPR as a function of pH and the addition of excess cyanide and azide (Figure 2.1). As prepared in pH 7.5 HEPES buffer, the EPR spectrum of *P. furiosus* SOR (Figure 2.1A) is composed of two overlapping  $S = 5/2$  resonances and the effective  $g$ -values of each are readily rationalized using an isotropic  $S = 5/2$  spin Hamiltonian of the form:

$$H_e = g_0\beta\mathbf{H}\cdot\mathbf{S} + D(\mathbf{S}_z^2 - S(S+1)/3) + E(\mathbf{S}_x^2 - \mathbf{S}_y^2) \quad (1)$$

where  $D$  and  $E$  are the axial and rhombic zero-field splitting parameters, respectively.

The major  $S = 5/2$  species gives rise to the broad absorption-shaped features centered at  $g = 7.3$  and  $5.8$ . On the basis of their temperature-dependence behavior, see Figure 2.2, the  $g = 7.3$  and  $5.8$  features are attributed to the low-field components of resonances from the upper and middle doublets, respectively, of an axial  $S = 5/2$  spin system with  $D < 0$ . For example, for  $D < 0$ ,  $E/D = 0.06$  and a  $g_0 = 2$ , eq. 1 predicts  $g_{x,y,z} = (9.99, 0.02, 0.03)$ ,  $(5.88, 1.35, 1.43)$ , and  $(1.89, 7.33, 4.55)$  for the lower ( $M_s = \pm 5/2$ ), middle ( $M_s = \pm 3/2$ ), and upper ( $M_s = \pm 1/2$ ) doublets, respectively. A resonance from the lowest doublet is predicted to have very low transition probability and is observable as a weak absorption-shaped band at  $g = 10.0$  in the spectrum recorded at 3.5 K, see Figure 2.2. For the upper and middle doublets, the components with  $g < 2$  are too broad to observe, and a broad derivative centered near  $g = 4.5$  from the  $M_s = \pm 1/2$  doublet is obscured by the  $g = 4.3$  resonance of the minor species. The energy separation between the middle and upper zero-field doublets, can be estimated from the slope of a plot of the logarithm of the ratio of the intensity of the two field resonances,  $\ln(I_{g=5.8}/I_{g=7.3})$  versus  $1/T$ , which yields a

straight line of slope  $1.62 \pm 0.10$  K. This indicates an energy separation of  $1.1 \pm 0.1$   $\text{cm}^{-1}$ , which translates to  $D = -0.50 \pm 0.05$   $\text{cm}^{-1}$ . The breadth of the  $g = 7.3$  and  $5.8$  features indicates significant  $E/D$  strain resulting from conformational heterogeneity in the frozen solution. In accord with the published EPR studies of *D. gigas* neelaredoxin,<sup>6</sup> the lineshapes indicate that the heterogeneity primarily involves two species with  $E/D$  values close to 0.05 and 0.08. Spin quantitations based on the total integrated area under the absorption-shaped features at  $g = 7.3$  and  $5.8$ , using the method developed by Aasa and Vännngård,<sup>28</sup> and allowing for the Boltzmann populations of the upper and middle doublets, respectively, indicate that the axial  $S = 5/2$  species accounts for  $\sim 80\%$  of the Fe in the sample.

The minor  $S = 5/2$  species is responsible for the sharp derivative-shaped feature centered at  $g = 4.3$  and a weak absorption-shaped feature at  $g = 9.7$  that is only clearly apparent at temperatures  $< 6$  K, see Figures 2.1 and 2.2. These resonances are indicative of a rhombic  $S = 5/2$  ground state,  $E/D = 0.33$ , which is predicted to have  $g_{x,y,z} = (0.86, 0.61, 9.68)$ ,  $(4.29, 4.29, 4.29)$ , and  $(0.86, 9.68, 0.61)$  for the lower, middle, and upper doublets, respectively, for  $g_0 = 2$ . Such resonances are commonly associated with adventitiously bound  $\text{Fe}^{3+}$  ion. Approximate spin quantitation of the rhombic  $S = 5/2$  species by double integration of the  $g = 4.3$  component and correcting for the Boltzmann population of the middle doublet using maximal assessments of the zero-field splitting (assuming  $|D| < 2$   $\text{cm}^{-1}$ ), indicates that this species accounts for  $< 10\%$  of the Fe in samples of recombinant *P. furiosus* SOR. The low spin quantitation, coupled with both the variation in the relative intensities of the axial and rhombic  $S = 5/2$  species in *P. furiosus* SOR and *D. gigas* neelaredoxin,<sup>6</sup> and the much lower redox potential of the

species responsible for the rhombic  $S=5/2$  species (see below), are consistent with assignment of this species to adventitious  $\text{Fe}^{3+}$  ion. However, it has not been possible to decrease the intensity of the rhombic  $S=5/2$  species relative to the axial  $S=5/2$  species in recombinant SOR by treatment with  $\text{Fe}^{3+}$  chelators such as EDTA, indicating that this adventitious  $\text{Fe}^{3+}$  ion is tightly bound or not solvent accessible.

Direct evidence that the axial ( $E/D = 0.06$ )  $S=5/2$  species, rather than the rhombic ( $E/D = 0.33$ )  $S=5/2$  species, is associated with active enzyme came from EPR studies of native *P. furiosus* SOR. As purified, native *P. furiosus* SOR was deficient in Fe (0.4 Fe atoms/subunit) and has very low SOR activity (48 units/mg),<sup>29</sup> compared to the recombinant enzyme (1.0 Fe atoms/subunit and specific activity of 2700 units/mg). However, reconstitution of the native enzyme with excess ferrous ion and repurification yielded samples with increased Fe content (0.7 Fe atoms/subunit) and activity (300 units/mg). The EPR spectra of both the as prepared and reconstituted samples of native *P. furiosus* SOR (data not shown) were completely dominated by the rhombic ( $E/D = 0.33$ )  $S=5/2$  species. The axial ( $E/D = 0.06$ )  $S=5/2$  species was only clearly apparent in the reconstituted sample, but the ratio of the axial and rhombic resonances in this sample was 10-fold less than in the recombinant enzyme. Hence there appears to be a direct correlation between the axial ( $E/D = 0.06$ )  $S=5/2$  species and SOR activity.

Dye-mediated EPR redox titrations of recombinant *P. furiosus* SOR using ascorbate as the reductant and ferricyanide as the oxidant revealed an unexpected complication. Oxidation of *P. furiosus* SOR with ferricyanide results in the appearance of a third type of  $S=5/2$  resonance, in addition to the  $E/D = 0.06$  and 0.33 species that are also present in the as-prepared samples (Figure 2.1C). This resonance dominates the

EPR spectrum and has a broad derivative centered around  $g = 4.3$  with a maximum at  $g = 4.5$  and a minimum at  $g = 4.2$ . In addition, it is associated with a weak absorption feature at  $g = 9.8$  which increases in relative intensity with decreasing temperature. These features are readily interpreted in terms of the spin Hamiltonian in eq. 1 with  $E/D = 0.27$  and  $D < 0$ . This resonance persists even after excess ferricyanide is removed by ultrafiltration, but is not observed in samples oxidized with either hexachloroiridate or hydrogen peroxide. Hence it appears to be an artifact of ferricyanide oxidation. On the basis of the close similarity to the azide-bound form (see below), this resonance is tentatively attributed to a species with ferrocyanide bound at the  $\text{Fe}^{3+}$  active site via a Fe-N-C-Fe linkage. EPR-monitored redox titrations facilitated discrimination between the adventitious and active-site  $\text{Fe}^{3+}$  species. The  $E/D = 0.33$  species, corresponding to adventitiously bound  $\text{Fe}^{3+}$  ion, is not reduced at potentials down to 0 mV, whereas the  $E/D = 0.06$  and  $0.27$  species both exhibit one-electron redox potentials  $= +250 \pm 20$  mV (see Figure 2.3). The EPR-determined redox potential for the  $E/D = 0.06$  species in frozen solution is in good agreement with the optically determined redox potential obtained at room temperature,  $E_m = +238 \pm 10$  mV (see Supporting Information, Figure S2.1). However, the ferricyanide-induced species cannot be distinguished from the as prepared enzyme based on redox potential and, therefore, is easily misinterpreted as arising from the active site of the oxidized resting enzyme.

Optical absorption studies of *D. gigas* neelaredoxin<sup>6</sup> and *P. furiosus* SOR (see Supporting Information, Figure S2.2), reveal an alkaline transition with a  $\text{pK}_a = 9.6$ . This transition is also evident by the appearance of a new  $S = 5/2$  resonance in EPR spectra recorded at pH 10 (Figure 2.1B). At pH 10, the EPR spectrum has contributions from

both the  $E/D = 0.06$  and  $0.33$  species that are present at neutral pH, but samples at higher pH exhibited poorer quality spectra due to progressive loss of Fe at pH values above 10.5. Temperature dependence studies show that the alkaline form of *P. furiosus* SOR exhibits a broad resonance with positive feature at  $g = 4.8$  and derivative centered near  $g = 4.1$  from the middle doublet and a low field absorption-shaped feature at  $g = 9.4$  from the lower doublet, see Figure 2.4. These effective  $g$ -values are readily rationalized by the spin Hamiltonian in eq. 1, with  $E/D = 0.25$ ,  $D > 0$ , and  $g_0 = 2$  which predicts  $g_{x,y,z} = (0.92, 9.40, 1.45)$ ,  $(4.76, 3.76, 4.08)$ , and  $(9.83, 0.36, 0.47)$  for the lower, middle, and upper doublets of the  $S = 5/2$  zero-field-split manifold, respectively. The energy separation between the middle and lower zero-field doublets was estimated from a plot of  $\ln(I_{g=4.8}/I_{g=9.4})$  versus  $1/T$  which yields a straight line of slope  $-4.8 \pm 0.4$  K (inset in Figure 2.4), and leads to an estimate of axial zero-field splitting parameter,  $D = +1.1 \pm 0.2$  cm<sup>-1</sup>.

EPR evidence for azide and cyanide binding to the Fe<sup>3+</sup> active site is shown in Figure 2.1(D) and 2.1(E), respectively. Addition of a 45-fold excess of sodium azide results in the emergence of an  $S = 5/2$  resonance indistinguishable from the ferricyanide-induced species, i.e. a broad derivative centered at  $g = 4.3$  with a maximum at  $g = 4.5$  and a minimum at  $g = 4.2$  and low-field absorption-shaped feature at  $g = 9.8$ . Temperature-dependence studies indicate analogous zero-field splitting parameters, i.e.  $E/D = 0.27$  and  $D < 0$ . Addition of a 30-fold excess of sodium cyanide results in quantitative conversion to a low-spin  $S = 1/2$  Fe<sup>3+</sup> species with near axial lineshape,  $g_{1,2,3} = 2.289, 2.251, 1.935$  and linewidths  $l_{1,2,3} = 7.5, 5.1, 3.7$  mT (based on spectral simulation). The resonance is observable at temperatures up to 50 K and corresponds to 90% of the Fe in the sample

based on spin quantitations under non-saturating conditions. A similar species was reported for cyanide-treated *D. desulfuricans* Dfx,  $g_{\perp} = 2.27$  and  $g_{\parallel} = 1.96$ .<sup>13</sup>

### **Absorption, CD and VHVT MCD.**

*Oxidized P. furiosus SOR*: The electronic excited state properties of oxidized recombinant *P. furiosus* SOR were investigated using the combination of absorption, CD, and VHVT MCD. UV-visible absorption spectra recorded at pH 6.0, 7.5, and 10, and after addition of excess azide and cyanide at pH 7.5, are shown in Figure 2.5. In each case the spectrum comprises an intense broad band centered near  $30000\text{ cm}^{-1}$  and a well-defined low energy band centered between  $14000$  and  $17500\text{ cm}^{-1}$ . The latter has been assigned to  $(\text{Cys})\text{S}^{-} \rightarrow \text{Fe}^{3+}$  charge transfer (CT) based on resonance Raman studies of the equivalent center in *D. desulfuricans* Dfx.<sup>11</sup> In accord with previous studies of *D. gigas* neelaredoxin,<sup>6</sup> the absorption spectrum *P. furiosus* SOR is pH dependent. The low-energy band centered at  $15150\text{ cm}^{-1}$  is invariant to pH over the range 6.0 to 8.5, but undergoes a blue shift to  $17000\text{ cm}^{-1}$  at pH 10.5 with a  $\text{pK}_{\text{a}} = 9.6$  (see Supporting Information, Figure S2.2). Above pH 10.5, the site is readily and irreversibly lost, as evidenced by the progressive decrease in the absorption intensity at  $\sim 17000\text{ cm}^{-1}$ . The addition of a 45-fold stoichiometric excess of sodium azide has no significant affect on the absorption spectrum. In contrast, cyanide binding, which induces a high-spin to low-spin transition as a result of increased d-orbital ligand-field splitting, is readily monitored by a red shift of the lower energy band to  $14600\text{ cm}^{-1}$ .

UV-visible CD and VHVT MCD studies were carried out on the samples of *P. furiosus* SOR used for absorption measurements. The absorption and EPR spectra were not perturbed by the addition of 55% (v/v) glycerol, which is required to form a low-

temperature glass for VHVT MCD studies. Negligible, room-temperature CD was observed in the visible region for the high-spin  $\text{Fe}^{3+}$  forms, i.e. pH 7.5, pH 10 and  $\text{N}_3^-$ -bound (data not shown). However, VTMCD studies of the high-spin  $\text{Fe}^{3+}$  derivatives facilitate greater resolution of electronic transitions from the paramagnetic Fe chromophore and therefore more detailed assignments of ligand-to-metal CT bands, see Figure 2.6 and Table 2.1. Moreover, the analysis of VHVT MCD saturation magnetization data for transitions originating from the highly anisotropic ground states Kramers doublets of a high-spin  $\text{Fe}^{3+}$  center, provides polarization information that places additional constraints on electronic assignments, see Figure 2.7 and Table 2.1. Comparison of the spectra shown in Figures 2.5 and 2.6 demonstrates that the relative intensities of discrete transitions are quite different in the absorption and VTMCD spectra of the same sample. In this connection, it is important to emphasize that absorption intensity of symmetry-allowed ligand-to-metal CT bands is directly related to the extent of orbital overlap and thereby metal-ligand covalency. Hence the symmetry-allowed  $\sigma \rightarrow \sigma^*$ ,  $(\text{Cys})\text{S}(\text{p}) \rightarrow \text{Fe}^{3+}(\text{d})$  and  $\pi \rightarrow \pi^*$ ,  $(\text{Cys})\text{S}(\text{p}) \rightarrow \text{Fe}^{3+}(\text{d})$  transitions associated with a Fe-S(Cys) unit would be expected to have intense S  $\rightarrow$  Fe CT bands in the absorption spectrum. However, to a first approximation these are uniaxial transitions, polarized parallel to the Fe-S bond, and consequently are expected to exhibit weak VTMCD intensity. This is because the low-temperature MCD spectra of half-integer-spin transition metal centers are invariably dominated by *C*-terms that require two perpendicular, non-zero transition dipole moments for intensity.<sup>30</sup>

The VTMCD spectrum of *P. furiosus* SOR at pH 6.0 and 7.5 in the 13000-22000  $\text{cm}^{-1}$  region is dominated by two positive *C*-terms centered at 15150 and 18980  $\text{cm}^{-1}$ , see

Figure 2.6, with the former corresponding to the intense absorption band centered at  $15150\text{ cm}^{-1}$ . These bands are in the region expected for  $S \rightarrow Fe^{3+}$  CT transitions involving the filled S p orbitals and the half-filled  $t_{2g}$  set of Fe d orbitals ( $d_{xy,yz,xz}$ ) that are available for  $\pi$  bonding, and the lower energy transition is assigned to the  $\pi \rightarrow \pi^*$  transition with optimal  $\pi$  interaction. By analogy with the detailed assignments that are available for blue copper proteins,<sup>31</sup> the three S p orbitals of the cysteinate are expected to split with one being primarily  $\sigma$  bonding to carbon and therefore not significantly involved in bonding to the metal. The other two S p orbitals are perpendicular to the S-C bond and will be degenerate for free cysteinate. For an Fe-ligated cysteine, these two S p orbitals will split into a higher energy  $p_{\pi}$  orbital that is perpendicular to the Fe-S-C plane and available for direct  $\pi$  overlap with the Fe  $t_{2g}$  d-orbital that is perpendicular to the Fe-S-C plane, and a lower energy  $p_{\text{pseudo } \sigma}$  orbital that is in the Fe-S-C plane with the extent of  $\sigma$  interaction being determined by the Fe-S-C angle (maximal for a  $90^{\circ}$  angle), see Figure 2.8. Since the average of the Fe-S-C angles in the crystal structure of oxidized *P. furiosus* SOR is close to  $120^{\circ}$ ,<sup>8</sup> the  $p_{\text{pseudo } \sigma}$  orbital will have  $\sigma$  overlap with the Fe d-orbital oriented along the Fe-S bond and  $\pi$  overlap with the Fe  $t_{2g}$  d-orbital that lies within the Fe-S-C plane.

VHVT MCD saturation magnetization studies were carried out for the MCD bands centered at  $15150$  and  $18980\text{ cm}^{-1}$ , see Figure 2.7, in order to assess the transition polarizations with respect to the unique ( $z$ ) axis of the predominantly axial zero-field splitting ( $E/D = 0.06$ ). Because the axial zero-field splitting of the  $S = 5/2$  ground state,  $D = -0.50\text{ cm}^{-1}$ , is comparable to the Zeeman interaction at fields up to 6 T, it is not appropriate to analyze only the lowest temperature data (isotherm at 1.7 K) under the

assumption that the magnetization data is determined solely by the effective  $g$ -values of the lowest doublet.<sup>30</sup> Rather, as the Zeeman splitting increases, the electron spin changes from being quantized along the molecular zero-field splitting axis to being quantized along the applied field direction. Neese and Solomon have developed a comprehensive methodology for analyzing VHVT MCD magnetization data in this regime.<sup>26</sup> Since the zero-field splitting parameters are determined by EPR ( $D = -0.50 \text{ cm}^{-1}$ ,  $E/D = 0.06$ ), the only variable parameters involved in the fitting procedure are a scaling factor and the effective  $xy$ ,  $yz$ , and  $xz$  transition dipole moments,  $M_{xy}$ ,  $M_{yz}$ , and  $M_{xz}$ , respectively, which approximate to the product of the two linear transition dipole moments.<sup>32</sup> The MCD magnetization data collected at  $15150 \text{ cm}^{-1}$  (corresponding to the absorption maximum) and at  $18980 \text{ cm}^{-1}$  are quite different, see Figure 2.7, and the differences can be rationalized exclusively in terms of transition polarization. The VT-MCD intensity at  $15150 \text{ cm}^{-1}$  band originates from a predominantly  $y$ -polarized transition, whereas the  $18980 \text{ cm}^{-1}$  band is predominantly  $z$  polarized. Since the  $15150\text{-cm}^{-1}$  band corresponds to the  $\pi \rightarrow \pi^*$  (Cys)S(p)  $\rightarrow$  Fe<sup>3+</sup>(d) transition, the MCD magnetization data indicate that the Fe-S bond is along the  $y$ -axis with respect to the zero-field splitting axis system.

The visible-region (Cys)S<sup>-</sup>  $\rightarrow$  Fe<sup>3+</sup> CT transitions that are observed in the absorption and VT-MCD spectra for *P. furiosus* SOR at pH 6.0 and 7.5 can now be assigned on the basis of the EPR-determined ground-state properties and transition polarizations deduced from MCD magnetization measurements. An axial ground state ( $E/D = 0.06$ ) with negative axial zero-field splitting ( $D = -0.5 \text{ cm}^{-1}$ ) is consistent with tetragonally-compressed octahedral coordination, i.e. octahedral with a strong ligand field along the  $z$ -axis.<sup>33</sup> Since the Fe-S bond is along the  $y$ -axis, the  $z$ -axis must

correspond to one of the two pairs of *trans* (His)N ligands. Hence, the half-filled  $t_{2g}$  set of Fe d-orbitals will split, with a near-degenerate pair,  $d_{xz}$  and  $d_{yz}$ , higher in energy than  $d_{xy}$ , see Figure 2.8. For the molecular  $z$ -axis parallel to the Fe-S-C plane, an appropriate orbital energy level diagram for the S 3p and Fe 3d orbitals is shown in Figure 2.8. Two (Cys)S<sup>-</sup> → Fe<sup>3+</sup> CT transitions are predicted in the visible region. The lower energy transition is the  $y$ -polarized S( $p_{\pi}$ ) → Fe( $d_{xy}$ ) transition that is predicted to be strong in absorption due to optimal  $\pi$  interaction, but weak in the VTMCD spectrum, since it is a uniaxial transition polarized almost exclusively along the Fe-S bond. Hence the S( $p_{\pi}$ ) → Fe( $d_{xy}$ ) transition is assigned to the absorption and VTMCD bands centered at 15150 cm<sup>-1</sup>, see Table 2.1. The higher energy transition is the predominantly  $z$ -polarized S( $p_{\text{pseudo } \sigma}$ ) → Fe( $d_{yz}$ ) transition that is expected to be weak in absorption due to weak  $\pi$  overlap, but strong in the VTMCD spectrum due to equal and opposite mixing of  $x$ - and  $y$ -polarized components. Hence the S( $p_{\text{pseudo } \sigma}$ ) → Fe( $d_{yz}$ ) transition is assigned to the VTMCD band centered at 18980 cm<sup>-1</sup> that is not resolved in the absorption spectrum, see Table 2.1.

The VTMCD spectra of *P. furiosus* SOR at pH 6.0 and 7.5 resolve four transitions in the 22000 - 33000 cm<sup>-1</sup> region under the broad envelop of the absorption band centered at ~30000 cm<sup>-1</sup>; positive MCD bands centered at 23430 and 29480 cm<sup>-1</sup> and two negative bands centered at 27040 and 32130 cm<sup>-1</sup>. On the basis of the active site structure, several LMCT transitions are expected in this region:  $x$ - or  $z$ -polarized  $\pi$  His → Fe<sup>3+</sup> CT bands involving the three N $\epsilon$ 2 and one N $\delta$ 2 equatorial His ligands, a  $y$ -polarized  $\sigma$  →  $\sigma^*$ , S( $p_{\text{pseudo } \sigma}$ ) → Fe<sup>3+</sup>( $d_{x^2-y^2}$ ) CT band, and a  $y$ -polarized glutamate-to-Fe<sup>3+</sup> CT band. VHVT MCD saturation magnetization data collected at 23430 and 29480 cm<sup>-1</sup>

(data not shown) are very similar to that obtained at  $18980\text{ cm}^{-1}$ , see Figure 2.7, and are readily analyzed in terms of predominantly z-polarized transitions. This demonstrates that  $\pi\text{ His} \rightarrow \text{Fe}^{3+}$  CT transitions contribute to the broad absorption band at  $30000\text{ cm}^{-1}$ , but does not rule out contributions from  $\sigma \rightarrow \sigma^*$ ,  $\text{S}(\text{pseudo } \sigma) \rightarrow \text{Fe}^{3+}(\text{d}_{x^2-y^2})$  CT or glutamate-to- $\text{Fe}^{3+}$  CT transitions. Additional VHVT MCD saturation studies, coupled with resonance Raman excitation profiles, electronic structure calculations and mutagenesis studies, will be required to effect detailed electronic assignments in this region.

The above assignments are readily transferred to the other two high-spin *P. furiosus* SOR derivatives investigated in this work, see Table 2.1. The high pH form exhibits the same pattern of  $\text{S} \rightarrow \text{Fe}$  CT bands in the visible VTMCD spectrum with equivalent transitions blue shifted by  $\sim 750\text{ cm}^{-1}$ . The VTMCD spectrum is broader and less well resolved than that of the low pH form, due to contributions from the low pH form at pH 10 ( $\text{pK}_a = 9.6$ ). This heterogeneity complicates the higher energy CT region of the MCD spectrum ( $22000 - 33000\text{ cm}^{-1}$ ), but high pH minus low pH difference spectra reveal the same pattern of VTMCD bands with equivalent bands blue shifted by  $\sim 1500\text{ cm}^{-1}$ . This indicates that the cysteinyl and histidyl Fe ligation are preserved in the high pH form and suggests that high pH transition involves hydroxyl ligation *trans* to cysteine. Azide binding does not perturb the VTMCD bands in the  $\text{S} \rightarrow \text{Fe}$  CT region, but is evident by the appearance of an intense negative band centered at  $28520\text{ cm}^{-1}$  that dominates the higher energy CT region. This band is attributed to  $\text{N}_3^- \rightarrow \text{Fe}^{3+}$  CT on the basis of VHVT MCD saturation magnetization data (not shown). The magnetization data is analogous to that observed at  $15150\text{ cm}^{-1}$  in Figure 2.7, indicating a y-polarized

transition, which is consistent with  $\text{N}_3^-$  binding *trans* to the cysteinyl S.

Cyanide binding induces a high-spin to low-spin transition and is manifest by small changes in the absorption spectrum (Figure 2.5), marked changes in the VTMCD spectrum (Figure 2.6) and the appearance of pronounced CD bands above  $17000 \text{ cm}^{-1}$  (Figure 2.9). VHVT MCD saturation data for each of the major bands in the VTMCD spectrum are well fit at all temperatures by simulated data constructed for an isolated  $S = 1/2$  doublet using the EPR determined  $g$ -values,  $g = 2.289, 2.251, 1.935$  (data not shown). The range of  $g$ -values is not sufficient to permit meaningful assessment of transition polarizations by fitting of the saturation magnetization data. However, analysis of the visible  $S \rightarrow \text{Fe}^{3+}$  CT bands for a low-spin system is greatly simplified, since there is only one hole in the  $t_{2g}$  set of Fe d-orbitals. Moreover, the splitting of the  $t_{2g}$  set of d-orbitals can be assessed from the EPR spectrum using the relationships between principal  $g$ -values,  $V$ ,  $\Delta$  and  $\xi$  developed by Taylor<sup>34</sup> (where  $V$  and  $\Delta$  are the rhombic and axial splitting parameters for the  $t_{2g}$  set of d-orbitals and  $\xi$  is the one-electron spin-orbit coupling constant for Fe):

$$\begin{aligned} V/\xi &= g_x/(g_x + g_y) + g_y/(g_z - g_x) \\ \Delta/\xi &= g_x/(g_z + g_y) + g_z/(g_y - g_x) - V/2\xi \end{aligned} \quad (2)$$

Using the EPR-determined  $g$ -values for  $\text{CN}^-$ -bound *P. furiosus* SOR, with  $g_z$ ,  $g_y$ , and  $g_x$  as the highest, middle and lowest  $g$ -values, respectively, eq. 2 yields  $V/\xi = 6.82$ ,  $\Delta/\xi = 4.26$ , and  $V/\Delta = 1.60$ . A reasonable estimate of  $\xi$  for Fe in a complex with significant covalent bonding is  $\sim 400 \text{ cm}^{-1}$ , which leads to  $V \sim 2700 \text{ cm}^{-1}$  and  $\Delta \sim 1700 \text{ cm}^{-1}$ , and the  $t_{2g}$  orbital splitting pattern shown in Figure 2.8 with  $d_{yz}$  and  $d_{xz}$  separated by  $\sim 1700 \text{ cm}^{-1}$  and  $d_{xz}$  and  $d_{xy}$  near degenerate and separated by  $\sim 350 \text{ cm}^{-1}$ . Hence the EPR

indicates tetragonally elongated octahedral coordination geometry with the weak-field axis along  $x$ , as dictated by the axis system adopted for the  $g$  tensor. The implication is that binding cyanide trans to the cysteinate results in a strong-field axis comparable to the strong-field bis-histidyl axis that is responsible for the tetragonal compression of the high-spin derivatives discussed above. A d-orbital splitting diagram for the  $x$ -axis along the weak-field bis-histidyl axis and the Fe-S bond along the  $y$ -axis is shown in Figure 2.8.

Only one  $(\text{Cys})\text{S}^- \rightarrow \text{Fe}^{3+}$  CT transition is predicted to occur in the visible region, corresponding to the  $y$ -polarized,  $\text{S}(\text{p}_\pi) \rightarrow \text{Fe}(\text{d}_{yz}) \pi \rightarrow \pi^*$  transition, see Figure 2.8. This transition is expected to have strong absorption intensity as a result of optimal orbital overlap, and weak VTMCD intensity since it is primarily a uniaxial transition. Some VTMCD intensity is expected since the hole in the  $t_{2g}$  set of Fe d-orbitals is best considered as a linear combination of all three one-electron d-orbitals, with coefficients that are defined by the EPR  $g$ -values.<sup>34,35</sup> Hence, the intense absorption band centered at  $14600 \text{ cm}^{-1}$  and the positive VTMCD band centered at  $14680 \text{ cm}^{-1}$  are assigned to the  $\text{S}(\text{p}_\pi) \rightarrow \text{Fe}(\text{d}_{yz}) \pi \rightarrow \pi^*$  transition, see Table 2.1.

In the low-spin cyanide adduct, multiple spin-allowed Fe d-d bands are expected with energies  $> 17000 \text{ cm}^{-1}$ . Such bands are expected to be weak and difficult to see in absorption, particularly in the presence of intense LMCT bands. However, since they are magnetic-dipole allowed transitions, they are expected to be more clearly apparent in the CD and VTMCD spectra. Indeed, cyanide addition results in the appearance of broad positive CD bands centered at  $20610$  and  $22710 \text{ cm}^{-1}$  and broad negative CD bands centered at  $26650$ ,  $30120$ , and  $32620 \text{ cm}^{-1}$ . These CD bands appear to correlate with positive VTMCD bands centered at  $19000$  and  $31000 \text{ cm}^{-1}$  and negative VTMCD bands

centered at  $17000\text{ cm}^{-1}$  and in the  $22000\text{-}27000\text{ cm}^{-1}$  region, see Figure 2.9. These bands are all excellent candidates for the complex pattern of ligand field  ${}^2T_2 \rightarrow {}^2A_2, {}^2T_1, {}^2T_2, {}^2E, {}^2T_1, {}^2A_2, {}^2T_2$  transitions (under idealized  $O_h$  symmetry) that are expected with increasing energy in the  $17000\text{-}35000\text{ cm}^{-1}$  region. On the basis of the lowest energy ligand-field transitions, the ligand field parameters are estimated to be  $10Dq \sim 22000\text{ cm}^{-1}$  and  $B \sim 750\text{ cm}^{-1}$ . Analysis of the high-energy region of the UV-visible absorption, CD and VTMCD spectra ( $22000\text{-}35000\text{ cm}^{-1}$ ) is a complex problem due to overlapping contributions for ligand field,  $\pi\text{ His} \rightarrow \text{Fe}^{3+}$  CT and  $\text{CN}^- \rightarrow \text{Fe}^{3+}$  CT transitions. More detailed ligand field analyses and DFT calculations are in progress to effect assignments of the ligand field and CT transitions and more accurate assessment of the ligand field parameters.

*Reduced P. furiosus SOR:* Reduction of *P. furiosus* SOR with ascorbate or dithionite occurs with complete bleaching of the blue color and results in samples with no absorption in the visible region. However, the combination of absorption, CD and VTMCD studies in the UV and near-IR regions facilitates investigation of CT and ligand-field transitions, and the results provide unique insight into the structural, electronic and magnetic properties of the high-spin ( $S = 2$ )  $\text{Fe}^{2+}$  active site. The UV absorption is dominated by the intense absorption centered at  $36000\text{ cm}^{-1}$  that arises from aromatic amino acid residues and the only feature attributable to CT transitions associated with the  $\text{Fe}^{2+}$  active site is the shoulder at  $31200\text{ cm}^{-1}$ , see Figure 2.10. In contrast, VTMCD provides a means of selectively investigating the electronic transitions associated with the paramagnetic  $\text{Fe}^{2+}$  active site. The positively signed temperature-dependent MCD band at  $31200\text{ cm}^{-1}$  correlates with the observable absorption band, and

additional CT transitions are identified by a positive MCD bands centered at 33900  $\text{cm}^{-1}$  and 38900  $\text{cm}^{-1}$ , see Figure 2.10. The correspondence to the visible VTMCD bands assigned to  $(\text{Cys})\text{S}^- \rightarrow \text{Fe}^{3+}$  CT transitions in oxidized high-spin derivatives of *P. furiosus* SOR (see Table 2.1 and Figure 2.6) is particularly striking. The signs and relative intensity of individual transitions are the same, and the only difference is that the corresponding transitions are shifted to higher energy by  $\sim 15500 \text{ cm}^{-1}$  in reduced SOR. Hence the positively signed VTMCD bands at 31200 and 33900  $\text{cm}^{-1}$  are tentatively assigned to an analogous set of  $(\text{Cys})\text{S}^- \rightarrow \text{Fe}^{2+}$  CT transitions. More detailed assignments are presented below, following assessment of the Fe d-orbital splittings via analysis of the ligand-field transitions.

The seminal work of Solomon and coworkers on reduced mononuclear Fe proteins and model complexes has laid a firm foundation for interpreting the ligand field transitions that are observable in near-IR absorption, CD and VTMCD spectra, in terms of coordination geometry and d-orbital splitting.<sup>27,33</sup> Near-IR absorption, CD and VTMCD spectra for ascorbate-reduced *P. furiosus* SOR in  $\text{D}_2\text{O}$  buffer are shown in Figure 2.11, and corresponding VTMCD spectra after the addition of a 45-fold excess of azide and a 30-fold excess of cyanide are shown in Figures 2.12 and 2.13, respectively. Absorption spectra are of limited utility in this region, since O-H stretching overtones from unexchanged water and protein groups and O-D stretching overtones obscure the region below 9000  $\text{cm}^{-1}$ . CD spectra are not reliable below 6000  $\text{cm}^{-1}$  due to the intense O-D overtone absorption and the possibility of contributions from protein vibrational CD. VTMCD spectra provide the most definitive assessment of ligand field transitions in the 14000-5000  $\text{cm}^{-1}$  region, since temperature dependent bands must originate from a

paramagnetic  $\text{Fe}^{2+}$  center.

The near-IR absorption spectrum of reduced *P. furiosus* SOR has a weak, broad band centered at  $12100\text{ cm}^{-1}$ , with corresponding positive CD band centered at  $12200\text{ cm}^{-1}$  and negative, temperature-dependent MCD band centered at  $12400\text{ cm}^{-1}$ , see Figure 2.11. Although it is not possible to record VTMCD spectra at energies below  $5000\text{ cm}^{-1}$  with the currently available instrumentation, the high frequency tail of a positive, temperature-dependent MCD band centered at  $<5000\text{ cm}^{-1}$  is readily apparent. The observation of two ligand field transitions, one  $>10000\text{ cm}^{-1}$  and one  $\sim 5000\text{ cm}^{-1}$ , is characteristic of a 5-coordinate, square-pyramidal  $\text{Fe}^{2+}$  site.<sup>27,33</sup> This is readily understood in terms of a large splitting in the  ${}^5\text{E}_g$  excited state of the parent  ${}^5\text{T}_{2g} \rightarrow {}^5\text{E}_g$  octahedral d-d band ( $\Delta^5\text{E}_g$ ), as a result of removal of one ligand along the  $z$  axis, i.e. large splitting of the  $d_{x^2-y^2}$  and  $d_{z^2}$  orbitals, see Figure 2.14. Hence the VTMCD data indicate square-pyramidal coordination geometry with  $10Dq < 8700\text{ cm}^{-1}$  and  $\Delta^5\text{E}_g > 7400\text{ cm}^{-1}$ , see Table 2.2.

Definitive evidence for azide and cyanide binding at the vacant coordination site of the square pyramidal  $\text{Fe}^{2+}$  site is provided by near-IR VTMCD studies. The addition of a 45-fold excess of azide did not significantly perturb the NIR absorption and CD spectra, but results in the appearance of positive VTMCD band centered at  $7300\text{ cm}^{-1}$  and weak negative band at  $12100\text{ cm}^{-1}$  (Figure 2.12). The latter band is superimposed on the intense negative VTMCD band centered at  $12400\text{ cm}^{-1}$  band from the square-pyramidal reduced form (Figure 2.11). The VTMCD bands associated with the reduced azide-bound form are readily apparent after subtraction of 85% of the reduced SOR VTMCD spectrum (Figure 2.12). Hence only 15% of the reduced SOR has azide-bound

in samples treated with a 45-fold stoichiometric excess of azide and the weak binding presumably accounts for the absence of significant changes in the NIR absorption and CD spectra. The addition of a 30-fold excess of cyanide is marked by a shift in the near-IR absorption from  $12100\text{ cm}^{-1}$  to a broad band centered at  $11500\text{ cm}^{-1}$  (not shown). Both the CD and VTMCD spectra facilitate resolution of this band into two transitions; positive and negative CD bands centered at  $9900$  and  $11600\text{ cm}^{-1}$ , respectively, and positive and negative VTMCD bands centered at  $10100$  and  $11900\text{ cm}^{-1}$ , respectively (Figure 2.13). Once again the VTMCD data show evidence for the presence of some of the unbound, square pyramidal form. Subtraction of 20% of the reduced SOR spectrum is required to obtain the VTMCD characteristics of the cyanide-bound  $\text{Fe}^{2+}$  species in isolation (Figure 2.13). Hence approximately 80% of the reduced SOR has cyanide bound in samples treated with a 30-fold stoichiometric excess of cyanide.

The ligand-field transitions for cyanide-bound reduced SOR, i.e. two components of  ${}^5\text{T}_{2g} \rightarrow {}^5\text{E}_g$  at  $10000$  and  $11800\text{ cm}^{-1}$ , corresponding to  $10Dq = 10900\text{ cm}^{-1}$  and  $\Delta^5\text{E}_g = 1800\text{ cm}^{-1}$ , (Table 2.2), are characteristic of a 6-coordinate octahedral  $\text{Fe}^{2+}$  site.<sup>27,33</sup> However, the ligand-field transitions for azide-bound reduced SOR, i.e. two components of  ${}^5\text{T}_{2g} \rightarrow {}^5\text{E}_g$  at  $7300$  and  $12100\text{ cm}^{-1}$ , corresponding to  $10Dq = 9700\text{ cm}^{-1}$  and  $\Delta^5\text{E}_g = 4800\text{ cm}^{-1}$  (Table 2.2), indicate coordination geometry intermediate between square-pyramidal and octahedral. The implication is that azide is only weakly bound at the vacant coordination site. With respect to the d-orbital energy diagram shown in Figure 2.14, the major consequence of azide or cyanide binding at the vacant coordination site is to increase the energy of the  $d_{z^2}$  orbital. The small changes in the energy of the  $d_{x^2-y^2}$  orbital as a function of exogenous ligand binding suggest that movement of the Fe into

the equatorial plane is compensated by weaker Fe-N bonding in the six coordinate species.

Analysis of VHVT MCD saturation magnetization data using the protocols developed by Solomon and coworkers for mononuclear  $S = 2$   $\text{Fe}^{2+}$  sites,<sup>27,33</sup> provides information on ground state zero-field splitting and thereby the splitting of the  $t_{2g}$  ( $d_{xy}$ ,  $d_{xz}$ ,  $d_{yz}$ ) set of orbitals. MCD saturation magnetization data for reduced SOR collected at  $12400\text{ cm}^{-1}$  are shown in Figure 2.15. The high degree of nesting for data collected at 1.70, 4.22 and 10.4 K is characteristic of a ground state with  $-D$  and large rhombic splitting,  $\delta$ , in the lowest lying “ $M_s = \pm 2$  doublet” or a ground state with  $+D$  which leaves the  $M_s = 0$  singlet lowest in energy. However, attempts to fit the data to the  $-D$  model and allowing for a substantial  $B$ -term component (up to 4% of  $C$ -term), gave values of  $\delta = 7 \pm 1\text{ cm}^{-1}$  and  $g_{\parallel} = 9 \pm 2$  which corresponds to spin Hamiltonian parameters of  $D = -21 \pm 3\text{ cm}^{-1}$  and  $E/D = 0.33$ . Such a large value of  $D$  is unprecedented for high-spin  $\text{Fe}^{2+}$  species,<sup>27</sup> and suggest that a  $+D$  fit is more appropriate. The data is readily fit with a three-level  $+D$  model (i.e. ignoring contributions from higher lying  $M_s = \pm 2$  levels), with an energy level spacing of 0, 7 and  $15\text{ cm}^{-1}$ , corresponding to  $D \sim +10\text{ cm}^{-1}$  and  $E/D \sim 0.1$ . This translates to ligand-field parameters  $\Delta = +700 \pm 200\text{ cm}^{-1}$  and  $|V/2\Delta| = 0.19 \pm 0.05$  and the splitting pattern shown in Figure 2.14 with  $d_{xz}$  and  $d_{yz}$  split by  $\sim 170\text{ cm}^{-1}$  and  $d_{xy} \sim 700\text{ cm}^{-1}$  lower in energy than the average of  $d_{xz}$  and  $d_{yz}$ .

The d-orbital splitting deduced from ligand-field spectroscopy suggests plausible assignments of the UV VT-MCD bands as  $(\text{Cys})\text{S}^- \rightarrow \text{Fe}^{2+}$  CT transitions, see Figure 2.14. The positively signed bands at  $31200$  and  $33900\text{ cm}^{-1}$  (Figure 2.10) are assigned to  $z$ -polarized  $\text{S}(p_{\pi}) \rightarrow \text{Fe}^{2+}(d_{xz})$  and the  $y$ -polarized,  $\text{S}(p_{\text{pseudo } \sigma}) \rightarrow \text{Fe}^{2+}(d_{yz}) \pi \rightarrow \pi^*$

transition, respectively. The  $S(p_{\pi}) \rightarrow Fe^{2+}(d_{xz}) \pi \rightarrow \pi^*$  transition is expected to be strong in absorption due to optimal overlap, and weak in the VTMCD spectrum since it is a uniaxial transition. In contrast the  $S(p_{\text{pseudo } \sigma}) \rightarrow Fe^{2+}(d_{yz}) \pi \rightarrow \pi^*$  transition is expected to be weak in absorption due to poor overlap, but strong in the VTMCD spectrum due to significant mixing with orthogonally polarized components. Since the  $d_{z^2}$  orbital is  $\sim 5000 \text{ cm}^{-1}$  higher in energy than the near-degenerate  $d_{xz}$  and  $d_{yz}$  orbitals, the positive VTMCD band at  $38900 \text{ cm}^{-1}$  is assigned to the z-polarized,  $S(p_{\text{pseudo } \sigma}) \rightarrow Fe^{2+}(d_{z^2}) \sigma \rightarrow \sigma^*$  transition. These assignments are tentative at present and require further assessment using DFT calculations, coupled detailed VHVT MCD saturation magnetization studies to assess transition polarizations.

**XAS.** Figure 2.16 shows the iron K near-edge spectra of recombinant *P. furiosus* SOR in air-oxidized, dithionite-reduced, and (incompletely) photo-reduced forms. Oxidized SOR is unusually sensitive to photo-reduction, showing detectable changes in the near-edge spectrum after only one 37-min scan; the spectrum in Figure 2.16 is the result of exposure to the X-ray beam for 4.5 hour. In contrast, the spectrum of dithionite-reduced SOR did not change on exposure to the X-ray beam (not illustrated). Fitting a linear combination of the air-oxidized and dithionite-reduced near-edge spectra reproduced the photo-reduced data sets exactly (not illustrated). This indicates that photo-reduced and dithionite-reduced SOR are essentially identical with respect to the iron site and analysis indicated first-order kinetics for the photoreduction with  $k = 2.17 \times 10^{-2} \text{ min}^{-1}$  (Figure 2.16). For the near-edge spectra single scans provide adequate signal-to-noise for our purposes, but for EXAFS spectra averaging is required. The oxidized EXAFS data set was collected by moving the sample in the X-ray beam so as to

interrogate a fresh spot with each scan. The near-edge and EXAFS spectra of all individual scans were compared, and were found to be identical within the noise. In this way, an average XAS data set for oxidized SOR containing no more than 10% photo-reduced enzyme was accumulated.

The EXAFS spectra of air-oxidized and dithionite-reduced SOR, together with the EXAFS Fourier transforms are shown in Figure 2.17. The results of curve-fitting analysis is also shown in Figure 2.17, and the parameters for the best fits given in Table 2.3. Based on the crystal structure, the first shell was modeled with four nitrogen (histidine) ligands and one oxygen, plus a single sulfur. We note that EXAFS analysis cannot readily distinguish between backscatterers of similar atomic number, such as nitrogen and oxygen. The outer shell Fourier transform peaks between 3 and 4 Å are due to backscattering from the outer shell carbons and nitrogen of the histidine ligands, and these were modeled using the approach of Poiarkova and Rehr.<sup>36</sup>

Curve-fitting analysis of the EXAFS of the oxidized sample thus indicated five nitrogen and oxygen ligands at 2.12 Å, and one sulfur at 2.36 Å. Attempts to resolve Fe-N and Fe-O ligands did not converge to significantly different bond-lengths. However, the Debye-Waller factor for the Fe-N/O ligand is unusually large at 0.0094 Å<sup>2</sup>. The Debye-Waller factor is comprised of both static and vibrational components:  $\sigma^2 = \sigma_{\text{stat}}^2 + \sigma_{\text{vib}}^2$ . Assuming a Fe-N stretch of 220 cm<sup>-1</sup>, we can compute  $\sigma_{\text{vib}}^2 = 0.0049 \text{ Å}^2$ ,<sup>36</sup> and the EXAFS-derived Debye-Waller factor thus indicates a significant distribution in Fe-N and Fe-O bond-lengths. The low-temperature high-resolution crystal structure shows two sites which resemble the oxidized EXAFS data (sites A and C)<sup>8</sup> and using the Fe-N and Fe-O bond-lengths of these we compute  $\sigma_{\text{stat}}^2 = 0.0031$ , which combine to give a  $\sigma^2$

value of  $0.008 \text{ \AA}^2$ , which is reasonably close to the EXAFS-derived value of  $0.0094 \pm 0.004 \text{ \AA}^2$  (Table 2.3). Modeling the Fe-N/O EXAFS using three different components was attempted, using two different sets of two Fe-N interactions, plus an Fe-O interaction. The two different Fe-N components were constrained to differ by at least  $0.1 \text{ \AA}$  and at most  $0.15 \text{ \AA}$ , and the  $\sigma^2$  values were linked to the individual bond-lengths. This resulted in a fit that was not significantly better or worse than using a single Fe-N/O component (fit-errors of 0.335 and 0.334, respectively), indicating that the data are at least consistent with a model of the active site which shows axial compression along one N-Fe-N axis, although direct support from EXAFS is not available.

As noted above, the low-temperature, high-resolution crystal-structure of oxidized SOR shows four sites, two of which (sites A and C) are six coordinate, while the other two (B and D) are five coordinate.<sup>8</sup> The EXAFS-derived Fe-N/O bond-length is very close to the crystallographic average bond-length for sites A and C of  $2.10 \text{ \AA}$ , but the Fe-S bond-length of  $2.36 \text{ \AA}$  is significantly shorter than the crystallographically-derived value of  $2.46 \text{ \AA}$  (for sites A and C). A search of the Cambridge Structure Database<sup>37</sup> for compounds with  $\text{Fe}(\text{N/O})_5\text{S}_1$  coordination, and excluding entries where the sulfur bridges between metals, gave an average Fe-S bond-length of  $2.34 \text{ \AA}$  in excellent agreement with the EXAFS-derived value. The crystal structure of sites B and D give an Fe-S bond-length of  $2.67 \text{ \AA}$ . A search of the Cambridge Structure Database<sup>37</sup> for compounds with Fe-S bond-lengths greater than  $2.6 \text{ \AA}$  (restricted to two coordinate sulfur) revealed only six entries, all of which were ferrous species. Thus, while the crystallographic Fe-S bond-lengths for sites B and D are unexpected, they are not without chemical precedence.

The reduced EXAFS data fit best to a first-shell coordination of  $\text{Fe}(\text{N/O})_4\text{S}_1$  with Fe-N bond-lengths of 2.15 and 2.37 Å, respectively. This is in agreement with the crystallographic analysis, which indicated a 5-coordinate species with four histidine and one cysteine coordinated to the metal.<sup>8</sup> For the reduced data set the Fe-N Debye-Waller factor is smaller than for the oxidized at 0.0045 Å<sup>2</sup>, and is close to the vibrational value discussed above. This indicates much less static disorder in individual Fe-N distances in the reduced site than the oxidized site. As for the oxidized enzyme, the crystallographic analysis of sites A and C are in reasonable agreement with the EXAFS, while B and D appear anomalous. Thus, for A and C the average crystallographic Fe-N and Fe-S distances are 2.12 and 2.42 Å, respectively, while for B and D the Fe-N and Fe-S bond-lengths are 2.4 and 2.7 Å, respectively. However, the crystallographically determined metal-ligand distances for sites B and D were not considered reliable due to the partial Fe occupancies (~20%),<sup>8</sup> and will not be considered further. Loss of up to 50% of the active-site Fe on exposure to high concentrations of dithionite (> 100-fold stoichiometric excess for 30 min) has since been confirmed by VT-MCD studies of reduced samples and absorption studies of reoxidized samples (data not shown).

We conclude that the EXAFS of both oxidized and reduced enzyme confirms the crystal structures for sites A and C, but that the crystal structures determined for sites B and D are not representative of the active site structure in frozen solution.

Crystallographic data collection from the oxidized sample was conducted on SSRL's beamline 9-1, and involved approximately 45 min of exposure to the X-ray beam. Beamline 9-1 has approximately 200 fold greater photon flux at the sample than beamline 7-3 (where the XAS data were collected), although a photon energy with

approximately 6-fold lower absorption cross section was used for the crystallography. The effective radiation dose rate in the crystallography experiment was thus about 30 times that of the XAS, but for a fifth of the time. Furthermore, the crystallography was conducted at the relatively high temperature of 90 K. All of these factors will contribute towards X-ray photo-reduction of the metal site. The observation that sites B and D are more sensitive to both photo-reduction and reductive degradation than site A and C suggests heterogeneity in the active-site structures at least in the crystalline state.

## **Discussion**

Homologs of *P. furiosus* SOR are found in the genomes of all strict anaerobes.<sup>2</sup> Hence the *P. furiosus* SOR active site is likely to represent a common strategy for oxygen detoxification in anaerobic microorganisms. The spectroscopic studies reported herein have provided detailed assessment of the ground- and excited-state electronic properties and ground-state structural information for oxidized and reduced forms of this new type of mononuclear Fe active site in solution. The results permit rationalization of apparent differences in spectroscopic properties, facilitate reconciliation of X-ray crystal structures with solution structures, and provide evidence for exogenous ligand binding at the Fe center in both the oxidized and reduced states. Each of these aspects, together with their implications for the catalytic mechanism and the role of the axial cysteine ligand, are discussed separately below.

Three subclasses of enzymes containing the SOR active site have been characterized thus far. In each case, the residues ligating the mononuclear Fe active site are rigorously conserved. The simplest are the low molecular weight proteins (subunit  $M_r$  ~14.5 kDa), initially termed neelaredoxins due to their intense blue color, which have

been purified to homogeneity from *D. gigas*,<sup>6</sup> *P. furiosus*,<sup>2</sup> and *Archaeoglobus fulgidus*.<sup>38</sup> While neelaredoxin from *D. gigas* was originally reported to contain two Fe atoms per monomer,<sup>6</sup> the crystallographic and analytical studies of the highly homologous *P. furiosus* protein have shown it to contain one active-site Fe center per monomer.<sup>2,8</sup> Compared to these proteins, Desulfoferrodoxins (subunit  $M_r$  ~14 kDa) have an ~30-residue N-terminal extension with high sequence homology to desulforedoxin, and containing four cysteine residues which ligate a rubredoxin-type Fe center. The neelaredoxin-type domain is highly conserved with a truncated C-terminus as well as 7-residue and 20-residue deletions compared to neelaredoxins. In addition to the crystallographically defined protein from *D. desulfuricans*,<sup>9-11</sup> Dfxs have been purified and characterized from two other sulfate-reducing bacteria, *D. vulgaris*<sup>10,12,14,15</sup> and *Ds. baarsii*<sup>3,16</sup> and are known to be present in at least two archaea, *A. fulgidus* and *Methanobacterium thermoautotrophicum*, based on sequence considerations. The third subclass corresponds to the enzyme from *T. pallidum*<sup>4,5</sup> which has high sequence homology to Dfxs, but lacks the rubredoxin-type Fe center and three of the four conserved cysteine residues in the N-terminal desulforedoxin domain.

On the basis of the UV-visible absorption and redox properties, the oxidized SOR active sites appear to be very similar in all three subclasses. However, marked differences in EPR properties have been reported. Axial  $S = 5/2$  resonances analogous to that reported herein for *P. furiosus* SOR ( $E/D \sim 0.06$ ) have been observed in *D. gigas* and *A. fulgidus* neelaredoxins,<sup>6,38</sup> although a  $g = 4.3$  feature from a rhombic ( $E/D \sim 0.33$ )  $S = 5/2$  component dominates the spectrum in the latter case. In *T. pallidum* SOR<sup>4,5</sup> and the Dfx proteins from sulfate-reducing bacteria,<sup>3,11,12,15</sup> a rhombic component ( $E/D = 0.27-0.33$ )

has been attributed to the oxidized resting SOR active site. These apparent inconsistencies can be at least partially reconciled by the EPR studies of *P. furiosus* SOR reported herein. In the most active preparations of *P. furiosus* SOR, the axial species ( $D = -0.5 \text{ cm}^{-1}$ ,  $E/D \sim 0.06$ ) has been shown to account for  $\sim 80\%$  of the Fe and to exhibit a redox potential ( $E_m = +250 \pm 20 \text{ mV}$ ) in accord with that determined by optical redox titrations at room temperature ( $E_m = +238 \pm 10 \text{ mV}$ ). Moreover, by comparing native, reconstituted and recombinant enzymes, enzymatic activity has been correlated with this axial  $S = 5/2 \text{ Fe}^{3+}$  EPR resonance and oxidation with ferricyanide has been found to result in a rhombic  $S = 5/2$  species attributed to a ferrocyanide bound form. Due to the high  $\text{Fe}^{3+}/\text{Fe}^{2+}$  midpoint potential, ferricyanide has been used as an oxidant in almost all the published EPR studies. Consequently it is possible that the rhombic  $S = 5/2$  species observed in *T. pallidum* SOR and the Dfx proteins are artifacts of ferricyanide oxidation and do not correspond to the functional conformation of the oxidized resting enzyme. Recent studies of *T. pallidum* SOR provide support for this hypothesis. EPR studies of hexachloroiridate-oxidized *T. pallidum* SOR revealed that 90% of Fe was present as the ( $D = -0.5 \text{ cm}^{-1}$ ,  $E/D \sim 0.06$ )  $S = 5/2 \text{ Fe}^{3+}$  species, with the remaining 10% contributing a rhombic  $g = 4.3$  signal attributable to adventitiously bound  $\text{Fe}^{3+}$  species.<sup>39</sup> The existence of an axial  $E/D \sim 0.06 \text{ } S = 5/2 \text{ Fe}^{3+}$  SOR active-site species in Dfx proteins is difficult to assess by EPR, due to overlap with resonance from the desulforedoxin  $S = 5/2 \text{ Fe}^{3+}$  center ( $D > 0$ ,  $E/D = 0.08$ ). However, Mössbauer studies of *D. desulfuricans* Dfx argue strongly in favor of a homogeneous, rhombic  $S = 5/2$  ground state ( $E/D = 0.28$ ,  $D = -1.4 \text{ cm}^{-1}$ ) for the oxidized SOR site (Center II), even in the absence of exogenous ligands or oxidants.<sup>11</sup> This suggests a different active-site conformation for the oxidized SOR center in Dfx. It

remains to be determined if this rhombic species corresponds to a functional conformation or if conditions can be found in Dfx to effect conversion to the axial species that is associated with the most active form of monoiron SORs

The X-ray crystal structures of *P. furiosus* SOR (oxidized and reduced)<sup>8</sup> and *D. desulfuricans* Dfx (oxidized)<sup>9</sup> have both revealed an SOR active site comprising a mononuclear Fe coordinated by the imidazole nitrogens of four equatorial histidines (three  $\epsilon$ N and one  $\delta$ N) and one apical cysteinyl sulfur. However, the ligation and coordination number of the oxidized Fe center was not fully resolved by the crystal structures. In two of the four subunits of *P. furiosus* SOR a conserved glutamate carboxylate serves as the sixth ligand, while in the other two subunits and in *D. desulfuricans* Dfx, the sixth coordination site is vacant or occupied by a weakly coordinated solvent molecule. After reduction of crystalline *P. furiosus* SOR with a large excess of dithionite, two of the Fe sites showed only partial occupancy (~20%) and the other two exhibited square pyramidal Fe sites with no indication of a solvent molecule at the vacant coordination site.

In light of the photo-reduction observed in XAS studies of oxidized *P. furiosus* SOR, it seems very likely that the discrepancies in oxidized crystal structures reflect partial (*P. furiosus* SOR) or complete (*D. desulfuricans* Dfx) photoreduction by the synchrotron radiation to yield a reduced SOR active site with square pyramidal coordination geometry. Furthermore, the electronic properties of the oxidized high-spin  $\text{Fe}^{3+}$  center in active *P. furiosus* SOR, as deduced by EPR and VTMCD, are consistent with the glutamate-bound structure. The ground-state zero-field splitting parameters,  $D = -0.5 \text{ cm}^{-1}$  and  $E/D \sim 0.06$ , indicate an octahedrally ligated  $\text{Fe}^{3+}$  center with a

predominantly axial compression.<sup>33</sup> The transition polarizations for the S-to-Fe<sup>3+</sup> CT bands deduced from VHVT MCD saturation magnetization studies dictate that the compression (zero-field-splitting) axis is perpendicular to the Fe-S axis. Hence the strong field axis is along one of the N-Fe-N axes, which is in accord with imidazole generally being a stronger field ligand than thiolate or carboxylate. In addition, the low-temperature crystallographic data for *P. furiosus* SOR indicate that the two N-Fe-N axes are not equivalent; the average Fe-N distances for one pair of trans His ligands (2.09 Å for His16(εN) and His47(εN)) ~ 0.1 Å shorter than the other pair (2.19 Å for His41(εN) and His114(δN)).<sup>8</sup> The strong-field axis is, therefore, defined by His16 and His47 and the crystallographic data indicates that this axis lies within the Fe-S-C plane, in accord with axis system used in making electronic assignments, see Figure 2.8.

The EXAFS data for oxidized *P. furiosus* SOR, one Fe-S at 2.33 Å and an Fe-N/O shell that can be fit equally well to five Fe-N/O at 2.12 Å or two Fe-N at 2.07 Å, two Fe-N at 2.17 Å, and one Fe-O at 2.15 Å, are also in good agreement with crystallographic data for the six-coordinate glutamate-bound form. The major difference lies in a shorter Fe-S distance (2.36 Å from the EXAFS data compared to 2.46 Å for the two glutamate-ligated sites in the crystal structure<sup>8</sup>). A long Fe-S distance of 2.46 Å is also incompatible with the strong  $p\pi$ - $d\pi$  S-Fe interaction that is evident from analysis of the excited state properties. While both the EXAFS and electronic properties are consistent with a distorted octahedral Fe<sup>3+</sup> site in oxidized SOR, neither can specifically address the identity of the sixth ligand. However, the crystallographic data for *P. furiosus* SOR,<sup>8</sup> coupled with the recent mutagenesis results for *D. vulgaris* and *Ds. baarsii* Dfx,<sup>14,16</sup> which reported an ~60-nm blue shift in the visible-absorption S-to-Fe<sup>3+</sup> CT band in

variants in which the conserved glutamate residue was replaced by alanine, strongly support the monodentate glutamate carboxylate as the sixth ligand to the oxidized Fe site in all three subclasses of SOR.

Near-IR VTMCD studies of reduced *P. furiosus* SOR have confirmed that the square pyramidal Fe coordination evident in the reduced crystal structure persists in solution. The large splitting in the near-IR ligand field transitions,  $\Delta^5E_g > 7400 \text{ cm}^{-1}$ , dictates a large separation in the  $d_{x^2-y^2}$  and  $d_{z^2}$  orbitals, suggesting a weak axial ligand with the Fe not far removed from the equatorial plane.<sup>27</sup> This is in good agreement with the crystallographic data, which positions the Fe at an angle of  $\sim 12^\circ$  above the plane of the four ligated N atoms. On the basis of purely geometric considerations, this square pyramidal ligand field would be expected to result in  $D < 0$ , i.e. the  $t_{2g}$  set of orbitals split with  $d_{xz}$  and  $d_{yz}$  nearly degenerate and lower in energy than  $d_{xy}$ . The observed inversion of this splitting pattern, as evidenced by  $D > 0$ , could be rationalized in terms of a strong axial ligand such that the Fe is extensively pulled out of the equatorial plane or covalency effects such as  $\pi$  interaction between the S  $p_\pi$  and  $p_{\text{pseudo } \sigma}$  orbitals and the Fe  $d_{xz}$  and  $d_{yz}$  orbitals. The large splitting in the  $e_g$  set of orbitals coupled with the crystallographic data and the UV VTMCD/absorption evidence for  $\pi \rightarrow \pi^*$  (Cys) $S^- \rightarrow Fe^{2+}$  CT transitions, therefore indicates that the positive axial zero-field splitting observed in reduced SOR is a result of significant  $p\pi$ - $d\pi$  Fe-S interaction. EXAFS of the reduced enzyme also agrees well with the reduced crystal structure with 4 Fe-N at 2.15 Å and one Fe-S at 2.37 Å. The Fe-S distance is significantly shorter than the average of the two crystallographically defined distances, 2.42 Å, but is consistent with the  $p\pi$ - $d\pi$  Fe-S interaction that is required to rationalize the ground-state and excited state electronic properties.

The opposite signs of the near-IR VTMCD ligand field bands of reduced SOR provide information on the nature of the active-site distortion from idealized square pyramidal coordination geometry. In the majority of square pyramidal  $\text{Fe}^{2+}$  inorganic complexes investigated thus far, both near-IR ligand field VTMCD bands are positively signed.<sup>40</sup> Opposite signs require a low symmetry point group in which the  $d_{x^2-y^2}$  and  $d_{z^2}$  orbitals transform as different irreducible representations. This can occur under  $C_s$  symmetry for the SOR active site, provided the mirror plane bisects rather than contains the Fe-N bonds. In agreement with this prediction, inspection of the active site crystal structure, including the imidazole rings of the coordinated histidines, does reveal an approximate mirror plane bisecting the His114 and His47 Fe-N bonds.

The spectroscopic studies reported in this work demonstrate that the *P. furiosus* SOR active site is accessible for exogenous ligand binding in both the oxidized and reduced states. Evidence has been presented for azide, hydroxide, ferrocyanide and cyanide binding to the  $\text{Fe}^{3+}$  site in place of the glutamate carboxylate. Cyanide binding induces a high-spin to low-spin transition and has afforded detailed insight into the ground and excited-state electronic properties of a low-spin  $\text{Fe}^{3+}$  derivative of SOR. Azide, hydroxide and ferricyanide binding occur with retention of the high-spin electronic configuration and are manifest by a change from a predominantly axial to a near-rhombic  $S = 5/2$  ground state. More work is required to establish definite evidence for hydroxide and ferrocyanide binding. The alkaline transition,  $\text{pK}_a = 9.6$ , that has been observed in *D. gigas* neelaredoxin<sup>6</sup> and *P. furiosus* SOR, has been attributed to hydroxide displacing the glutamate ligand, on the basis of the VTMCD studies which indicate that the same pattern of  $(\text{Cys})\text{S}^- \rightarrow \text{Fe}^{3+}$  and  $\pi \text{ His} \rightarrow \text{Fe}^{3+}$  CT bands each blue-shifted by

$\sim 1500\text{ cm}^{-1}$ . This implies that the histidyl and cysteinyl ligation is retained and the blue shift in the CT bands is consistent with hydroxide binding and a concomitant increase in electron density at the Fe site. Ferrocyanide binding appears to be the most reasonable explanation of the “azide-like” changes in the ground state properties that are induced on ferricyanide oxidation. Near-IR VTMCD studies have provided compelling evidence for azide and cyanide binding at the vacant coordination site of the square-pyramidal ferrous active site of reduced *P. furiosus* SOR. Azide binds weakly with a coordination geometry intermediate between octahedral and square pyramidal, whereas cyanide binds to give an octahedrally ligated high-spin ferrous derivative.

The ability to bind exogenous ligands to both the ferric and ferrous active sites is consistent with an inner sphere mechanism for superoxide reduction. The most plausible, albeit unproven, mechanism involves superoxide binding at the vacant coordination site of reduced SOR coupled with electron transfer from iron to superoxide to yield ferric-peroxo and/or ferric-hydroperoxo intermediates. Under this scenario, the cysteine, which is *trans* to the superoxide binding site, would play a crucial role in pushing electron density on to the iron in order to promote ferrous-to-superoxide electron transfer and/or product dissociation from the ferric-(hydro)peroxo intermediate. Hence the strong  $p\pi-d\pi$  Fe-S bonding interactions that have been identified in this study in both the oxidized and reduced forms of SOR are likely to provide an important electronic contribution to active-site reactivity. In addition, by analogy with blue copper proteins,<sup>41</sup> the  $p\pi-d\pi$  Fe-S bonding interaction in SOR may provide a superexchange pathway to facilitate electron transfer from rubredoxin.

Recent pulse radiolysis kinetic studies of Dfx from *D. vulgaris*<sup>14</sup> and *D. baarsii*<sup>16</sup>

and SOR from *T. pallidum*<sup>17</sup> have facilitated characterization of the visible absorption spectra of transient intermediates in the catalytic mechanism of superoxide reduction. While the results of these studies are not in good agreement, it is appropriate to evaluate the published interpretations in light of the detailed assessment of the electronic properties presented herein. The study of *D. vulgaris* Dfx reported a transient intermediate, characterized by a visible absorption band at 600 nm (16700 cm<sup>-1</sup>), that appears as a result of a bimolecular reaction occurring at a nearly diffusion controlled rate,  $1.5 \times 10^9 \text{ M}^{-1}\text{s}^{-1}$ , and disappears in a slower unimolecular reaction with a rate of  $40 \text{ s}^{-1}$ . By analogy with the optical properties of ferric-(hydro)peroxo complexes,<sup>33</sup> this absorption band was attributed to the (hydro)peroxo-to-ferric CT band of a putative ferric (hydro)peroxo intermediate. However, since the hydroxide-bound form of oxidized *P. furiosus* SOR and the E47A variant of *D. vulgaris* Dfx<sup>14</sup> both exhibit intense absorption bands at 600 nm that arise exclusively from cysteinyl S-to-ferric CT transitions, assignment to a (hydro)peroxo-to-ferric CT band may be premature at this stage. It is also important to note that the hydroperoxo-to-ferric CT band in activated bleomycin,<sup>33,42</sup> as well as a wide range of related end-on, low-spin ferric hydroperoxy complexes,<sup>43</sup> have weak absorption intensity compared to that of the intense cysteinyl S-to-ferric CT transitions seen in SOR.

The results and interpretation of the kinetic study of *Ds. baarsii*<sup>16</sup> are more perplexing. Two intermediates were identified. The first forms rapidly as a result of a bimolecular reaction at near diffusion-controlled rates,  $1.1 \times 10^9 \text{ M}^{-1}\text{s}^{-1}$ , and is characterized by intense visible absorption bands at 550 nm (18200 cm<sup>-1</sup>) and 610 nm (16400 cm<sup>-1</sup>). Without explanation, this intermediate was tentatively attributed to a

ferrous-superoxide species. Although the possibility that one or both of these bands arises from an unprecedented ferrous-to-superoxide CT transition cannot be completely discounted, assigning these transitions to a ferrous species is considered extremely unlikely in light of the visible absorption properties of the ferrous and ferric SOR derivatives investigated in this work. The initial intermediate is reported to decay to a second intermediate in a unimolecular reaction with a rate of  $500 \text{ s}^{-1}$ . This intermediate is characterized by an intense absorption band at 630 nm ( $15900 \text{ cm}^{-1}$ ) that was attributed to the peroxy-to-ferric CT band of a ferric-(hydro)peroxy species. However, assignment of this species as catalytic intermediate must be viewed as questionable at this stage. The visible absorption properties deduced for this intermediate are very similar to those of the oxidized SOR center in this enzyme (absorption maximum at 644 nm,  $15500 \text{ cm}^{-1}$ ) and the absorption spectrum of the final species was not determined. Even if it does correspond to an intermediate, we conclude that the 630-nm absorption band is more likely to be result from cysteinyl S-to-ferric CT than peroxy-to-ferric CT.

Optical absorption changes during pulse radiolysis studies of *T. pallidum* SOR are easier to assess than in Dfx due to the absence of the additional rubredoxin-type iron center. Two intermediates were identified.<sup>17</sup> The first was formed at near diffusion controlled rates,  $6 \times 10^8 \text{ M}^{-1}\text{s}^{-1}$ , and is characterized by a visible absorption band centered near 610 nm ( $16400 \text{ cm}^{-1}$ ). This decays in a slower step,  $4800 \text{ s}^{-1}$ , to yield second intermediate exhibiting an absorption band at 670 nm ( $14900 \text{ cm}^{-1}$ ). The first and second intermediates were assigned to ferric-peroxy and ferric-hydroperoxy species, respectively, with the visible absorption bands attributed to peroxy-to-ferric and hydroperoxy-to-ferric CT transitions, respectively. However, this assignment is not

consistent with the energies of the observed CT bands. Peroxo-to-ferric CT is predicted to occur at *lower* energy than hydroperoxo-to-ferric CT in the absence of other changes in iron coordination geometry or ligation. This prediction has been verified experimentally in the only model complex for which both ferric-peroxo and ferric-hydroperoxo forms have been characterized. Protonation of the side-on peroxo ligand ( $\eta^2\text{-O}_2^{2-}$ ) in  $[(\text{trispicMeen})\text{Fe}(\text{O}_2)]^+$  to yield the end-on hydroperoxo complex  $[(\text{trispicMeen})\text{Fe}(\text{OOH})]^{2+}$  is marked by a dramatic blue shift in the visible CT band from 740 nm ( $13500\text{ cm}^{-1}$ ) to 540 nm ( $18500\text{ cm}^{-1}$ ).<sup>44</sup> Ironically, the published assignment for the two intermediate species identified in *T. pallidum* SOR<sup>17</sup> is quite reasonable provided the observed visible CT bands are assigned to cysteinyl S-to-ferric CT rather than (hydro)peroxo-to-ferric CT. Protonation of the ligand *trans* to cysteine would be expected to shift the cysteinyl S-to-ferric CT to lower energy as observed. Hence the published interpretation may be correct, albeit for the wrong reasons.

In summary, the three kinetic studies of the SOR mechanism reported thus far do not concur and none has provided compelling spectroscopic evidence for a putative ferric-peroxy or ferric-hydroperoxy intermediate. The observed changes in the energy of visible charge transfer band are best interpreted in terms of changes in the energy of the cysteinyl S-to-ferric CT transition that are induced by changes in the *trans* ligand, rather than the appearance of intense (hydro)peroxo-to-ferric CT bands. We conclude that there is still much to be learnt about the catalytic mechanism of SOR and that understanding the electronic transitions associated with the cysteine ligand will be crucial in this endeavor. The present study has provided a detailed understanding of the structural, electronic, magnetic and ligand binding properties of the mononuclear iron active site in

wild-type SOR. In addition to providing insight into the electronic properties and bonding of a unique non-heme iron active site with a single cysteine ligand, the results set the stage for future kinetic, mutagenesis and spectroscopic studies designed to elucidate the catalytic mechanism and the role of key residues in optimizing the active site for superoxide reduction as opposed to dismutation.

**Acknowledgments.** This work was supported by grants from the National Institutes of Health (GM60329 to M.W.W.A and M.K.J.) and a National Science Foundation Research Training Group Award to the Center for Metalloenzyme Studies (DBI9413236). Work at SSRL was funded by the Department of Energy, Offices of Basic Energy Sciences and Biological and Environmental Research and the National Institutes of Health (RR01209). We thank Professor E. I. Solomon and Dr. Frank Neese for supplying the programs used in analyzing VHVT MCD magnetization data and for stimulating discussions.

## References

- (1) Liochev, S. I.; Fridovich, I. *J. Biol. Chem.* **1997**, *272*, 25573-25575.
- (2) Jenney, F. E.; Verhagen, M. F. J. M.; Cui, X.; Adams, M. W. W. *Science* **1999**, *286*, 306-309.
- (3) Lombard, M.; Fontecave, M.; Touati, D.; Nivière, V. *J. Biol. Chem.* **2000**, *275*, 115-121.
- (4) Lombard, M.; Touati, D.; Fontecave, M.; Nivière, V. *J. Biol. Chem.* **2000**, *275*, 27021-27026.
- (5) Jovanovi'c, T.; Ascenso, C.; Hazlett, K. R. O.; Sikkink, R.; Krebs, C.; Litwiller, L. M.; Benson, L. M.; Moura, I.; Moura, J. J. G.; Radolf, J. D.; Huynh, B. H.; Naylor, S.; Rusnak, F. M. *J. Biol. Chem.* **2000**, *275*, 28439-28448.
- (6) Chen, L.; Sharma, P.; LeGall, J.; Mariano, A. M.; Teixeira, M.; Xavier, A. V. *Eur. J. Biochem.* **1994**, *226*, 613-618.
- (7) Silva, G.; Oliveira, S.; Gomes, C. M.; Pacheco, I.; Liu, M.-Y.; Xavier, A. V.; Teixeira, M.; LeGall, J.; Rodrigues-Pousada, C. *Eur. J. Biochem.* **1999**, *259*, 235-243.
- (8) Yeh, A. P.; Hu, Y.; Jenney, F. E.; Adams, M. W. W.; Rees, D. C. *Biochemistry* **2000**, *39*, 2499-2508.
- (9) Coelho, A. V.; Matias, P.; Fülöp, V.; Thompson, A.; Gonzalez, A.; Carrondo, M. *A. J. Biol. Inorg. Chem.* **1997**, *2*, 680-689.
- (10) Moura, I.; Tavares, P.; Moura, J. J. G.; Ravi, N.; Huynh, B. H.; Liu, M.-Y.; LeGall, J. *J. Biol. Chem.* **1990**, *265*, 21596-21602.
- (11) Tavares, P.; Ravi, N.; Moura, J. J. G.; LeGall, J.; Huang, Y.-H.; Crouse, B. R.;

- Johnson, M. K.; Huynh, B. H.; Moura, I. *J. Biol. Chem.* **1994**, *269*, 10504-10510.
- (12) Ascenso, C.; Rusnak, F. M.; Cabrito, I.; Lima, M. J.; Naylor, S.; Moura, I.; Moura, J. J. G. *J. Biol. Inorg. Chem.* **2000**, *5*, 720-729.
- (13) Romão, C. V.; Liu, M.-Y.; LeGall, J.; Gomes, C. M.; Braga, V.; Pacheco, I.; Xavier, A. V.; Teixeira, M. *Eur. J. Biochem.* **1999**, *261*, 438-443.
- (14) Coulter, E. D.; Emerson, J. P.; Kurtz, D. M., Jr.; Cabelli, D. E. *J. Am. Chem. Soc.* **2000**, *122*, 11555-11556.
- (15) Verhagen, M. F. J. M.; Voorhorst, W. G. B.; Kolkman, J. A.; Wolbert, R. B. G.; Hagen, W. R. *FEBS Lett.* **1993**, *336*, 13-18.
- (16) Lombard, M.; Houée-Levin, C.; Touati, D.; Fontecave, M.; Nivière, V. *Biochemistry* **2001**, *40*, 5032-5040.
- (17) Nivière, V.; Lombard, M.; Fontecave, M.; Houée-Levin, C. *FEBS Lett.* **2001**, *497*, 171-173.
- (18) Sambrook, J.; Fritsch, E. F.; Maniatis, T. *Molecular Cloning: a Laboratory Manual*, 2<sup>nd</sup> ed.; Cold Spring Harbor Laboratory Press: Cold Spring Harbor, New York, 1998.
- (19) Bryant, F. O.; Adams, M. W. W. *J. Biol. Chem.* **1989**, *264*, 5070-5079.
- (20) Venters, R. A.; Calderone, T. L.; Spicer, L. D.; Fierke, C. A. *Biochemistry* **1991**, *30*, 4491-4494.
- (21) (a) Goa, J. *Scand. J. Clin. Lab. Invest.* **1953**, *5*, 218-222. (b) Bensadoun, A.; Weinstein, D. *Anal. Biochem.* **1976**, *70*, 241-250.
- (22) Cramer, S. P.; Tench, O.; Yocum, M.; George, G. N. *Nucl. Instrum. Methods Phys. Res.* **1998**, *A266*, 586-591.

- (23) (a) <http://ssrl.slac.stanford.edu/exafspak.html>; (b) George, G. N.; Garrett, R. M.; Prince, R. C.; Rajagopalan, K. V. *J. Am. Chem. Soc.* **1996**, *118*, 8588-8592.
- (24) (a) Rehr, J. J.; Mustre de Leon, J.; Zabinsky, S. I.; Albers, R. C. *J. Am. Chem. Soc.* **1991**, *113*, 5135-5140. (b) Mustre de Leon, J.; Rehr, J. J.; Zabinsky, S. I.; Albers, R. C. *Phys. Rev.* **1991**, *B44*, 4146-4156.
- (25) (a) Johnson, M. K. In *Metal Clusters in Proteins*; Que, L., Jr., Ed.; American Chemical Society: Washington, D.C., 1988; pp 326-342; (b) Thomson, A. J.; Cheesman, M. R.; George, S. J. *Meth. Enzymol.* **1993**, *226*, 199-232.
- (26) Neese, F.; Solomon, E. I. *Inorg. Chem.* **1999**, *38*, 1847-1865.
- (27) Solomon, E. I.; Pavel, E. G.; Loeb, K. E.; Campochiaro, C. *Coord. Chem. Rev.* **1995**, *144*, 369-460.
- (28) Aasa, R.; Vänngård, T. *J. Magn. Reson.* **2000**, *19*, 308-315.
- (29) Jenney, F. E., Jr.; Adams, M. W. W. A., unpublished results.
- (30) Johnson, M. K. In *Physical Methods in Bioinorganic Chemistry. Spectroscopy and Magnetism*; Que, L., Jr., Ed.; University Science Books: Sausalito, CA, 2000; pp 233-286.
- (31) (a) Gewirth, A. A.; Solomon, E. I. *J. Am. Chem. Soc.* **1988**, *110*, 3811-3819. (b) LaCroix, L. B.; Randall, D. W.; Nersissian, A. M.; Hoitink, C. W. G.; Canters, G. W.; Valentine, J. S.; Solomon, E. I. *J. Am. Chem. Soc.* **1998**, *120*, 9621-9631.
- (32) Uniaxial polarization percentages have been estimated from  $M_{xy}$ ,  $M_{yz}$ , and  $M_{xz}$ , using the cyclic permutations of the following expression:<sup>26</sup>
- $$\% x = 100(M_{xy}M_{xz})^2 / [(M_{xy}M_{xz})^2 + (M_{xy}M_{yz})^2 + (M_{xz}M_{yz})^2]$$
- (33) Solomon, E. I.; Brunold, T. C.; Davis, M. I.; Kemsley, J. N.; Lee, S.-K.; Lehnert,

- N.; Neese, F.; Skulan, A. J.; Yang, Y.-S.; Zhou, J. *Chem. Rev.* **2000**, *100*, 235-349.
- (34) Taylor, C. P. S. *Biochim. Biophys. Acta* **1977**, *491*, 137-149.
- (35) McKnight, J.; Cheesman, M. R.; Thomson, A. J.; Miles, J. S.; Munro, A. W. *Eur. J. Biochem.* **1993**, 683-687.
- (36) Poiarkova, A. V.; Rehr, J. J. *Phys. Rev.* **1999**, *B59*, 948-957.
- (37) Allen, F. H.; Kennard, O. *Chem. Des. Autom. News* **1993**, *1*, 31-37.
- (38) Abreu, I. A.; Saraiva, L. M.; Carita, J.; Huber, H.; Stetter, K. O.; Cabelli, D. E.; Teixeira, M. *Mol. Microbiol.* **2000**, *38*, 322-334.
- (39) Clay, M. D.; Rusnak, F. M.; Johnson, M. K., unpublished results.
- (40) Pavel, E. G.; Kitajima, H.; Solomon, E. I. *J. Am. Chem. Soc.* **1998**, *120*, 3949-3962.
- (41) Lowery, M. D.; Guckert, J. A.; Gebhard, M. S.; Solomon, E. I. *J. Am. Chem. Soc.* **1993**, *115*, 3012-3013.
- (42) Neese, F.; Zaleski, J. M.; Loeb Zaleski, K.; Solomon, E. I. *J. Am. Chem. Soc.* **2000**, *122*, 11703-11724.
- (43) Girerd, J.-J.; Banse, F.; Simaan, A. J. *Struct. Bonding* **2000**, *97*, 145-177.
- (44) Simaan, A. J.; Banse, F.; Mialan, P.; Bousac, A.; Un, S.; Kargar-Grisel, T.; Bouchoux, G.; Girerd, J.-J. *Eur. J. Inorg. Chem.* **1999**, 993-996.

**Table 2.1** Excited state electronic assignments for derivatives of oxidized recombinant *P. furiosus* SOR<sup>a</sup>

Assignments	Absorption			MCD			CD	
	Energy cm <sup>-1</sup> (nm)	$\epsilon$ mM <sup>-1</sup> cm <sup>-1</sup>	Predicted polarization	Energy cm <sup>-1</sup> (nm)	Sign	Observed Polarization	Energy cm <sup>-1</sup> (nm)	Sign
Oxidized SOR pH 7.5 CysS <sup>-</sup> → Fe <sup>3+</sup> CT S(p $\pi$ ) → Fe(d <sub>xy</sub> ) S(p <sub>pseudo <math>\sigma</math></sub> ) → Fe(d <sub>yz</sub> ) His → Fe <sup>3+</sup> CT {	15150 (660)	2.5	y	15150 (660)	+	y		
			z	18980 (527)	+	z		
	~30000 (333)	7.2	x or z	23430 (427)	+	z		
27040 (370)?				-	z			
29480 (339)				+	z			
32130 (311)?				-				
Oxidized SOR pH 10.0 CysS <sup>-</sup> → Fe <sup>3+</sup> CT S(p $\pi$ ) → Fe(d <sub>xy</sub> ) S(p <sub>pseudo <math>\sigma</math></sub> ) → Fe(d <sub>yz</sub> ) His → Fe <sup>3+</sup> CT {	16940 (590)	1.8	y	16500 (606)	+	y		
			z	19720 (507)	+	z		
	~31000 (333)	6.2	x or z	24200 (405)	+	z		
				31060 (322)	+	z		
Oxidized SOR + N <sub>3</sub> <sup>-</sup> CysS <sup>-</sup> → Fe <sup>3+</sup> CT S(p $\pi$ ) → Fe(d <sub>xy</sub> ) S(p <sub>pseudo <math>\sigma</math></sub> ) → Fe(d <sub>yz</sub> )	15150 (660)	2.3	y	15150 (660)	+	y		
			z	18980 (527)	+	z		

His $\rightarrow$ Fe <sup>3+</sup> CT	~30000 (333)	6.5	x or z	23430 (427)	+	z				
N <sub>3</sub> <sup>-</sup> $\rightarrow$ Fe <sup>3+</sup> CT				33700 (296)?	+					
Oxidized SOR + CN <sup>-</sup>	14600 (685)	2.7	y	28520 (351)	-	y				
CysS <sup>-</sup> $\rightarrow$ Fe <sup>3+</sup> CT										
S(p $\pi$ ) $\rightarrow$ Fe(d <sub>yz</sub> )							14680 (681)	+		
Low Spin Fe <sup>3+</sup> d-d							17000 (588)	-		
							19000 (526)	+		
				23000 (435)	-		20610 (485)	+		
His $\rightarrow$ Fe <sup>3+</sup> CT	~31000 (322)	5.8	x or z				22710 (440)	-		
CN <sup>-</sup> $\rightarrow$ Fe <sup>3+</sup> CT								26650 (375)	-	
							30120 (332)?			
							32620 (307)?			
His $\rightarrow$ Fe <sup>3+</sup> CT				30800 (325)?	+					
CN <sup>-</sup> $\rightarrow$ Fe <sup>3+</sup> CT			y	30800 (325)?	+					

<sup>a</sup>Assignments marked with a question mark are tentative, since polarization data is not currently available; see Fig. 8 for the axis systems used in the assignments of the high-spin (pH 7.5, pH 10, N<sub>3</sub><sup>-</sup>) and low-spin (CN<sup>-</sup>) forms of oxidized SOR

**Table 2.2** NIR excited state transition energies and ligand field splittings for high-spin Fe<sup>2+</sup> center reduced recombinant *P. furiosus* SOR

Sample	Method <sup>a</sup>	Observed d-d transitions, <sup>b</sup> cm <sup>-1</sup>		10Dq, cm <sup>-1</sup>	Δ <sup>5</sup> E <sub>g</sub> , cm <sup>-1</sup>
As prepared	Abs	12100			
	CD	12200 (+)			
	MCD	12400 (-)	<5000 (+)	<8700	>7400
Azide-bound <sup>c</sup>	MCD	12100 (-)	7300 (+)	9700	4800
Cyanide-bound <sup>c</sup>	Abs	11500			
	CD	11600 (-)	9900 (+)	10800	1700
	MCD	11900 (-)	10100 (+)	11000	1800

<sup>a</sup>Absorption at room temperature, CD at room temperature and 1.6 K, MCD at 1.6 K

<sup>b</sup>Signs of CD and MCD bands are given in parenthesis

<sup>c</sup>The azide- and cyanide-bound forms are both mixtures of exogenous ligand bound forms and as prepared square pyramidal forms. The parameters shown are only for the ligand bound forms.

**Table 2.3** EXAFS curve-fitting results for air-oxidized and dithionite-reduced *P. furiosus* SOR.<sup>a</sup>*P. furiosus* SOR.<sup>a</sup>

		Fe-N/O			Fe-S				
		<i>N</i>	<i>R</i> (Å)	$\sigma^2$ (Å <sup>2</sup> )	<i>N</i>	<i>R</i> (Å)	$\sigma^2$ (Å <sup>2</sup> )	$\Delta E_0$	<i>F</i> <sup>b</sup>
Oxidized	Fe-N/O	5	2.124(3)	0.0094(4)	1	2.361(5)	0.0065(5)	-9.8(1)	0.334
Oxidized	Fe-N	2	2.072(9) <sup>c</sup>	0.0067(3) <sup>d</sup>	1	2.361(5)	0.0066(8)	-9.8(1)	0.335
	Fe-N	2	2.172 <sup>c</sup>	0.0070 <sup>d</sup>					
	Fe-O	1	2.150(11)	0.0069 <sup>d</sup>					
Reduced	Fe-N/O	4	2.146(2)	0.0045(2)	1	2.368(2)	0.0026(2)	-9.8(1)	0.239

<sup>a</sup>*N* are the coordination numbers, *R* the interatomic distances in Å and  $\sigma^2$  the mean-square deviation in *R* (the Debye-Waller factor) in Å<sup>2</sup>. The values in parenthesis are the estimated standard deviations (precisions) obtained from the diagonal elements of the covariance matrix. We note that the accuracies will always be larger than and related to the precisions; *R* is expected to be better than  $\pm 0.02$  Å.

<sup>b</sup>The fit-error *F* is defined as  $\sum [k^6(\chi_{\text{exptl}} - \chi_{\text{calcd}})^2 / \sum k^6 \chi_{\text{exptl}}^2]^{1/2}$ .

<sup>c</sup>Bond-lengths were constrained to differ by at least 0.1 Å and at most 0.15 Å.

<sup>d</sup>The Fe-N and Fe-O  $\sigma^2$  values were constrained to be proportional to the individual bond-lengths.

Figure 2.1 X-band EPR spectra of recombinant *P. furiosus* SOR. (A) 50 mM HEPES buffer, pH 7.5. (B) 100 mM CHES buffer, pH 10.0. (C) Sample A after oxidation with a 5-fold excess of ferricyanide and removal of ferricyanide by ultrafiltration. (D) Sample A after addition of a 45-fold stoichiometric excess of sodium azide at room temperature. (E) 50 mM Taps buffer, pH 8.5, after addition of a 30-fold stoichiometric excess of sodium cyanide at room temperature. All samples were approximately 0.5 mM in SOR and all spectra were recorded at 9.60 GHz, using a modulation amplitude of 0.63 mT. The microwave power and temperature were 40 mW and 4.2 K for A, B, C, and D and 1 mW and 15 K for E. Selected g-values are shown on each spectrum.

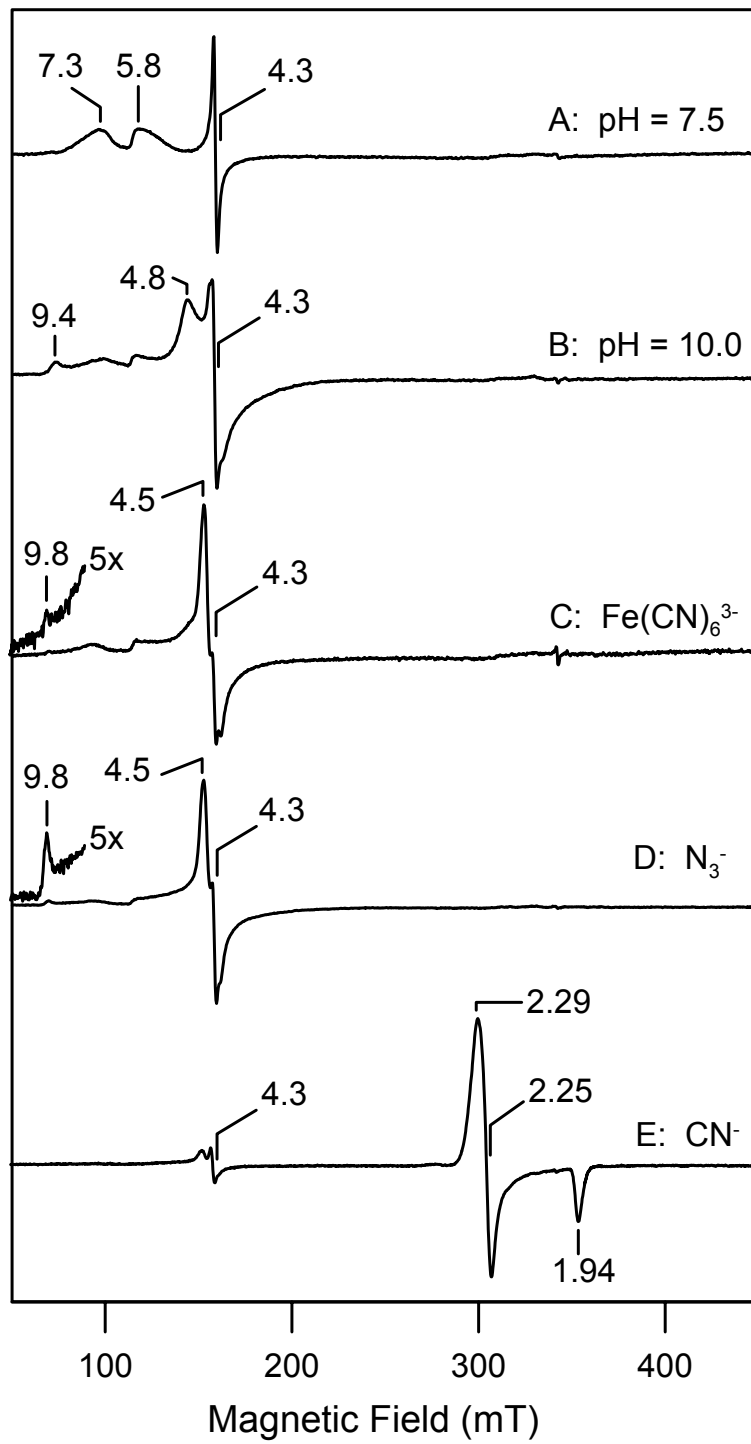


Figure 2.2 Temperature dependence of the EPR spectrum of recombinant *P. furiosus* SOR in 50 mM HEPES buffer, pH 7.5. The sample and conditions of measurement are as described in Figure 1 except for the temperatures, which are indicated on the spectra. Selected  $g$ -values are shown on the 4.0 K spectrum. The inset shows a plot of  $\ln(I_{g=5.8}/I_{g=7.3})$  versus  $1/T$  which yields a straight line of slope  $1.62 \pm 0.10$  K.

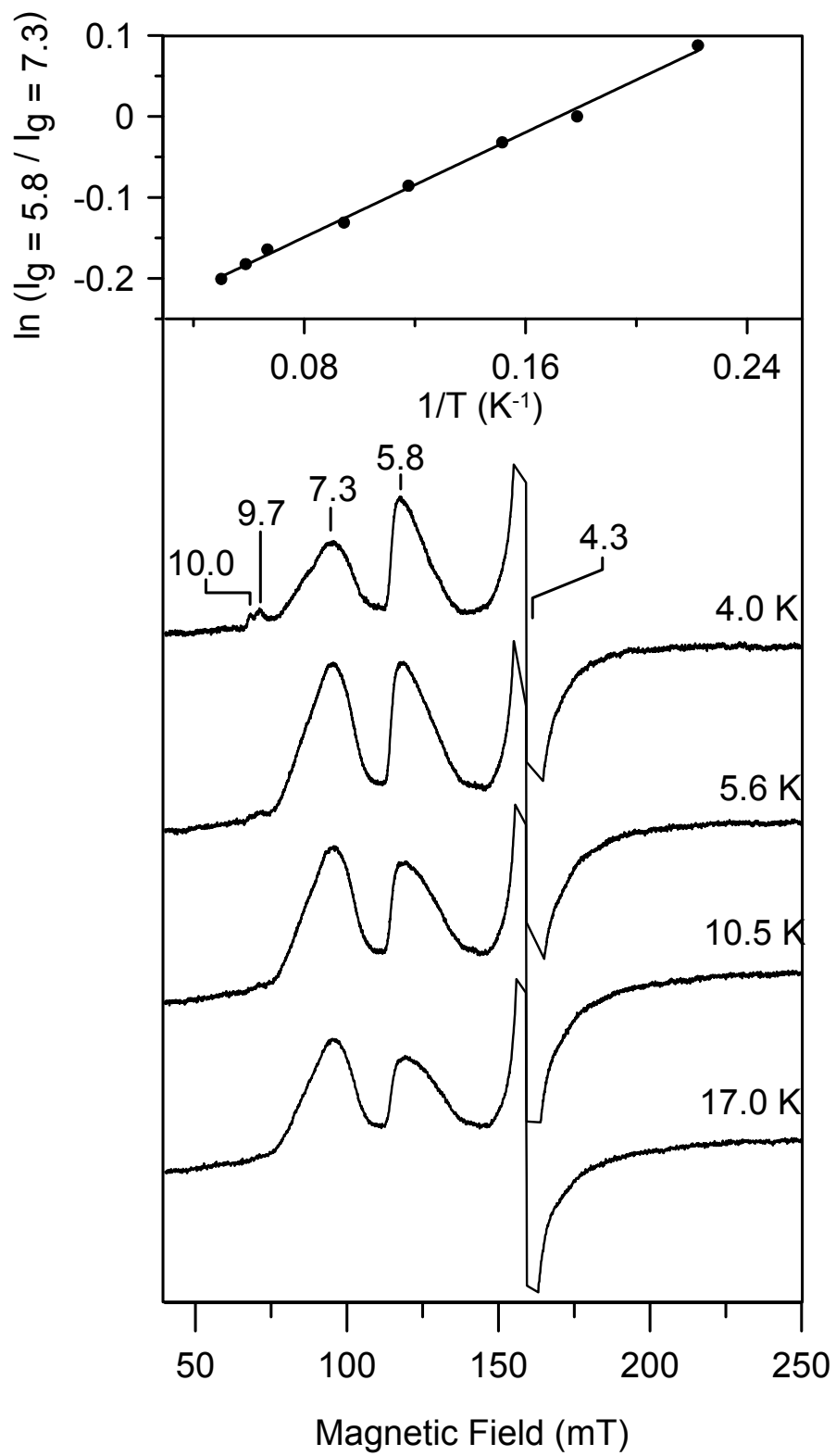


Figure 2.3 Dye-mediated EPR redox titration of recombinant *P. furiosus* SOR in 50 mM HEPES buffer, pH 7.5. Intensities at  $g = 7.3$  ( $\square$ ) and  $g = 4.5$  ( $\circ$ ) are plotted as a function of redox potential (*versus* NHE). Samples for EPR were taken at selected poised potentials during ascorbate reduction of the ferricyanide-oxidized enzyme. The solid line is a one-electron Nernst plot with  $E_m = +250$  mV.

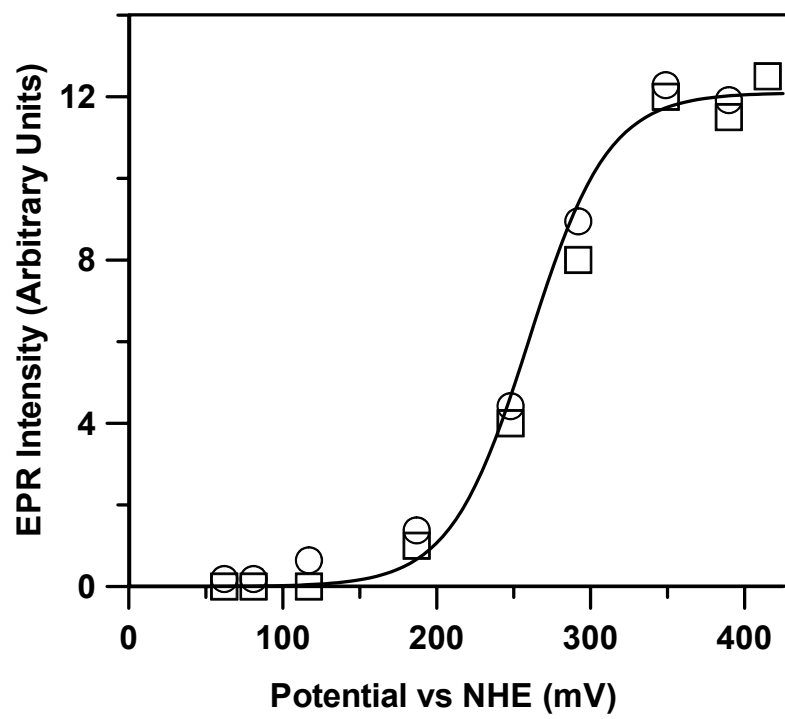


Figure 2.4 Temperature dependence of the EPR spectrum of recombinant *P. furiosus* SOR exchanged into 50 mM CHES buffer, pH 10.0. The sample and conditions of measurement are as described in Figure 1 except for the temperatures, which are indicated on the spectra. Selected *g*-values are shown on the 4.0 K spectrum. The inset shows a plot of  $\ln(I_{g=4.8}/I_{g=9.4})$  versus  $1/T$  which yields a straight line of slope  $-4.8 \pm 0.4$  K.

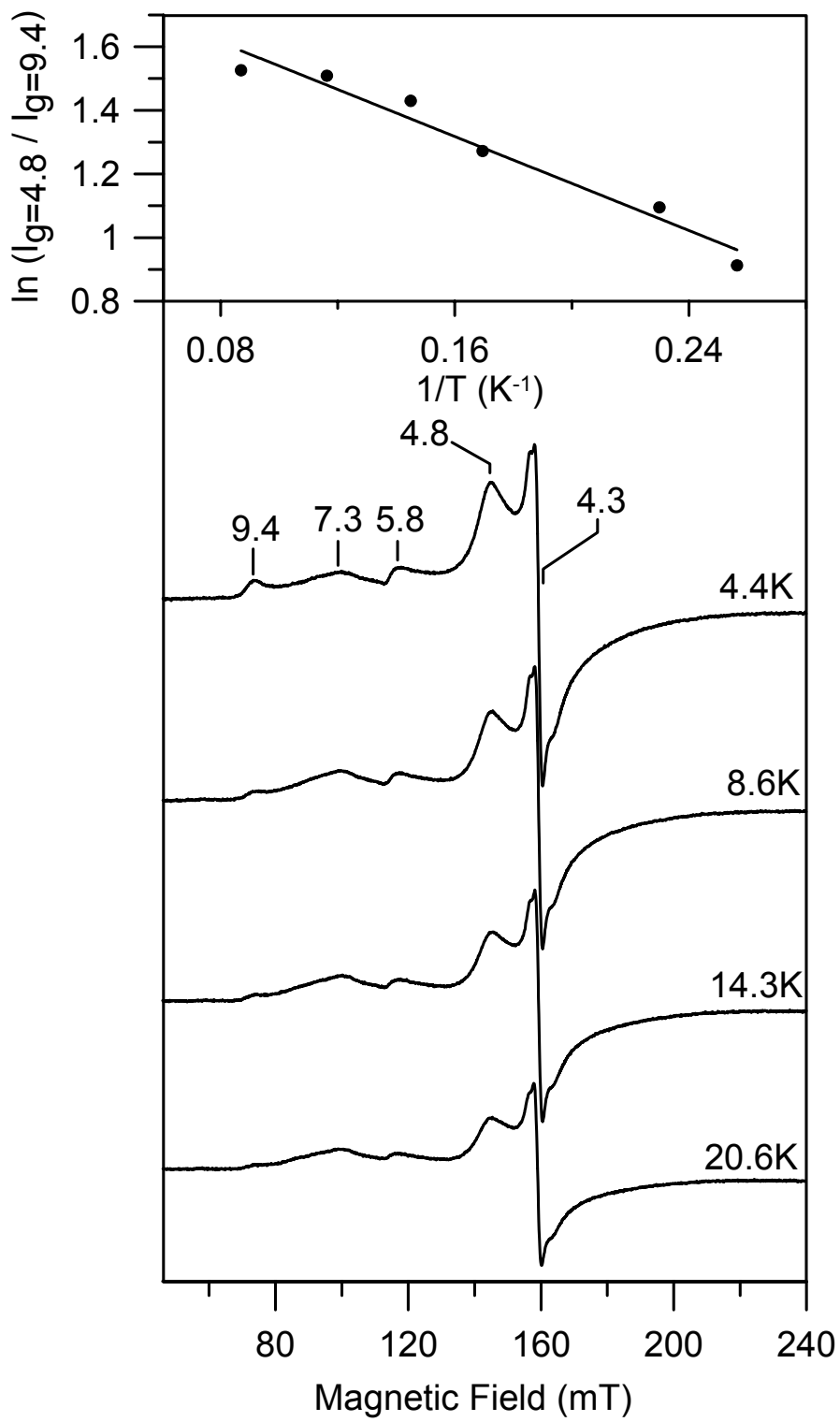


Figure 2.5 UV-visible absorption spectra of recombinant *P. furiosus* SOR. (A) 100 mM MES buffer, pH 6.0. (B) 50 mM HEPES buffer, pH 7.5. (C) 100 mM CHES buffer, pH 10.0. (D) Sample B after addition of a 45-fold stoichiometric excess of sodium azide. (E) 50 mM TAPS buffer, pH 8.5, after addition of a 30-fold stoichiometric excess of sodium cyanide. All samples were ~ 1 mM in SOR and spectra were recorded in 1 mm cuvettes,

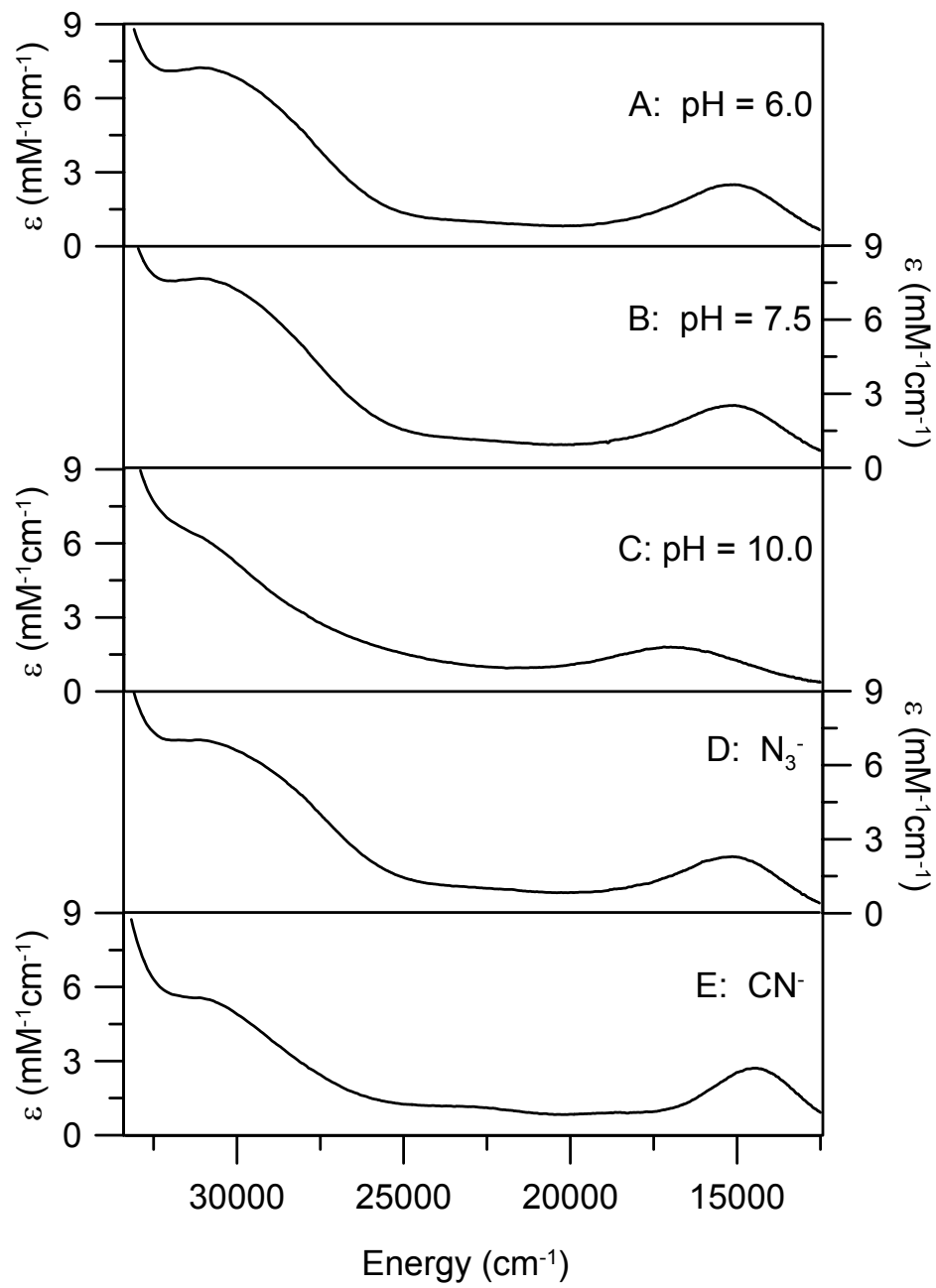


Figure 2.6 UV-visible VTMCD spectra of recombinant *P. furiosus* SOR. Samples are the same as those used in Figure 5 except for the addition of 55% (v/v) glycerol. Spectra were recorded with a magnetic field of 6 T at 1.68, 4.22, 10.0, 25.0 and 50.0 K. MCD intensity for all bands increases with decreasing temperature.

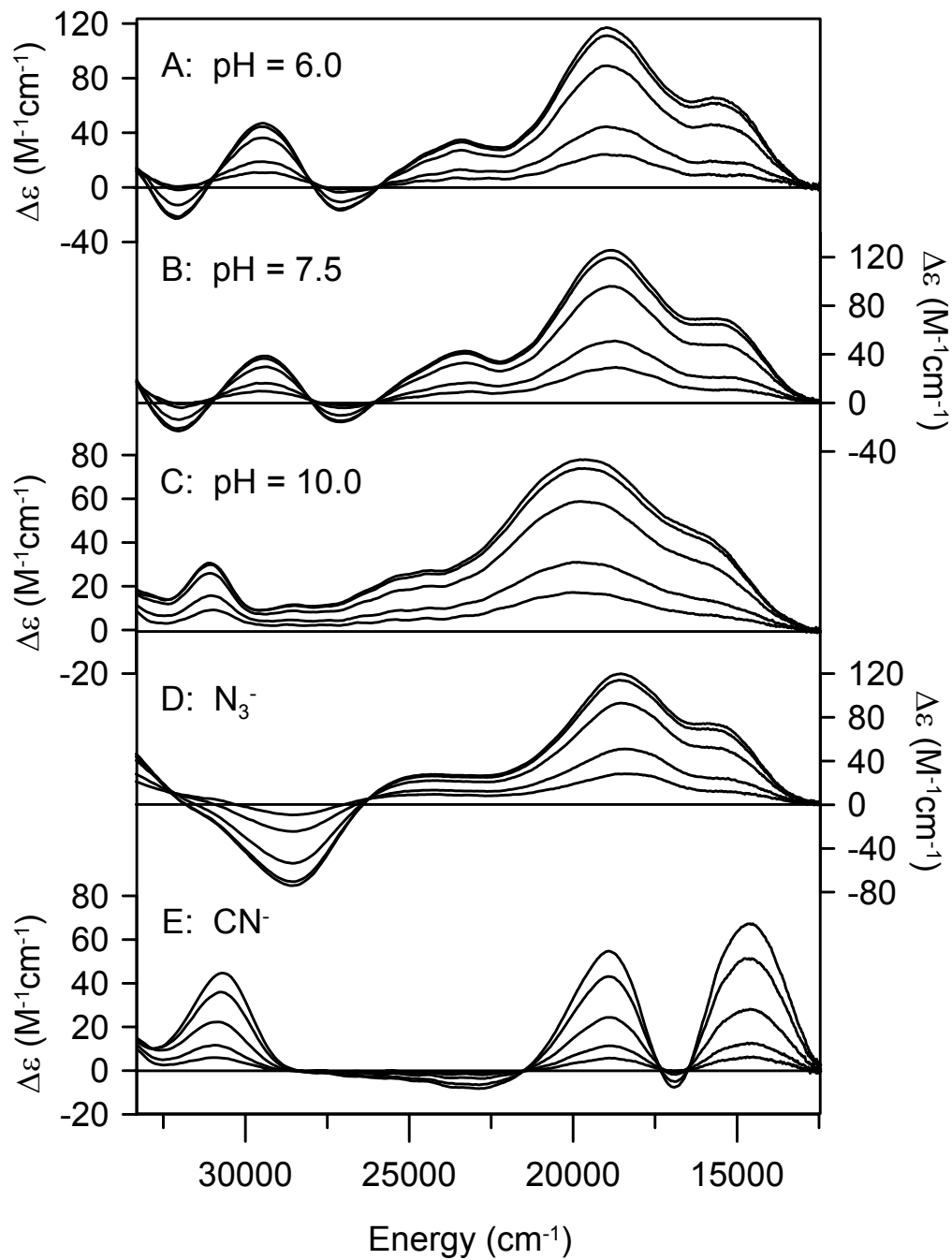


Figure 2.7 VHVT MCD saturation magnetization data for recombinant *P. furiosus* SOR at pH 7.5. The sample corresponds to Figure 6(B) and the data were collected at fixed temperatures of 1.68, 4.22 and 10.0 K for magnetic fields in the range 0-6 T. The solid lines are best fits using the EPR-determined zero-field splitting parameters with  $M_{xy}$ ,  $M_{xz}$ , and  $M_{yz}$  as variable parameters. Uniaxial polarizations are estimated to be 98%  $z$ , 1%  $x$  and 1%  $y$  at 23430 and 18980  $\text{cm}^{-1}$  and 98%  $y$  and 2%  $x$  at 15151  $\text{cm}^{-1}$ .<sup>32</sup>

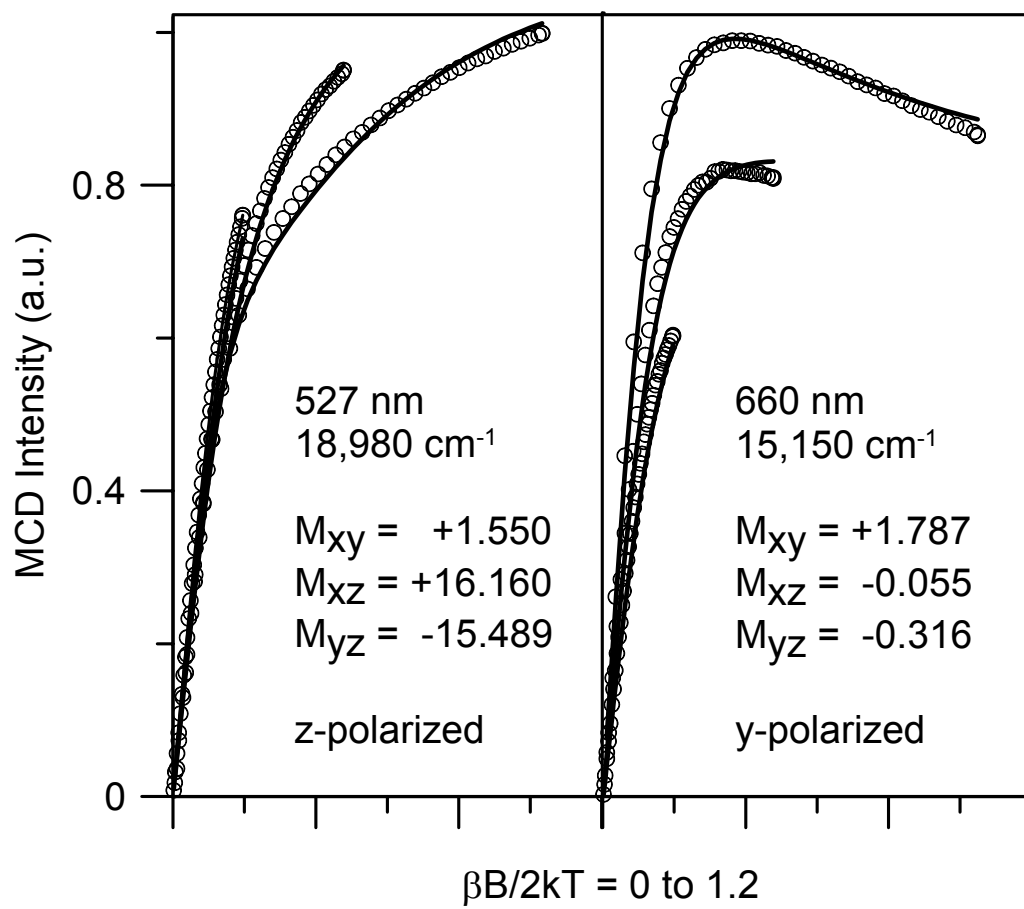


Figure 2.8 Schematic orbital energy level diagram and depiction of the (Cys)S(p)  $\rightarrow$  Fe<sup>3+</sup>(d) charge transfer transitions associated with the as-prepared (high-spin) and CN<sup>-</sup>-bound (low-spin) octahedral Fe<sup>3+</sup> centers in SOR. Uniaxial polarizations corresponding to the axes systems shown are indicated to the right of each transition. The relative orbital energies are based on the electronic assignments and the EPR properties, as discussed in the text.

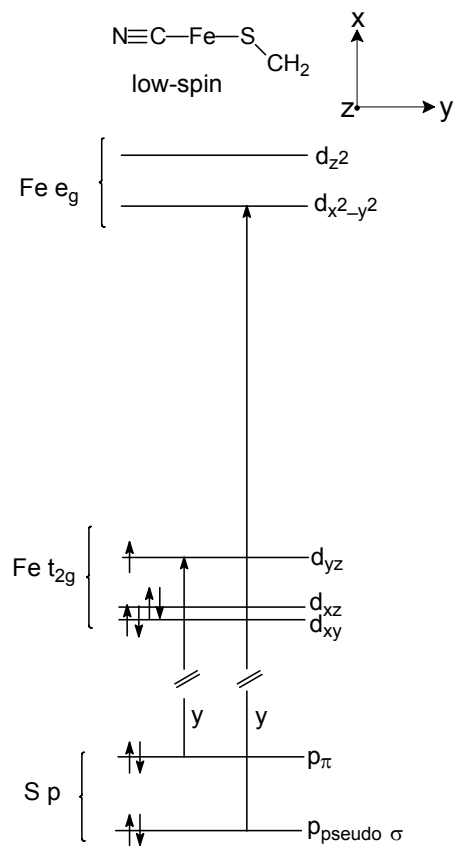
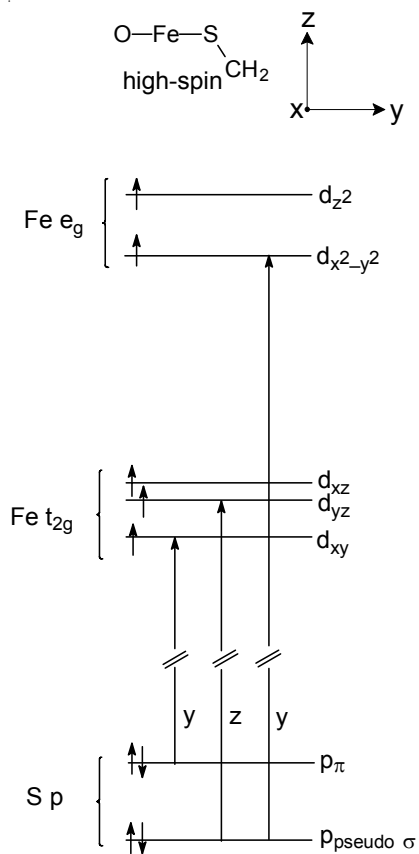


Figure 2.9 Comparison of the UV-visible absorption, CD and VTMCD spectra of cyanide-bound recombinant *P. furiosus* SOR. The sample is the same as that described in Figure 5(E), except for the addition of 55% (v/v) glycerol for the samples used for CD and VTMCD. The absorption spectrum was recorded at room temperature. The MCD spectrum was recorded at 1.68 K and 6 T and the CD spectrum was recorded at 4.22 K. None of the observed CD bands result from strain in the frozen glass, since an equivalent, albeit less well-resolved, spectrum was observed at room temperature.

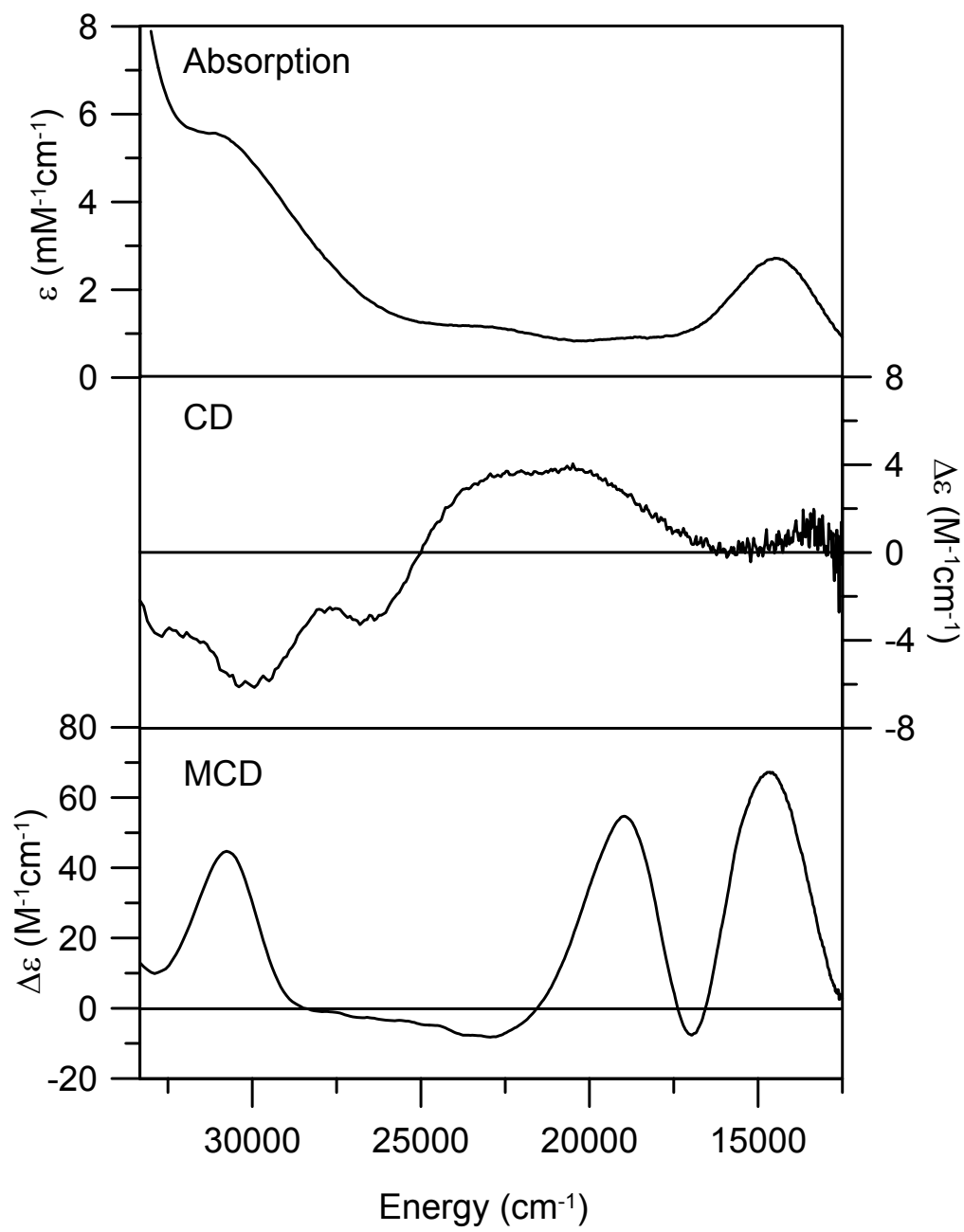


Figure 2.10 UV absorption and VTMCD spectra of ascorbate-reduced recombinant *P. furiosus* SOR. The sample was 0.9 mM in SOR and was in 100 mM D<sub>2</sub>O MOPS buffer, pD 7.5, with 55% (v/v) *d*<sub>3</sub>-glycerol. *Upper panel*: room-temperature absorption spectrum in a 1-mm pathlength cell. *Lower panel*: VTMCD spectra recorded in a 1-mm pathlength cell at 1.70, 4.22, 10.2, 24.3, and 52.0 K with an applied field of 6 T. All MCD bands increase in intensity with decreasing temperature.

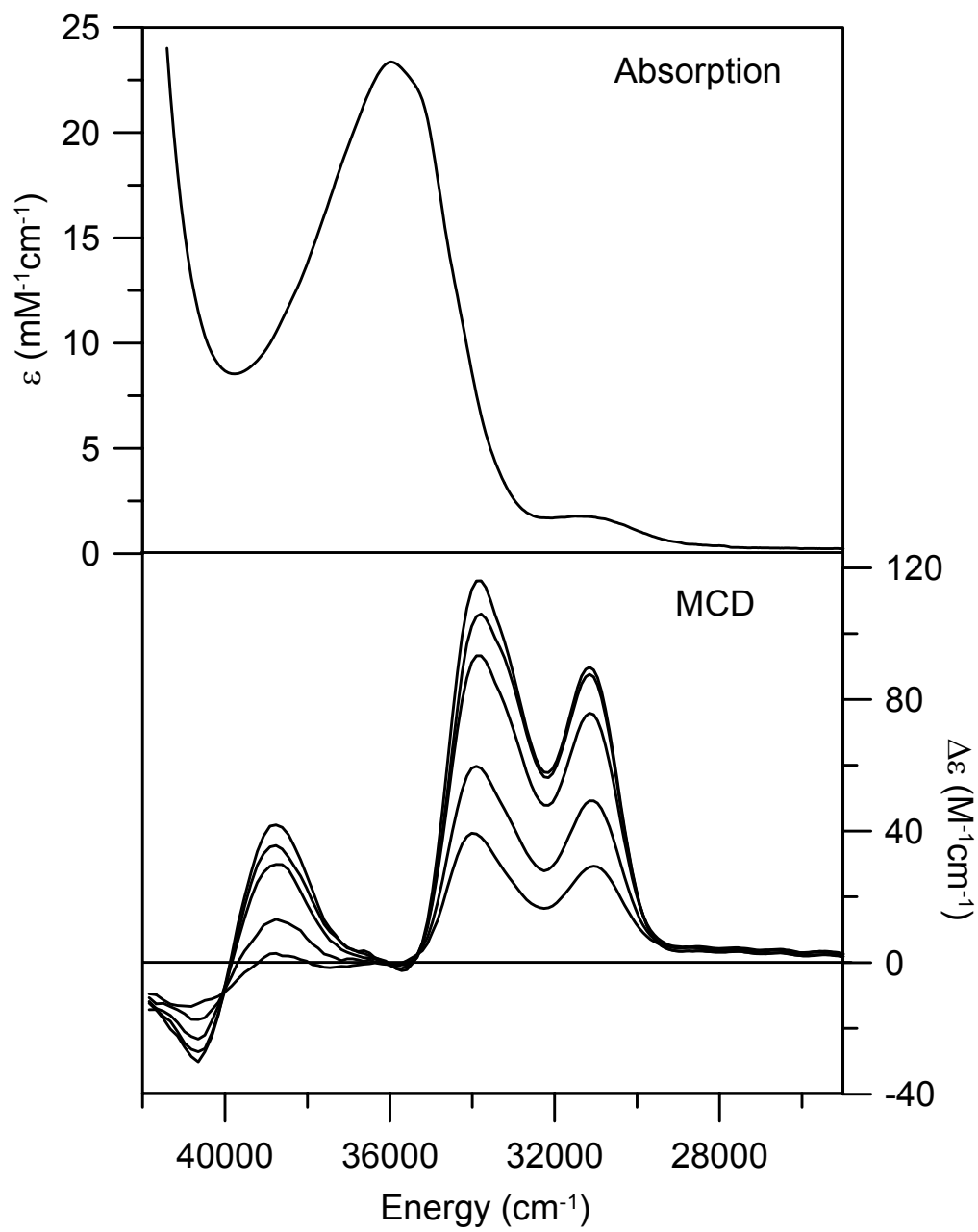


Figure 2.11 Near-IR absorption, CD and VTMCD spectra of ascorbate-reduced recombinant *P. furiosus* SOR. The sample was 4.5 mM in SOR and was in 100 mM D<sub>2</sub>O MOPS buffer, pD 7.5, with 55% (v/v) *d*<sub>3</sub>-glycerol. *Upper panel*: room-temperature absorption spectrum. *Middle panel*: room-temperature CD spectrum. *Lower panel*: VTMCD spectra. All MCD bands increase in intensity with decreasing temperature.

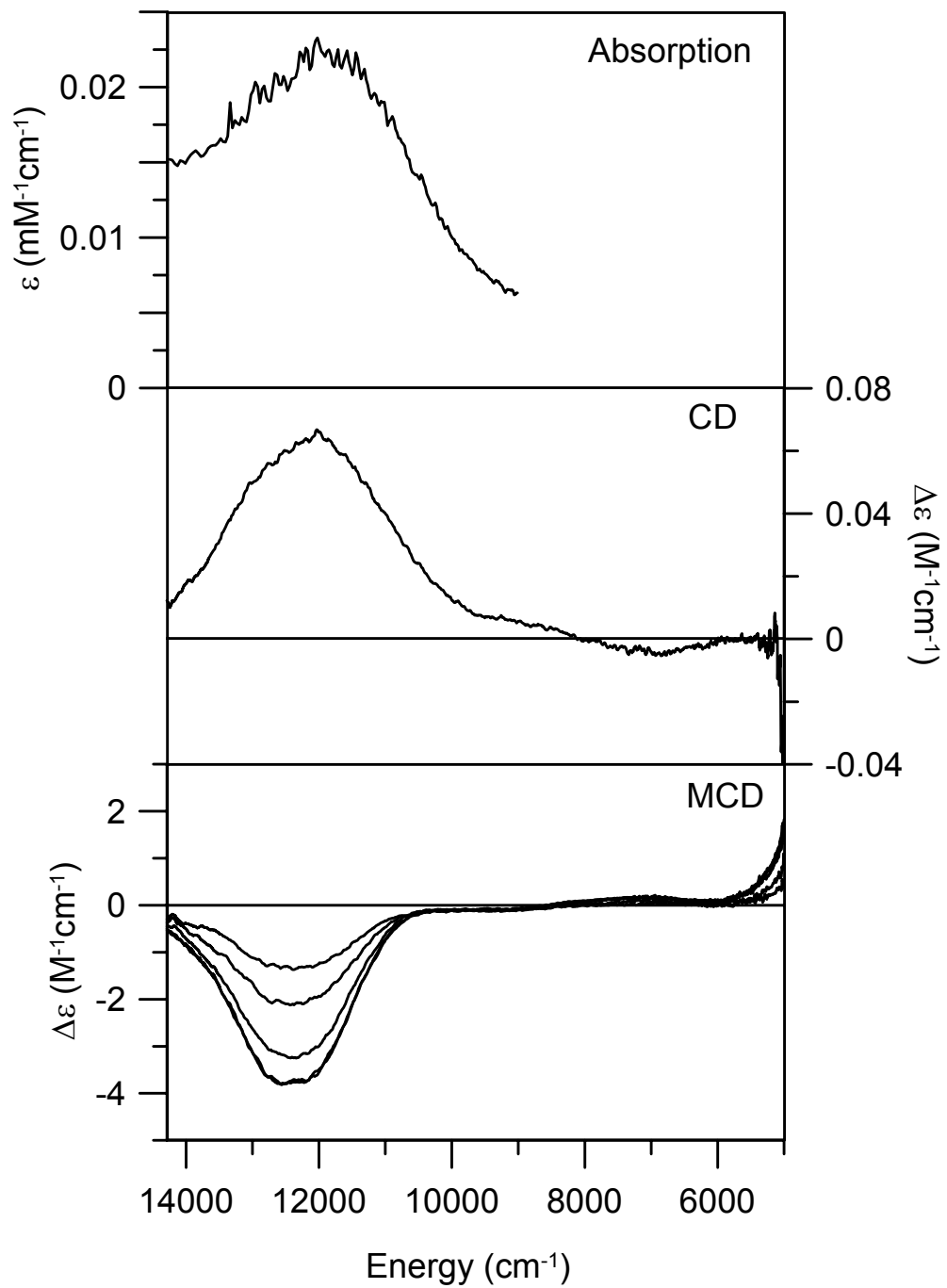


Figure 2.12 Near-IR VTMCD spectra of ascorbate-reduced recombinant *P. furiosus* SOR in the presence of a 45-fold stoichiometric excess of azide. The sample is as described in Figure 11 except for the addition of a 45-fold stoichiometric excess of sodium azide. *Upper panel*: VTMCD spectra recorded in a 1-mm pathlength cell at 1.70 , 4.22, 10.2, 24.6, and 51.0 K with an applied field of 6 T. All MCD bands increase in intensity with decreasing temperature. *Lower panel*: MCD difference spectrum corresponding to the azide-treated ascorbate-reduced spectrum at 1.70 K minus 85% of the ascorbate-reduced spectrum recorded under the same conditions.

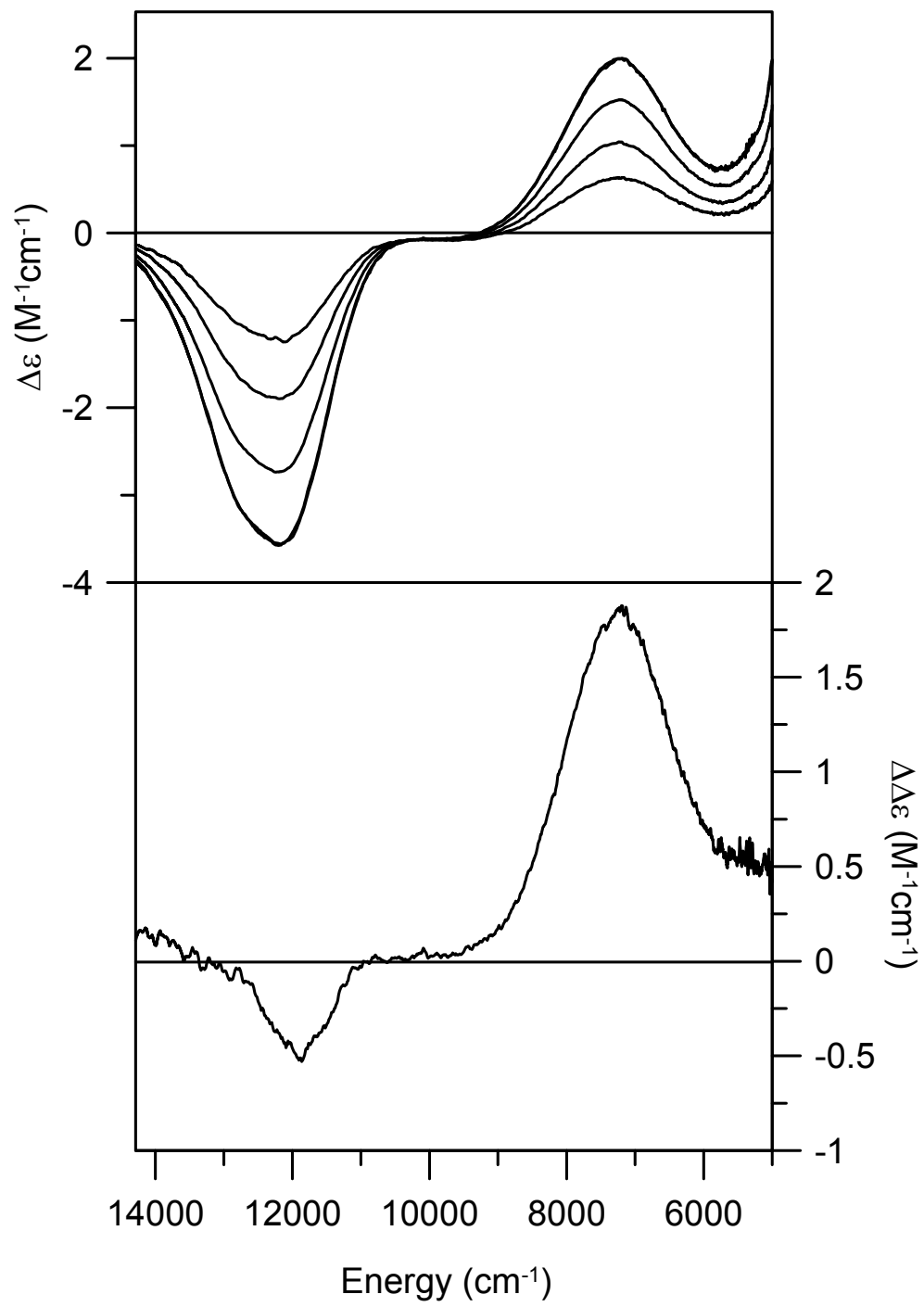


Figure 2.13 Near-IR CD and VTMCD spectra of ascorbate-reduced recombinant *P. furiosus* SOR in the presence of a 30-fold stoichiometric excess of cyanide. The sample is as described in Figure 11 except for the addition of a 30-fold stoichiometric excess of potassium cyanide. *Upper panel*: CD spectrum recorded at 4.22 K. *Middle panel*: VTMCD spectra recorded in a 1-mm pathlength cell at 1.70, 4.22, 10.0, 25.2, and 52.0 K with an applied field of 6 T. All MCD bands increase in intensity with decreasing temperature. *Lower panel*: MCD difference spectrum corresponding to the cyanide-treated ascorbate-reduced spectrum at 1.70 K minus 20% of the ascorbate-reduced spectrum recorded under the same conditions.

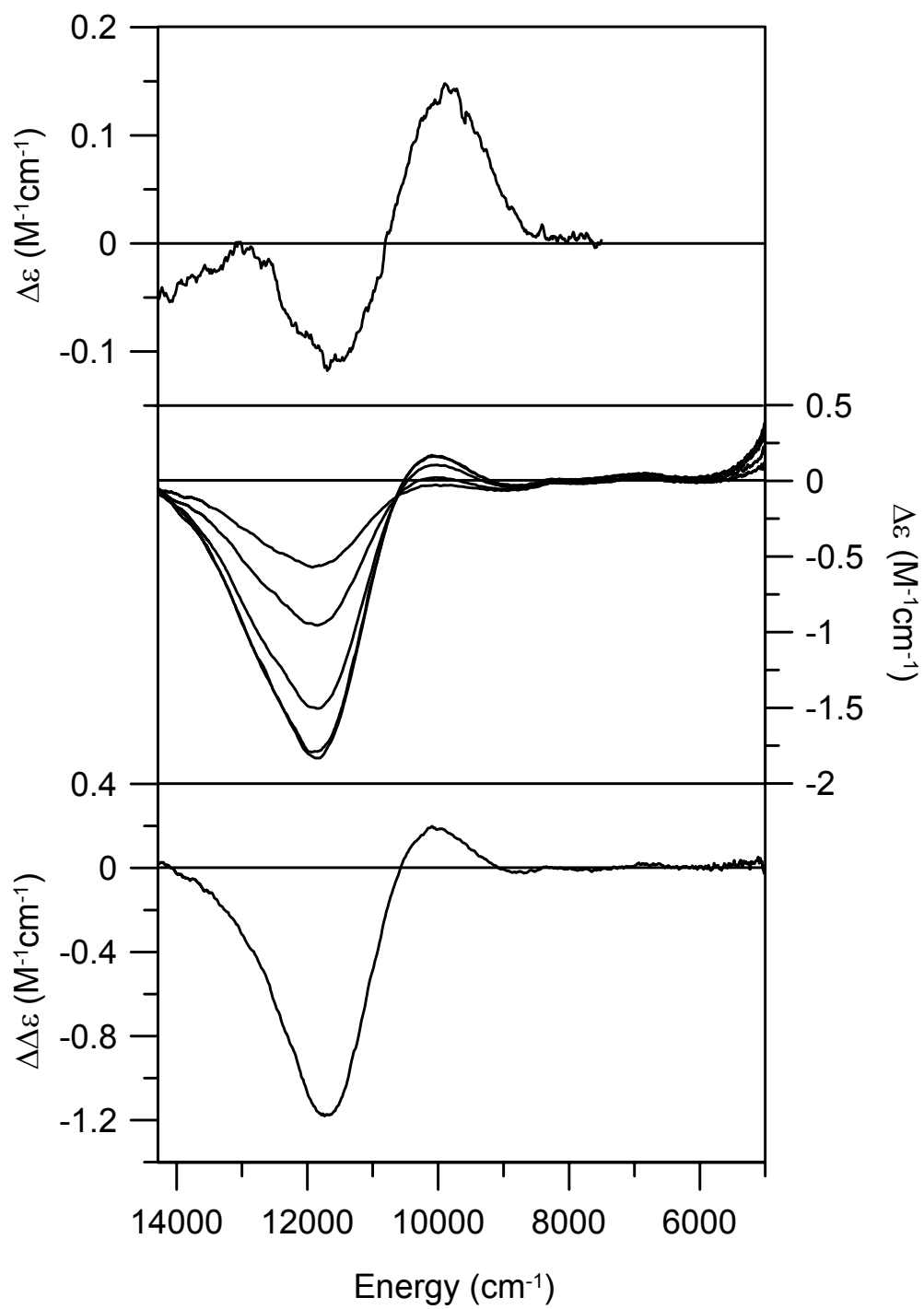


Figure 2.14 Schematic orbital energy level diagram for the square-pyramidal  $\text{Fe}^{2+}$  center in reduced SOR and depiction of the Fe d-d and proposed  $(\text{Cys})\text{S}^- \rightarrow \text{Fe}^{2+}$  CT transitions. The relative orbital energies are based on the electronic assignments and VTVH MCD saturation data discussed in the text.

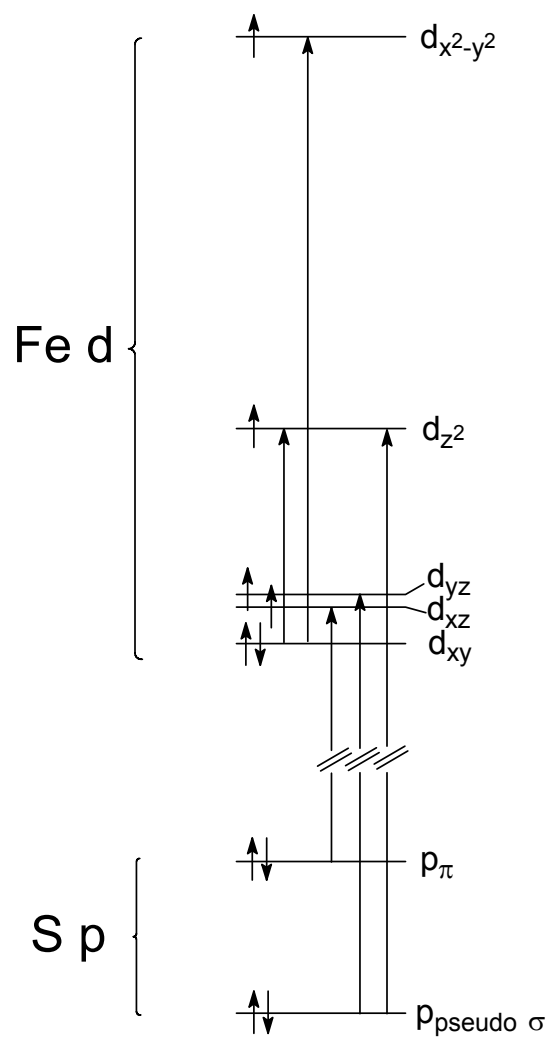
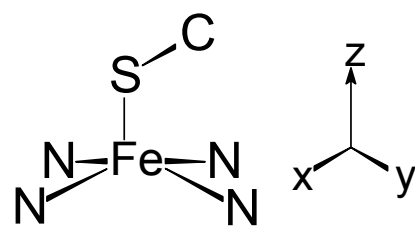


Figure 2.15 VHVT MCD saturation magnetization data for ascorbate-reduced recombinant *P. furiosus* SOR collected at  $12400\text{ cm}^{-1}$ . Data collected at 1.70, 4.22, 10.4, 15.6, 25.3, and 34.6 K with magnetic fields between 0 and 6 T. Solid lines are theoretical data computed according to ref. 24 for an  $xy$ -polarized transition from a three-level  $+D$  model with a zero-field energy level spacing of 0, 7 and  $15\text{ cm}^{-1}$  between the lowest three components of the  $S = 2$  ground state.

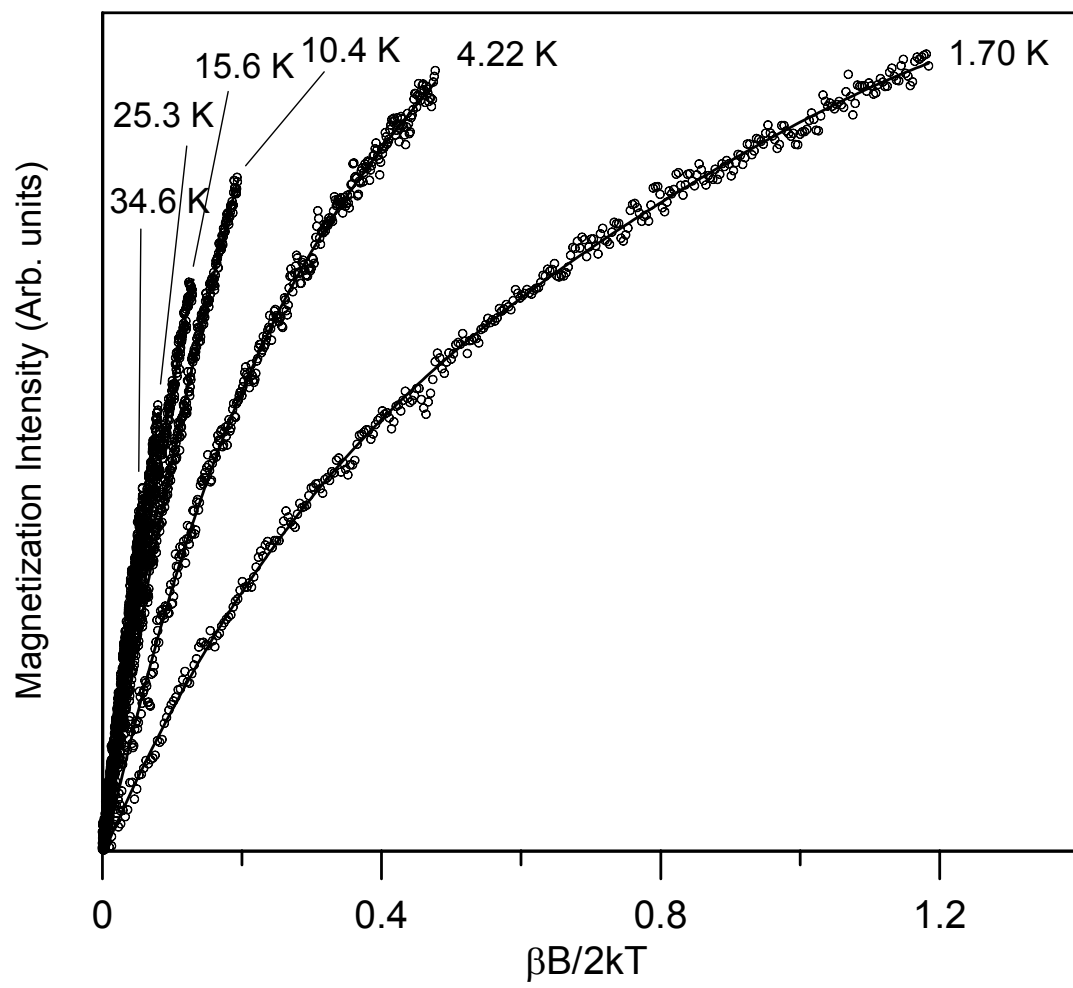


Figure 2.16 *Upper panel:* Iron K near-edge spectra of recombinant *P. furiosus* SOR in air-oxidized, dithionite-reduced and 4.5-hour photo-reduced forms. The samples of SOR (4mM) were in 50 mM Tris/HCl buffer, pH 7.8 with 55% (v/v) glycerol, and were reduced with a 5-fold excess of sodium dithionite. *Lower panel:* Kinetics of X-ray induced photo-reduction estimated by curve-fitting of individual scans to linear combination of oxidized (5-min beam exposure) and dithionite-reduced spectra. The ordinate scale is logarithmic. The beam current varied from 80 to 82 mA during the experiment.

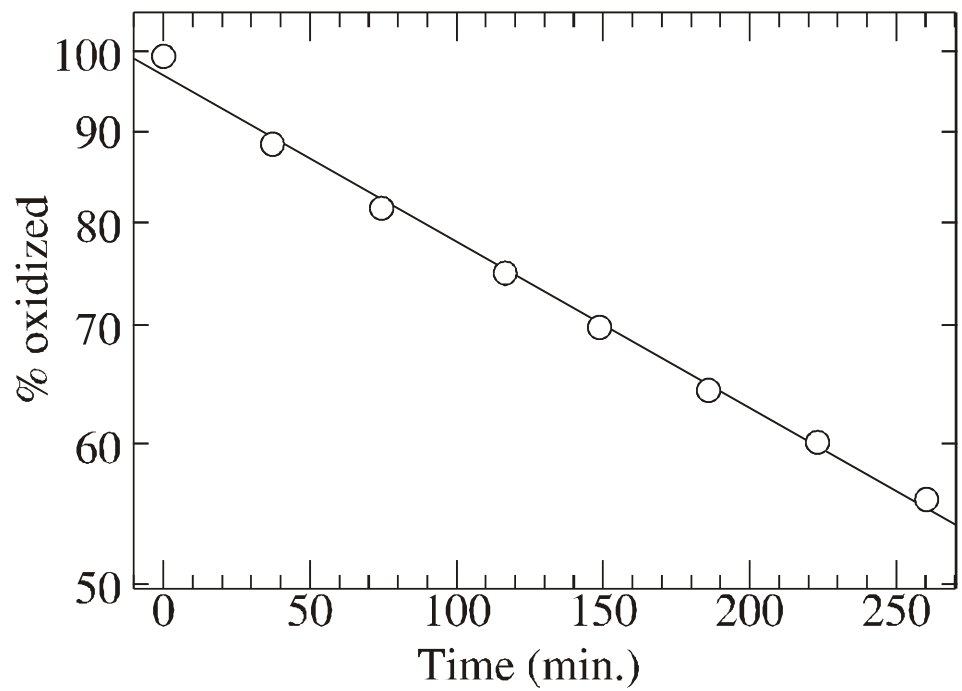
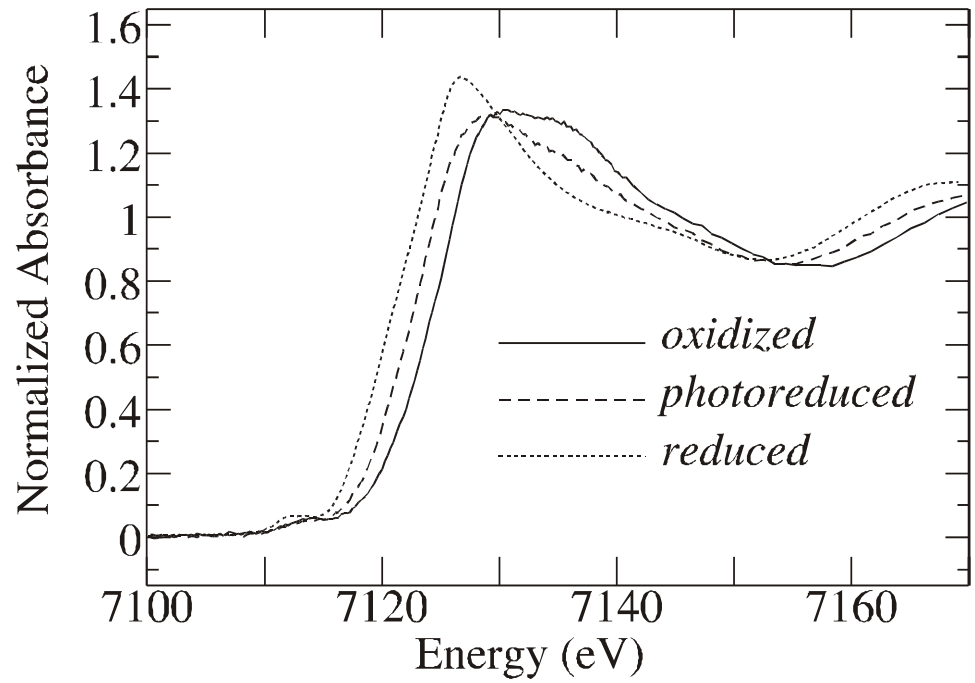


Figure 2.17 EXAFS oscillations (upper panel) and EXAFS Fourier transforms (lower panel) of air-oxidized and dithionite-reduced *P. furiosus* SOR. Samples are described in Figure 16. The Fourier transforms are phase-corrected for Fe-N backscattering. The solid lines show experimental data while the broken lines show the results of curve-fitting analysis (Table 2.3).

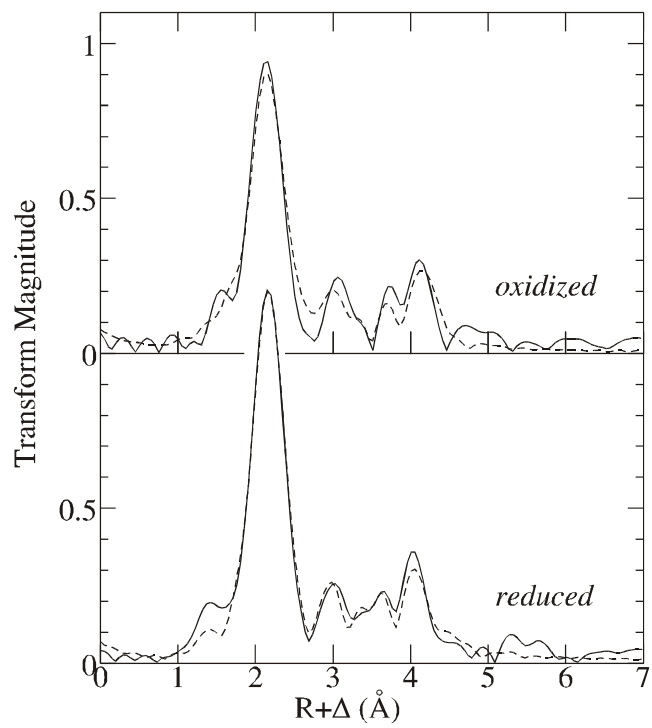
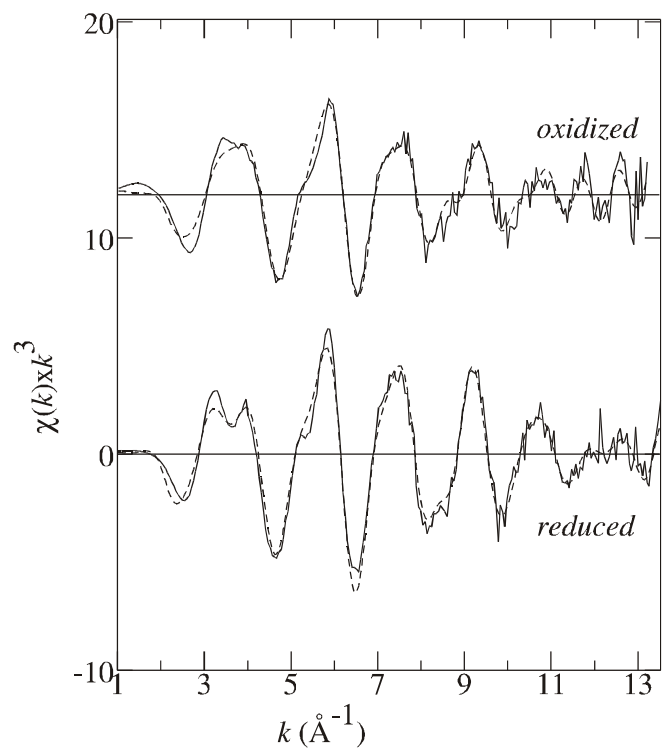


Figure S2.1 Redox titration of *P. furiosus* SOR at pH 7.0 as monitored by UV-visible absorption at 660 nm. Redox titrations were performed using a platinum wire working electrode and saturated Ag/AgCl<sub>2</sub> reference electrode in a sealed, stirred anaerobic cell at 23 °C in 100 mM MOPS pH 7.0 containing 100 μM SOR and the following mediators: 1,2-naphthoquinone, N,N,N',N'-tetramethyl-*p*-phenylene diamine, β-(1,2)naphthoquinone-4-sulfonate, phenazine methosulfate, phenazine ethosulfate, duroquinone, 2-hydroxy 1,4-naphthoquinone, anthroquinone 2,6-disulfonic acid, N,N-dimethyl-*p*-phenylene diamine all at 1 μM and benzyl viologen (0.05 μM). A second titration was performed with mediators at 2x the above concentrations and similar results were obtained (data not shown). The potential of the solution was poised with small additions (1-5 μl) of either 100 mM sodium dithionite or 100 mM potassium ferricyanide in 500 mM MOPS pH 7.0. Data were fit to the Nernst equation for a one-electron reaction. The average fits of two titrations give a midpoint potential of  $238 \pm 10$  mV versus NHE.

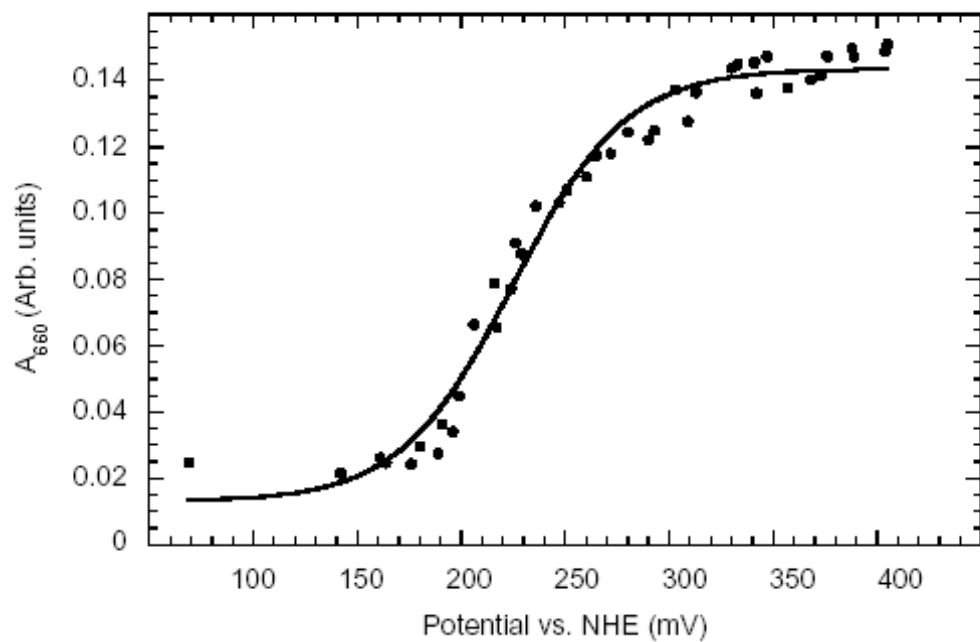
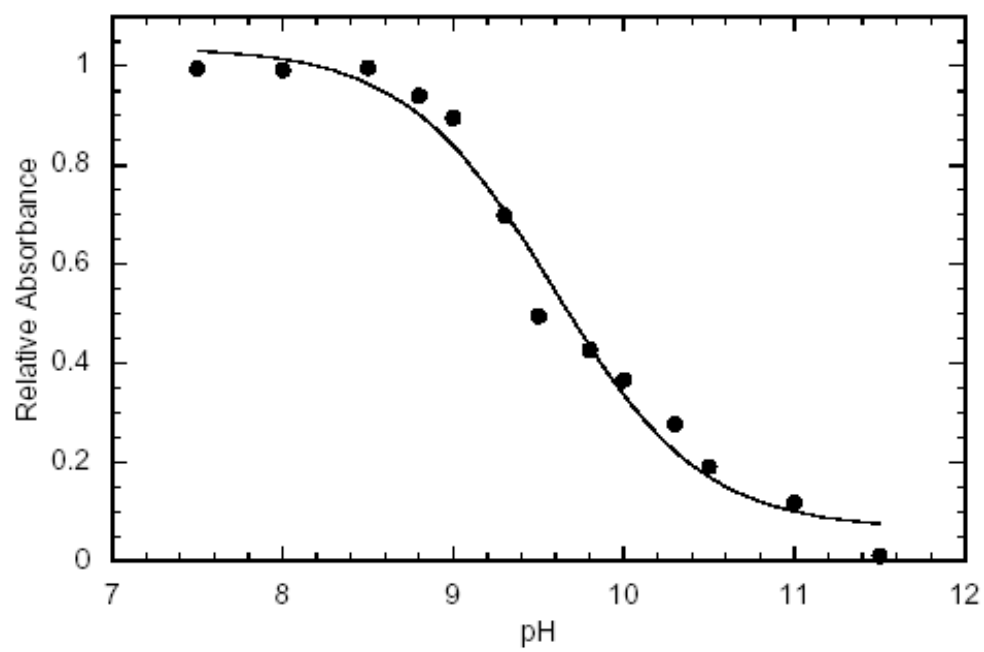


Figure S2.2 Effect of pH on the visible absorption maximum of *P. furiosus* SOR. The broad maximum shifts from 660 nm below pH 8 to 566 nm at pH 11.5. The ratio of absorbance at 660 and 566 nm (normalized to 1 at pH 7.5) is plotted against pH and the solid line is the fit for one ionizable group with a  $pK_a = 9.6$ .



**CHAPTER 3**

**RESONANCE RAMAN CHARACTERIZATION OF THE  
MONONUCLEAR IRON ACTIVE-SITE VIBRATIONS AND  
PUTATIVE ELECTRON TRANSPORT PATHWAYS IN  
*PYROCOCCUS FURIOSUS* SUPEROXIDE REDUCTASE1**

---

<sup>1</sup> Clay, Michael D.,<sup>‡</sup> Francis E. Jenney, Jr.,<sup>§</sup> HakJoon Noh,<sup>§</sup> Peter L. Hagedoorn,<sup>‡,||</sup> Michael W. W. Adams,<sup>§</sup> Michael K. Johnson<sup>‡,\*</sup> (2002) *Biochemistry* **41**, 9833-9841. Departments of <sup>‡</sup>Chemistry and <sup>§</sup>Biochemistry & Molecular Biology, and <sup>‡,§</sup>Center for Metalloenzyme Studies, University of Georgia, Athens GA 30602, USA. <sup>||</sup>Department of Biotechnology, Delft University of Technology, The Netherlands

### **Textual Footnotes**

<sup>1</sup>Abbreviations: SOR, superoxide reductase; VHVT MCD, variable-field, variable-temperature magnetic circular dichroism; charge transfer, CT

<sup>2</sup>Yeh, A. P., Hu, Y., Jenney, F. E., Adams, M. W. W., and Rees, D. C., unpublished observations.

<sup>3</sup>Clay, M. D., Cospers, C. A., Jenney, F. E., Adams, M. W. W., and Johnson, M. K., manuscript in preparation.

## Abstract

The resonance Raman spectrum of oxidized wild-type *P. furiosus* SOR at pH 7.5 and 10.5 has been investigated using excitation wavelengths between 406 and 676 nm and vibrational modes have been assigned based on isotope shifts resulting from global replacements of  $^{32}\text{S}$  with  $^{34}\text{S}$ ,  $^{14}\text{N}$  with  $^{15}\text{N}$ ,  $^{56}\text{Fe}$  with  $^{54}\text{Fe}$ , and exchange into a  $\text{H}_2^{18}\text{O}$  buffer. The results are interpreted in terms of the crystallographically defined active-site structure involving a six-coordinate mononuclear Fe center with four equatorial histidine ligands and axial cysteine and monodentate glutamate ligands (Yeh, A. P., Hu, Y., Jenney, F. E., Adams, M. W. W., and Rees, D. C. (2000) *Biochemistry* 39, 2499-2508). Excitation into the intense (Cys)S( $p_\pi$ )-to-Fe( $d_\pi$ ) CT transition centered at 660 nm results in strong enhancement of modes at  $298\text{ cm}^{-1}$  and  $323\text{ cm}^{-1}$  that are assigned to extensively mixed cysteine S- $\text{C}_\beta$ - $\text{C}_\alpha$  bending and Fe-S(Cys) stretching modes, respectively. All other higher energy vibrational modes are readily assigned to overtone or combination bands or to fundamentals corresponding to internal modes of the ligated cysteine. Weak enhancement of Fe-N(His) stretching modes is observed in the  $200\text{-}250\text{ cm}^{-1}$  region. The enhancement of internal cysteine modes and Fe-N(His) stretching modes are a consequence of a near-planar Fe-S- $\text{C}_\beta$ - $\text{C}_\alpha$ -N unit for the coordinated cysteine and significant (His)N( $p_\pi$ )-Fe( $d_{xy}$ )-(Cys)S( $p_\pi$ ) orbital overlap, respectively, and have close parallels to type 1 copper proteins. By analogy with type 1 copper proteins, putative superexchange electron-transfer pathways to the mononuclear Fe active site are identified involving either the tyrosine and cysteine residues or the solvent-exposed  $\delta\text{N}$  histidine residue in a Y-C-X-X-H arrangement. Studies of wild-type at pH 10.5 and the E14A variant indicate that the resonance Raman spectrum is remarkably insensitive to changes

in the ligand *trans* to cysteine and hence are inconclusive concerning the origin of the alkaline transition and the nature of sixth Fe ligand in the E14A variant.

## Introduction

Evidence has recently accumulated for a novel oxidative stress pathway in anaerobes involving superoxide reduction rather than dismutation (1;2). The key enzyme in this pathway, superoxide reductase (SOR),<sup>1</sup> catalyzes the reduction of superoxide to hydrogen peroxide and appears to use rubredoxin as the immediate electron donor (1;3). Distinct forms of SOR containing 1Fe and 2Fe atoms per monomer have been characterized, and are commonly referred to by the trivial names neelaredoxin (4) and desulfoferrodoxin (5), respectively. Both contain a common mononuclear non-heme Fe site, but the 2Fe-SORs contain an additional desulforedoxin domain containing a rubredoxin-type Fe(SCys)<sub>4</sub> center. Crystallographic and spectroscopic studies of the 2Fe-SOR from *Desulfovibrio desulfuricans* (6;7) and the 1Fe-SOR from *Pyrococcus furiosus* (8;9) have revealed an SOR active-site comprising a mononuclear Fe with four equatorial histidyl ligands (one δN and three εN) and one axial cysteinyl ligand. A monodentate glutamate (E14) completes octahedral coordination in oxidized *P. furiosus* SOR, but is removed on reduction, creating a binding site *trans* to the cysteinate for substrate binding and activation (8;9).

The ground- and excited-state electronic properties of the ferric and ferrous sites in *P. furiosus* SOR have recently been extensively characterized using the combination of EPR, absorption, CD and variable-field, variable-temperature magnetic circular dichroism (VHVT MCD) spectroscopies (9). This has led to detailed assignments of ligand-field and ligand-to-metal charge transfer (CT) transitions and assessment of the important role of (Cys)S(p<sub>π</sub>)-Fe(d<sub>π</sub>) interactions for optimizing the active site for reductive binding of superoxide and dissociation of the peroxide product (9;10). In

addition, the results indicate the potential of resonance Raman, using excitation into S-to-Fe CT transitions, for monitoring Fe-S(Cys) vibrational modes and the changes in the active site during catalytic turnover. Although resonance Raman of the 2Fe-SOR from *D. desulfuricans* provided the original evidence for cysteinate coordination of the oxidized SOR active site (6), detailed vibrational assignments were not attempted due to the complications associated with the presence of an additional cysteinyl-ligated Fe site. In this work, we report assignment of the resonance Raman spectrum of oxidized wild-type *P. furiosus* SOR at pH 7.5 and 10.5, based on isotope shifts resulting from global replacements of  $^{32}\text{S}$  with  $^{34}\text{S}$ ,  $^{14}\text{N}$  with  $^{15}\text{N}$ ,  $^{56}\text{Fe}$  with  $^{54}\text{Fe}$ , exchange into a  $\text{H}_2^{18}\text{O}$  buffer, and parallel resonance Raman studies of the oxidized E14A variant. The results reveal extensive coupling between the Fe-S stretching mode and the internal vibrational modes of cysteine. On the basis of the evidence for substantial  $\text{S}(\text{p}\pi)\text{-Fe}(\text{d}\pi)$  interactions (9;10) and the close analogy with type 1 (blue) copper proteins, the resonance Raman results suggest superexchange pathways for mediating electron transfer from rubredoxin to the mononuclear Fe active site.

## **Materials and Methods**

*Sample preparation:* The gene encoding wild-type *P. furiosus* SOR was expressed in *Escherichia coli* and the recombinant protein was purified to homogeneity according to the published procedure (9). The E14A variant of *P. furiosus* SOR was generated using a standard mutagenesis kit (QuikChange Site-Directed Mutagenesis Kit, Stratagene, La Jolla, CA), and the DNA sequence was confirmed. The recombinant E14A SOR was

purified in the same manner as the wild type protein. Samples of wild-type *P. furiosus* SOR globally labeled with  $^{15}\text{N}$  and  $^{34}\text{S}$  SOR were obtained in the same way, except that *E. coli* was grown in 2.8 L flasks (6 x 1 L), shaking at 250 rpm. For the  $^{15}\text{N}$ -labeled sample,  $^{15}\text{NH}_4\text{Cl}$  (98 % enriched; Cambridge Isotopes) was substituted for  $\text{NH}_4\text{Cl}$  and  $\text{FeCl}_3$  substituted for  $\text{Fe}(\text{NH}_4)_2(\text{SO}_4)_2$  in the M9 salts. For the  $^{34}\text{S}$ -labeled sample,  $\text{MgCl}_2$  was substituted for  $\text{MgSO}_4$  and the sole source of sulfur was  $2\text{mM } ^{34}\text{SO}_4^{2-}$  prepared in a 100 mM potassium phosphate buffer.  $^{34}\text{SO}_4^{2-}$  was prepared by heating elemental  $^{34}\text{S}$  (99.8 % enriched; Trace isotopes) to  $85\text{ }^\circ\text{C}$  in *aqua regia*. For the  $^{54}\text{Fe}$ -labeled sample,  $^{54}\text{Fe}$  ferric citrate (95 % enrichment) was substituted for  $\text{FeCl}_3$  in the M9 salts. The  $^{54}\text{Fe}$  ferric citrate solution was prepared from  $^{54}\text{Fe}$  metal by dissolving in *aqua regia*, adding stoichiometric sodium citrate, and neutralizing with 10% ammonium hydroxide. Prior to use for spectroscopic studies, samples were oxidized with excess hexachloroiridate and the excess oxidant was removed by Amicon ultrafiltration. Samples at pH 7.5 were in 50 mM HEPES buffer. Samples at pH 10.5 were prepared by Amicon buffer exchange into a 50 mM CAPS, pH 10.5 buffer and samples in  $\text{H}_2^{18}\text{O}$  (95-98% enrichment) were prepared by Amicon buffer exchange using the equivalent  $\text{H}_2^{18}\text{O}$  buffer. In each case buffer exchange involved three 10-fold dilution and concentration cycles

*Spectroscopic methods:* Resonance Raman spectra were recorded using an Instruments SA Ramanor U1000 spectrometer fitted with a cooled RCA-31034 photomultiplier tube with  $90^\circ$  scattering geometry. Spectra were recorded digitally using photon counting electronics and improvements in signal-to-noise were achieved by signal averaging multiple scans. Absolute band positions were calibrated using the excitation frequency and  $\text{CCl}_4$  and are accurate to  $\pm 1\text{ cm}^{-1}$ . Lines from a Coherent Sabre 100 10-W

Argon Ion Laser or Coherent Innova 200-K2 Krypton Ion Laser were used for excitation, and plasma lines were removed using a Pellin Broca prism premonochromator. Scattering was collected from the surface of a frozen 10- $\mu$ l droplet of sample using a custom-designed anaerobic sample cell (11), attached to the cold finger of an Air Products Displex Model CSA-202E closed cycle refrigerator. This arrangement enables samples to be cooled down to 17 K, which facilitates improved spectral resolution and prevents laser-induced sample degradation. For excitation profiles, 0.5 M sodium sulfate was added to the sample in order to provide an internal standard for the SOR vibrational modes. For assessment of isotope shifts, both the natural abundance and isotopically enriched samples were placed on the sample probe and frequency calibration was checked before and after measurements to ensure relative accuracy of band positions to at least  $\pm 0.1 \text{ cm}^{-1}$ . Isotope shifts ( $\Delta\nu$ ) were assessed to an accuracy of  $\pm 1 \text{ cm}^{-1}$  for weak bands based on spectral overlays and to an accuracy of  $\pm 0.2 \text{ cm}^{-1}$  for more intense bands based on the natural abundance minus isotopically labeled difference spectrum using the relationship  $\Delta\nu = I_D\Gamma/2.6I$ , where  $I_D$  is the peak-to-trough intensity of the difference spectrum,  $I$  is the maximum peak intensity, and  $\Gamma$  is the full width at half-height (12).

## Results

*Fe-S(Cys) vibrational modes:* The visible absorption spectrum of oxidized wild-type *P. furiosus* SOR is dominated by an intense (Cys)S( $p_\pi$ )-to-Fe( $d_\pi$ ) CT transition centered at 660 nm (9), see Figure 3.1. In accord with this assignment, strong enhancement of vibrational modes associated with the Fe-S(Cys) unit are observed in the resonance Raman spectrum using 647-nm excitation, see Figures 3.2, 3.3, and 3.4, and

Table 3.1. The excitation profile for the most intense band at  $323\text{ cm}^{-1}$ , which contains a major contribution from Fe-S(Cys) stretching (see below), reveals maximal enhancement to the low-energy side of the 660-nm absorption band, see Figure 3.1. Analogous excitation profiles, albeit with lower cross-sections, were observed for all of the Raman bands in  $250\text{-}800\text{ cm}^{-1}$  region (data not shown), indicating that all are enhanced via kinematic coupling with the Fe-S(Cys) stretching mode or an excited-state *A*-term mechanism involving the extended Fe-cysteinate chromophore. The vibrational assignments in this region, based on globally labeled  $^{34}\text{S}$ ,  $^{15}\text{N}$ , and  $^{54}\text{Fe}$  isotope shift data (Figures 3.2, 3.3, and 3.4 respectively), are presented in Table 3.1, and discussed below.

The low-frequency region is dominated by three bands centered at 298, 323 and  $748\text{ cm}^{-1}$ , which are identified as fundamental vibrations involving movement of cysteinyl S via  $^{34}\text{S}$  downshifts in excess of  $2\text{ cm}^{-1}$ . The 298 and  $748\text{ cm}^{-1}$  bands are assigned to S-C $_{\beta}$ -C $_{\alpha}$  bending and S-C $_{\beta}$  stretching modes, respectively, based on the extensive vibrational studies and normal modes calculations that are available for Fe-S proteins (*13-16*) and type 1 copper proteins (*15-19*). The most intense band at  $323\text{ cm}^{-1}$  has the largest  $^{34}\text{S}$  downshift and is, therefore, assigned primarily to Fe-S(Cys) stretching. However, the observed  $3.3\text{-cm}^{-1}$   $^{34}\text{S}$ -downshift and  $1.1\text{-cm}^{-1}$   $^{54}\text{Fe}$ -upshift, see Table 3.1, are just over half of the  $6\text{-cm}^{-1}$   $^{34}\text{S}$ -downshift and  $2\text{-cm}^{-1}$   $^{54}\text{Fe}$ -upshift that are predicted based on a simple Fe-S diatomic oscillator approximation, suggesting significant mixing with internal vibrational modes of the coordinated cysteine residue.

Evidence for mixing of the Fe-S(Cys) stretching mode with cysteine deformations comes from the enhancement of at least six modes, at 361, 400, 438, 471, 487, and  $510\text{ cm}^{-1}$ , in the region associated with deformation modes of the coordinated cysteine and

the peptide backbone of adjacent residues in type 1 copper proteins (17-21). In support of this assignment, the bands at 361, 400 and 471  $\text{cm}^{-1}$  in *P. furiosus* SOR, each exhibit  $^{34}\text{S}$  downshifts of approximately 1  $\text{cm}^{-1}$ , see Figure 3.2 and Table 3.1, indicating significant kinematic coupling. Moreover, each of the bands in this region exhibits a  $^{15}\text{N}$  downshift in the range 2-5  $\text{cm}^{-1}$ , indicating contributions from the  $\text{C}_\beta\text{-C}_\alpha\text{-N}$ ,  $\text{C(O)-C}_\alpha\text{-N}$  and  $\text{C}_\alpha\text{-N-C(O)}$  deformations of the coordinating cysteine and the peptide backbone of adjacent residues.  $^{15}\text{N}$  downshifts of similar magnitude have been observed for the equivalent bands in type 1 copper proteins (18;19;21;22) and, in the case of type 1 copper proteins, selective  $^{15}\text{N}$  labeling of the imidazoles of the coordinating histidines has shown these modes are primarily associated with deformation modes of the coordinated cysteine and the peptide backbone of adjacent residues, rather than of coordinating histidine residues (18).

Since kinematic coupling is critically dependent on the energy separation of the uncoupled modes, the most extensive mixing is expected to occur between the Fe-S(Cys) stretching and cysteine S- $\text{C}_\beta\text{-C}_\alpha$  bending modes, which are assigned to the intense bands at 323 and 298  $\text{cm}^{-1}$ , respectively. This is confirmed by the  $^{54}\text{Fe}$  isotope shifts, 1.1- $\text{cm}^{-1}$  upshifts for both the 323- and 298- $\text{cm}^{-1}$  bands, see Figure 3.4 and Table 3.1, indicating that these vibrational modes are extensively mixed. In addition, evidence for mixing of the 361 and 298  $\text{cm}^{-1}$  modes with the 323  $\text{cm}^{-1}$  mode in SOR comes from the change in the relative intensity of the 323 and 298  $\text{cm}^{-1}$  modes in the  $^{15}\text{N}$  globally labeled spectrum, see Figure 3.3. This change in relative intensity is reproducible with different samples and is responsible for the unsymmetrical derivatives associated with the 298- and 323- $\text{cm}^{-1}$  bands in the  $^{14}\text{N}\text{-}^{15}\text{N}$  difference spectrum (Figure 3.3). The change in relative

intensity is readily rationalized in terms of enhanced mixing between the 323 and 361  $\text{cm}^{-1}$  modes in the  $^{15}\text{N}$  globally labeled spectrum, as a result of the large  $^{15}\text{N}$ -downshift in the 361  $\text{cm}^{-1}$  band (4  $\text{cm}^{-1}$ ), coupled with a concomitant decrease in the mixing between the 323 and 298  $\text{cm}^{-1}$  modes.

Weak bands in the 520-750  $\text{cm}^{-1}$  region are readily assigned to overtones and combination bands on the basis of additivity of natural abundance frequencies and  $^{34}\text{S}$ ,  $^{15}\text{N}$ , and  $^{54}\text{Fe}$  isotope shifts, see Figures 3.2-3.4 and Table 3.1. The only exception is the band at 660  $\text{cm}^{-1}$ , which has a negligible  $^{34}\text{S}$  downshift and a large  $^{15}\text{N}$  downshift (7  $\text{cm}^{-1}$ ). The absence of a  $^{34}\text{S}$  downshift rules out assignment to a 298 + 361  $\text{cm}^{-1}$  combination band. Hence it is assigned to a fundamental with significant cysteine  $\text{C}_\alpha\text{-N}$  stretching character, on the basis of normal mode calculations for L-cysteine (23). In accord with this assignment, numerous additional modes associated with internal modes of the ligated cysteine are observed in the high-frequency region, see Figure 3.5. With the exception of the weak band at 1003  $\text{cm}^{-1}$ , which is assigned to the most intense mode of non-resonantly enhanced phenylalanine (there are four Phe residues in *P. furiosus* SOR), the bands at 1100, 1227, 1302, 1431, 1553, and 1662  $\text{cm}^{-1}$  are all enhanced in resonance with the 660-nm absorption band. On the basis of the isotope shifts observed in cysteine- $\text{C}_\beta\text{D}_2$  labeled type 1 copper proteins (19), normal mode calculations for L-cysteine (23), and the frequency ranges observed for polypeptide amide I, II, and III modes in Raman spectra (24), these modes are readily assigned to the  $\text{C}_\beta\text{-C}_\alpha$  stretching,  $\text{C}_\beta\text{H}_2$  twisting, amide III,  $\text{C}_\beta\text{H}_2$  scissoring, amide II and amide I vibrations, respectively, primarily involving the ligated cysteine. All of these modes exhibit negligible  $^{34}\text{S}$  isotope shifts indicating enhancement via an excited-state *A*-term mechanism, i.e. distortion of internal

cysteine bonds in the electronic excited state associated with the (Cys)S(p $\pi$ )-to-Fe(d $\pi$ ) CT transition.

*Fe-N(His) stretching modes:* Weakly enhanced modes that are candidates for Fe-N(His) stretching modes are observed in the 190-250 cm<sup>-1</sup> region, see Figure 3.6. Exchanging the buffer from H<sub>2</sub><sup>16</sup>O to H<sub>2</sub><sup>18</sup>O, in order to shift the lattice modes of ice from 231 cm<sup>-1</sup> to 222 cm<sup>-1</sup>, facilitates observation of a band centered at 210 cm<sup>-1</sup> and another at 234 cm<sup>-1</sup> with a pronounced shoulder at 242 cm<sup>-1</sup>, that each exhibit 1-2 cm<sup>-1</sup> isotope shift in <sup>15</sup>N globally labeled samples and negligible isotope shifts in <sup>34</sup>S globally labeled samples, see Figure 3.6 and Table 3.1. The <sup>15</sup>N isotope shifts are in the range expected for Fe-N(His) stretching modes, which is predicted to be ~1.5 cm<sup>-1</sup> based on a diatomic Fe-imidazole oscillator. These modes are therefore good candidates for the symmetric and asymmetric stretching modes, respectively, of one or both pairs of *trans* histidine residues which have Fe-N distances in the range 2.1-2.2 Å (8;9). Fe-N(His) stretching modes are not expected to be enhanced by kinematic coupling with Fe-S(Cys) stretching, since the Fe-S bond is perpendicular to the FeN<sub>4</sub> plane, and this is in accord with the lack of measurable <sup>34</sup>S isotope shifts. However, Fe-N(His) stretching modes could be weakly enhanced via an *A*-term mechanism, i.e. distortion of the Fe-N(His) bonds in the electronic excited state associated with the (Cys)S(p $\pi$ )-to-Fe(d $\pi$ ) CT transition. UV resonance Raman studies are planned, using excitation into the intense CT band centered at 330 nm, in order to assess the validity of these assignments. The 330-nm absorption band has been shown to have contributions from His-to-Fe<sup>3+</sup> CT transitions based on VHVT MCD studies (9).

*Wild-type pH 10.5 and E14A variant:* Optical pH titrations of oxidized *P. furiosus* SOR revealed an alkaline transition with a  $pK_a = 9.6$  (9). The alkaline transition is marked by a shift in the (Cys)S( $p_\pi$ )-to-Fe( $d_\pi$ ) CT transition from 660 nm to 590 nm (9). Moreover, the resultant UV-visible absorption spectrum for wild-type SOR at pH 10.5 is almost indistinguishable from that of the E14A variant at pH 7.5 (see supporting information, Figure S3.1), suggesting that the change in Fe ligation induced by mutating the glutamate ligand is the same as that induced in wild-type at alkaline pH. In an attempt to investigate the change in ligation, resonance Raman spectra of wild-type SOR at pH 10.5 and the E14A variant at pH 7.5 were recorded in the region 200-800  $\text{cm}^{-1}$  using 647-nm excitation, and compared with equivalent spectra obtained for wild-type at pH 7.5, see Figure 3.7. Remarkably the spectra of all three samples are essentially the same within experimental error, both in terms of the relative intensities and the frequencies of individual modes. Moreover, the same result was observed using 568-nm excitation which is close to the maxima of the (Cys)S( $p_\pi$ )-to-Fe( $d_\pi$ ) CT absorption in the wild-type pH 10.5 and E14A samples (see supporting information, Figure S3.2). The only minor difference is that the intensities of the internal cysteine modes were significantly increased relative to the Fe-S(Cys) stretching modes in the E14A variant compared to the wild-type samples using 568-nm excitation. The resonance Raman results clearly demonstrate that the marked changes in the energy of the (Cys)S( $p_\pi$ )-to-Fe( $d_\pi$ ) CT transition that are associated with the alkaline transition and the E14A mutation do not result from changes in the cysteinyl or histidyl Fe ligation.

Unfortunately, the resonance Raman spectra of wild-type samples at pH 7.5 and 10.5 and of the E14A variant provide no direct evidence in the form of a Fe-ligand

stretching mode for the existence of a ligand *trans* to the cysteinyl S. Such a mode might be expected to be weakly enhanced via excitation into (Cys)S( $p_\pi$ )-to-Fe( $d_\pi$ ) CT transition via kinematic coupling with the Fe-S(Cys) stretching mode. Since no bands are lost or undergo a significant decrease in intensity in the wild-type pH 10.5 or E14A spectra, we conclude that a Fe-O(Glu) stretching mode is either not present or not enhanced. The possibility that the sixth ligand in the three derivatives investigated is derived from an exchangeable water molecule (i.e. H<sub>2</sub>O or OH<sup>-</sup>) was investigated by recording resonance Raman spectra of the wild-type pH 7.5, wild-type pH 10.5, and E14A variant samples after exchange into equivalent H<sub>2</sub><sup>18</sup>O buffer (see supporting information Figures S3.3, S3.4, and S3.5, respectively). Other than the expected isotope shift in the lattice mode of ice from 231 cm<sup>-1</sup> to 222 cm<sup>-1</sup>, none of the bands in any of these derivatives was perturbed by exchange into H<sub>2</sub><sup>18</sup>O buffer. Once again this result should not be interpreted in terms of the absence of a water derived ligand, merely that such a ligand, if present, is either not exchangeable or has an Fe-O stretching mode that is not significantly resonantly enhanced. Since a weak mode at 580 cm<sup>-1</sup> was observed with 647-nm excitation in the wild-type pH 10.5 and E14A variant spectra, but not in the wild-type pH 7.5 spectra (Figure 3.7), we explored the possibility that this mode may originate from a Fe-N stretching mode of a coordinated lysine ligand. Several observations argue against this interpretation. First a weak mode at 580 cm<sup>-1</sup> is observed in for wild-type SOR at pH 7.5 with 568 cm<sup>-1</sup> excitation (see supporting information Figure S3.2). Second, the 580-cm<sup>-1</sup> band in the wild-type pH 10.5 sample undergoes a 4-cm<sup>-1</sup> downshift in samples globally labeled with <sup>15</sup>N (see supporting information Figure S3.6). Hence the observed isotope shift is more in line with an internal cysteine mode than a Fe-N(Lys) mode which

would be expected to have a  $15\text{-cm}^{-1}$   $^{15}\text{N}$ -downshift based on a simple diatomic oscillator approximation.

## Discussion

Resonance Raman studies of *P. furiosus* SOR using excitation into the intense (Cys)S( $p_\pi$ )-to-Fe( $d_\pi$ ) CT transition, have revealed extensive enhancement of vibrational modes associated with the ligated cysteine residue and weak enhancement of Fe-N(His) stretching modes. While the most intense band is attributed primarily to Fe-S(Cys) stretching, numerous fundamentals of the ligated cysteine, including  $\delta(\text{S-C}_\beta\text{-C}_\alpha)$ ,  $\delta(\text{C}_\beta\text{-C}_\alpha\text{-C}(\text{O}))$ ,  $\delta(\text{C}_\beta\text{-C}_\alpha\text{-N})$ ,  $\delta(\text{C}(\text{O})\text{-C}_\alpha\text{-N})$ ,  $\delta(\text{C}_\alpha\text{-N-C}(\text{O}))$ ,  $\nu(\text{C}_\alpha\text{-N})$ ,  $\nu(\text{S-C}_\beta)$ ,  $\nu(\text{C}_\beta\text{-C}_\alpha)$ ,  $\text{C}_\beta\text{H}_2$  twisting,  $\text{C}_\beta\text{H}_2$  scissoring, amide I, II, and III modes, are also enhanced. Isotope shift data using samples globally labeled with  $^{34}\text{S}$  and  $^{54}\text{Fe}$  indicate that the enhancements arise from both kinematic coupling with the Fe-S(Cys) stretching mode and an excited-state  $A$ -term mechanism involving the extended Fe-cysteinate chromophore and one or more of the Fe-N(His) ligands.

By analogy with type 1 copper proteins, kinematic coupling between Fe-S stretching and internal cysteine modes in SOR is likely to be mediated by the  $\text{HC}_\alpha\text{-C}_\beta\text{H}$  torsional mode (20) and is expected to be maximal for a Fe-S-C $_\beta$ -C $_\alpha$  dihedral angle close to  $180^\circ$  and a planar Fe-S-C $_\beta$ -C $_\alpha$ -N unit (15;18;25). This prediction is borne out by the crystal structure of *P. furiosus* SOR which indicates Fe-S-C $_\beta$ -C $_\alpha$  and S-C $_\beta$ -C $_\alpha$ -N dihedral angles close to  $155^\circ$  and  $170^\circ$  and hence a near-planar Fe-S-C $_\beta$ -C $_\alpha$ -N unit (8). Only the modes that are close in energy to the Fe-S(Cys) stretching mode ( $\pm 150\text{ cm}^{-1}$ ) appear to be enhanced via kinematic coupling as evidenced by significant  $^{34}\text{S}$  and/or  $^{54}\text{Fe}$  shifts.

Cysteine internal modes and Fe-N(His) stretching modes that exhibit negligible  $^{34}\text{S}$  isotope shifts appear to be enhanced by an excited-state  $A$ -term mechanism, whereby the vibrations mimic the distortion in the electronic excited state of the (Cys)S( $p_\pi$ )-to-Fe( $d_\pi$ ) CT transition. Previous studies of the ground- and excited-state electronic structure of *P. furiosus* SOR have emphasized the importance of the S( $p_\pi$ )-Fe( $d_\pi$ ) interaction in facilitating substrate reduction and promoting product release in SOR (9;10). Hence the modes enhanced in the resonance Raman spectrum via an  $A$ -term mechanism may be directly relevant to the electron transfer pathway (19;26;27), since the charge-transfer excited state with a hole on the cysteinyl S can correspond to a virtual state in a superexchange model of the electron transfer process (28).

The parallels between type 1 copper proteins and SORs with respect to electron transport pathways are particularly striking. For example, in plastocyanin, an archetypical type 1 copper protein, the tyrosine residue and cysteine ligands that mediate electron transport from cytochrome  $b_6f$  to Cu (29;30) and the  $\delta\text{N}$ -histidine ligand that mediates electron transfer from Cu to photosystem I (31;32), are in Y-C-X-P-H arrangement (19). The tyrosine side chain is solvent exposed and the superexchange pathway for electron entry is maximized by extending the coplanar arrangement of the Cu-S-C $_\beta$ -C $_\alpha$ -N unit to the adjacent tyrosine residue, thereby facilitating long-range electronic coupling (19). An analogous Y-C-X-X-H arrangement of the cysteine and sole  $\delta\text{N}$ -histidine ligands to the Fe center is conserved in all 2Fe-SORs and the majority of the 1Fe-SORs (33). The only exceptions are the 1Fe-SORs from *Treponema pallidum* and *Desulfovibrio gigas* (F in place of Y) and from *Methanococcus jannaschii* (R in place of Y) (33). The crystal structures of the 2Fe-SOR from *D. desulfuricans* (7) and the 1Fe-SOR from *P. furiosus*

(8) show that the coplanar arrangement of the Fe-S-C<sub>β</sub>-C<sub>α</sub>-N unit extends to the adjacent tyrosine residue, but with the tyrosine side chain perpendicular rather than coplanar as in type 1 copper proteins, see Figure 3.8.

An electron transfer pathway via the tyrosine and cysteine residues is an attractive possibility in 2Fe-SORs, since the tyrosine side chain lies on the direct path between the rubredoxin-type Fe(SCys)<sub>4</sub> center the mononuclear Fe active site. Previously, the viability of electron transfer from the Fe(SCys)<sub>4</sub> center in 2Fe-SORs has been questioned since the Fe-Fe distance, ~ 22 Å (34), is significantly longer than the range commonly associated with electron tunneling between metal centers in metalloproteins (≤ 14 Å) (35). Characterization of a superexchange pathway contributes a high electronic coupling matrix element that may facilitate tunneling over such distances. However, it is unlikely that an electron transfer pathway involving the equivalent tyrosine and cysteine residues is operative for mediating electron transfer from exogenous reduced rubredoxin in 1Fe-SORs. In the crystal structure of *P. furiosus* SOR, tyrosine (Tyr110) is at a subunit interface of the homotetramer, and buried in the interior of the protein (8). The possibility that the tetrameric quaternary structure is an artifact of crystallization has been considered, but seems unlikely in light of the extensive subunit interfaces (8) and light scattering evidence for tetramers, but not monomers or dimers, in solution.<sup>2</sup>

By analogy with type 1 copper proteins, the alternative electron transfer pathway in both 1Fe and 2Fe-SORs is via the solvent exposed δN-histidine Fe ligand in the Y-C-X-X-H sequence (His114 in *P. furiosus* SOR and His118 in *D. desulfuricans* 2Fe-SOR). In type 1 copper proteins, the vibrational modes of the equivalent histidine are selectively enhanced in the resonance Raman spectrum using excitation into the intense (Cys)S(p<sub>π</sub>)-

to-Cu( $d_{\pi}$ ) CT transition, because the N( $p_{\pi}$ ) orbital is aligned (imidazole ring makes an angle of  $72^{\circ}$  to the  $\text{CuN}_2\text{S}$  plane) for overlap Cu( $d_{x^2-y^2}$ )  $d_{\pi}$  orbital (19). In SORs, the imidazole rings of the *trans* histidines, His114 and His41 in *P. furiosus* SOR and His 118 and His 68 in *D. desulfuricans* 2Fe-SOR, have a propeller twist with each at an angle of  $\sim 50^{\circ}$  (*P. furiosus* SOR) and  $\sim 60^{\circ}$  (*D. desulfuricans* 2Fe-SOR) to the  $\text{FeN}_2\text{S}$  plane. Optimal overlap would require the imidazole rings to be orthogonal ( $90^{\circ}$ ), see Figure 3.8(b), but both are positioned for partial overlap of the N( $p_{\pi}$ ) orbital with the Fe( $d_{xy}$ ) orbital, which is the acceptor orbital for the (Cys)S( $p_{\pi}$ )-to-Fe( $d_{\pi}$ ) CT transition, see Figure 3.8(b). This overlap is presumably responsible for the weak enhancement of the symmetric and asymmetric Fe-N(His) stretching modes in *P. furiosus* SOR and *D. desulfuricans* 2Fe-SOR (6) in the  $190\text{-}250\text{ cm}^{-1}$  region, via an *A*-term mechanism. Hence electron transfer via the solvent-exposed histidine residues in 1Fe and 2Fe-SORs will result in increased electron density in Fe( $d_{xy}$ )  $d_{\pi}$  orbital, thereby facilitating substrate reduction via electron transfer to the superoxide  $\pi^*$  orbital and promoting release of the resultant peroxide (10). Further experiments, including mutational studies, will clearly be required to address if one or both of the two potential electron pathways are operational in 2Fe-SORs.

While the above discussion serves to emphasize the close parallels between the electron transfer pathways and resonance Raman enhancement mechanisms in SOR and type 1 copper proteins, the correlation in the resonance Raman spectra is not immediately apparent. The resonance Raman spectra of SOR and type 1 copper proteins using excitation into the equivalent (Cys)S( $p_{\pi}$ )-to-Fe( $d_{\pi}$ ) and (Cys)S( $p_{\pi}$ )-to-Cu( $d_{\pi}$ ) CT are very different in the low-frequency region. However, the differences are readily interpretable

in terms of the Metal-S(Cys) bond lengths. The short Cu-S bond length in type 1 copper proteins ( $\sim 2.1$  Å (36)) results in a Cu-S(Cys) stretching frequency near  $400\text{ cm}^{-1}$ . This leads to strong kinematic coupling and resonance enhancement of cysteinyl deformation modes in the  $350\text{-}450\text{ cm}^{-1}$  region in type 1 copper proteins (17-21). The longer Fe-S bond length in oxidized SOR (2.36 Å based on EXAFS measurements (9)), results in a Fe-S(Cys) stretching frequency near  $320\text{ cm}^{-1}$ , and optimal kinematic coupling and resonance enhancements for cysteinyl deformation modes in the  $270\text{-}370\text{ cm}^{-1}$  region. In accord with this interpretation, the resonance Raman spectrum of *P. furiosus* SOR is very similar to that observed for the type 2 Cu center in the exogenous histidine-bound form of the His119Gly variant of azurin (17;18). The type 2 adduct has a CT band at 400 nm, as opposed to 625 nm for the type 1 imidazole-bound adduct of the His119Gly variant. The dramatic change in the energy of the CT band and the resonance Raman spectrum has been attributed to bidentate binding of the exogenous histidines to yield a four-coordinate square planar site with concomitant lengthening of the Cu-S(Cys) bond to  $\sim 2.29$  Å (17;18).

The crystallographic data for the oxidized active sites in *P. furiosus* SOR (8) and the *D. desulfuricans* 2Fe-SOR (7), was ambiguous with respect to the identity or existence of the ligand *trans* to the cysteine. In two of the four subunits of *P. furiosus* SOR, the conserved glutamate provided the sixth ligand, whereas in the other two subunits of *P. furiosus* SOR and in *D. desulfuricans* 2Fe-SOR, the sixth coordination site is either vacant or occupied by a water molecule. On the basis of x-ray absorption studies of *P. furiosus* SOR, it now seems likely that photoreduction in the x-ray beam is responsible for this discrepancy (9). Furthermore, the detailed electronic properties of the

oxidized Fe site in *P. furiosus* SOR as deduced by EPR and VHVT MCD spectroscopy (9), the number of ligands in the first coordination sphere of the oxidized Fe site in *P. furiosus* SOR as deduced by Fe EXAFS analysis (9), and the marked changes in the oxidized absorption spectra that accompany mutation of the conserved glutamate in both 1Fe-SORs (37 and this work) and 2Fe-SORs (38;39), are all consistent with sixth coordinate site with glutamate as the ligand *trans* to cysteine. While the breadth and asymmetry of the predominantly Fe-S(Cys) stretching mode at 323 cm<sup>-1</sup> suggests some heterogeneity in the high-spin ferric active sites within the homotetramer, the frequency is also best interpreted in terms of a six-coordinate Fe site.

Hemoproteins provide the best frame of reference for comparing the frequencies of axial Fe-S(Cys) stretching modes in five- and six-coordinate sites. The Fe-S(Cys) stretching mode has thus far only been positively identified at 312 cm<sup>-1</sup> in one six-coordinate heme: the cysteine/histidine axially ligated low-spin ferric heme in cystathionine β-synthase (40). As expected, the Fe-S(Cys) stretching frequency increases significantly to ~350 cm<sup>-1</sup> for the five-coordinate high spin ferric hemes in cytochrome P450<sub>cam</sub> (41) and chloroperoxidase (42). Resonance Raman studies of the cyanide-bound, low-spin adduct of oxidized *P. furiosus* SOR have shown that the Fe-S(Cys) stretching frequency is also relatively insensitive to spin-state changes associated with cyanide binding *trans* to the cysteinate ligand.<sup>3</sup> Hence, the Fe-S(Cys) stretching frequency in both low-spin and high-spin derivatives of *P. furiosus* SOR is consistent with a six-coordinate site.

The absence of any significant changes in the resonance Raman spectra of wild-type *P. furiosus* SOR on increasing the pH from 7.5 to 10.5 and on mutating the ligating

glutamate residue to alanine, coupled with the parallel changes in the UV-visible absorption spectra, suggests that the glutamate ligand is replaced by a common ligand as a result of both the alkaline transition and the E14A mutation. The best candidates for the ligand that replaces the glutamate are hydroxide or lysine 15. The latter suggestion is based on the crystallographic data, which show that the glutamate 14 moves to a position 10.6 Å from the Fe on reduction and that the closest residue to Fe in the reduced active-site structure is lysine 15 which is located 6.6 Å from the Fe. Precedent for an alkaline transition with a similar  $pK_a$  involving deprotonation and coordination of a lysine residue adjacent to the ligand coordinating at neutral pH is provided by cytochrome *c* (43). Unfortunately our attempts to discriminate between these two possibilities by detailed resonance Raman studies of samples exchanged into H<sub>2</sub><sup>18</sup>O buffer and globally labeled with <sup>15</sup>N have been unsuccessful due to lack of resonance enhancement of the stretching mode of the Fe-ligand bond that is *trans* to the Fe-S(Cys). While the identity of the ligand remains to be determined, the resonance Raman data demonstrate that the change in ligation induced by the alkaline transition or the E14A mutation has little effect on the strength of the Fe-S(Cys) bond.

Finally, it is appropriate to reevaluate the published resonance Raman results for *D. desulfuricans* 2Fe-SOR (6), in light of the more detailed and higher quality data presented herein for *P. furiosus* SOR. The resonance Raman results for *D. desulfuricans* 2Fe-SOR provided the first evidence for cysteinyl ligation of the novel mononuclear Fe center that is now known to constitute the SOR active site (Center II). However, prior to the crystallographic data (7), it was not possible to discriminate between one or two cysteinyl ligands based on the resonance Raman data (6). Moreover, detailed assignments

for the SOR center were complicated by resonance enhancement of the rubredoxin-type Fe(SCys)<sub>4</sub> center (Center I), even with 647-nm excitation. Nevertheless, it is now clear that the majority of the observed bands can be assigned by direct analogy with data presented herein for *P. furiosus* SOR. The only ambiguity comes in the assignment of the bands that predominantly correspond to Fe-S(Cys) stretching and S-C<sub>β</sub>-C<sub>α</sub> bending modes of the SOR site in 2Fe-SOR. Attempts to remove contributions from Center I involved subtraction of the spectrum of the partially reduced sample (Center II reduced and Center I oxidized), under the assumption that the dominant band in the partially reduced spectrum at 314 cm<sup>-1</sup> originated exclusively from Center I. This assumption no longer appears to be valid and it now seems likely that Center II also has a band at 314 cm<sup>-1</sup>. However, the relative intensities of the 300 and 314 cm<sup>-1</sup> bands for the SOR center are inverted compared to the 298 and 323 in *P. furiosus* SOR. As in *P. furiosus* SOR, the Fe-S(Cys) stretching and S-C<sub>β</sub>-C<sub>α</sub> bending modes are likely to be extensively mixed in *D. desulfuricans* 2Fe-SOR, and investigation of <sup>34</sup>S- and <sup>54</sup>Fe-enriched samples will be required to address the contributions of these modes to the 300 and 314 cm<sup>-1</sup> bands. However, it is clear that the Fe-S(Cys) stretching mode of the SOR active site in *D. desulfuricans* 2Fe-SOR occurs at a significantly lower frequency than in *P. furiosus* SOR indicating a longer Fe-S(Cys) bond. Since the Fe-N(His) stretching modes have stronger enhancement in *D. desulfuricans* 2Fe-SOR than in *P. furiosus* SOR (6), this presumably reflects decreased S(p<sub>π</sub>)-Fe(d<sub>π</sub>) interaction at the expense of the increased histidine N(p<sub>π</sub>)-Fe(d<sub>π</sub>) interaction. In accord with this interpretation, the histidine imidazole rings that are available for N(p<sub>π</sub>)-Fe(d<sub>π</sub>) interaction are closer to orthogonality with the FeN<sub>2</sub>S plane in

*D. desulfuricans* 2Fe-SOR ( $\sim 60^\circ$ ) than in *P. furiosus* SOR ( $\sim 50^\circ$ ) and hence are expected to have better overlap with the Fe( $d_{xy}$ ) $d_\pi$  orbital.

### **Supporting Information Available**

The following supporting information is available: Visible absorption spectra of wild-type *P. furiosus* SOR at pH 7.5 and 10.5 and of the E14A variant at pH 7.5; Resonance Raman spectra of wild-type *P. furiosus* SOR at pH 7.5 and 10.5 and of the E14A variant at pH 7.5 using 568-nm excitation; Resonance Raman spectra of wild-type *P. furiosus* SOR at pH 7.5 in H<sub>2</sub><sup>16</sup>O and H<sub>2</sub><sup>18</sup>O buffer solutions; Resonance Raman spectra of wild-type *P. furiosus* SOR at pH 10.5 in H<sub>2</sub><sup>16</sup>O and H<sub>2</sub><sup>18</sup>O buffer solutions; Resonance Raman spectra of E14A *P. furiosus* SOR at pH 7.5 in H<sub>2</sub><sup>16</sup>O and H<sub>2</sub><sup>18</sup>O buffer solutions; Resonance Raman spectra of natural abundance (NA) and <sup>15</sup>N globally labeled wild-type *P. furiosus* SOR at pH 10.5. This material is available free of charge via the Internet at <http://pubs.acs.org>.

## References

1. Jenney, F. E., Verhagen, M. F. J. M., Cui, X., and Adams, M. W. W. (1999) *Science* 286, 306-309.
2. Lombard, M., Touati, D., Fontecave, M., and Nivière, V. (2000) *J. Biol. Chem.* 275, 27021-27026.
3. Coulter, E. D. and Kurtz, D. M., Jr. (2001) *Arch. Biochem. Biophys.* 394, 76-86.
4. Chen, L., Sharma, P., LeGall, J., Mariano, A. M., Teixeira, M., and Xavier, A. V. (1994) *Eur. J. Biochem.* 226, 613-618.
5. Moura, I., Tavares, P., Moura, J. J. G., Ravi, N., Huynh, B. H., Liu, M.-Y., and LeGall, J. (1990) *J. Biol. Chem.* 265, 21596-21602.
6. Tavares, P., Ravi, N., Moura, J. J. G., LeGall, J., Huang, Y.-H., Crouse, B. R., Johnson, M. K., Huynh, B. H., and Moura, I. (1994) *J. Biol. Chem.* 269, 10504-10510.
7. Coelho, A. V., Matias, P., Fülöp, V., Thompson, A., Gonzalez, A., and Carrondo, M. A. (1997) *J. Biol. Inorg. Chem.* 2, 680-689.
8. Yeh, A. P., Hu, Y., Jenney, F. E., Adams, M. W. W., and Rees, D. C. (2000) *Biochemistry* 39, 2499-2508.
9. Clay, M. D., Jenney, F. E. Jr., Hagedoorn, P. L., George, G. N., Adams, M. W. W., and Johnson, M. K. (2002) *J. Am. Chem. Soc.* 124, 788-805.
10. Adams, M. W. W., Jenney, F. E. Jr., Clay, M. D., and Johnson, M. K. (2002) *J. Biol. Inorg. Chem.* 7, in press.
11. Drozdowski, P. M. and Johnson, M. K. (1988) *Appl. Spectrosc.* 42, 1575-1577.

12. Shelnutt, J. A., Rousseau, D. L., Dethemers, J. K., and Margoliash, E. (1979) *Proc. Natl. Acad. Sci. USA* 76, 3865-3871.
13. Czernuszewicz, R. S., LeGall, J., Moura, I., and Spiro, T. G. (1986) *Inorg. Chem.* 25, 696-700.
14. Czernuszewicz, R. S., LaTonya, K. K., Koch, S. A., and Spiro, T. G. (1994) *J. Am. Chem. Soc.* 116, 7134-7141.
15. Loehr, T. M. (1992) *J. Raman. Spectrosc.* 23, 531-537.
16. Spiro, T. G. and Czernuszewicz, R. S. (1995) *Meth. Enzymol.* 246, 416-460.
17. Andrew, C. R. and Sanders-Loehr, J. (1996) *Acc. Chem. Res.* 29, 365-372.
18. Andrew, C. R., Han, J., den Blaauwen, T., van Pouderoyen, G., Vijgenboom, E., Canters, G. W., Loehr, T. M., and Sanders-Loehr, J. (1997) *J. Biol. Inorg. Chem.* 2, 98-107.
19. Dong, S. and Spiro, T. G. (1998) *J. Am. Chem. Soc.* 120, 10434-10440.
20. Qiu, D., Kilpatrick, L., Kitajima, N., and Spiro, T. G. (1994) *J. Am. Chem. Soc.* 116, 2585-2590.
21. Qiu, D., Dasgupta, S., Kozlowski, P. M., Goddard, W. A., and Spiro, T. G. (1998) *J. Am. Chem. Soc.* 120, 12791-12797.
22. Czernuszewicz, R. S., Fraczkiewicz, G., Fraczkiewicz, R., Dave, B. C., and Germanas, J. P. (1995) in *Spectroscopy of Biological Molecules* (Merlin, J. C., Ed.) pp 273-276, Kluwer, The Netherlands.
23. Li, H., Wurrey, C. J., and Thomas, G. J., Jr. (1992) *J. Am. Chem. Soc.* 114, 7463-7469.
24. Fabian, H. and Anzenbacher, P. (1993) *Vib. Spectrosc.* 4, 125-148.

25. Han, S., Czernuszewicz, R. S., and Spiro, T. G. (1989) *J. Am. Chem. Soc.* *111*, 3496-3504.
26. Fraga, E., Webb, M. A., and Loppnow, G. R. (1996) *J. Phys. Chem.* *100*, 3278-3287.
27. Ungar, L. W., Scherer, N. F., and Voth, G. A. (1997) *Biophys. J.* *72*, 5-17.
28. Newton, M. D. (1991) *Chem. Rev.* *91*, 767-792.
29. Farver, O. and Pecht, I. (1981) *Proc. Natl. Acad. Sci. USA* *78*, 4190-4193.
30. He, S., Modi, S., Bendall, D. S., and Gray, J. C. (1991) *EMBO J.* *10*, 4011-4016.
31. Sigfridsson, K., Young, S., and Hansson, Ö. (1996) *Biochemistry* *35*, 1249-1257.
32. Qin, L. and Kostic, N. M. (1996) *Biochemistry* *35*, 3379-3386.
33. Ascenso, C., Rusnak, F. M., Cabrito, I., Lima, M. J., Naylor, S., Moura, I., and Moura, J. J. G. (2000) *J. Biol. Inorg. Chem.* *5*, 720-729.
34. Lombard, M., Fontecave, M., Touati, D., and Nivière, V. (2000) *J. Biol. Chem.* *275*, 115-121.
35. Page, C. C., Moser, C. C., Chen, X., and Dutton, P. L. (1999) *Nature* *402*, 47-52.
36. Guss, J. M., Bartunk, H. D., and Freeman, H. C. (1992) *Acta Crystallogr. B* *48*, 790-811.
37. Abreu, I. A., Saraiva, L. M., Soares, C. M., Teixeira, M. and Cabelli, D. E. (2001) *J. Biol. Chem.* *276*, 38995-39001.
38. Coulter, E. D., Emerson, J. P., Kurtz, D. M., Jr., and Cabelli, D. E. (2000) *J. Am. Chem. Soc.* *122*, 11555-11556.
39. Lombard, M., Houée-Levin, C., Touati, D., Fontecave, M., and Nivière, V. (2001) *Biochemistry* *40*, 5032-5040.

40. Green, E. L., Taoka, S., Banerjee, R., and Loehr, T. M. (2001) *Biochemistry* 40, 459-463.
41. Champion, P. M., Stallard, B. R., Wagner, G. C., and Gunsalus, R. P. (1982) *J. Am. Chem. Soc.* 104, 5469-5472.
42. Bangcharoenpaourpong, O., Hall, K. S., Hager, L. P., and Champion, P. M. (1986) *Biochemistry* 25, 2374-2378.
43. Ferrer, J. C., Guillemette, J. G., Bogumil, R., Inglis, S. C., Smith, M., and Mauk, A. G. (1993) *J. Am. Chem. Soc.* 115, 7507-7508.

**Table 3.1** Assignment of the resonance Raman spectrum of oxidized wild-type *P. furiosus* SOR

Frequency, cm <sup>-1</sup>	<sup>34</sup> S shift, <sup>a</sup> cm <sup>-1</sup>	<sup>15</sup> N shift, <sup>a</sup> cm <sup>-1</sup>	<sup>54</sup> Fe shift, <sup>a</sup> cm <sup>-1</sup>	Assignment <sup>b</sup>
210	0	-2	0	$\nu(\text{Fe-N(His)})$
234	0	-1	nd	$\nu(\text{Fe-N(His)})^c$
242	0	-2	+1	$\nu(\text{Fe-N(His)})$
298	-2.2	-2.2	+1.1	$\delta(\text{S-C}_\beta\text{-C}_\alpha) + \nu(\text{Fe-S})$
323	-3.3	-1.5	+1.1	$\nu(\text{Fe-S}) + \delta(\text{S-C}_\beta\text{-C}_\alpha)$
361	-1.0	-4.0	0	} $\delta(\text{C}_\beta\text{-C}_\alpha\text{-C(O)}) +$ } $\delta(\text{C}_\beta\text{-C}_\alpha\text{-N}) + \delta(\text{C(O)-C}_\alpha\text{-N}) +$ } $\delta(\text{C}_\alpha\text{-N-C(O)}) + \delta(\text{S-C}_\beta\text{-C}_\alpha) +$ } $\nu(\text{Fe-S})$ }
400	-1	-3	0	
438	0	-2	0	
471	-1	-5	0	
487	0	-3	0	
510	0	-5	0	
533	-3	-4	+1	Combination (210 + 323)
620	-5	-4	+2	Combination (298 + 323)
640	-5	-3	+2	Overtone (2 × 323)
660	0	-7	0	$\nu(\text{C}_\alpha\text{-N})$
682	-3	-5	+1	Combination (323 + 361)
712	-1	-6	0	Overtone (2 × 361)
748	-2.7	-1.1	0	$\nu(\text{S-C}_\beta)$
1003	0	nd	nd	Phenylalanine
1110	0	nd	nd	$\nu(\text{C}_\beta\text{-C}_\alpha)$
1227	0	nd	nd	$\text{C}_\beta\text{H}_2$ twisting
1302	0	nd	nd	Amide III
1431	0	nd	nd	$\text{C}_\beta\text{H}_2$ scissoring
1553	0	nd	nd	Amide II
1662	0	nd	nd	Amide I

<sup>a</sup>Isotope shifts given to two significant figures have an estimated uncertainty of  $\pm 0.2$  cm<sup>-1</sup>

and those given to one significant figure have an estimated uncertainty of  $\pm 1$  cm<sup>-1</sup>; nd, not-determined.

<sup>b</sup>Unless otherwise indicated, all assignments correspond to vibrational modes of Cys111 and indicate the major contributing modes.

<sup>c</sup>Obscured by lattice mode of ice in H<sub>2</sub><sup>16</sup>O buffer

Figure 3.1 Visible absorption spectrum and resonance Raman excitation profile for the 323-cm<sup>-1</sup> vibrational mode of wild-type *P. furiosus* SOR. The sample and Raman measurement conditions are the same as those described in Figure 3.2, except for the addition of 500 mM sodium sulfate, which served as an internal standard for the excitation profile. The excitation profile ( $\Delta$ ) is in arbitrary units and corresponds to the ratio of the intensity of the 323-cm<sup>-1</sup> band of SOR to the 990-cm<sup>-1</sup> symmetric stretch of the sulfate anion at different excitation wavelengths.

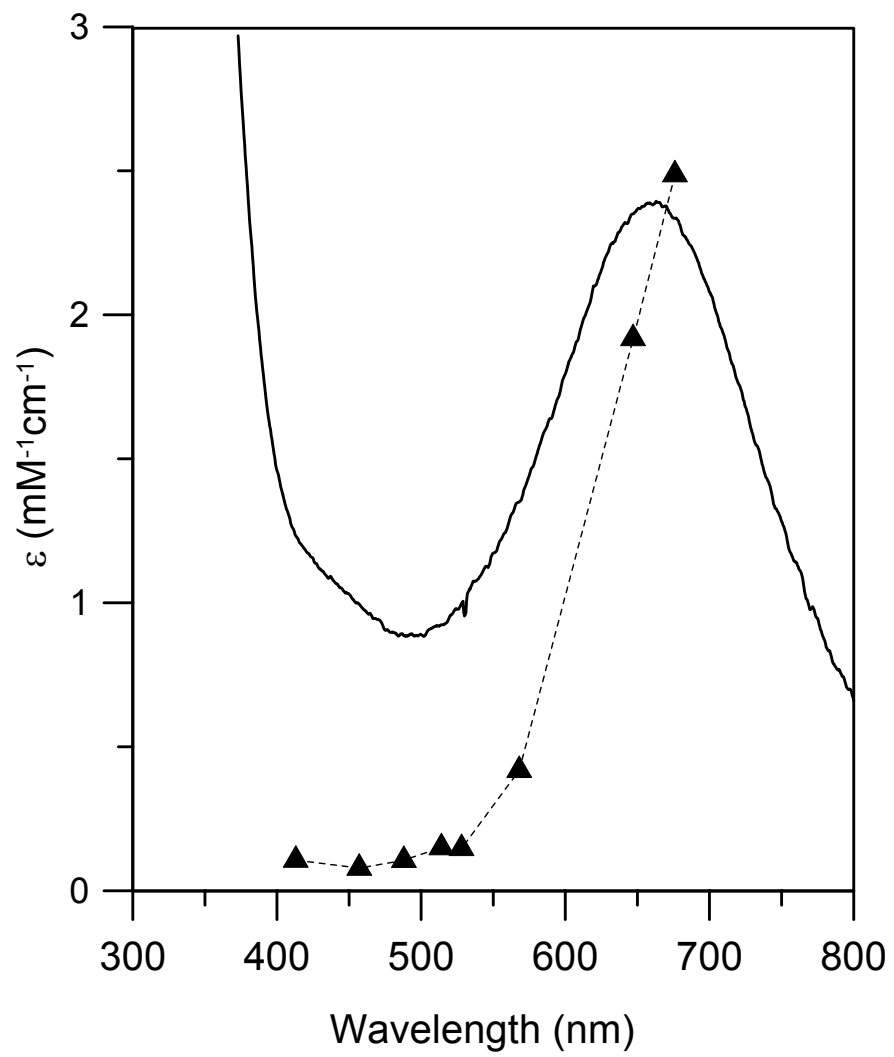


Figure 3.2 Resonance Raman spectra of natural abundance (NA) and  $^{34}\text{S}$  globally labeled wild-type *P. furiosus* SOR. Upper spectrum: natural abundance. Middle panel: globally enriched with  $^{34}\text{S}$ . Lower panel: Natural abundance minus  $^{34}\text{S}$  globally enriched difference spectrum. Spectra recorded using 647-nm excitation with samples as frozen droplets maintained at 17 K. Samples were  $\sim 5$  mM in SOR and were in 50 mM HEPES pH 7.5 buffer. Spectra were recorded using  $6\text{ cm}^{-1}$  resolution by photon counting for 1 sec every  $1\text{ cm}^{-1}$  and are the sum of 30-50 scans. The asterisks indicate lattice modes of ice.

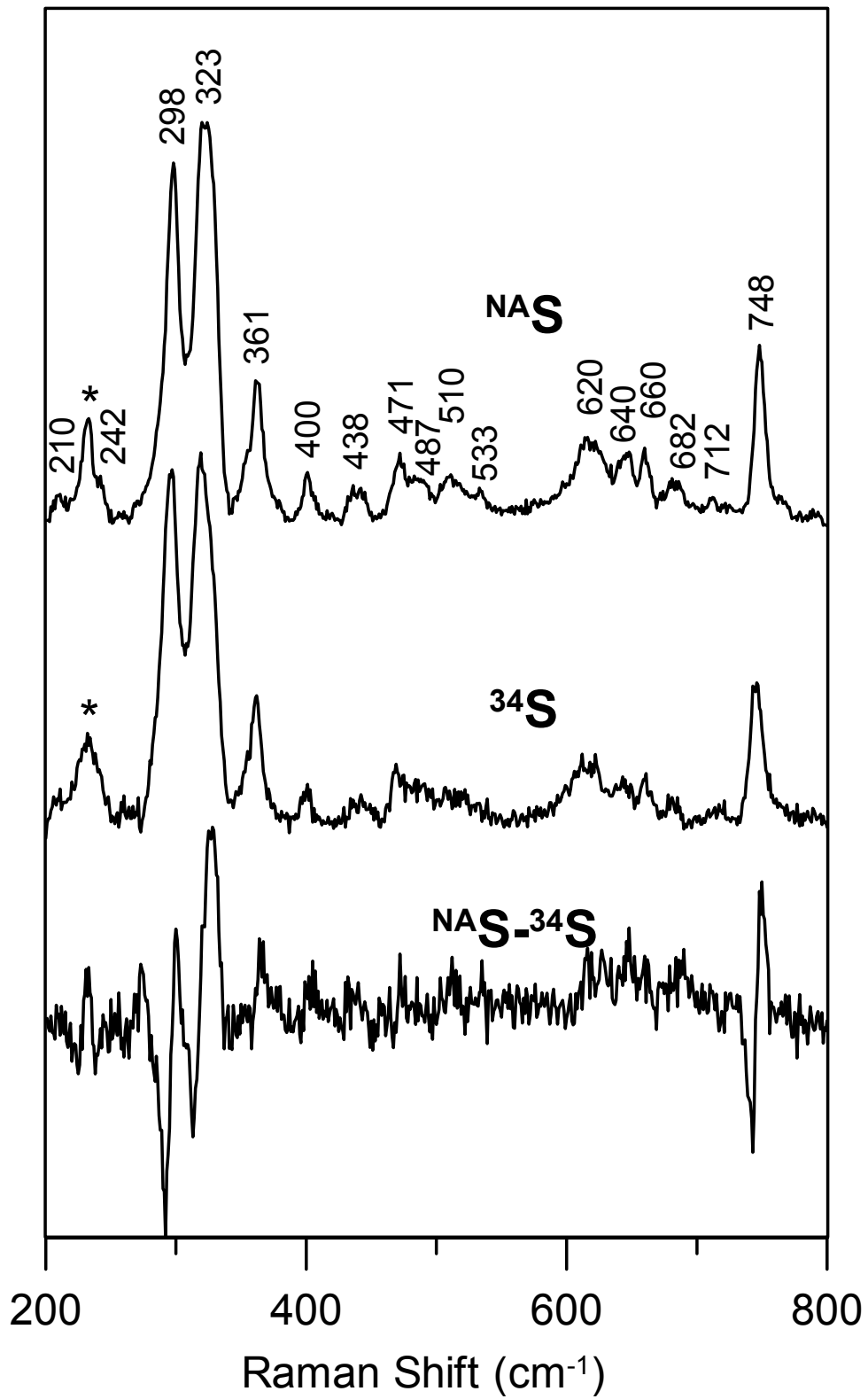


Figure 3.3 Resonance Raman spectra of natural abundance (NA) and  $^{15}\text{N}$  globally labeled wild-type *P. furiosus* SOR. Upper spectrum: natural abundance. Middle panel: globally enriched with  $^{15}\text{N}$ . Lower panel: Natural abundance minus  $^{15}\text{N}$  globally enriched difference spectrum. The sample and measurement conditions are the same as those described in Figure 3.2, and asterisks indicate the lattice modes of ice.

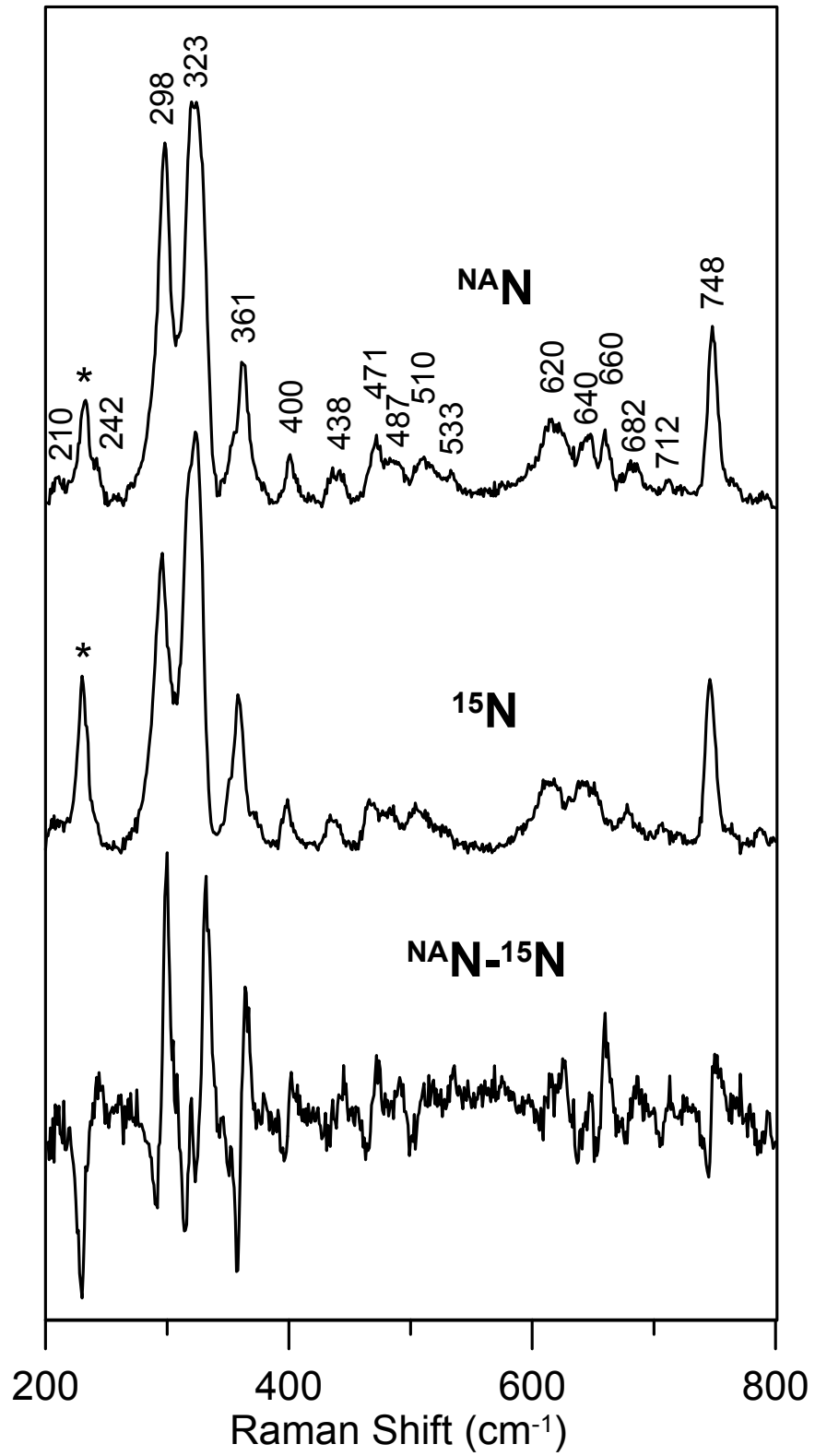


Figure 3.4 Resonance Raman spectra of natural abundance (NA) and  $^{54}\text{Fe}$  globally labeled wild-type *P. furiosus* SOR. Upper spectrum: natural abundance. Middle panel: globally enriched with  $^{54}\text{Fe}$ . Lower panel:  $^{54}\text{Fe}$  minus natural abundance difference spectrum. The sample and measurement conditions are the same as those described in Figure 3.2, and asterisk indicates a lattice mode of ice.

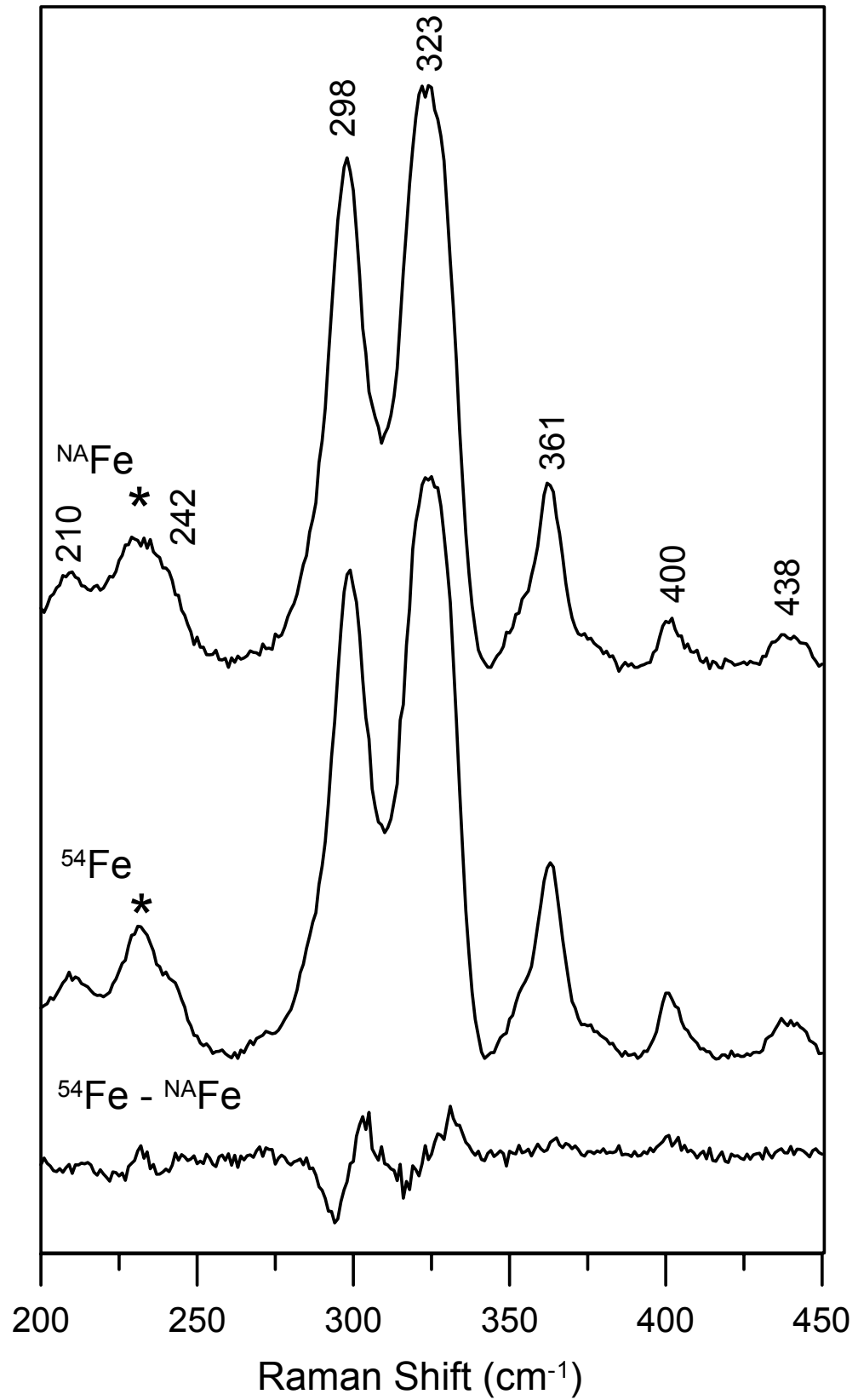


Figure 3.5 Resonance Raman spectrum of wild-type *P. furiosus* SOR in the high frequency region, 800-2000  $\text{cm}^{-1}$ . The sample and measurement conditions are the same as those described in Figure 3.2.

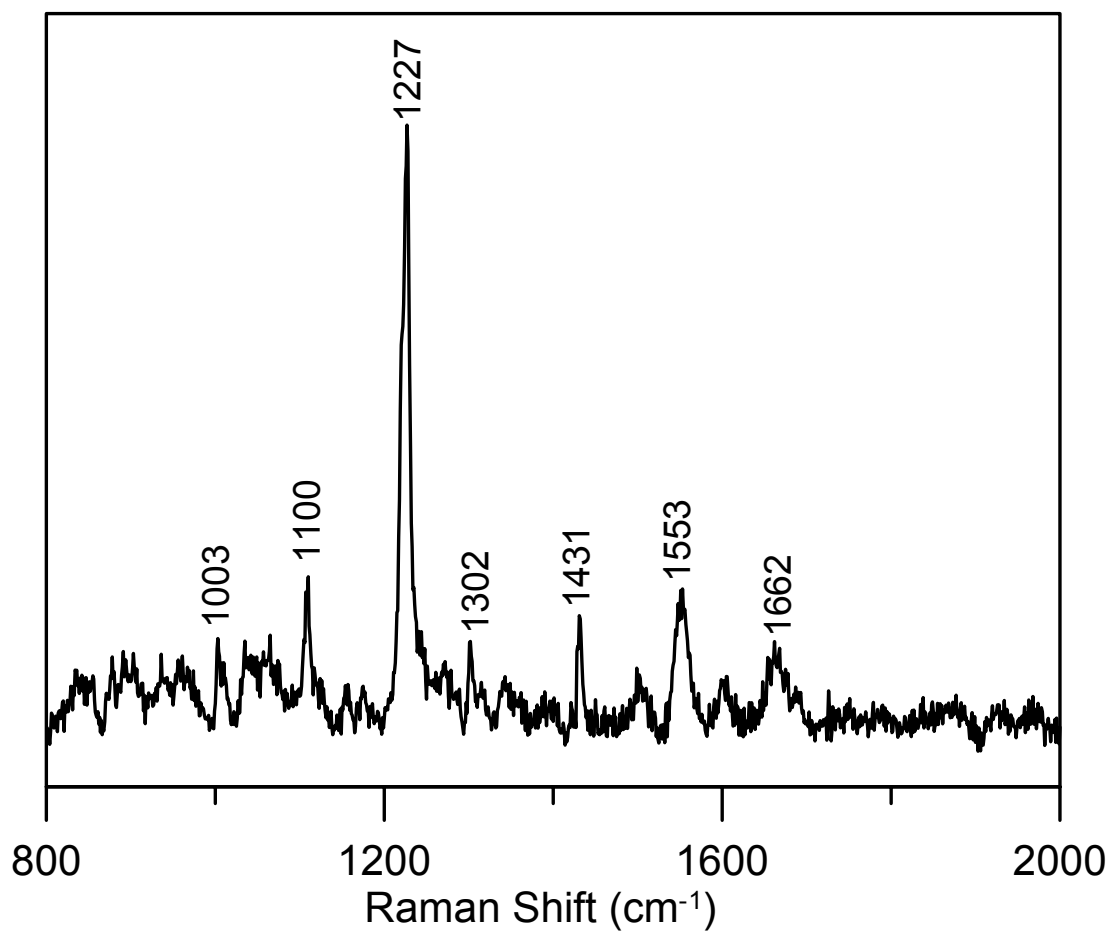


Figure 3.6 Resonance Raman spectra of natural abundance (NA) and  $^{15}\text{N}$  globally labeled wild-type *P. furiosus* SOR in the Fe-N(His) stretching region, 190-260  $\text{cm}^{-1}$  region. The two upper spectra were recorded in  $\text{H}_2^{16}\text{O}$  50 mM HEPES pH 7.5 buffer and the two lower spectra were recorded after exchange into  $\text{H}_2^{18}\text{O}$  50 mM HEPES pH 7.5 buffer. All other sample and measurement conditions are the same as those described in Figure 3.2, except that each spectrum is the sum of at least 100 scans. Bands arising from lattice modes of frozen  $\text{H}_2^{16}\text{O}$  or  $\text{H}_2^{18}\text{O}$  are indicated by asterisks.

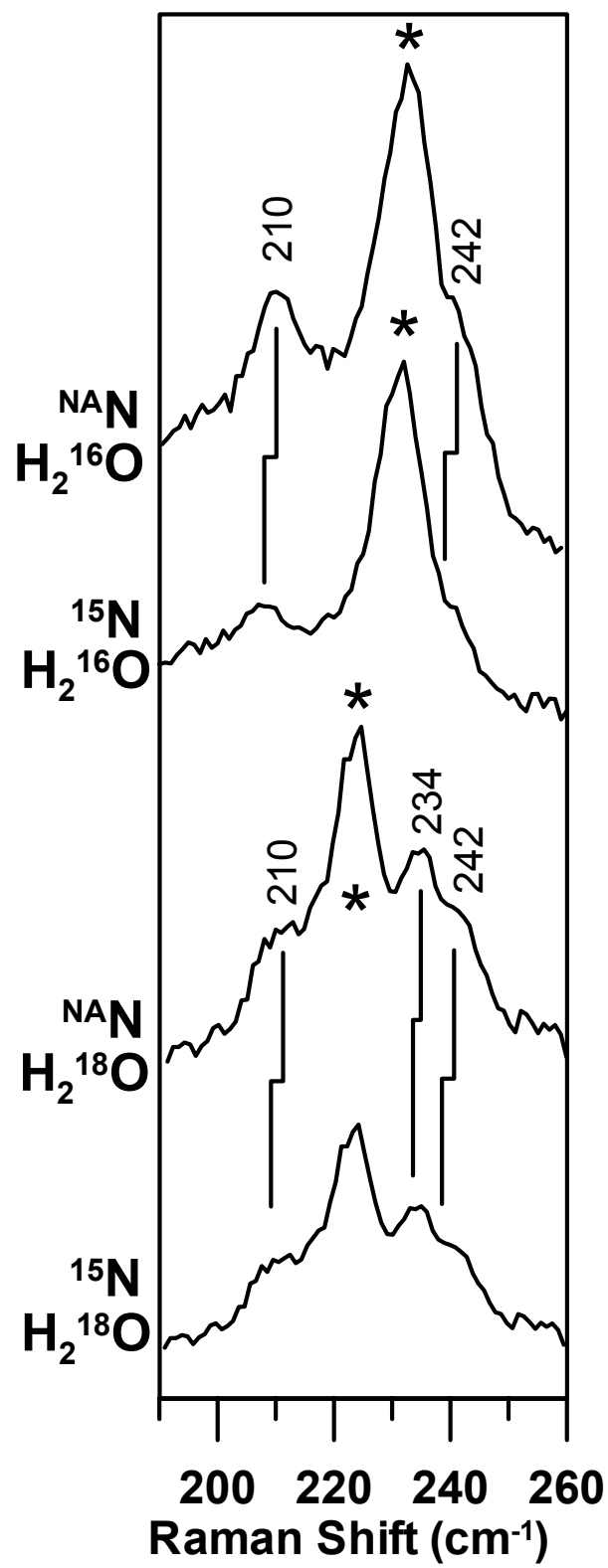


Figure 3.7 Comparison of the resonance Raman spectra of wild-type *P. furiosus* SOR at pH 7.5 and 10.5 with the E14A variant at pH 7.5. Upper spectrum: wild-type at pH 7.5. Middle spectrum: wild-type at pH 10.5. Lower spectrum E14A variant at pH 7.5. The sample and measurement conditions are the same as those described in Figure 3.2, except that pH 10.5 sample was in 50 mM CAPS buffer. The asterisk indicates a lattice mode of ice.

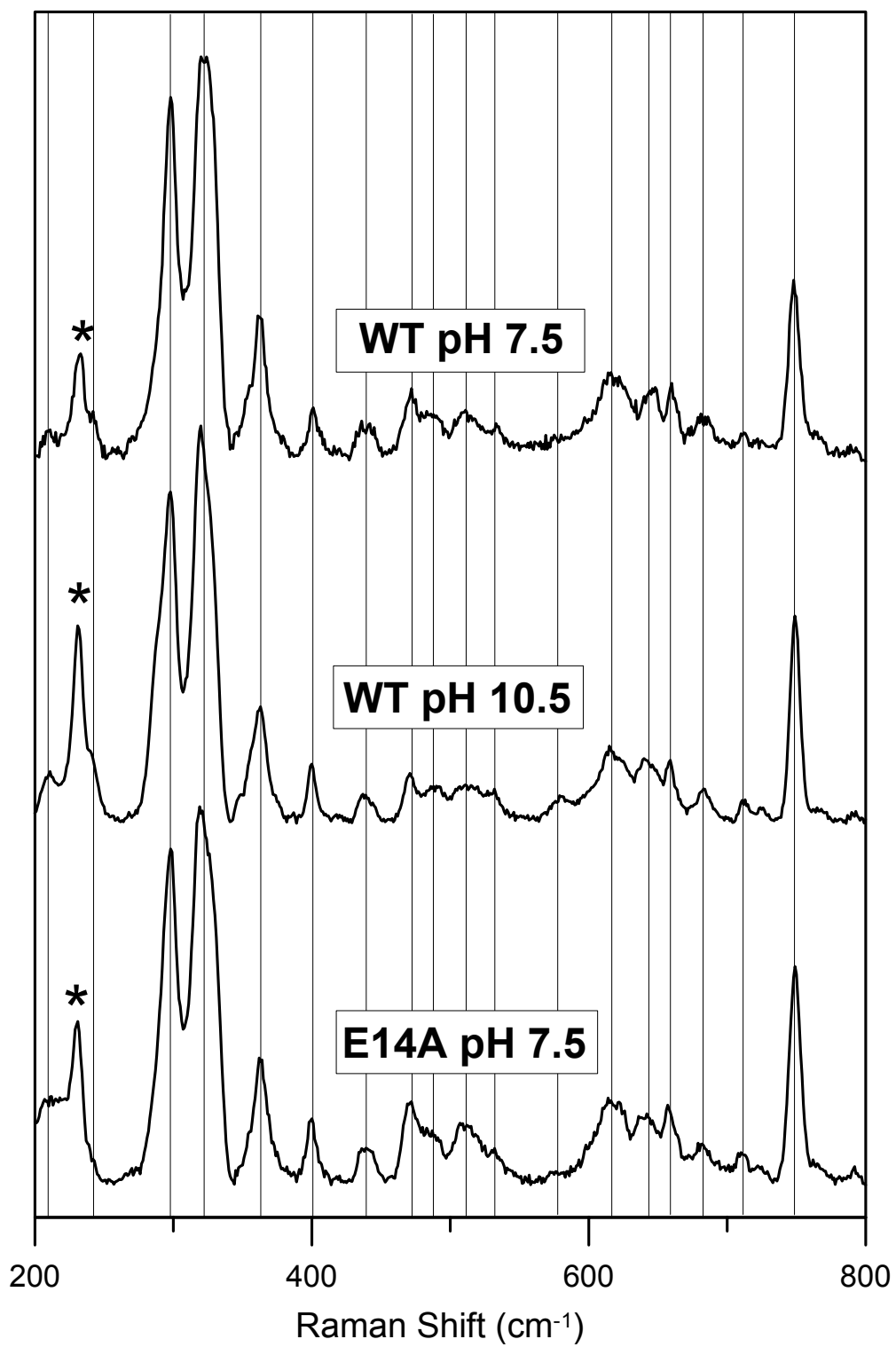


Figure 3.8 (a) Top and side view of the *P. furiosus* SOR active site showing the near-planar arrangement of the Fe-S-C<sub>β</sub>-C<sub>α</sub>-N unit and the orientation of the histidine imidazoles with respect to the FeN<sub>2</sub>S plane defined by His114(δN) and His41(εN). The coordinates were taken from the Protein Data Base entry for oxidized *P. furiosus* SOR (subunit A) (8) and the axes correspond to the zero-field splitting axis system as determined by EPR and VHVT MCD studies (9). The imidazole rings of the two other equatorial histidines, His16(εN) and His47(εN), have been omitted for clarity. (b) Schematic depiction of optimal orbital overlap between the Fe(d<sub>xy</sub>) and CysS(p<sub>π</sub>) and HisN(p<sub>π</sub>) orbitals, i.e. with the plane of the imidazole ring 90° to the FeN<sub>2</sub>S plane. In *P. furiosus* SOR the imidazole rings of His41(εN) and His114(δN) are ~50° to the FeN<sub>2</sub>S plane.

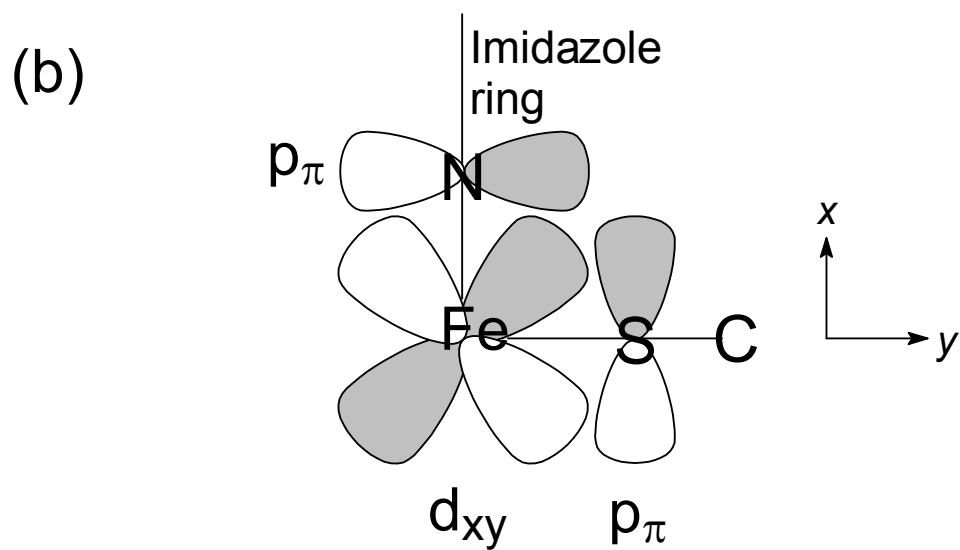
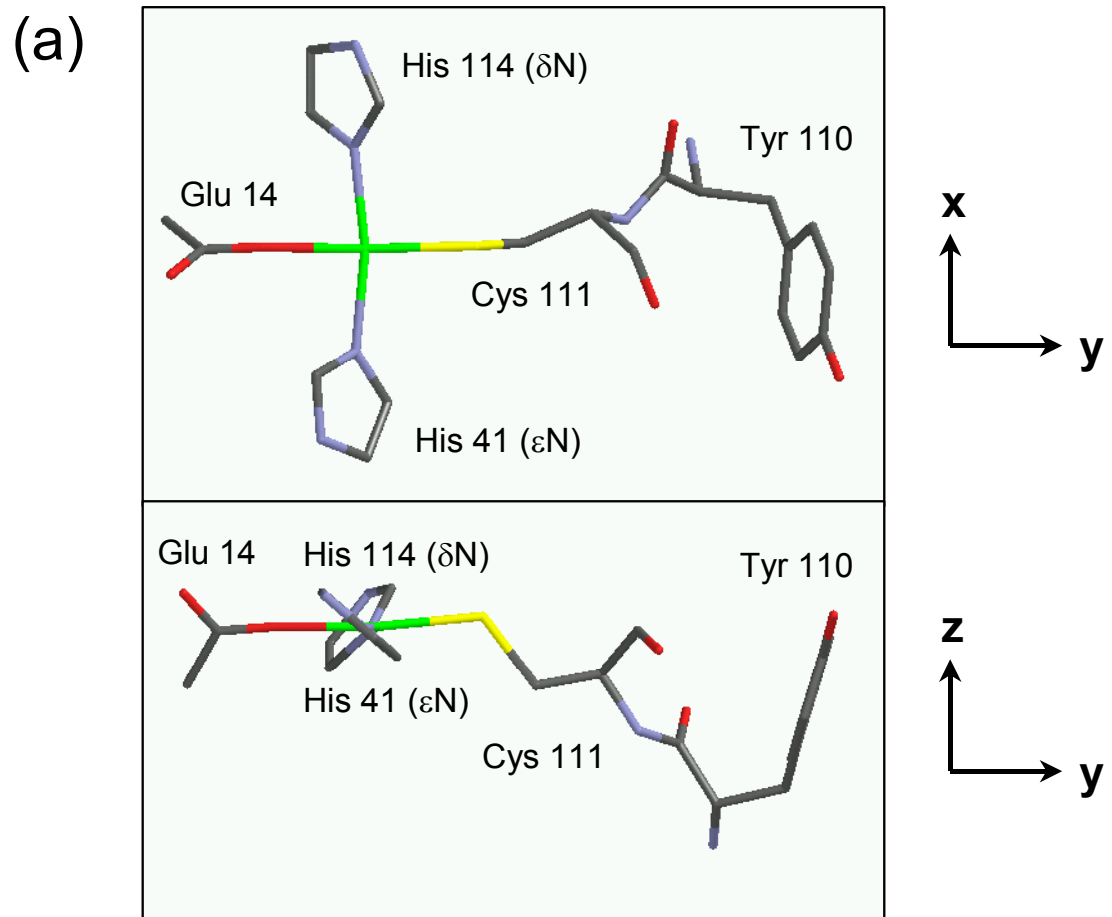


Figure S3.1 Visible absorption spectra of wild-type *P. furiosus* SOR at pH 7.5 and 10.5 and of the E14A variant at pH 7.5.

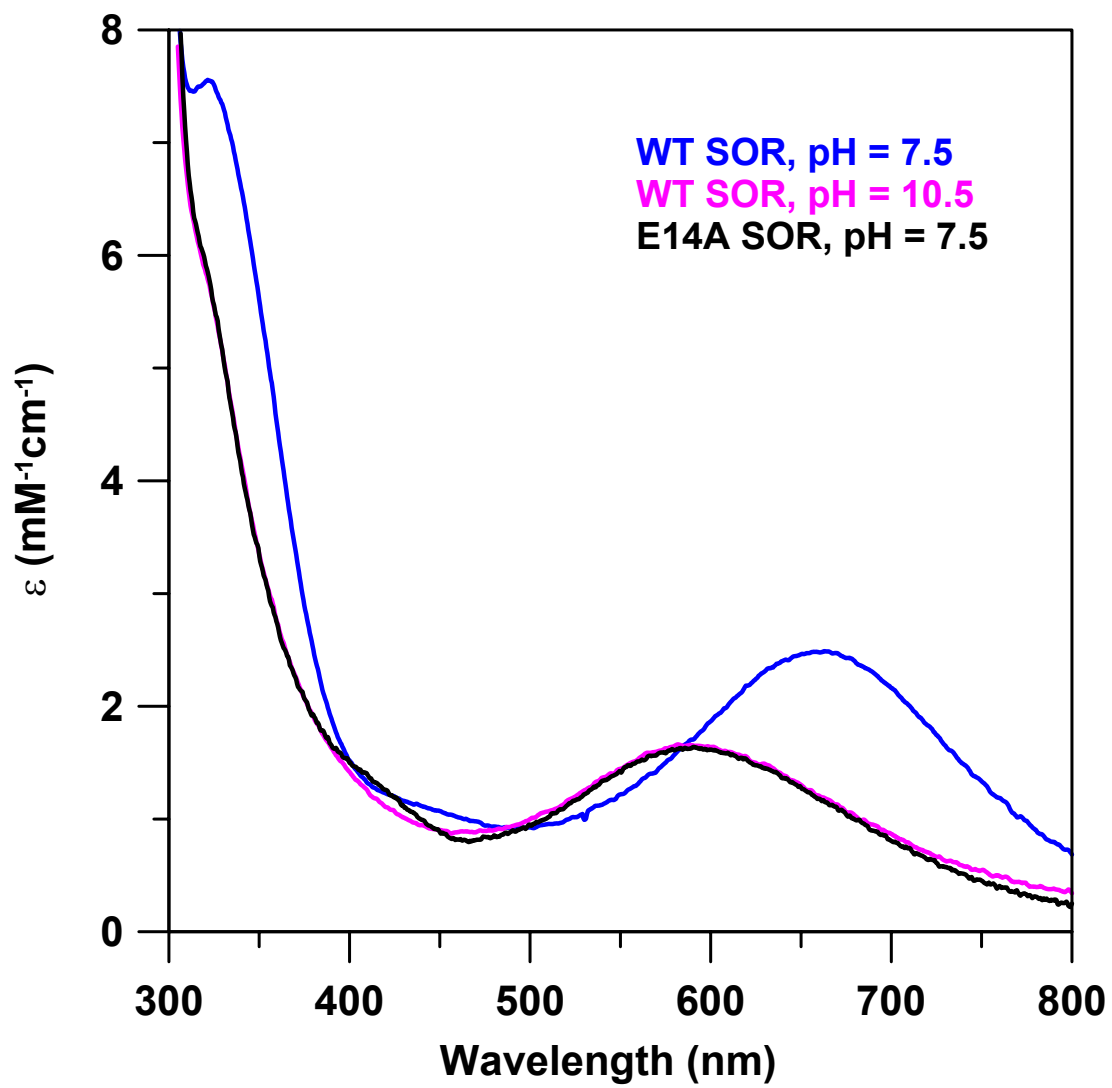


Figure S3.2 Resonance Raman spectra of wild-type *P. furiosus* SOR at pH 7.5 and 10.5 and of the E14A variant at pH 7.5 using 568-nm excitation. Except for the excitation wavelength, the samples and measurement conditions are the same as those described in Figure 3.7 of the manuscript. The asterisk indicates a lattice mode of ice.

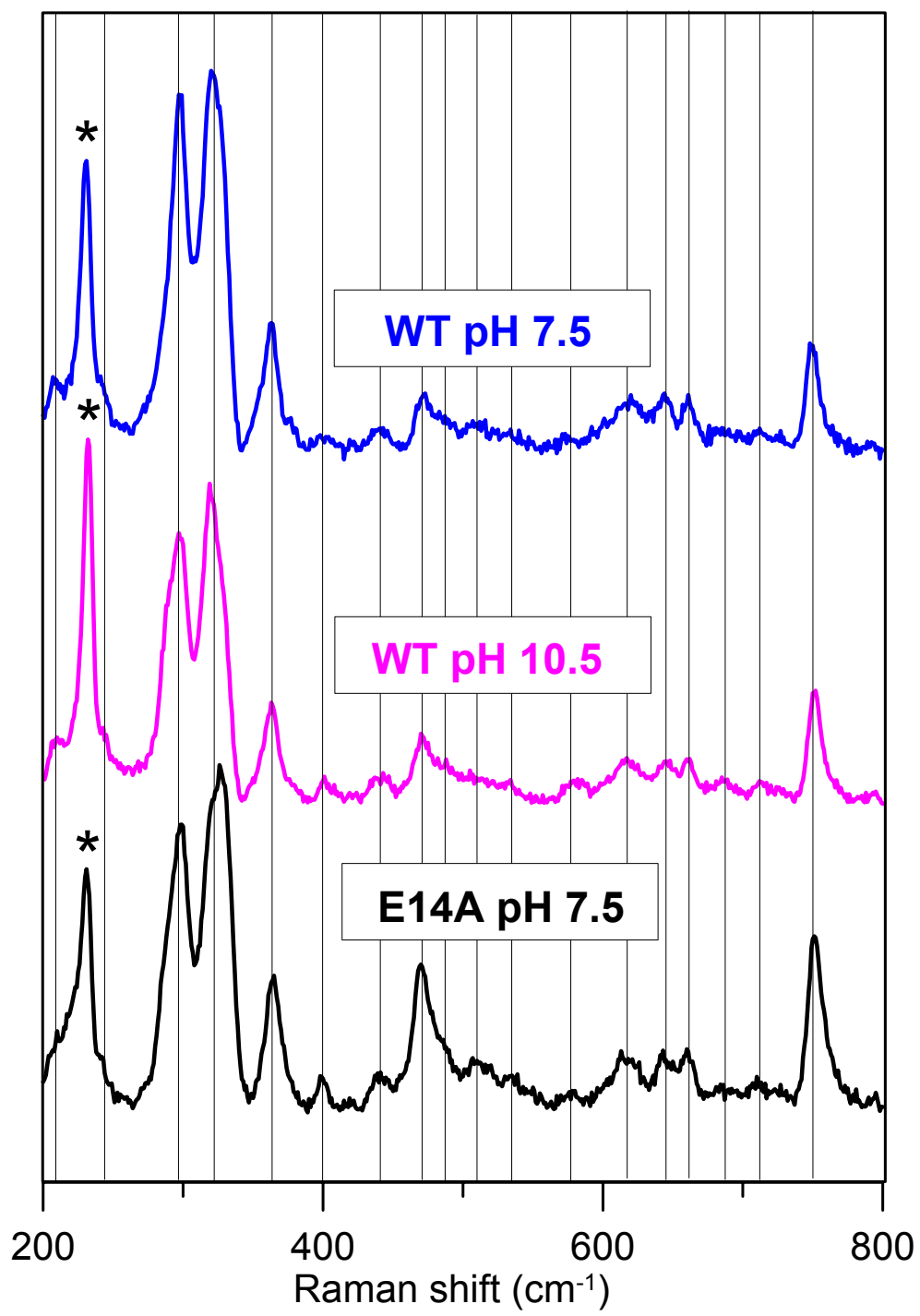


Figure S3.3 Resonance Raman spectra of wild-type *P. furiosus* SOR at pH 7.5 in  $\text{H}_2^{16}\text{O}$  and  $\text{H}_2^{18}\text{O}$  50 mM HEPES buffers using 647-nm excitation. Measurement conditions are given in the legend to Figure 3.2 in the manuscript. Asterisks indicate lattice modes of ice.

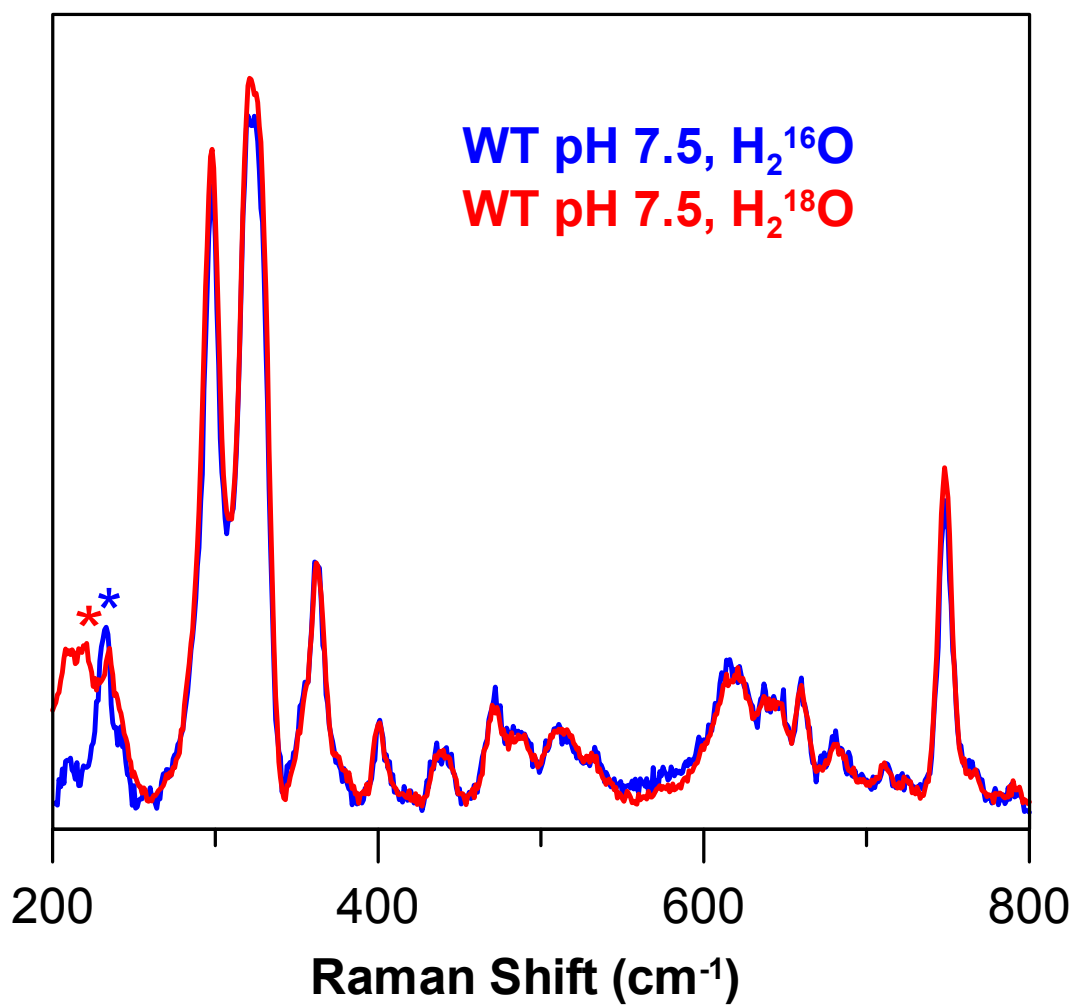


Figure S3.4 Resonance Raman spectra of wild-type *P. furiosus* SOR at pH 10.5 in  $\text{H}_2^{16}\text{O}$  and  $\text{H}_2^{18}\text{O}$  50 mM CAPS buffer with 647-nm excitation. Measurement conditions are given in the legend to Figure 3.2 in the manuscript. Asterisks indicate lattice modes of ice.

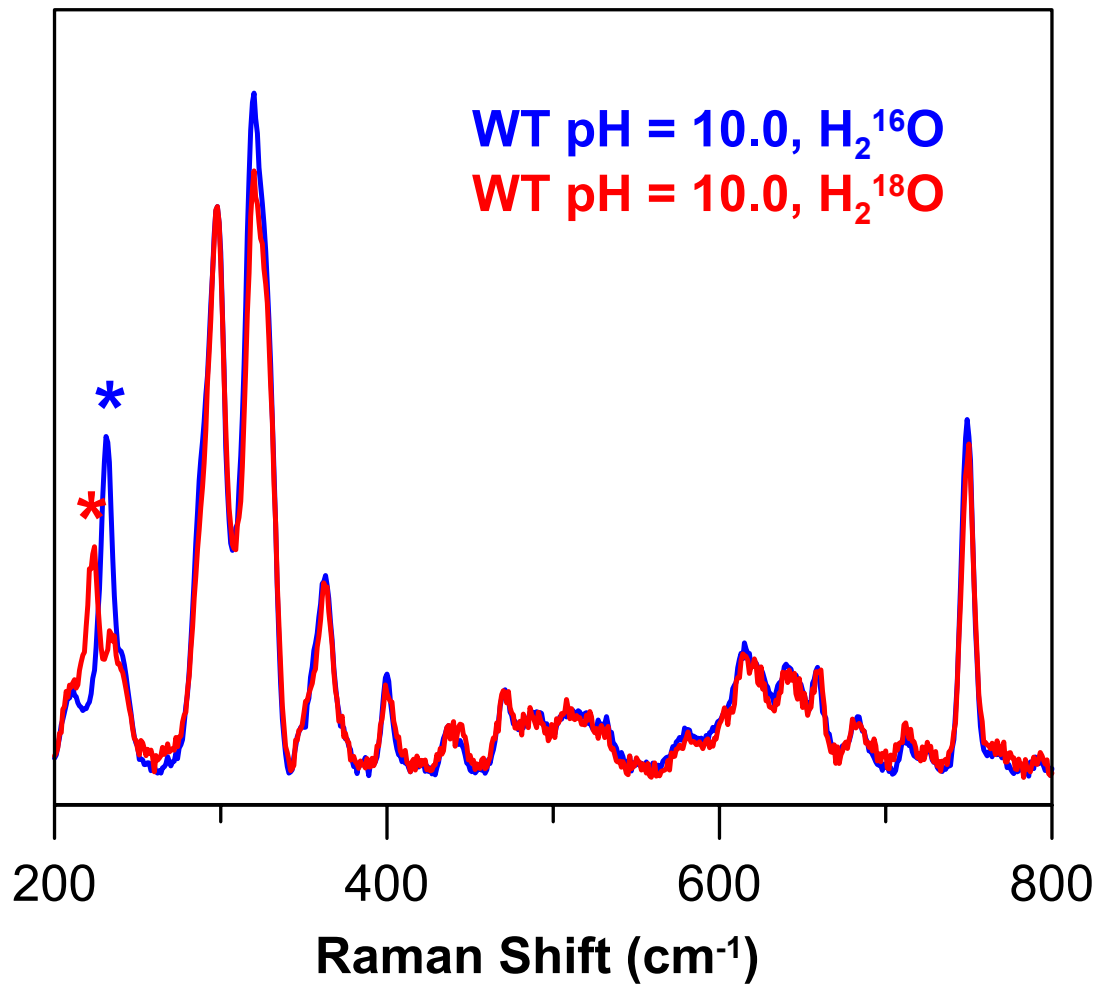


Figure S3.5 Resonance Raman spectra of E14A *P. furiosus* SOR at pH 7.5 in H<sub>2</sub><sup>16</sup>O and H<sub>2</sub><sup>18</sup>O 50 mM HEPES buffers using 647-nm excitation. Measurement conditions are given in the legend to Figure 3.2 in the manuscript. Asterisks indicate lattice modes of ice.

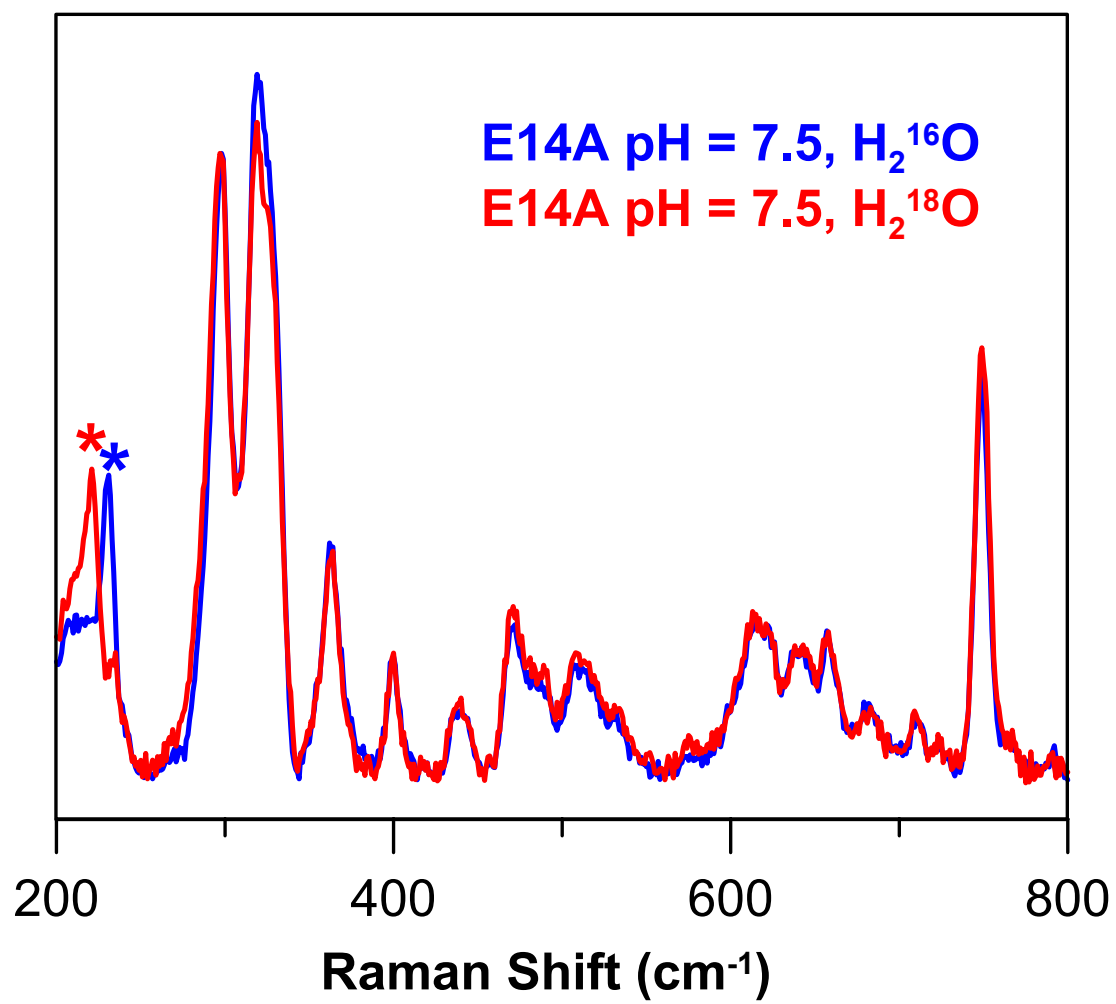
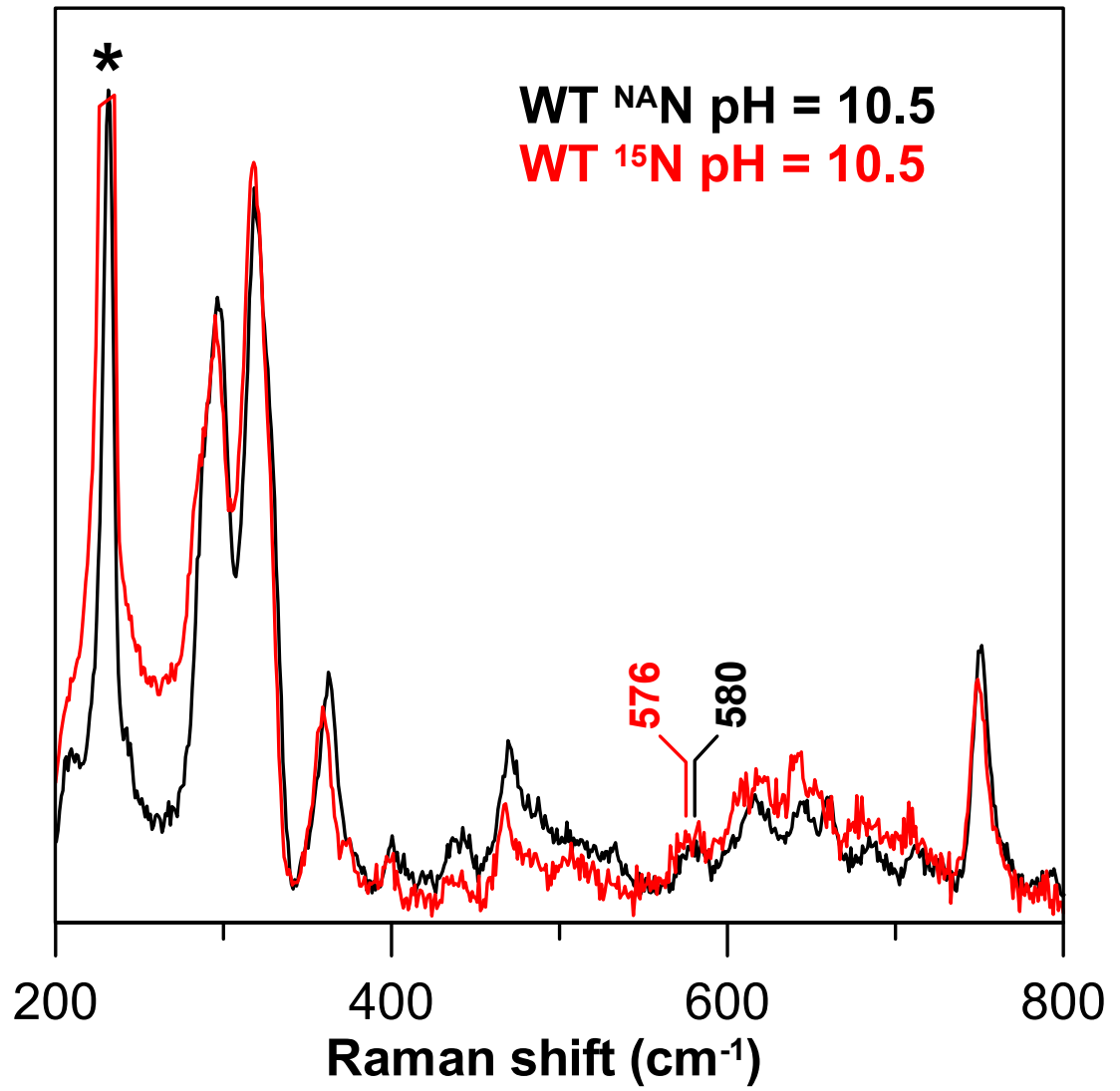


Figure S3.6 Resonance Raman spectra of natural abundance (NA) and  $^{15}\text{N}$  globally labeled wild-type *P. furiosus* SOR at pH 10.5. The samples were in 50 mM CAPS buffer, pH 10.5 and the excitation wavelength was 568 nm. All other sample and measurement conditions are given in the legend to Figure 3.2 in the manuscript. The asterisk indicates a lattice mode of ice.



## CHAPTER 4

# NITRIC OXIDE BINDING AT THE MONONUCLEAR ACTIVE SITE OF REDUCED *PYROCOCCUS FURIOSUS* SUPEROXIDE REDUCTASE: IMPLICATIONS FOR THE STRUCTURAL AND ELECTRONIC DETERMINANTS OF ENZYMATIC SUPEROXIDE REDUCTION 1

---

<sup>†</sup> Clay, Michael D. \*, Christopher A. Coper\*, Francis E. Jenney, Jr.<sup>†</sup>, Michael W. W. Adams<sup>†</sup>, and Michael K. Johnson\* (2002) *Proc. Natl. Acad. Sci. U.S.A.* submitted, Departments of \*Chemistry and <sup>†</sup>Biochemistry & Molecular Biology and the \*<sup>†</sup>Center for Metalloenzyme Studies, University of Georgia, Athens, GA 30602

### **Textual Footnotes**

Abbreviations: SOR, superoxide reductase; VTVH MCD, variable-temperature variable-field magnetic circular dichroism; CT, charge transfer; MAHMA, methylamine hexamethylene methylamine

## Abstract

Nitric oxide has been used as a substrate analog in order to explore the structural and electronic determinants of enzymatic superoxide reduction at the mononuclear iron active site of *Pyrococcus furiosus* superoxide reductase (SOR) through the use of EPR, resonance Raman, FTIR, UV-visible absorption, and variable-temperature variable-field magnetic circular dichroism (VTVH MCD) spectroscopies. The NO adduct of reduced SOR is shown to have a near-axial  $S = 3/2$  ground state with  $E/D = 0.06$  and  $D = 12 \pm 2$   $\text{cm}^{-1}$  and the UV-visible absorption and MCD spectra are dominated by an out-of-plane  $\text{NO}^-(\pi^*)\text{-to-Fe}^{3+}(\text{d}_\pi)$  charge transfer transition, polarized along the zero-field splitting axis. Resonance Raman studies indicate that the NO-adduct is six-coordinate with NO ligated in a bent conformation (Fe–N–O bond angle  $\sim 156^\circ$ ) trans to the cysteinyl S, as evidenced by the identification of  $\nu(\text{N–O})$  at  $1721 \text{ cm}^{-1}$ ,  $\nu(\text{Fe–NO})$  at  $475 \text{ cm}^{-1}$ ,  $\nu(\text{Fe–S}(\text{Cys}))$  at  $291 \text{ cm}^{-1}$ , via  $^{34}\text{S}$  and  $^{15}\text{NO}$  isotope shifts. The electronic and vibrational properties of the  $S = 3/2$   $\{\text{FeNO}\}^7$  unit are rationalized in terms of a limiting formulation involving a high-spin ( $S = 5/2$ )  $\text{Fe}^{3+}$  center antiferromagnetically coupled to a ( $S = 1$ )  $\text{NO}^-$  anion, with a highly covalent  $\text{Fe}^{3+}\text{–NO}^-$  interaction. The results support a catalytic mechanism for SOR with the first step involving reductive binding of superoxide to form a ferric-peroxo intermediate and indicate the important roles that the Fe spin state and the trans cysteinate ligand play in effecting superoxide reduction and peroxide release.

## Introduction

Over the past four years evidence has accumulated for a novel pathway for detoxification of reactive oxygen species that is specific for anaerobic and microaerophilic microorganisms (1-3). The key enzyme in this pathway is superoxide reductase (SOR), which catalyzes the reduction of superoxide to hydrogen peroxide (4), with rubredoxin as the probable physiological electron donor (2, 5). While all SORs have a  $\beta$ -barrel domain containing a unique type of mononuclear Fe center that serves as the site for superoxide reduction (6, 7), some have an additional N-terminal domain that contains an intrinsic, rubredoxin-like, mononuclear Fe site, which is ligated by four cysteines in a distorted tetrahedral arrangement analogous to that found in desulfiredoxin (6). These two classes are conveniently referred to as 1Fe- and 2Fe-SORs, but they are also known by their trivial names, neelaredoxins and desulfoferrodoxins, respectively.

Spectroscopic and crystallographic studies of the 1Fe-SOR from *Pyrococcus furiosus* (7-9) and the 2Fe-SOR from *Desulfovibrio desulfuricans* (6, 10, 11) have shown that the mononuclear iron active site is ligated by four equatorial histidines (3 $\epsilon$ N and 1 $\delta$ N) and one axial cysteinate in a square-pyramidal arrangement. The sixth coordination site appears to be occupied by a monodentate glutamate in the oxidized state, but is vacant or occupied by a weakly coordinated water molecule in the reduced state, thereby providing a site for superoxide binding and reduction. These structural studies, combined with recent mutagenesis and pulse radiolysis kinetic results (12-16), have led to the proposal for the catalytic mechanism shown in Figure 4.1. The key steps involve reductive binding of superoxide to the ferrous form of SOR to yield a ferric-peroxo intermediate, protonation possibly by a conserved lysine residue in the reduced active-site

pocket to yield a ferric-hydroperoxo intermediate, and dissociation of the ferric-hydroperoxo intermediate, via Fe-O bond cleavage coupled with glutamate binding, to yield the H<sub>2</sub>O<sub>2</sub> product. This mechanism is further supported by the recent characterization of a transient ferric-peroxo species in peroxide-treated samples of a variant of *Desulfoarculus baarsii* in which the active site glutamate is replaced by alanine (17).

Characterization of enzymatic intermediates is required both for detailed understanding of the mechanism of SOR and addressing the key questions of how and why the SOR active site preferentially catalyzes reduction rather than dismutation of superoxide. However, these intermediates are short lived and difficult to study experimentally. NO has been extensively used as a substrate analog of molecular oxygen in order to form stable nitrosyl derivatives that provide insight into oxygen transport and activation intermediates in many heme (18-21) and non-heme (22-29) iron enzymes. Hence, we report here the formation and spectroscopic characterization of a stable NO-bound derivative of the reduced 1Fe-SOR from *P. furiosus* using the combination of EPR, UV-visible absorption and variable-temperature, variable-field magnetic circular dichroism (VTVH MCD), resonance Raman and FTIR spectroscopies. The structural and electronic characterization of the NO adduct of SOR facilitate understanding of how the active site is tuned for reductive binding of superoxide and release rather than intraligand cleavage of the peroxide product.

## Materials and Methods

**Biochemical Techniques and Sample Preparation.** Recombinant natural abundance and  $^{34}\text{S}$  globally enriched *P. furiosus* SOR was over-expressed in *Escherichia coli* and purified to homogeneity according to published procedures (8, 9). Unless otherwise indicated, the samples of *P. furiosus* SOR used in this work were in 100 mM HEPES buffer at pH 7.5 and were reduced using 10 mM ascorbate. NO derivatives were prepared under strictly anaerobic conditions by adding an NO generator, methylamine hexamethylene methylamine (MAHMA) NONOate (Cayman Chemical), or by addition of saturated buffered solutions of NO, or by exchanging the headspace above the SOR solution with NO gas.  $^{14}\text{NO}$  gas (> 98%, Aldrich) and  $^{15}\text{NO}$  gas (99%, ICON) were further purified prior to use by bubbling through a concentrated KOH solution to remove  $\text{NO}_2$ . No changes in pH were detected on addition of MAHMA NONOate or exposure to NO gas. All samples were handled in a Vacuum Atmospheres glove box (<1 ppm  $\text{O}_2$ ).

**Spectroscopic Methods.** X-band (~9.6 GHz) EPR spectra were recorded on a Bruker ESP-300E EPR spectrometer with a dual-mode ER-4116 cavity and equipped with an Oxford Instruments ESR-9 flow cryostat (4.2-300 K). Spin quantitations were assessed as previously described (8) and EPR simulations were carried out using the SimFonia software package (Bruker). Resonance Raman spectra were recorded as previously described (9) on samples frozen at 17 K, using a scanning Instruments SA Ramanor U1000 spectrometer fitted with a cooled RCA-31034 photomultiplier tube using lines from a Coherent Sabre 100 10-W Argon Ion laser. FTIR measurements were recorded using a Bio-Rad FTS 575C spectrometer equipped with an MCT detector. Absorption spectra were recorded on Shimadzu UV3101PC spectrophotometer. VTVH MCD

measurements were recorded on samples containing 55% (v/v) glycerol using a Jasco J-715 (180-1000 nm) spectropolarimeter mated to an Oxford Instruments Spectromag 4000 (0-7 T) split-coil superconducting magnet. VTVH MCD saturation magnetization data of the SOR  $S = 3/2$  iron-nitrosyl species were analyzed according to the published procedure (30), using software supplied by Dr. Frank Neese and Professor Edward I. Solomon.

## Results

**EPR.** No X-band EPR signals were observed for ascorbate-reduced samples of *P. furiosus* SOR, but intense resonances corresponding to two overlapping  $S = 3/2$  species were observed in samples exposed to NO gas or the NO generator, MAHMA NONOate. For samples containing NO and SOR in an approximate 1:1 stoichiometry (Figure 4.2), the major component is a rhombic resonance with  $g = 4.34, 3.76, 2.00$  that is readily rationalized in terms of a conventional spin Hamiltonian as originating from the lower  $M_s = \pm 1/2$  doublet of an  $S = 3/2$  ground state with  $E/D = 0.06$  and  $D > 0$  parameters, where  $D$  and  $E$  are the axial and rhombic zero-field splitting parameters, respectively. The minor resonance exhibits a more axial resonance with  $g = 4.07, 4.00, 2.00$  that originates from the lower  $M_s = \pm 1/2$  doublet of an  $S = 3/2$  ground state with  $E/D = 0.01$  and  $D > 0$ . No resonance from the upper  $M_s = \pm 3/2$  doublet was observed over the temperature range 4 - 60 K. Consequently, estimates of the separation between the  $M_s = \pm 1/2$  and  $\pm 3/2$  doublets ( $2D$ ) were obtained by fitting plots of the EPR intensity versus  $1/T$  to a Boltzmann population distribution over a two level system:  $D = 12 \pm 2 \text{ cm}^{-1}$  for the  $E/D = 0.06$  component and  $D = 5 \pm 1 \text{ cm}^{-1}$  for the  $E/D = 0.01$  component. Quantitation versus a CuEDTA standard indicates that the entire resonance corresponds to 20% of the Fe

containing SOR, and simulation of the spectra as the sum of two overlapping resonances, revealed that the  $E/D = 0.06$  and  $0.01$  species account for 84% and 16%, respectively. The substoichiometric spin quantitation is attributed to reversible binding of NO, as both resonances are progressively lost on repeated exchange of NO by Ar in the headspace above stirred solutions. Moreover, redox cycling and exposure to a 3-fold excess of NO did not result in any significant loss of Fe from *P. furiosus* SOR, as judged by quantitative restoration of the oxidized absorption spectrum (8), after ascorbate reduction, NO treatment, and reoxidation with hexachloroiridate.

The origin of the heterogeneity in the ground state properties of the NO adduct of reduced SOR was investigated by EPR studies as a function of pH, exposure to light, and the NO:SOR stoichiometry. The ratio of the  $E/D = 0.01$  and  $0.06$   $S = 3/2$  species was not significantly perturbed by varying the pH over the range 5.5 to 9.0, and both resonances were lost at  $\text{pH} > 9.5$ . In addition, neither resonance exhibited significant photolability, as evidenced by EPR studies at 10 K while irradiating the sample in the cavity with a Xe arc lamp. However, the ratio of the intensities of the  $E/D = 0.01$  and  $0.06$   $S = 3/2$  species was found to be dependent on the stoichiometry of NO to SOR. As the stoichiometry was increased from 0.3 to 3.0, the spin quantitation of the entire  $S = 3/2$  resonance increased from 15% to 30% of the Fe-containing SOR, and the resonance changed from being almost exclusively that of the  $E/D = 0.06$  species to being a 60:40 mixture of the  $E/D = 0.06$  and  $0.01$  species.

Analogous near-axial  $S = 3/2$  EPR signals to those observed for SOR have been observed for the nitrosyl adducts of a wide range of reduced mononuclear non-heme enzymes (22-27) and ferrous nitrosyl inorganic complexes (28, 31, 32). Under

Enemark/Feltham notation (33), these species are conveniently represented as  $\{\text{FeNO}\}^7$ , which treats the iron-nitrosyl as a bracketed unit with a superscript to represent the total number of Fe d and NO  $\pi^*$  electrons. Detailed spectroscopic studies and electronic structure calculations for complexes containing  $S = 3/2$   $\{\text{FeNO}\}^7$  units (31, 32) have shown that the ground and excited state properties are best rationalized in terms of a limiting formulation involving high-spin  $\text{Fe}^{3+}$  ( $S = 5/2$ ) antiferromagnetically coupled to  $\text{NO}^-$  ( $S = 1$ ). The EPR results for the nitrosyl adduct of ferrous SOR, therefore, support reductive binding of NO to yield species with substantial  $\text{Fe}^{3+}\text{-NO}^-$  character.

**Absorption and VTVH MCD.** The room temperature absorption and 4.2 K MCD spectra for the NO adduct of ascorbate-reduced *P. furiosus* SOR are shown in Figure 4.3. The NO-treated samples were prepared by exposing samples containing 55% (v/v) glycerol to an atmosphere of NO for 30 seconds prior to transfer under Ar into sealed cuvettes for the spectroscopic measurements. Parallel EPR studies on identical samples frozen at the same time as MCD samples exhibited EPR spectra very similar to those shown in Figure 4.2, with the total  $S = 3/2$  resonance accounting for 20% of the Fe containing SOR and 90% of this resonance arising from the  $E/D = 0.06$  component.

Ascorbate-reduced SOR is colorless and has no significant absorption or MCD bands in the 14000 – 29000  $\text{cm}^{-1}$  region. On addition of NO, the solution turns a red-brown color and the absorption spectrum is dominated by a well-resolved band centered at 21050  $\text{cm}^{-1}$  (475 nm;  $\epsilon = 530 \text{ M}^{-1} \text{ cm}^{-1}$ ) and a shoulder centered near 28000  $\text{cm}^{-1}$  (357 nm;  $\epsilon \sim 900 \text{ M}^{-1} \text{ cm}^{-1}$ ), see Figure 4.3. Analogous absorption bands have been reported for the  $S = 3/2$  NO adducts of a wide range non-heme proteins and inorganic complexes (22, 28, 31, 34, 35) and have been attributed to charge transfer (CT) transitions associated

with the  $\{\text{FeNO}\}^7$  unit. The 4.2 K MCD spectrum of the NO adduct of ascorbate-reduced *P. furiosus* SOR in the 14000 – 29000  $\text{cm}^{-1}$  region correlates closely with the absorption spectrum and is dominated by a positive MCD  $C$ -term centered at 21050  $\text{cm}^{-1}$  (475 nm) with less pronounced positive  $C$ -terms apparent at 28000  $\text{cm}^{-1}$  (357 nm) and as a shoulder at  $\sim 23,500 \text{ cm}^{-1}$  (425 nm), see Figure 4.3. The negative  $C$ -term centered at 12400  $\text{cm}^{-1}$  that is present in the samples before and after NO treatment, corresponds to the  ${}^5\text{T}_{2g}(\text{d}_{xy}) \rightarrow {}^5\text{E}_g(\text{d}_{x^2-y^2})$  ligand field transition of the square-pyramidal high-spin  $\text{Fe}^{2+}$  center in unreacted reduced SOR. Evidence for unreacted reduced SOR is also apparent by the characteristic pattern of (Cys) $\text{S}^-$ -to- $\text{Fe}^{2+}$  CT bands (8) that are observed in the low temperature MCD spectrum in the 29000-40000  $\text{cm}^{-1}$  region (data not shown). In agreement with EPR spin quantitations, which indicated that only 20% of the reduced SOR is in the NO-bound form, the intensity of (Cys) $\text{S}^-$ -to- $\text{Fe}^{2+}$  CT MCD bands in the NO-treated sample was  $\sim 80\%$  of that observed for samples prior to NO treatment.

Well-resolved absorption bands centered between 20000 and 24000  $\text{cm}^{-1}$  that give rise to positive MCD  $C$ -terms centered at the same energies, are a unifying attribute of the absorption and MCD spectra of all  $S = 3/2$   $\{\text{FeNO}\}^7$  species investigated thus far (28, 31, 34). This transition has been assigned to the out-of-plane  $\text{NO}^-(\pi^*)$ -to- $\text{Fe}^{3+}(\text{d}_\pi)$  CT within the idealized  $\text{Fe}^{3+}$ - $\text{NO}^-$  unit, since these orbitals are predicted to have optimal overlap based on SCF- $X\alpha$ -SW calculations (31). In order to test the validity of the proposed assignment, the transition polarization was assessed via VTVH MCD saturation magnetization studies on the MCD band centered at 21050  $\text{cm}^{-1}$  (475 nm), see supporting information Figure S4.1. The results indicate a uniaxial transition polarized along the unique ( $z$ ) axis of the predominantly axial zero-field splitting. This is in complete accord

with assignment to an out-of-plane  $\text{NO}^-(\pi^*)\text{-to-Fe}^{3+}(\text{d}_\pi)$  CT transition, and the MCD magnetization data indicate that the Fe – NO bond is collinear with the zero-field splitting axis.

**Resonance Raman and FTIR.** In order to assign vibrational bands based on  $^{15}\text{NO}$  isotope shifts, samples for resonance Raman and FTIR studies were prepared by incubating concentrated samples of ascorbate-reduced SOR, 4-5 mM, under an atmosphere of NO gas. Parallel EPR studies of the samples used for resonance Raman and FTIR investigations displayed resonances that were almost exclusively (>95%) from the  $S = 3/2$  species with  $E/D = 0.06$ .

In accord with the assignment of the absorption band at  $21050\text{ cm}^{-1}$  (475 nm) to the out-of-plane  $\text{NO}^-(\pi^*)\text{-to-Fe}^{3+}(\text{d}_\pi)$  CT transition, resonance Raman studies using 476-nm excitation revealed enhancement of vibrational modes associated with the  $\{\text{FeNO}\}^7$  unit, see Figure 4.4. The high frequency intraligand stretching region shows a band that shifts from  $1721\text{ cm}^{-1}$  in the  $^{14}\text{NO}$  adduct to a shoulder at  $1690\text{ cm}^{-1}$  in the  $^{15}\text{NO}$  adduct, in addition to modes at  $1552$ ,  $1616$ , and  $1668\text{ cm}^{-1}$  that show no  $^{15}\text{NO}/^{14}\text{NO}$  shift and are assigned to vibrations of the polypeptide backbone (9). On the basis of the  $31\text{-cm}^{-1}$  isotope shift, the  $1721\text{ cm}^{-1}$  band is assigned to the  $\nu(\text{N-O})$  stretching mode, which is predicted to exhibit a  $31\text{-cm}^{-1}$   $^{14}\text{N}/^{15}\text{N}$  isotope shift based on a simple diatomic oscillator approximation. A band with a  $32\text{-cm}^{-1}$   $^{15}\text{NO}/^{14}\text{NO}$  shift was also observed in the FTIR spectrum at  $1728\text{ cm}^{-1}$ , see supporting information Figure S4.2. The difference in the frequencies of the  $\nu(\text{N-O})$  stretching mode as determined by resonance Raman ( $1721\text{ cm}^{-1}$ ) and FTIR ( $1728\text{ cm}^{-1}$ ) is attributed to the measurement conditions, i.e. frozen solution at 17 K for Raman and aqueous solution at room temperature for FTIR.

The low-frequency metal-ligand stretching region shows one  $^{15}\text{NO}/^{14}\text{NO}$ -sensitive vibration that shifts from  $475\text{ cm}^{-1}$  in the  $^{14}\text{NO}$  adduct to  $468\text{ cm}^{-1}$  in the  $^{15}\text{NO}$  adduct, Figure 4.4. Both  $\nu(\text{Fe}-\text{NO})$  stretching and  $\delta(\text{Fe}-\text{N}-\text{O})$  bending modes are expected in this region and these modes are likely to be extensively mixed. Nevertheless several lines of evidence favor assignment of the band at  $475\text{ cm}^{-1}$  to a mode that predominantly involves  $\nu(\text{Fe}-\text{NO})$  stretching. First, in the absence of a specific enhancement mechanism, bending modes generally exhibit weaker resonance enhancement than stretching modes and hence are weaker in resonance Raman spectra. This general observation is borne out by resonance Raman studies of nitrosyl hemes in which the  $\nu(\text{Fe}-\text{NO})$  stretching and  $\delta(\text{Fe}-\text{N}-\text{O})$  bending modes have been rigorously assigned based on  $^{15}\text{NO}$ ,  $\text{N}^{18}\text{O}$ , and  $^{15}\text{N}^{18}\text{O}$  isotope shifts and normal mode calculations (19-21). The  $\nu(\text{Fe}-\text{NO})$  stretching modes are invariably more strongly enhanced than the  $\delta(\text{Fe}-\text{N}-\text{O})$  bending modes and the enhancement of the bending mode generally decreases as the  $\text{Fe}-\text{N}-\text{O}$  angle approaches  $180^\circ$ . Second, the observed  $^{15}\text{N}$  downshift,  $7\text{ cm}^{-1}$ , is consistent with a bent  $\text{FeNO}$  unit with an angle closer to  $180^\circ$  than  $90^\circ$ . A  $\nu(\text{Fe}-\text{NO})$  stretching mode at  $475\text{ cm}^{-1}$  is predicted to have a  $^{15}\text{N}$  downshift in the range  $5\text{-}13\text{ cm}^{-1}$  based on a simple two-body diatomic oscillator approximation, with the smallest shift predicted for  $\text{Fe}-\text{N}-\text{O}$  bond angles close to  $180^\circ$  and the largest shift predicted for  $\text{Fe}-\text{N}-\text{O}$  bond angles close to  $90^\circ$ . The range of  $^{15}\text{N}$  downshifts for  $\nu(\text{Fe}-\text{NO})$  stretching modes predicted for this simple model is generally in good agreement with experimental data obtained for well characterized nitrosyl hemes, i.e. downshifts as low as  $2\text{ cm}^{-1}$  for linear  $\text{FeNO}$  and as high as  $14\text{ cm}^{-1}$  for bent  $\text{FeNO}$  with an  $\text{Fe}-\text{N}-\text{O}$  angle of  $115^\circ$  (19-21).

In addition to the  $\nu(\text{Fe-NO})$  and  $\nu(\text{N-O})$  stretching modes, vibrational modes associated with the Fe-S(Cys) unit are also weakly enhanced in resonance with the absorption band at  $21050\text{ cm}^{-1}$  (475 nm). A comparison of the resonance Raman spectra obtained for the NO-adducts of natural abundance and  $^{34}\text{S}$  globally labeled SOR using 476 nm excitation revealed two  $^{34}\text{S}$ -sensitive bands, located at  $291\text{ cm}^{-1}$  and  $758\text{ cm}^{-1}$ , that exhibit  $3\text{ cm}^{-1}$  downshifts in the  $^{34}\text{S}$  labeled samples, see Figure 4.5. These two bands are readily assigned to the  $\nu(\text{Fe-S})$  and  $\nu(\text{S-C})$  stretching modes of the Fe-S(Cys) unit, respectively, on the basis of previous assignments for oxidized *P. furiosus* SOR (9). Enhancement of vibrations associated with the (Cys)S-Fe-NO unit was observed with 476 nm excitation, but not with 647 nm excitation (the optimal wavelength for enhancing vibrations of the Fe-S(Cys) unit in oxidized *P. furiosus* SOR (9)), see Figure 4.5. Hence the observed vibrational modes associated with the Fe-S(Cys) unit are not the result of partial oxidation. Rather they are enhanced via kinematic coupling with the  $\nu(\text{Fe-NO})$  stretching mode and/or an excited-state *A*-term mechanism involving the competing  $\pi$  interactions within the trans (Cys)S-Fe-NO unit. Irrespective of the enhancement mechanism, the observation of vibrational modes associated with the Fe-S(Cys) unit demonstrates that cysteinate is ligated trans to NO.

## Discussion

Interaction of ascorbate-reduced *P. furiosus* SOR with NO has been shown to result in the reversible formation of a stable six-coordinate derivative of the mononuclear Fe active site with NO bound trans to the cysteinate ligand. The ground and excited state electronic properties of this NO-adduct, i.e. near-axial  $S = 3/2$  ground state with zero-

field splitting parameters  $E/D = 0.06$  and  $D = 12 \pm 2 \text{ cm}^{-1}$  and visible absorption and low-temperature MCD spectra dominated by a well-resolved band centered at  $21050 \text{ cm}^{-1}$  (475 nm), are characteristic of non-heme iron proteins and inorganic complexes containing  $S = 3/2$   $\{\text{FeNO}\}^7$  units (22, 31, 34). Moreover, on the basis of the detailed spectroscopic and electronic structure calculations that are available for inorganic complexes containing  $S = 3/2$   $\{\text{FeNO}\}^7$  units (31, 32), the ground and excited state properties are best rationalized in terms of a limiting formulation involving a high-spin ( $S = 5/2$ )  $\text{Fe}^{3+}$  center antiferromagnetically coupled to a ( $S = 1$ )  $\text{NO}^-$  anion. The resulting  $\text{Fe}^{3+}\text{-NO}^-$  interaction is highly covalent as a result of strong  $\text{NO}^-$   $\sigma$ - and  $\pi$ -donor bonding to  $\text{Fe}^{3+}$  and the strong  $\pi$  overlap is manifest by the visible absorption band at  $21050 \text{ cm}^{-1}$  which is attributed to the out-of-plane  $\text{NO}^-(\pi^*)\text{-to-Fe}^{3+}(\text{d}_\pi)$  CT transition that is shown to be polarized along the unique ( $z$ ) axis of the predominantly axial zero-field splitting via VTVH MCD studies.

The resonance Raman and FTIR studies of the NO-adduct of reduced SOR reported herein constitute the first vibrational characterization of a  $S = 3/2$   $\{\text{FeNO}\}^7$  unit in a mononuclear non-heme iron enzyme and provide assessment of the structure and bonding within the trans (Cys)S-Fe-NO unit. Using excitation at 476 nm into the out-of-plane  $\text{NO}^-(\pi^*)\text{-to-Fe}^{3+}(\text{d}_\pi)$  CT transition, resonance Raman studies have identified the  $\nu(\text{N-O})$  stretching mode at  $1721 \text{ cm}^{-1}$  and  $\nu(\text{Fe-NO})$  stretching mode at  $475 \text{ cm}^{-1}$ , on the basis of  $^{15}\text{NO}$  downshifts of  $31 \text{ cm}^{-1}$  and  $7 \text{ cm}^{-1}$ , respectively. In accord with the limiting  $\text{Fe}^{3+}\text{-NO}^-$  formulation, the frequency of the intraligand  $\nu(\text{N-O})$  stretching mode is substantially reduced compared to NO gas,  $\nu(\text{N-O})$  at  $1876 \text{ cm}^{-1}$  (36), as a result of electron transfer into the NO  $\pi^*$  orbital. The only other vibrational data for a biological

$\{\text{FeNO}\}^7$  unit comes from resonance Raman studies of the NO-adduct of deoxyhemerythrin using 647-nm excitation. Although the  $\nu(\text{N-O})$  stretching mode was not observed, a band at  $433\text{ cm}^{-1}$  and a weak shoulder at  $421\text{ cm}^{-1}$  were assigned to the  $\nu(\text{Fe-NO})$  and  $\delta(\text{Fe-N-O})$  modes, respectively, of the  $\{\text{FeNO}\}^7$  unit, based on  $6\text{-}7\text{ cm}^{-1}$   $^{15}\text{NO}$  and  $\text{N}^{18}\text{O}$  downshifts (29). The frequencies of the  $\nu(\text{Fe-NO})$  modes dictate a substantially weaker Fe-NO bond in hemerythrin than in SOR, and this is likely to be a consequence of a strong H-bonding interaction between the bent FeNO and the  $\mu$ -hydroxo bridge of the diiron center (29).

Greater insight into the structure of the  $\{\text{FeNO}\}^7$  unit in the NO-adduct of SOR is provided by comparison with the resonance Raman data for the  $S = 3/2$   $\{\text{FeNO}\}^7$  unit in the inorganic complexes,  $\text{Fe}(\text{L})(\text{NO})(\text{N}_3)_2$  (L is  $N,N',N''$ -trimethyl-1,4,7-triazacyclonane) and  $\text{Fe}(\text{EDTA})(\text{NO})$  which have Fe-N-O bond angles of  $156^\circ$  (31, 37). Both complexes exhibit resonance Raman spectra similar to that of the NO adduct of SOR with bands at  $1712$  and  $1776\text{ cm}^{-1}$ , respectively, that were identified as  $\nu(\text{N-O})$  stretching modes based on  $^{15}\text{NO}$  downshifts of  $31\text{-}32\text{ cm}^{-1}$ , and strong bands at  $497$  and  $496\text{ cm}^{-1}$ , respectively, with downshifts of  $6\text{-}8\text{ cm}^{-1}$  (31). However, the bands at  $497$  and  $496\text{ cm}^{-1}$  were assigned to  $\delta(\text{Fe-N-O})$  bending rather than  $\nu(\text{Fe-NO})$  stretching (31) on the basis of IR studies of metal nitrosyl complexes which indicated larger  $^{15}\text{NO}$  isotope shifts for  $\delta(\text{M-N-O})$  modes ( $6\text{-}15\text{ cm}^{-1}$ ) than for  $\nu(\text{M-NO})$  modes ( $1\text{-}6\text{ cm}^{-1}$ ) (38, 39). Subsequent resonance Raman studies of nitrosyl hemes (19-21) have clearly shown that these ranges are only applicable to near-linear MNO units. Moreover, the pattern of isotope shifts observed for the  $497$  and  $496\text{ cm}^{-1}$  bands in these complexes, i.e. larger isotope shift for  $^{15}\text{NO}$  than  $\text{N}^{18}\text{O}$  (31), is a characteristic of the  $\nu(\text{M-NO})$  modes of bent

FeNO units in nitrosyl hemes (20). Taken together with the strong resonance enhancement of these bands, reassignment to modes predominantly involving  $\nu(\text{Fe-NO})$  stretching is clearly warranted.

The structure of the FeNO unit in the six-coordinate nitrosyl adduct of SOR is likely to be very similar to that found in the structurally characterized six-coordinate  $\text{Fe(L)(NO)(N}_3)_2$  complex ( $\text{Fe-N-O}$  angle =  $156^\circ$ ), on the basis of similar frequencies for the  $\nu(\text{N-O})$  and  $\nu(\text{Fe-NO})$  modes. The most significant difference is a weaker Fe-NO bond in SOR, as evidenced by the  $21\text{-cm}^{-1}$  decrease in the frequency of the  $\nu(\text{Fe-NO})$  mode. This is attributed to the mutual trans influence of the cysteinate and  $\text{NO}^-$  ligands which compete for the same set of Fe d-orbitals for both  $\sigma$  and  $\pi$  bonding interactions, see Figure 4.6. The principal bonding interactions within the  $\{\text{FeNO}\}^7$  involve  $\pi$ -donor interactions involving the half-filled  $\pi^*$  orbitals on  $\text{NO}^-$  and the half-filled  $\text{Fe}^{3+}$   $d_{xz}$  and  $d_{yz}$  orbitals and the  $\sigma$ -donor interaction between the filled  $\sigma^*$  orbital on  $\text{NO}^-$  and the half-filled  $\text{Fe}^{3+}$   $d_{z^2}$  orbital (31). For the Fe-S(Cys) fragment, the principal bonding interactions involve  $\pi$ -donor interactions involving the filled S  $p_\pi$  and  $p_{\text{pseudo } \sigma}$  orbitals and the half-filled  $\text{Fe}^{3+}$   $d_{xz}$  and  $d_{yz}$  orbitals and the  $\sigma$ -donor interaction between the filled S  $p_{\text{pseudo } \sigma}$  orbital and the half-filled  $\text{Fe}^{3+}$   $d_{z^2}$  orbital (8). Evidence for the weakening of the Fe-S(Cys) bond in the NO-adduct of SOR relative to the six-coordinate high-spin  $\text{Fe}^{3+}$  site in the oxidized enzyme comes from the  $32\text{-cm}^{-1}$  decrease in the frequency of the vibrational mode that primarily involves Fe-S(Cys) stretching ( $323\text{ cm}^{-1}$  in oxidized native SOR (9) compare to  $291\text{ cm}^{-1}$  in the NO-adduct of SOR). The trans influence of a cysteinate ligand on the Fe-NO bonding interaction is also evident in the resonance Raman studies of six-coordinate nitrosyl hemes containing  $S = 1/2$   $\{\text{FeNO}\}^7$  units. Nitrosyl heme

proteins with cysteinate trans to the bound NO exhibit  $\nu(\text{Fe-NO})$  frequencies 10-20  $\text{cm}^{-1}$  lower than those with histidyl ligation.

The trans influence of NO binding is also manifest in the cleavage of weak proximal Fe-His bond in many ferrous heme proteins, particularly those with regulatory roles involving the sensing of small molecules such as NO (soluble guanylate cyclase),  $\text{O}_2$  (FixL) and CO (CooA) (40). This observation suggests a plausible rationalization for the heterogeneity in the NO-bound forms of SOR that is apparent in EPR studies. While spectroscopic studies indicate that the  $E/D = 0.06$  species is a six-coordinate nitrosyl derivative with NO bound trans to cysteine, it has not yet been possible to characterize the optical and vibrational properties of the  $E/D = 0.01$  species that is progressively formed as the stoichiometry of NO to SOR increases. Attributing the more axial  $E/D = 0.01$  species to a five-coordinate  $\{\text{FeNO}\}^7$  species in which the Fe-S(Cys) bond has been cleaved is in accord with the observed trans influence of NO and the reversible formation of this species. Moreover, similar near axial  $S = 3/2$   $\{\text{FeNO}\}^7$  EPR signals have been observed in several non-heme Fe proteins prior to binding substrate or substrate analogs to form six-coordinate  $S = 3/2$   $\{\text{FeNO}\}^7$  species which exhibit more rhombic resonances (22, 27).

Comparison of the  $\nu(\text{N-O})$  and  $\nu(\text{Fe-NO})$  frequencies for the six coordinate  $S = 3/2$   $\{\text{FeNO}\}^7$  species in the NO-adduct of SOR and the  $\text{Fe(L)(NO)(N}_3)_2$  complex with those of six-coordinate  $S = 1/2$  in heme proteins reveals dramatic differences in the bonding in  $S = 1/2$  and  $3/2$   $\{\text{FeNO}\}^7$  species. Six-coordinate  $S = 1/2$   $\{\text{FeNO}\}^7$  species in heme proteins have much stronger Fe-NO bonds, as evidenced by  $\nu(\text{Fe-NO})$  frequencies in the range 536-558  $\text{cm}^{-1}$  (20, 21, 41) and much weaker N-O bonds, as evidenced by

$\nu(\text{N-O})$  frequencies in the range 1555-1624  $\text{cm}^{-1}$  (20, 21). Although no clear consensus has emerged concerning the most appropriate description of the electronic structure and bonding in  $S = 1/2$   $\{\text{FeNO}\}^7$  species (18, 32, 42), the increase in Fe-NO bond strength and concomitant decrease in the N-O bond strength, compared to  $S = 3/2$   $\{\text{FeNO}\}^7$  species, appear to be a direct consequence of increased  $\sigma$ -donation into the empty  $d_{z^2}$  orbital that results from lowering the Fe spin state from high-spin to low-spin or intermediate-spin.

Finally, we address the implications of the spectroscopic characterization of the NO-adduct of SOR for understanding how the mononuclear Fe active site of SOR is tuned for superoxide reduction. Clearly, reductive binding of NO at the vacant coordination site of the ferrous active site is consistent with an inner sphere mechanism for superoxide reduction, with the first step involving reductive binding of superoxide to yield a ferric-peroxo intermediate. Moreover, the reductive binding of  $\pi$ -bonded diatomics is enhanced by the electron donating ability of the trans cysteinate ligand. Absorption and VTVH MCD studies of the square-pyramidal ferrous active site have shown intense (Cys) $\text{S}^-$ -to- $\text{Fe}^{2+}$  CT bands (8), indicative of strong  $p_{\pi}$ - $d_{\pi}$  S-Fe bonding. The resulting increased electron density in the Fe  $d_{\pi}$  orbitals therefore facilitates ligand reduction via Fe  $d_{\pi}$  to ligand  $\pi^*$  electron transfer. The  $S = 3/2$   $\{\text{FeNO}\}^7$  species in SOR is proposed as a stable analog of the  $S = 5/2$   $\{\text{FeOO}\}^9$  high-spin ferric (hydro)peroxo intermediate, albeit with one rather than two electrons in each of the  $\pi^*$  orbitals, see Figure 4.6. Filled  $\pi^*$  orbitals, coupled with the trans influence of the cysteinate, would be expected to weaken the Fe-OO(H) bond relative to the Fe-NO bond as a result of decreased  $\pi^*$ - $d_{\pi}$  bonding. This accounts for the instability of the ferric-(hydro)peroxo

intermediate with respect to cleavage of the Fe–OO(H) bond. On the basis of the differences in the bonding that are apparent from the vibrational studies of  $S = 1/2$  and  $S = 3/2$  {FeNO}<sup>7</sup>, a high-spin ferric-(hydro)peroxo intermediate is likely to be essential in order to promote breakdown via Fe–O rather O–O bond cleavage. This is in accord with recent studies by the Solomon and Que groups which have shown that high-spin Fe<sup>3+</sup>-(alkyl)peroxo have much weaker Fe–O bonds and much stronger O–O bonds than their low-spin counterparts (43, 44). Overall, characterization of the NO-adduct of SOR indicates that the Fe spin state and the trans cysteinate ligand play important roles in effecting superoxide reduction and peroxide release at the SOR active site. By providing a stable analog of the ferric-(hydro)peroxo intermediate, the NO-adduct of SOR is likely to be very useful for probing H-bonding interactions in the active-site pocket.

### **Acknowledgments**

This work was supported by a grant from the National Institute of Health (GM60326 to M.W.W.A. and M.K.J.) and a National Science Foundation Research Training Group Award to the Center for Metalloenzyme Studies (DBI9413236)

## References

1. Liochev, S. I. & Fridovich, I. (1997) *J. Biol. Chem.* **272**, 25573-25575.
2. Jenney, F. E., Verhagen, M. F. J. M., Cui, X. & Adams, M. W. W. (1999) *Science* **286**, 306-309.
3. Lombard, M., Fontecave, M., Touati, D. & Nivière, V. (2000) *J. Biol. Chem.* **275**, 115-121.
4. Adams, M. W. W., Jenney, Jr. F. E., Clay, M. D. & Johnson, M. K. (2002) *J. Biol. Inorg. Chem.* **7**, 647-652.
5. Coulter, E. D. & Kurtz, D. M., Jr. (2001) *Arch. Biochem. Biophys.* **394**, 76-86.
6. Coelho, A. V., Matias, P., Fülöp, V., Thompson, A., Gonzalez, A. & Carrondo, M. A. (1997) *J. Biol. Inorg. Chem.* **2**, 680-689.
7. Yeh, A. P., Hu, Y., Jenney, F. E., Adams, M. W. W. & Rees, D. C. (2000) *Biochemistry* **39**, 2499-2508.
8. Clay, M. D., Jenney, F. E. Jr., Hagedoorn, P. L., George, G. N., Adams, M. W. W. & Johnson, M. K. (2002) *J. Am. Chem. Soc.* **124**, 788-805.
9. Clay, M. D., Jenney, Jr. F. E., Noh, H. J., Hagedoorn, P. L., Adams, M. W. W. & Johnson, M. K. (2002) *Biochemistry* **41**, 9833-9841.
10. Tavares, P., Ravi, N., Moura, J. J. G., LeGall, J., Huang, Y.-H., Crouse, B. R., Johnson, M. K., Huynh, B. H. & Moura, I. (1994) *J. Biol. Chem.* **269**, 10504-10510.
11. Moura, I., Tavares, P., Moura, J. J. G., Ravi, N., Huynh, B. H., Liu, M.-Y. & LeGall, J. (1990) *J. Biol. Chem.* **265**, 21596-21602.
12. Coulter, E. D., Emerson, J. P., Kurtz, D. M., Jr. & Cabelli, D. E. (2000) *J. Am. Chem. Soc.* **122**, 11555-11556.

13. Nivière, V., Lombard, M., Fontecave, M. & Houée-Levin, C. (2001) *FEBS Lett.* **497**, 171-173.
14. Emerson, J. P., Coulter, E. D., Cabelli, D. E., Phillips, R. S. & Kurtz, Jr. D. M. (2002) *Biochemistry* **41**, 4348-4357.
15. Lombard, M., Houée-Levin, C., Touati, D., Fontecave, M. & Nivière, V. (2001) *Biochemistry* **40**, 5032-5040.
16. Abreu, I. A., Saraiva, L. M., Soares, C. M., Teixeira, M. & Cabelli, D. E. (2001) *J. Biol. Chem.* **276**, 38995-39001.
17. Mathé, C., Mattioli, T. A., Horner, O., Lombard, M., Latour, J.-M., Fontecave, M. & Nivière, V. (2002) *J. Am. Chem. Soc.* **124**, 4966-4967.
18. Scheidt, W. R. & Ellison, M. K. (1999) *Acc. Chem. Res.* **32**, 350-359.
19. Hu, S. & Kincaid, J. R. (1991) *J. Am. Chem. Soc.* **113**, 2843-2850.
20. Hu, S. & Kincaid, J. R. (1991) *J. Am. Chem. Soc.* **113**, 9760-9766.
21. Tomita, T., Hirota, S., Ogura, T., Olson, J. S. & Kitagawa, T. (1999) *J. Phys. Chem. B* **103**, 7044-7054.
22. Chen, V. J., Orville, A. M., Harpel, M. R., Frolik, C. A., Surerus, K. K., Münck, E. & Lipscomb, J. D. (1989) *J. Biol. Chem.* **264**, 21677-21681.
23. Nelson, M. J. (1987) *J. Biol. Chem.* **262**, 12137-12142.
24. Salerno, J. C. & Siedow, J. N. (1979) *Biochim. Biophys. Acta* **579**, 246-251.
25. Twilfer, H., Bernhardt, F.-H. & Gersonde, K. (1985) *Eur. J. Biochem.* **147**, 171-176.
26. Arciero, D. M. & Lipscomb, J. D. (1986) *J. Biol. Chem.* **261**, 2170-2178.

27. Arciero, D. M., Orville, A. M. & Lipscomb, J. D. (1985) *J. Biol. Chem.* **260**, 14035-14044.
28. Zhang, Y., Pavlosky, M. A., Brown, C. A., Westre, T. E., Hedman, B., Hodgson, K. O. & Solomon, E. I. (1992) *J. Am. Chem. Soc.* **114**, 9189-9191.
29. Nocek, J. M., Kurtz, D. M., Jr., Sage, J. T., Xia, Y.-M., Debrunner, P., Shiemke, A. K., Sanders-Loehr, J. & Loehr, T. M. (1988) *Biochemistry* **27**, 1014-1024.
30. Neese, F. & Solomon, E. I. (1999) *Inorg. Chem.* **38**, 1847-1865.
31. Brown, C. A., Pavlosky, M. A., Westre, T. E., Zhang, Y., Hedman, B., Hodgson, K. O. & Solomon, E. I. (1995) *J. Am. Chem. Soc.* **117**, 715-732.
32. Hauser, C., Glaser, T., Bill, E., Weyhermüller, T. & Wieghardt, K. (2000) *J. Am. Chem. Soc.* **122**, 4352-4365.
33. Enemark, J. H. & Feltham, R. D. (1974) *Coord. Chem. Rev.* **13**, 339-406.
34. Farrar, J. A., Grinter, R., Pountney, D. L. & Thomson, A. J. (1993) *J. Chem. Soc. Dalton Trans.* **18**, 2703-2709.
35. Wanat, A., Schnepf, T., Stochel, G., van Eldik, R., Bill, E. & Wieghardt, K. (2002) *Inorg. Chem.* **41**, 1-10.
36. Nakamoto, K. (1997) *Infrared and Raman Spectra of Inorganic and Coordination Compounds* (Wiley, New York).
37. Westre, T. E., Di Cicco, A., Filipponi, A., Natoli, C. R., Hedman, B., Solomon, E. I. & Hodgson, K. O. (1994) *J. Am. Chem. Soc.* **116**, 6757-6768.
38. Miki, E., Mizumacji, K., Ishimoro, T. & Okuno, H. (1973) *Bull. Chem. Soc. Jpn.* **46**, 3779-3784.
39. Quinby-Hunt, M. & Feltham, R. D. (1978) *Inorg. Chem.* **17**, 2515-2520.

40. Schelvis, J. P. M., Seibold, S. A., Cerda, J. F., Garavito, R. M. & Babcock, G. T. (2000) *J. Phys. Chem. B* **104**, 10844-10850.
41. Reynolds, M. F., Parks, R. B., Burstyn, J. N., Shelver, D., Thorsteinsson, M. V., Kerby, R. L., Roberts, G. P., Vogel, K. M. & Spiro, T. G. (2000) *Biochemistry* **39**, 388-396.
42. Li, M., Bonnet, D., Bill, E., Neese, F., Weyhermüller, T., Blum, N., Sellmann, D. & Wiegardt, K. (2002) *Inorg. Chem.* **41**, 3444-3456.
43. Lehnert, N., Ho, R. Y. N., Que, L. & Solomon, E. I. (2001) *J. Am. Chem. Soc.* **123**, 12802-12816.
44. Lehnert, N., Ho, R. Y. N., Que, L. & Solomon, E. I. (2001) *J. Am. Chem. Soc.* **123**, 8271-8290.

Figure 4.1 Proposed catalytic mechanism of SOR.

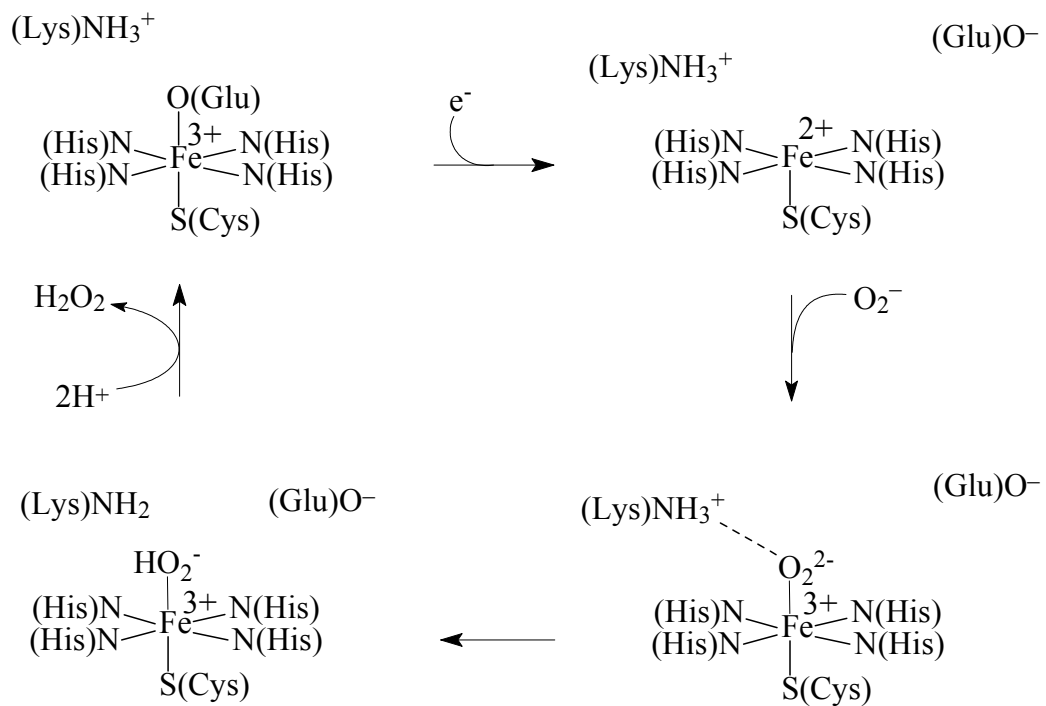


Figure 4.2 X-band EPR spectrum of the NO adduct of ascorbate-reduced *P. furiosus* SOR. Upper panel: experimental spectrum. Lower panel: simulated spectrum corresponding to 84% of a resonance with  $g_{1,2,3} = 4.343, 3.763, 1.997$  and linewidths  $l_{1,2,3} = 2.4, 4.3, 2.0$  mT, and 16% of a resonance with  $g_{1,2,3} = 4.070, 3.999, 2.000$  and line widths  $l_{1,2,3} = 3.0, 3.5, 2.0$  mT. The sample was 0.40 mM in SOR and was prepared by addition of 0.2 mM MAHMA NONOate and incubating at room temperature for 6 mins. The EPR spectrum was recorded at 9.60 GHz, using a modulation amplitude of 0.63 mT, a microwave power of 20 mW, and a temperature of 6.0 K.

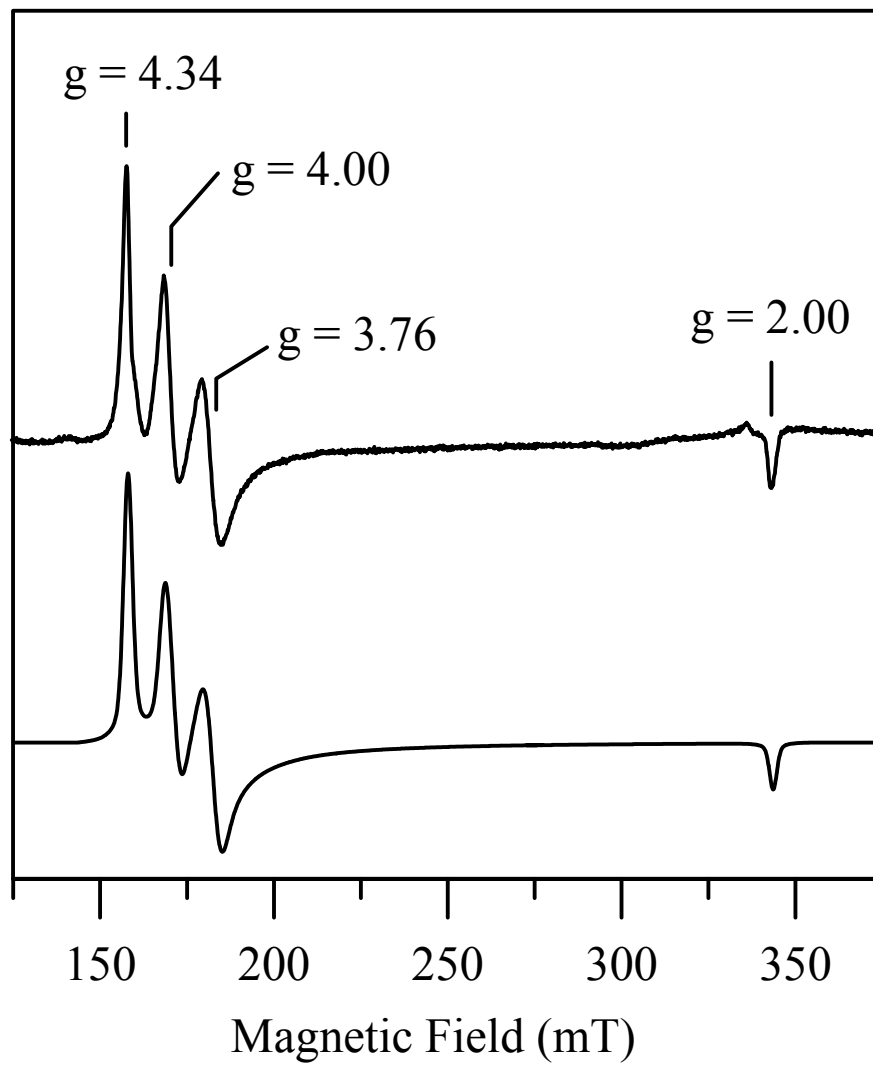


Figure 4.3 UV-visible absorption and MCD spectra of the NO adduct of ascorbate-reduced *P. furiosus* SOR. Upper panel: room-temperature absorption spectra in a 1-mm path length cell. Lower panel: MCD spectra recorded in a 1-mm path length cell at 4.22 K with an applied magnetic field of 6 T. The sample was 0.9 mM in SOR and the buffering medium was in 50 mM HEPES (pH 7.5) with 55% (v/v) glycerol and the spectra shown are before (broken line) and after (solid line) exposure to NO gas.

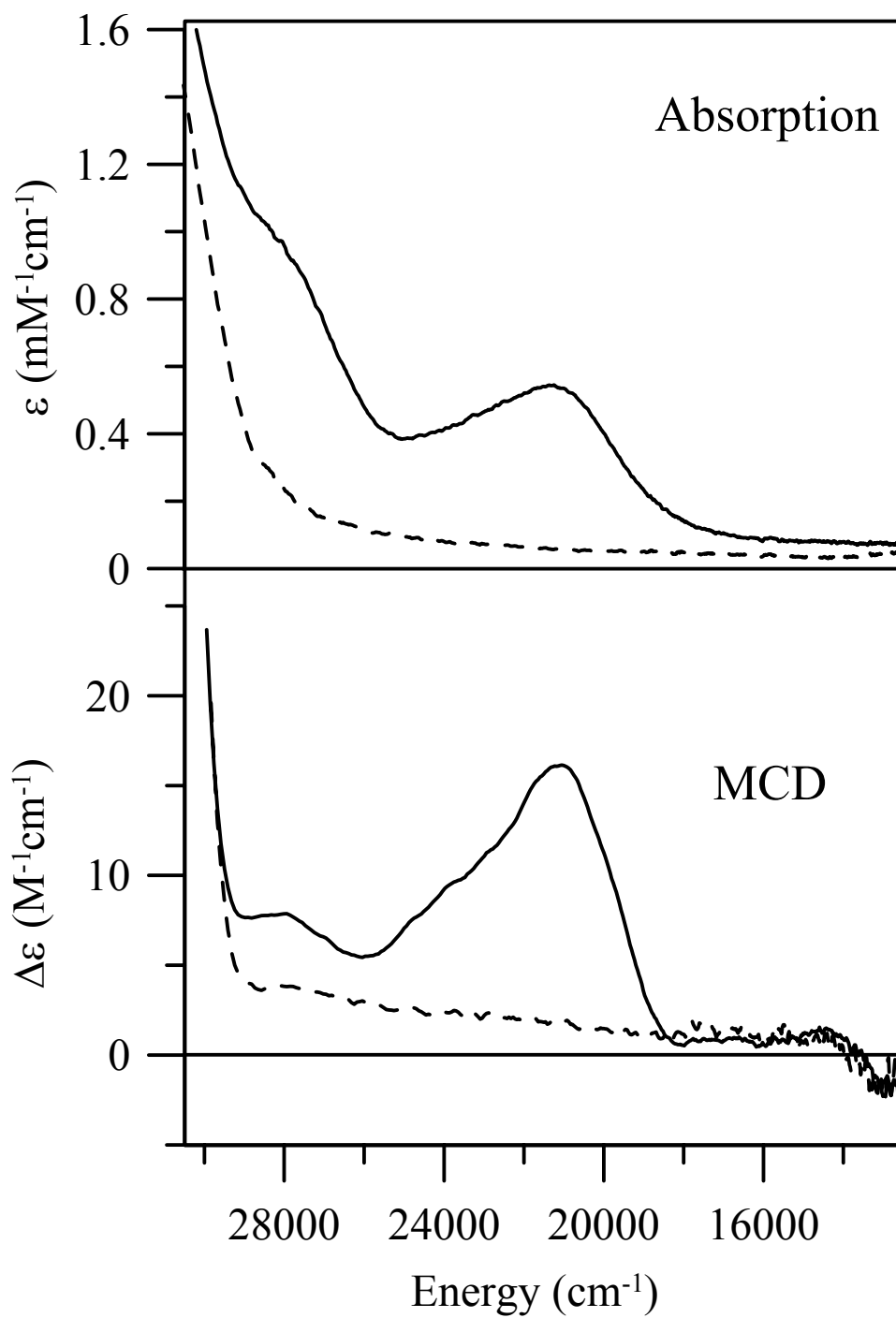


Figure 4.4 Resonance Raman spectra of the  $^{14}\text{NO}$  and  $^{15}\text{NO}$  adducts of ascorbate-reduced *P. furiosus* SOR in the N-O and Fe-N stretching regions. The samples were  $\sim 4$  mM in SOR and were prepared by reduction with 10 mM ascorbate followed by incubation under an atmosphere of NO gas for 15 s, before being transferred to the sample cell under Ar and rapidly frozen. Each panel shows the  $^{14}\text{NO}$  spectrum (upper), the  $^{15}\text{NO}$  spectrum (middle) and the  $^{15}\text{NO}$  minus  $^{14}\text{NO}$  difference spectrum (lower). The spectra were obtained for samples maintained at 17 K using 476-nm excitation. Each spectrum was recorded using  $6\text{ cm}^{-1}$  resolution by photon counting for 1 s every  $1\text{ cm}^{-1}$ , and is the sum of 50 – 60 scans.

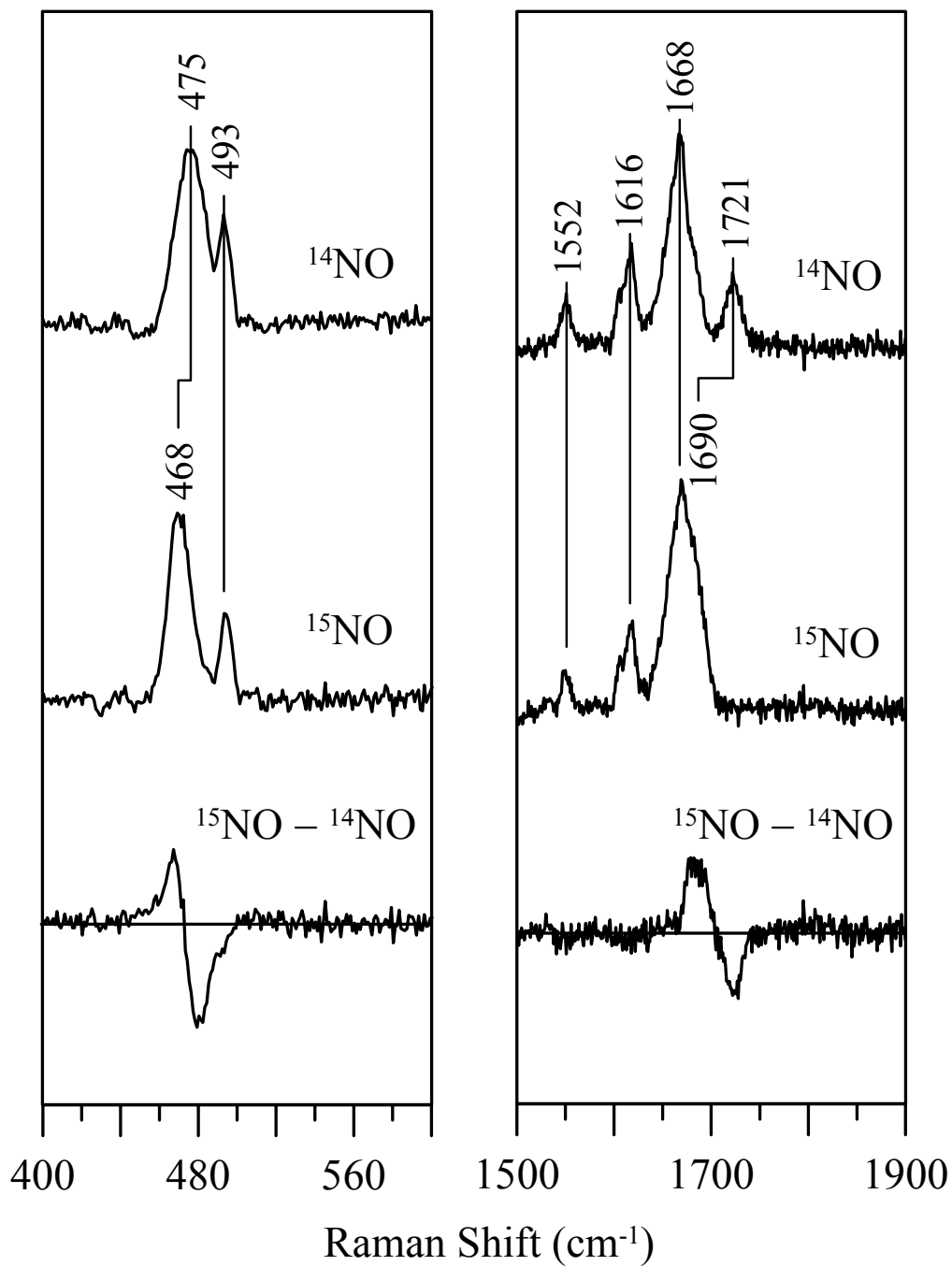


Figure 4.5 Resonance Raman spectra of NO adduct of natural abundance (NA) and  $^{34}\text{S}$  globally labeled ascorbate-reduced *P. furiosus* SOR in the low frequency region. (A) NO adduct of natural abundance SOR using 476-nm excitation, (B) NO adduct  $^{34}\text{S}$  globally labeled SOR using 476-nm excitation, and (C) NO adduct of natural abundance SOR using 647-nm excitation. The sample preparation and measurement conditions are the same as those described in Figure 4.4, except for 647-nm excitation for spectrum (C). The asterisks indicate lattice modes of ice.

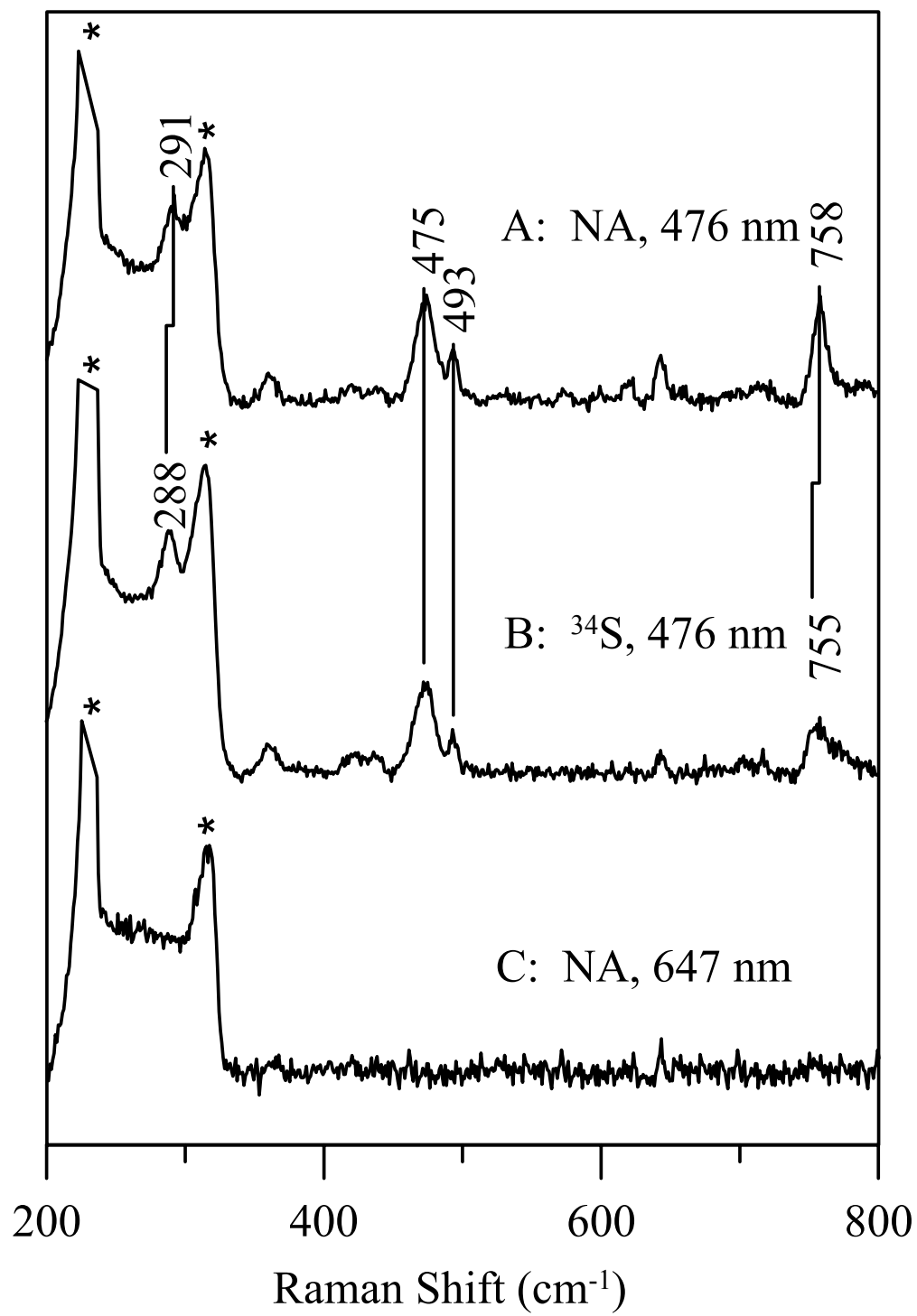


Figure 4.6 Schematic depiction of the principal in-plane (upper) and out-of-plane (lower) bonding interactions for trans (Cys)S–Fe–NO with a  $S = 3/2$  {FeNO}<sup>7</sup> unit.

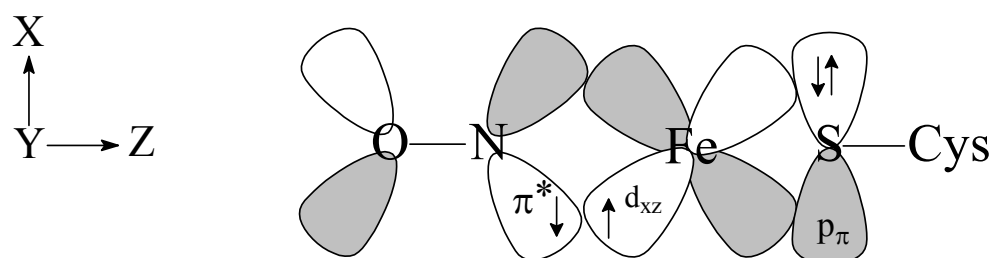
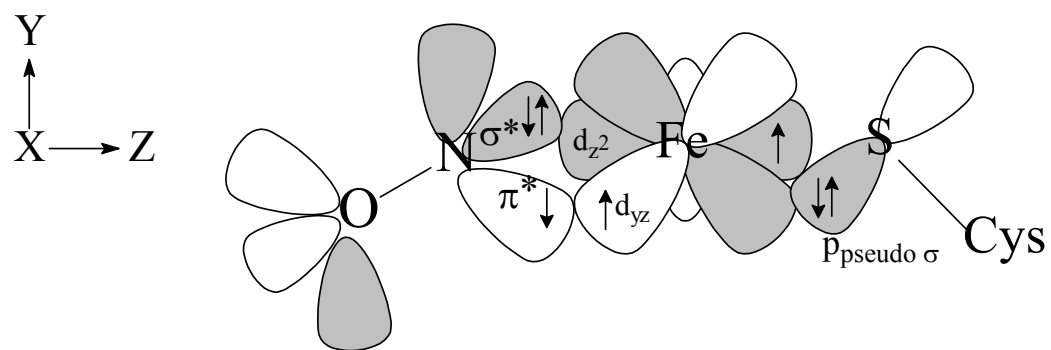


Figure S4.1 VTVH MCD saturation magnetization data for the NO adduct of *P. furiosus* SOR at 21050 cm<sup>-1</sup> (475 nm). The sample is as described in Figure 4.3 and the data were collected at fixed temperatures of 1.71, 4.22, and 10.1 K for magnetic fields in the range of 0 – 6 T. The experimental data points are represented by + symbols and the solid lines are best fits obtained using the methodology developed by Neese and Solomon (Neese, F. & Solomon, E. I. (1999) *Inorg. Chem.* **38**, 1847-1865) for a  $S = 3/2$  ground state with the EPR-determined zero-field splitting parameters ( $E/D = 0.06$  and  $D = 12$  cm<sup>-1</sup>) and treating the effective  $xy$ ,  $xz$ , and  $yz$  transition dipole moments,  $M_{xy}$ ,  $M_{xz}$ , and  $M_{yz}$ , respectively, as variable parameters. On the basis of the values of  $M_{xy}$ ,  $M_{xz}$ , and  $M_{yz}$ , the uniaxial polarizations at 21050 cm<sup>-1</sup> (475 nm) are estimated to be 99.0%  $z$ , 0.5%  $x$ , and 0.5%  $y$ .

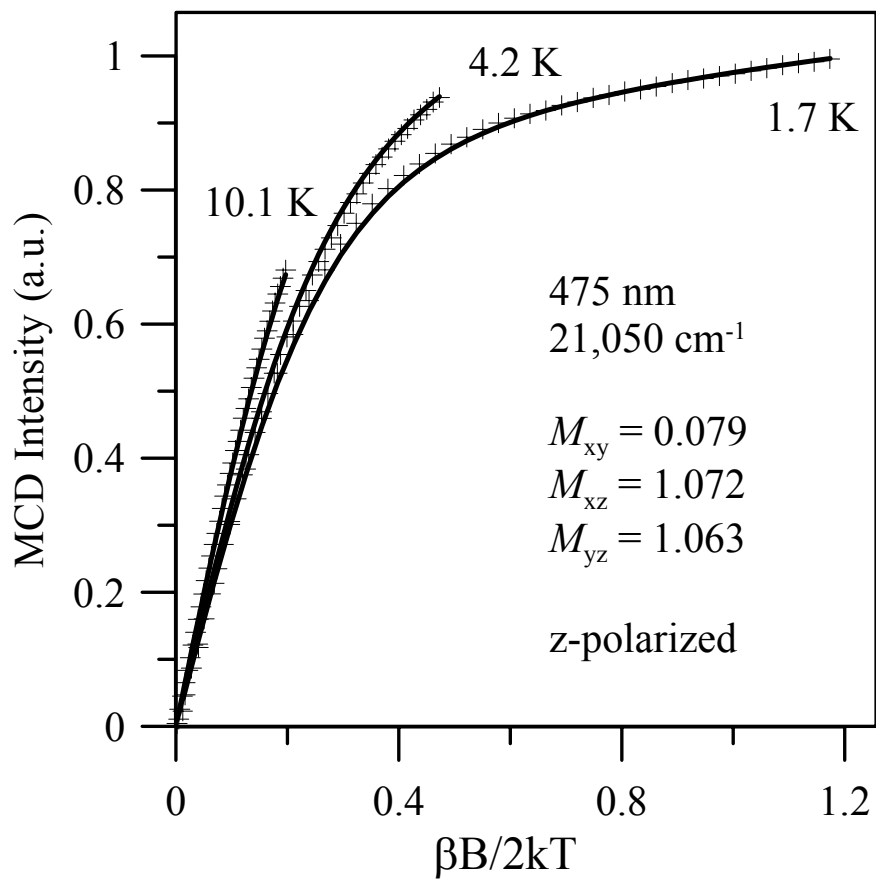
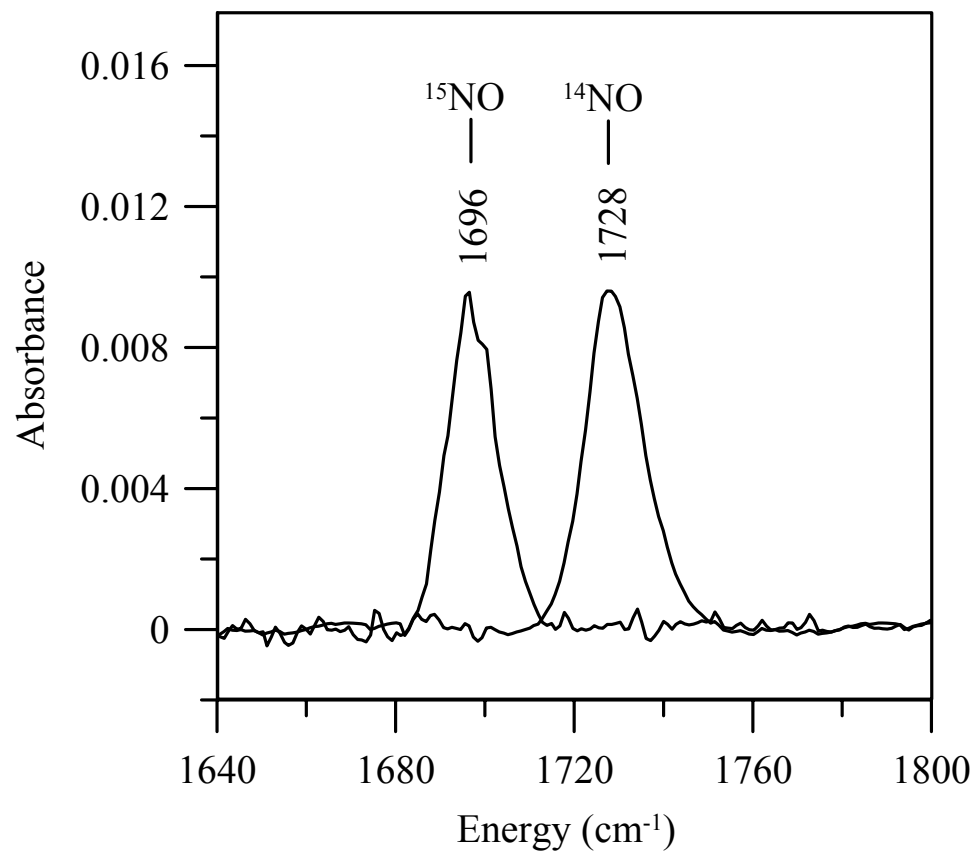


Figure S4.2 FTIR spectra of the  $^{14}\text{NO}$  and  $^{15}\text{NO}$  adducts of ascorbate-reduced *P. furiosus* SOR in the N-O stretching region. The sample was  $\sim 5$  mM in SOR and the buffer was 100 mM HEPES  $\text{D}_2\text{O}$  buffer, pH 7.5. The sample was prepared by reduction with 10 mM ascorbate and incubation under an atmosphere of NO gas for 15 s, before being transferred to the sample cell under Ar. The spectra were collected in the mid-IR region ( $4000 - 400 \text{ cm}^{-1}$ ) at room temperature and  $2\text{-cm}^{-1}$  resolution, using a Spectra-Tech  $\text{CaF}_2$  sample cell with a  $50 \mu\text{m}$  Teflon spacer, and each is the average of 256 scans. The spectrum of an identical sample of ascorbate-reduced SOR that was not treated with NO gas has been subtracted from both spectra.



**CHAPTER 5**

**SPECTROSCOPIC CHARACTERIZATION OF THE 2FE-  
SUPEROXIDE REDUCTASE FROM *DESULFOVIBRIO VULGARIS***

---

<sup>1</sup> Clay, Michael D., Joseph P. Emerson, Eric D. Coulter, Donald M. Kurtz Jr., and Michael K. Johnson (2002) manuscript in preparation for *J. Biol. Inorg. Chem.*, Department of Chemistry and the Center for Metalloenzyme Studies, University of Georgia, Athens, GA 30602

## **Textual Footnotes**

**Keywords** Desulfoferrodoxin · Neelaredoxin · Superoxide reductase · EPR · Resonance Raman · Magnetic Circular Dichroism

**Abbreviations** *Dfx*: desulfoferrodoxin · *SOR*: superoxide reductase · *VTMCD*: variable-temperature magnetic circular dichroism

## Abstract

The electronic and vibrational properties of the mononuclear Fe site responsible for superoxide reduction (Center II) in the 2Fe-SOR from *Desulfovibrio vulgaris*, have been investigated using the combination of EPR, resonance Raman, UV/visible/near-IR absorption, CD and VTMCD spectroscopies. Deconvolution of the spectral contributions from Center I and Center II has been achieved by parallel investigations of the C13S variant, which does not assemble Center I, and the resonance Raman spectrum of oxidized Center II has been assigned based on isotope shifts for  $^{34}\text{S}$  and  $^{15}\text{N}$  globally labeled samples. As for the 1Fe-SOR from *Pyrococcus furiosus*, the spectroscopic properties of oxidized and reduced Center II in *D. vulgaris* 2Fe-SOR are indicative of distorted octahedral and square pyramidal coordination geometries, respectively. Differences in the properties of the oxidized SOR active sites in 1Fe- and 2Fe-SORs are apparent in the rhombicity of the  $S = 5/2$  ground state ( $E/D = 0.06$  and  $0.28$  in 1Fe- and 2Fe-SORs, respectively), the energy for the  $\text{CysS}^-(\text{p}\pi) \rightarrow \text{Fe}^{3+}(\text{d}\pi)$  CT transition ( $15150 \pm 150 \text{ cm}^{-1}$  and  $15600 \pm 150 \text{ cm}^{-1}$ , in 1Fe- and 2Fe-SORs, respectively) and in changes in the Fe–S stretching region of the resonance Raman spectrum that are indicative of a weaker Fe–S(Cys) bond in 2Fe-SORs. These differences are interpreted in terms of small structural perturbations in the extended Fe–S(Cys) unit in order to maximize electronic coupling and enhance electron transfer rates from the desulforedoxin-type Center I in the 2Fe-SORs. Observation of the characteristic intervalence charge transfer transition of a cyano-bridged  $[\text{Fe}^{\text{III}}-\text{NC}-\text{Fe}^{\text{II}}(\text{CN})_5]$  unit in the near-IR VTMCD spectra of ferricyanide-oxidized samples of both *P. furiosus* 1Fe-SOR and *D. vulgaris* 2Fe-SOR has confirmed the existence of novel ferrocyanide-bound adducts in both 1Fe- and 2Fe-SORs.

## Introduction

Reactive oxygen species (ROS) detoxification in aerobic organisms has been intensively studied for the past thirty years [1, 2]. Recently, evidence has pointed towards a novel pathway of ROS detoxification in anaerobic and microaerophilic microorganisms [3-5]. This new pathway involves the reduction rather than disproportionation of superoxide, to yield hydrogen peroxide and is catalyzed by superoxide reductase (SOR) [4-9]. The hydrogen peroxide is subsequently reduced *in vitro* to water by the enzyme rubrerythrin [10-12]. The available evidence suggests that both SOR and rubrerythrin obtain their reducing equivalents from rubredoxin, which is likely to be reduced via a NADPH:rubredoxin oxidoreductase, although the latter enzyme has yet to be identified in *Desulfovibrio vulgaris* [4, 13].

Over the past three years, SORs have been the subject of mutagenesis investigations [14-17], biochemical/enzymological studies [4, 5, 18, 19], pulse radiolytic kinetic studies [14-17, 20], crystallographic structure determinations [21, 22], and a wide array of spectroscopic investigations [23-29]. Although the catalytic function of the SOR class of enzymes is preserved, structural differences have emerged between SORs in different organisms [21, 22]. The most significant difference involves the number of mononuclear Fe sites. SORs containing one and two Fe sites have been identified and categorized as 1Fe-SORs (also known by the trivial name of neelaredoxins) and 2Fe-SORs (also known by the trivial name of desulfoferrodoxins), respectively [18, 30].

The combination of crystallographic and spectroscopic studies has been used to characterize the Fe sites in the 1Fe-SOR from *Pyrococcus furiosus* [21, 26, 27] and the 2Fe-SOR from *Desulfovibrio desulfuricans* [22, 24, 25]. Both contain a unique type of

mononuclear Fe center (termed Center II in 2Fe-SOR), which is ligated by four equatorial histidines (3 $\epsilon$ N and 1 $\delta$ N), one axial cysteinate in a square-pyramidal arrangement, and the crystal structure of the 1Fe-SOR indicates that a monodentate glutamate occupies the sixth coordination site in the oxidized state. However, in the reduced form, the sixth coordination site is vacant or occupied by a weakly coordinated H<sub>2</sub>O molecule, thereby providing a site for superoxide binding. 2Fe-SORs contain an additional mononuclear Fe site, termed Center I, that is ligated by four cysteinate residues in a distorted rubredoxin-like tetrahedral arrangement with properties similar to desulforedoxin [25, 31]. The tertiary structures of 1Fe- and 2Fe-SORs have an analogous immunoglobulin-like  $\beta$ -barrel fold which comprises the C-terminal domain in 2Fe-SORs, and the major structural difference is that 2Fe-SORs contain an additional N-terminal domain containing the rubredoxin-like Center I [22]. There is also a third type of SOR that has a higher sequence homology to 2Fe-SORs, but does not contain three of the four cysteine residues in the N-terminal domain that ligate Center I. This type of SOR is consequently unable to assemble the rubredoxin-like Center I and is technically a 1Fe-SOR, even though the amino acid sequences are more similar to those of 2Fe-SORs [18].

Despite the overall structural similarity in the sites for superoxide reduction in 1Fe- and 2Fe-SORs, spectroscopic studies of the oxidized forms suggest significant differences that may have structural and mechanistic importance. Differences in the Fe-cysteinate ligation are suggested by the shift in the energy of the CysS( $p_\pi$ )-to-Fe<sup>3+</sup>( $d_\pi$ ) charge transfer band ( $\sim 15,150\text{ cm}^{-1}$  (660 nm) in 1Fe-SORs [26, 32] and  $\sim 15,600\text{ cm}^{-1}$  (641 nm) in 2Fe-SORs [5, 15, 24] and the changes in the resonance Raman spectra in the Fe-S stretching region [24, 27]. EPR studies indicate high-spin,  $S = 5/2$ , Fe<sup>3+</sup> sites with

distinctive ground state electronic properties;  $E/D \sim 0.06$  and  $D \sim -0.5 \text{ cm}^{-1}$  in 1Fe-SORs [26, 32] and  $E/D \sim 0.28$  and  $D \sim -1.4 \text{ cm}^{-1}$  in 2Fe-SORs [24]. However, these apparent differences require reinvestigation due to problems associated with overlapping contributions from Center I in the 2Fe-SORs and changes in properties due to the potential binding of ferrocyanide [26], the product of reduction of ferricyanide which is the oxidant used in most of the published spectroscopic studies of 1Fe- and 2Fe-SORs.

In this work, we report a detailed investigation of the electronic and vibrational properties of the oxidized and reduced mononuclear Fe site responsible for superoxide reduction (Center II) in the 2Fe-SOR from *D. vulgaris*, using the combination of EPR, resonance Raman, UV/visible/near-IR absorption, CD and variable-temperature magnetic circular dichroism (VTMCD) spectroscopies. The problem of deconvoluting the contributions from Center I and Center II has been addressed by parallel investigations of the C13S variant, which does not assemble Center I. Comparison with the analogous spectroscopic studies that have recently been reported for the 1Fe-SOR from *P. furiosus* [26, 27], confirms and facilitates characterization of the differences in the properties of the oxidized centers, but reveals no significant differences in the reduced centers. Near-IR VTMCD studies also confirm the existence of a ferrocyanide-bound adduct in ferricyanide-oxidized samples of both 1Fe- and 2Fe-SORs.

## Materials and Methods

**Biochemical Techniques and Sample Preparation.** Recombinant wild-type and C13S *D. vulgaris* 2Fe-SOR were overexpressed in *Escherichia coli* and purified to homogeneity according to the published procedure [14].  $^{15}\text{N}$  globally labeled C13S 2Fe-

SOR was prepared in the same way with  $^{15}\text{NH}_4\text{Cl}$  (98% enriched; Cambridge Isotopes) substituted for  $\text{NH}_4\text{Cl}$  and  $\text{FeCl}_3$  substituted for  $\text{Fe}(\text{NH}_4)_2(\text{SO}_4)_2$  in the M9 salts.  $^{34}\text{S}$  globally labeled C13S 2Fe-SOR was prepared by substituting  $\text{MgSO}_4$  with  $\text{MgCl}_2$ , and the sole source of sulfur was 2 mM  $^{34}\text{SO}_4^{2-}$  prepared in a 100 mM phosphate buffer.  $^{34}\text{SO}_4^{2-}$  was prepared by heating elemental  $^{34}\text{S}$  (99.9% enriched; Trace Isotopes) to 85 °C in aqua regia. Wild-type and C13S *D. vulgaris* 2Fe-SOR were prepared in 50 mM HEPES buffer at pH 7.5, and three distinct forms were used for spectroscopic investigations: oxidized using a 5-fold excess ammonium hexachloroiridate (Sigma) or potassium ferricyanide (Sigma), reduced with 5-fold excess ascorbic acid (Sigma) and reduced with a 5-fold excess sodium dithionite (Sigma). All reagents were prepared as stock solutions in 50 mM HEPES buffer at pH 7.5 and excess was removed by Amicon ultrafiltration prior to spectroscopic measurements. Reduced samples were handled in a Vacuum Atmospheres glove box (<1 ppm  $\text{O}_2$ ). Samples for near-IR VTMCD studies were exchanged into  $\text{D}_2\text{O}$  50 mM HEPES at pH 7.5 by three 10-fold dilution and concentration cycles.

**Spectroscopic Methods.** X-band (~9.6 GHz) EPR spectra were recorded on a Bruker ESP-300E EPR spectrometer with a dual-mode ER-4116 cavity and equipped with an Oxford Instruments ESR-9 flow cryostat (4.2-300 K). Frequencies were measured with a Hewlett-Packard 5350B frequency counter, and the field was calibrated with a Bruker ER 035M gaussmeter.

Resonance Raman spectra were recorded using an Instruments SA Ramanor U1000 spectrometer fitted with a cooled RCA-31034 photomultiplier tube with 90° scattering geometry. Spectra were recorded digitally using photon counting electronics

and improvements in signal-to-noise were achieved by signal averaging multiple scans. Absolute band positions were calibrated using the excitation frequency and  $\text{CCl}_4$  and are accurate to  $\pm 1 \text{ cm}^{-1}$ . Lines from a Coherent Sabre 100 10-W Argon Ion Laser or Coherent Innova 200-K2 Krypton Ion Laser were used for excitation, and plasma lines were removed using a Pellin Broca prism premonochromator. Scattering was collected from the surface of a frozen 15- $\mu\text{l}$  droplet of sample using a custom-designed anaerobic sample cell [33], attached to the cold finger of an Air Products Displex Model CSA-202E closed cycle refrigerator. This arrangement enables samples to be cooled down to 17 K, which facilitates improved spectral resolution and prevents laser-induced sample degradation. Isotope shifts ( $\Delta\nu$ ) were assessed to an accuracy of  $\pm 1 \text{ cm}^{-1}$  for weak bands based on spectral overlays and to an accuracy of  $\pm 0.2 \text{ cm}^{-1}$  for more intense bands based on the natural abundance minus isotopically labeled difference spectrum using the relationship  $\Delta\nu = I_D\Gamma/2.6I$ , where  $I_D$  is the peak-to-trough intensity of the difference spectrum,  $I$  is the maximum peak intensity, and  $\Gamma$  is the full width at half-height [34].

Absorption spectra were recorded on a Shimadzu UV3101PC spectrophotometer. VTMCD measurements were recorded on samples containing 55% (v/v) glycerol or glycerol- $d_3$  using a Jasco J-715 (180-1000 nm) or J-730 (700-2000 nm) spectropolarimeter mated to an Oxford Instruments Spectromag 4000 (0-7 T) split-coil superconducting magnet. The experimental protocols for measuring MCD spectra of oxygen-sensitive samples over the temperature range 1.5 – 300 K with magnetic fields up to 7 T have been described elsewhere [35, 36].

## Results and Analysis

**EPR.** X-band EPR spectra of ascorbate-reduced and hexachloroiridate-oxidized wild-type *D. vulgaris* 2Fe-SOR are shown in Figure 5.1A and B, respectively. In accord with the midpoint potentials of Centers I and II in *D. desulfuricans* 2Fe-SOR,  $+4 \pm 10$  mV and  $+240 \pm 10$  mV, respectively [24], the hexachloroiridate-oxidized sample has contributions from the high-spin  $\text{Fe}^{3+}$  forms of both Centers I and II, whereas the ascorbate-reduced sample shows the resonance from oxidized Center I in isolation. The resonance from wild-type oxidized Center II, as assessed by the hexachloroiridate-oxidized minus ascorbate-reduced difference spectra (not shown), was identical to that observed for the hexachloroiridate-oxidized C13S variant shown in Figure 5.1C. Thus, the C13S variant is shown to be devoid of Center I, and the ground state properties of Center II are shown to be independent of the presence of Center I.

The resonances from oxidized Centers I and II are readily rationalized using an isotropic  $S = 5/2$  spin Hamiltonian of the form

$$H_e = g_0\beta\mathbf{H}\cdot\mathbf{S} + D(\mathbf{S}_z^2 - S(S+1)/3) + E(\mathbf{S}_x^2 - \mathbf{S}_y^2) \quad (1)$$

where  $D$  and  $E$  are the axial and rhombic zero-field splitting parameters, respectively.

Oxidized Center I is consistent with  $E/D = 0.08$ ,  $D > 0$  and  $g_0 = 0$  [25], which predicts for  $g_{x,y,z} = (1.80, 7.70, 4.09)$ ,  $(5.79, 1.74, 1.87)$ , and  $(9.99, 0.41, 0.44)$  for the lower ( $M_s = \pm 1/2$ ), middle ( $M_s = \pm 3/2$ ), and upper ( $M_s = \pm 5/2$ ) doublets, respectively. Center II is comprised of two  $S = 5/2$  resonances in hexachloroiridate-oxidized samples of the C13S variant and very similar EPR spectra to that shown in Figure 5.1C were observed for samples oxidized with peroxide or ferricyanide. The major component is responsible for the absorption-shaped features at  $g = 9.8$  and the broad derivative-shaped feature centered

at  $g = 4.3$ , and is consistent with  $E/D = 0.28$ ,  $D < 0$ , and  $g_0 = 2$  [24], which predicts  $g_{x,y,z} = (9.79, 0.45, 0.59)$ ,  $(4.59, 3.97, 4.21)$ , and  $(0.80, 9.52, 1.20)$  for the lower (“ $M_s = \pm 5/2$ ”), middle (“ $M_s = \pm 3/2$ ”), and upper (“ $M_s = \pm 1/2$ ”) doublets, respectively. The minor component is more clearly apparent in the first integral spectrum and corresponds to a more axial  $S = 5/2$  component with broad low-field features centered near  $g = 9.2$  and  $5.0$  indicative of  $E/D \sim 0.22$  ( $g_{x,y,z} = (9.89, 0.29, 0.36)$ ,  $(4.94, 3.53, 3.89)$ , and  $(1.07, 9.24, 1.75)$ ).

### **Absorption, CD and VTMCD**

**(a) Wild-type *D. vulgaris* 2Fe-SOR:** UV-visible absorption spectra of hexachloroiridate-oxidized, ascorbate-reduced and dithionite-reduced samples of wild-type *D. vulgaris* 2Fe-SOR are shown in Figure 5.2. The oxidized forms of Centers I and II contribute to the visible absorption in the hexachloroiridate-oxidized sample. In accord with the midpoint potentials determined for *D. desulfuricans* 2Fe-SOR [24] and the EPR results presented above, only Center II is reduced by ascorbate, whereas both Centers I and II are reduced by dithionite to give a sample with no visible absorption bands. Hence the ascorbate-reduced spectrum (Figure 5.2B) and the hexachloroiridate-oxidized minus ascorbate-reduced difference spectrum (Figure 5.2D) correspond to the visible absorption spectra of oxidized Centers I and II, respectively. The visible absorption properties of Center I are characteristic of rubredoxin-type centers with  $D_{2d}$  distorted tetrahedral  $\text{Fe}(\text{S}(\text{Cys}))_4$  units, such as in desulfiredoxin [25, 37]. The visible absorption characteristics of Center II in *D. vulgaris* 2Fe-SOR (bands centered at  $15600 \text{ cm}^{-1}$  and  $30000 \text{ cm}^{-1}$ ) are in excellent agreement with those determined previously for 2Fe-SORs (bands at centered at  $15600 \pm 150 \text{ cm}^{-1}$  and  $30000 \pm 500 \text{ cm}^{-1}$  [5, 24]). However, the lower energy band of Center II is

observed at significantly lower energies in 1Fe-SORs (bands at  $15150 \pm 150 \text{ cm}^{-1}$  and  $30000 \pm 500 \text{ cm}^{-1}$  [16, 26, 32, 38]).

VTMCD facilitates resolution of overlapping electronic transitions for non-heme iron centers and provides a means of assessing transition polarizations in the absence of single crystal polarization data, via saturation magnetization studies [39, 40]. Moreover, VTMCD has proven to be essential for effecting detailed electronic assignments in rubredoxin-type centers [40, 41] and the SOR active site in *P. furiosus* 1Fe-SOR [26]. Comparison of the VTMCD spectra of the hexachloroiridate-oxidized and ascorbate-reduced samples of *D. vulgaris* 2Fe-SOR (Figure 5.3A and B) with each other and the published VTMCD spectrum of oxidized desulforedoxin [42] shows that oxidized Center II does not contribute significantly to the visible VTMCD spectrum of the hexachloroiridate-oxidized sample. Moreover, the pattern of intense positive and negative MCD *C*-terms in the  $15000\text{-}28000 \text{ cm}^{-1}$  region are readily assigned as  $(\text{Cys})\text{S}^-(p_\sigma) \rightarrow \text{Fe}^{3+}(d_\sigma)$  CT transitions of a  $\text{FeS}_4$  unit under effective  $D_{2d}$  symmetry based on experimental and theoretical studies on *Desulfovibrio gigas* rubredoxin and ferric tetrathiolate model complexes [40, 43]. The close correspondence in the VTMCD spectra of dithionite-reduced *D. vulgaris* 2Fe-SOR (Figure 5.3C) and reduced desulforedoxin [42] in the  $28000\text{-}35000 \text{ cm}^{-1}$  region suggests that CT transitions involving reduced Center II spectrum are not observable in the presence of reduced Center I. Although detailed assignments are not available for the CT bands of reduced rubredoxin or desulforedoxin, the field and temperature dependence of the MCD bands are characteristic of a high-spin ( $S = 2$ ) ferrous center.

Overlap with the more intense MCD bands of oxidized or reduced Center I clearly impedes characterization of both oxidized and reduced Center II in 2Fe-SORs using the UV-visible VTMCD. In contrast near-IR VTMCD studies of *D. vulgaris* 2Fe-SOR provide useful insights into the electronic properties of both the oxidized and reduced forms of Center II, see Figure 5.4. The hexachloroiridate-oxidized, ferricyanide-oxidized, and ascorbate-reduced samples exhibit a weak positive *C*-term centered at 12300 cm<sup>-1</sup> and weak negative *C*-term centered at 14000 cm<sup>-1</sup> that are attributed to (Cys)S<sup>-</sup>(p<sub>π</sub>) → Fe<sup>3+</sup>(d<sub>π</sub>) CT transitions of oxidized Center I [40, 43]. The weakness of the (Cys)S<sup>-</sup>(p<sub>π</sub>) → Fe<sup>3+</sup>(d<sub>π</sub>) CT transitions compared to the (Cys)S<sup>-</sup>(p<sub>σ</sub>) → Fe<sup>3+</sup>(d<sub>σ</sub>) CT transitions in both the absorption and VTMCD spectra indicates the overwhelming dominance of σ bonding over π bonding in the FeS<sub>4</sub> core unit. Of particular importance is the observation of a broad positive *C*-term centered at 10000 cm<sup>-1</sup> that is present in the ferricyanide-oxidized but not the hexachloroiridate-oxidized samples after removal of excess oxidant, see Figure 5.4A and B. An analogous band is observed in the near-IR VTMCD spectrum of ferricyanide-oxidized samples *P. furiosus* 1Fe-SOR (data not shown). Parallel VTMCD studies of Prussian blue, which contains the cyano-bridged [Fe<sup>III</sup>-NC-Fe<sup>II</sup>(CN)<sub>5</sub>]<sup>+</sup> cation, revealed an analogous positive *C*-term centered at 12500 cm<sup>-1</sup> (data not shown) that is assigned to the intervalence CT transition of this mixed valence complex [44]. Hence the near-IR VTMCD spectra of ferricyanide-oxidized samples of both 1Fe and 2Fe-SORs provide compelling evidence in support of the proposal for the formation of a ferrocyanide adduct in which ferrocyanide is coordinated at the oxidized active-site via a cyano bridge [26].

The near-IR VTMCD spectra of ascorbate-reduced and dithionite-reduced *D. vulgaris* 2Fe-SOR provide a direct assessment of the ligand-field transitions of reduced Center II. A temperature-dependent positive *C*-term with a maximum  $< 5000 \text{ cm}^{-1}$  (5000  $\text{cm}^{-1}$  is the detection limit of the near-IR CD spectrometer) appears in the ascorbate-reduced sample (Figure 5.4C) and hence is attributed to reduced Center II. An analogous band, together with a negative *C*-term centered at  $12400 \text{ cm}^{-1}$  were observed in the VTMCD spectrum of ascorbate-reduced *P. furiosus* 1Fe-SOR and attributed to the d-d bands of the five-coordinate, square-pyramidal ferrous active site [26]. The latter band is obscured by transitions from oxidized Center I in the ascorbate-reduced sample, but is observed as a negative *C*-term centered at  $12800 \text{ cm}^{-1}$  in the dithionite reduced sample, see Figure 5.4D. Hence reduced Center II is shown to have ligand field transitions at  $12800 \text{ cm}^{-1}$  and  $< 5000 \text{ cm}^{-1}$  corresponding to the two components of the parent  ${}^5\text{T}_{2g} \rightarrow {}^5\text{E}_g$  ligand-field transition (under octahedral symmetry), and the crystal field splitting,  $10Dq > 8900 \text{ cm}^{-1}$ , and the excited state splitting,  $\Delta{}^5\text{E}_g > 7800 \text{ cm}^{-1}$ , are characteristic of five-coordinate, square-pyramidal ferrous centers [39]. The dithionite-reduced sample (Figure 5.4D) also exhibits a much more intense positive *C*-term with a shoulder at  $5400 \text{ cm}^{-1}$  and a maximum  $< 5000 \text{ cm}^{-1}$  that is attributed to the split  ${}^5\text{E} \rightarrow {}^5\text{T}_2$  ligand-field transition of the distorted tetrahedral  $\text{FeS}_4$  unit of reduced Center I ( $10Dq < 5000 \text{ cm}^{-1}$ ), based on optical studies of reduced rubredoxin [37].

**(b) C13S *D. vulgaris* 2Fe-SOR:** The loss of Center I in the C13S variant of *D. vulgaris* 2Fe-SOR facilitates assessment of excited-state electronic properties of Center II.

Absorption and VTMCD spectra of the hexachloroiridate-oxidized C13S variant in the UV-visible region are shown in Figure 5.5. In accord with the hexachloroiridate-oxidized

minus ascorbate-reduced difference spectrum obtained for the wild-type enzyme which corresponds to the spectrum of oxidized Center II minus the protein absorption bands (Figure 5.2D), the absorption spectrum of the C13S variant has a broad shoulder centered at  $30000\text{ cm}^{-1}$  and a well-resolved band at  $15600\text{ cm}^{-1}$ . Hence the loss of Center I does not perturb the optical properties of Center II.

The VTMCD spectrum of oxidized Center II in the C13S variant (Figure 5.5) closely parallels that observed for the mononuclear high spin ferric center in *P. furiosus* 1Fe-SOR and analyzed based on polarizations deduced from MCD saturation magnetization data [26]. Hence the shoulder at  $15600\text{ cm}^{-1}$  is assigned to the  $\text{CysS}^-(p_\pi) \rightarrow \text{Fe}^{3+}(d_\pi)$  CT transition which is strong in absorption as a result of optimal orbital overlap, but weak in the VTMCD spectrum because it is a uniaxial transition, polarized along the Fe-S axis. The most intense positive C-term in the VTMCD spectrum is the  $\text{CysS}^-(p_{\text{pseudo } \sigma}) \rightarrow \text{Fe}^{3+}(d_\pi)$  CT transition centered at  $19000\text{ cm}^{-1}$  which is weak in absorption due to weak  $\pi$  overlap, but strong in VTMCD due to mixing of orthogonal transition moments. Several positive and negative C-terms are resolved under the broad envelope of the  $30000\text{-cm}^{-1}$  absorption band and these are attributed to  $\text{His}(p_\pi) \rightarrow \text{Fe}^{3+}(d_\pi)$  CT transitions involving the three  $\text{N}\epsilon$  and one  $\text{N}\delta$  equatorial histidine ligands, although contributions from  $\text{CysS}^-(p_{\text{pseudo } \sigma}) \rightarrow \text{Fe}^{3+}(d_\sigma)$  and glutamate-to- $\text{Fe}^{3+}$  CT transitions cannot be ruled out. Overall the only significant difference in the excited state properties between the oxidized SOR active sites in the 1Fe- and 2Fe-SORs is that the  $\text{CysS}^-(p_\pi) \rightarrow \text{Fe}^{3+}(d_\pi)$  CT transition is shifted to higher energy by  $450\text{ cm}^{-1}$  in the 2Fe-SOR.

Absorption and VTMCD spectra of the ascorbate-reduced C13S variant in the UV region are shown in Figure 5.6. Although the absorption spectrum is dominated by the intense band centered at  $36000\text{ cm}^{-1}$  from the protein aromatic residues, the CT transitions associated with the high-spin ( $S = 2$ ) ferrous Center II are revealed by positive  $C$ -terms centered at  $31500$ ,  $34100$ , and  $39200\text{ cm}^{-1}$  in the VTMCD spectrum. Analogous bands were observed in the UV VTMCD spectrum of ascorbate-reduced *P. furiosus* 1Fe-SOR, albeit shifted to lower energy by  $200\text{-}300\text{ cm}^{-1}$ , and assigned to  $\text{CysS}^-(\text{p}\pi) \rightarrow \text{Fe}^{2+}(\text{d}\pi)$ ,  $\text{CysS}^-(\text{p}_{\text{pseudo}}\sigma) \rightarrow \text{Fe}^{2+}(\text{d}\pi)$ , and  $\text{CysS}^-(\text{p}_{\text{pseudo}}\sigma) \rightarrow \text{Fe}^{2+}(\text{d}\sigma)$  CT transitions, respectively [26]. Absorption, CD and VTMCD spectra of the ascorbate-reduced C13S variant in the near-IR region are shown in Figure 5.7. The high-energy component of the  ${}^5\text{T}_{2g} \rightarrow {}^5\text{E}_g$  ligand-field transition of reduced Center II is assigned to absorption and positive CD bands centered at  $12400\text{ cm}^{-1}$  and by a negative  $C$ -term centered at  $12800\text{ cm}^{-1}$  in the VTMCD spectra. The low-energy component is evident in the VTMCD spectra as a temperature-dependent band with a maximum  $< 5000\text{ cm}^{-1}$ . This is in complete accord with ligand field transitions deduced for reduced Center II in the wild-type 2Fe-SOR (see above) and the energies of ligand field transitions are very similar to those identified by VTMCD in reduced *P. furiosus* 1Fe-SOR, i.e.  $12400\text{ cm}^{-1}$  and  $< 5000\text{ cm}^{-1}$  [26]. Hence the reduced SOR active sites in 1Fe- an 2Fe-SORs are shown to have very similar excited state electronic properties and both have square-pyramidal coordination geometry with four equatorial histidyl ligands and one axial cysteinyl ligand.

**Resonance Raman.** The resonance Raman spectra recorded for the hexachloroiridate-oxidized (gray) form of wild-type *D. vulgaris* 2Fe SOR using  $496\text{-nm}$  and  $647\text{-nm}$

excitation were indistinguishable from those previously published for *D. desulfuricans* 2Fe-SOR [24]. The vibrations of the desulforedoxin-type center, Center I, are very strongly enhanced with 496-nm excitation and were readily assigned and analyzed in terms of an axially distorted tetrahedral FeS<sub>4</sub> unit based on resonance Raman studies of wild-type and <sup>54</sup>Fe-enriched desulforedoxin [24]. However, uncertainty in terms of the extent to which Centers I and II contribute to the spectrum obtained with 647-nm excitation inhibited characterization of Center II using resonance Raman spectroscopy. Hence the vibrational properties of oxidized Center II were assessed by resonance Raman studies of the C13S variant of *D. vulgaris* 2Fe-SOR using 647-nm excitation into the (Cys)S<sup>-</sup>(p<sub>π</sub>) → Fe<sup>3+</sup>(d<sub>π</sub>) CT band located at 641 nm (15600 cm<sup>-1</sup>), see Figures 5.8 and 5.9 and Table 5.1.

The complete absence of Center I in the C13S variant of *D. vulgaris* 2Fe-SOR was evident by resonance Raman studies using 496-nm excitation. No evidence of Center I vibrations was apparent and the spectrum was dominated by the lattice modes of ice at 230 and 320 cm<sup>-1</sup> (data not shown) indicating negligible resonance enhancement of Center II vibrational modes with 496-nm excitation. Moreover, the resonance Raman spectrum of the oxidized C13S variant with 647-nm excitation is almost identical to that reported using the same excitation wavelength for the fully oxidized (gray) form of wild-type *D. desulfuricans* 2Fe-SOR [24] and to that obtained for wild-type *D. vulgaris* 2Fe-SOR (data not shown). Hence, Center I does not significantly contribute to the resonance Raman spectra of wild-type *D. desulfuricans* and *D. vulgaris* 2Fe-SORs using 647-nm excitation and the spectrum of Center II is unperturbed by loss of the Center I in the C13S variant.

The resonance Raman spectrum of oxidized Center II in the C13S variant of *D. vulgaris* 2Fe-SOR is similar to that reported and analyzed in detail for oxidized *P. furiosus* 1Fe-SOR [27]. Band assignments based on isotope shifts in  $^{15}\text{N}$  and  $^{34}\text{S}$  globally labeled samples, see Figure 5.8, and comparison with the published assignments for oxidized *P. furiosus* 1Fe-SOR [27], are given in Table 5.1. The key element of the resonance Raman spectra of the SOR active site is strong enhancement of internal stretching and deformation modes of the coordinated cysteine residue via kinematic coupling to the Fe–S(Cys) stretching mode or an excited state *A*-term mechanism involving the (Cys)S( $p\pi$ )  $\rightarrow$  Fe $^{3+}$ ( $d\pi$ ) CT transition centered at 641 nm. This situation parallels that observed in Type-1 (blue) copper proteins [45-49] and is a consequence of the near-planar arrangement of the Fe–S $_{\gamma}$ –C $_{\beta}$ –C $_{\alpha}$ –N units in both the 1Fe- and 2Fe-SORs [21, 22].

In the metal–ligand stretching region, 200-520  $\text{cm}^{-1}$ , extensive mixing of the Fe–S stretching mode with the low frequency internal deformation modes of the coordinated cysteine residue, i.e.  $\delta(\text{C}_{\beta}\text{--C}_{\alpha}\text{--C}(\text{O}))$ ,  $\delta(\text{C}_{\beta}\text{--C}_{\alpha}\text{--N})$ ,  $\delta(\text{C}(\text{O})\text{--C}_{\alpha}\text{--N})$ ,  $\delta(\text{C}_{\alpha}\text{--N--C}(\text{O}))$ , and  $\delta(\text{S--C}_{\beta}\text{--C}_{\alpha})$ , is evident by the significant  $^{15}\text{N}$  and  $^{34}\text{S}$  downshifts that are observed for almost all the bands in this region, see Figure 5.8 and Table 5.1. As found for Type-1 (blue) copper proteins [45-49], the extent of the contribution from M–S(Cys) stretching to individual modes in the M–S stretching region can be gauged by the extent of resonance enhancement and the magnitude of the  $^{34}\text{S}$  isotope shift. In the resonance Raman spectrum of oxidized Center II in *D. vulgaris* 2Fe-SOR, the band at 299  $\text{cm}^{-1}$  therefore has the maximum contribution from Fe–S(Cys) stretching, since it has the strongest enhancement and the largest  $^{34}\text{S}$  downshift, 2.6  $\text{cm}^{-1}$ , see Figure 5.8. In contrast,

the mode with maximum contribution from Fe–S(Cys) stretching in the resonance Raman spectrum of oxidized *P. furiosus* 1Fe-SOR, is found at 323 cm<sup>-1</sup>, since this band has the strongest enhancement and the largest <sup>34</sup>S downshift (3.3 cm<sup>-1</sup>) [27]. Although the extensive vibrational mixing complicates accurate quantitative assessment of Fe–S stretching force constants, the resonance Raman data clearly point to a weaker Fe–S(Cys) bond in the oxidized SOR active sites of 2Fe-SORs than in 1Fe-SORs.

The resonance Raman spectrum of the C13S variant of *D. vulgaris* 2Fe-SOR in the metal–ligand regions (Figure 5.8) exhibits additional differences compared to that of *P. furiosus* 1Fe-SOR [27]. First, the shoulders on each of the dominant bands at 299, 314 and 357 cm<sup>-1</sup> (Figure 5.8) suggests structural heterogeneity that does not appear to be present in *P. furiosus* 1Fe-SOR active site and presumably relates to the heterogeneity that is apparent in the EPR spectra (see above). Second, the Fe–N(His) stretching at 210 and 240 cm<sup>-1</sup>, that are identified based on negligible <sup>34</sup>S downshifts and 2-cm<sup>-1</sup> <sup>15</sup>N downshifts, see Figure 5.8 and Table 5.1, have much stronger enhancement than in *P. furiosus* 1Fe-SOR. Since the Fe–N(His) bonds are approximately orthogonal to the Fe–S(Cys) bond, Fe–N(His) stretching modes are unlikely to be enhanced via kinematic coupling. Rather, we have proposed that symmetric and asymmetric vibrations of the Fe–N(His) bonds that are perpendicular to the Fe–S–C plane are enhanced via an excited-state *A*-term mechanism as a result of N(p<sub>π</sub>)-Fe(d<sub>π</sub>)-S(p<sub>π</sub>) orbital overlap [27]. Hence the greater enhancement of Fe–N(His) stretching modes in the 2Fe-SOR is likely to be a consequence of improved N(p<sub>π</sub>)-Fe(d<sub>π</sub>)-S(p<sub>π</sub>) orbital overlap due to rotation of the histidine imidazole rings (His 69 and His 119) to bring them closer to orthogonality with the FeN<sub>2</sub>S plane, with the N associated with His 69 and His 119.

The resonance Raman spectra of the C13S variant of *D. vulgaris* 2Fe-SOR and *P. furiosus* 1Fe-SOR [27] in the 500-2000  $\text{cm}^{-1}$  region both show strong enhancement of internal modes of the coordinated cysteine residue. The 500-800  $\text{cm}^{-1}$  region (Figure 5.8) is dominated by the S-C $_{\beta}$  stretching mode of the coordinated cysteine residue which occurs at 743  $\text{cm}^{-1}$  in *D. vulgaris* 2Fe-SOR and at 748  $\text{cm}^{-1}$  in *P. furiosus* 1Fe-SOR [27]. In addition, this region in *D. vulgaris* 2Fe-SOR exhibits overtones of the intense fundamentals at 299, 314, and 357  $\text{cm}^{-1}$ , and bands at 647 and 659  $\text{cm}^{-1}$  that exhibit large  $^{15}\text{N}$ -downshifts (6-7  $\text{cm}^{-1}$ ) and negligible  $^{34}\text{S}$  downshifts. The latter rules out assignment as combination bands. Hence the band at 659  $\text{cm}^{-1}$  is assigned to the C $_{\alpha}$ -N stretching mode of the cysteine backbone and the band at 647  $\text{cm}^{-1}$  is attributed to a histidine imidazole out-of-plane deformation mode, on the basis of normal mode calculations of L-cysteine [50] and imidazole [51], respectively, see Table 5.1. The 800-2000  $\text{cm}^{-1}$  region (Figure 5.9) is dominated by the C $_{\beta}$ H $_2$  twisting mode of the coordinated cysteine which occurs at 1222  $\text{cm}^{-1}$  in *D. vulgaris* 2Fe-SOR and at 1227  $\text{cm}^{-1}$  in *P. furiosus* 1Fe-SOR [27]. As for *P. furiosus* SOR, the C $_{\beta}$ -C $_{\alpha}$  stretching mode and C $_{\beta}$ H $_2$  scissoring mode of the coordinated cysteine are also enhanced in this region, see Figure 5.9 and Table 5.1.

## Discussion

The sequence homology between the N-terminal and C-terminal domains of 2Fe-SORs (desulfoferrodoxins) with desulforedoxin and 1Fe-SORs (neelaredoxins), respectively, led to the suggestion that 2Fe-SORs are modular proteins that originated from gene fusion of two ancestral genes [32, 52]. The modularity was subsequently confirmed by the crystal structure of *D. desulfuricans* 2Fe-SOR which revealed distinct N-terminal and

C-terminal iron binding domains with the mononuclear iron centers separated by  $\sim 22$  Å [22]. Moreover, the N-terminal and C-terminal domains of *D. vulgaris* 2Fe-SOR have been expressed separately and the recombinant fragments were found to have redox, absorption and EPR properties similar to metal-binding domains in the intact enzyme [18]. The results reported herein for the wild-type and C13S variant forms of *D. vulgaris* 2Fe-SOR demonstrate that the absence of Center I has no detectable effect on the absorption, VTMCD, EPR, or resonance Raman properties of Center II and hence fully support the concept of completely independent iron binding sites in 2Fe-SORs.

The ability to investigate the spectroscopic properties of oxidized and reduced Center II in the C13S variant of *D. vulgaris* 2Fe-SOR without interference from Center I has facilitated detailed comparison of the electronic and vibrational properties of the SOR active sites in 1Fe and 2Fe SORs. Overall the results indicate very similar oxidized and reduced active-site structures in both 1Fe- and 2Fe-SORs. This is particularly evident in the excited-state properties of the oxidized and reduced active sites as revealed by VTMCD studies and the extensive kinematic and electronic coupling within the extended Fe-S(Cys) unit as revealed by resonance Raman studies using excitation into the CysS<sup>-</sup> ( $p_{\pi}$ )  $\rightarrow$  Fe<sup>3+</sup>( $d_{\pi}$ ) CT transition. Moreover, near-IR VTMCD studies demonstrate that the active sites of both 1Fe- and 2Fe-SORs have a common square-pyramidal coordination geometry in the reduced state with an open coordination site trans to the cysteine for substrate binding and reduction.

Oxidation of *P. furiosus* 1Fe-SOR with ferricyanide resulted in conversion of the axial  $S = 5/2$  ground state ( $E/D \sim 0.06$ ), that was observed in samples oxidized with air, peroxide or hexachloroiridate, to a rhombic  $S = 5/2$  ( $E/D \sim 0.27$ ) ground state [26]. This

result suggested the existence of a ferrocyanide-bound adduct of the oxidized SOR active site [26]. Moreover, since ferricyanide had been the oxidant of choice for the majority of EPR studies of 1Fe- and 2Fe SORs, this raised the possibility that the ground state properties assessed by EPR studies may not correspond to those of the wild-type oxidized enzyme. Observation of the characteristic intervalence CT of the cyano-bridged  $[\text{Fe}^{\text{III}}-\text{NC}-\text{Fe}^{\text{II}}(\text{CN})_5]$  unit in the near-IR VT-MCD spectra of ferricyanide-oxidized samples of both *P. furiosus* 1Fe-SOR and *D. vulgaris* 2Fe-SOR has now confirmed the existence of ferrocyanide-bound adducts in both 1Fe- and 2Fe-SORs. However, in contrast to 1Fe-SORs, the EPR results for wild type and the C13S variant of *D. vulgaris* SOR indicate that the ground state properties of the SOR active-site oxidized by hexachloroiridate or peroxide ( $S = 5/2$  and  $E/D \sim 0.28$ ), are very similar to those of the ferricyanide-adduct. This result is in accord with the Mössbauer studies of oxidized *D. desulfuricans* 2Fe-SOR which were analyzed in terms of a rhombic  $S = 5/2$  ground state ( $E/D = 0.28$ ,  $D = -1.4 \text{ cm}^{-1}$ ) for the oxidized SOR site (Center II) [24]

Comparison of the spectroscopic results presented herein for *D. vulgaris* 2Fe-SOR with those established for *P. furiosus* 1Fe-SOR [26, 27] have revealed small, but well-defined, differences in the properties of the oxidized SOR active sites in 1Fe- and 2Fe-SORs that cannot be rationalized as being artifacts of ferricyanide oxidation. These differences are manifest in terms of the ground- and excited-state electronic properties and the vibrational properties of the high-spin ferric active sites: more axial ground state in 1Fe-SORs ( $E/D = 0.06$ ) than in 2Fe-SORs ( $E/D = 0.28$ ); higher energy for the  $\text{CysS}^- (\text{p}\pi) \rightarrow \text{Fe}^{3+} (\text{d}\pi)$  CT transition in 2Fe-SORs ( $15600 \pm 150 \text{ cm}^{-1}$ ) than in 1Fe-SORs ( $15150 \pm 150 \text{ cm}^{-1}$ ); changes in the Fe–S stretching region indicative of differences in the

kinematic and electronic coupling within the extended Fe-S(Cys) unit and a weaker Fe-S(Cys) bond in 2Fe-SORs.

The structural origin of the differences in the oxidized active site properties is unclear at present. We have considered two possibilities. The first involves differences in ligation trans to the axial cysteine ligand. A monodentate glutamate residue was identified as the ligand trans to cysteine in two of the four subunits of the homotetrameric *P. furiosus* 1Fe-SOR in the oxidized crystal structure [21]. In contrast, the active site was found to be square pyramidal with four equatorial histidines and one axial cysteine in the crystal structure of *D. desulfuricans* 2Fe-SOR [22]. However, the SOR active-site structure in *D. desulfuricans* 2Fe-SOR is likely an artifact of photoreduction in the x-ray beam [26], since a six-coordinate oxidized SOR active site is supported by the spectroscopic results reported herein and those previously reported for *P. furiosus* 1Fe-SOR [26, 27]. In addition, evidence for glutamate as the sixth ligand is supported by both mutagenesis and FTIR results. Replacement of the glutamate with alanine results in marked and equivalent changes in the optical properties of the SOR centers in 1Fe- and 2Fe-SORs with the  $\text{CysS}^-(p_\pi) \rightarrow \text{Fe}^{3+}(d_\pi)$  CT transition shifting to  $\sim 17000 \text{ cm}^{-1}$  [15-17, 27]. Redox-induced changes in the IR modes of the glutamate residue also provide compelling evidence for monodentate glutamate coordination in the oxidized forms of the 1Fe-SOR from *T. pallidum* and the 2Fe-SOR from *D. baarsii* [28]. Hence the available evidence strongly suggests that the oxidized SOR centers in 1Fe- and 2Fe-SORs both have a monodentate glutamate ligand trans to the cysteine. Moreover, the absence of any significant change in the resonance Raman spectrum of *P. furiosus* 1Fe-SOR on mutating the ligating glutamate residue to an alanine [27], strongly suggests that changes in the

ligand trans to cysteine are not responsible for the differences in the spectroscopic properties of the SOR oxidized active site in 1Fe- and 2Fe-SORs.

The second and more likely possibility is that the differences reflect structural perturbations in the extended Fe-S(Cys) unit that are designed to maximize electronic coupling and hence electron transfer rates from Center I in the 2Fe-SORs. An electron-transfer pathway via the coordinated cysteine and the adjacent tyrosine residue is an attractive possibility in 2Fe-SORs, because the tyrosine side chain is on the direct path between Centers I and II [22, 27]. A similar electron transfer pathway has been established in Type-1 (blue) copper proteins [53, 54] and the coplanar arrangement of the Cu-S<sub>γ</sub>-C<sub>β</sub>-C<sub>α</sub>-N unit to the adjacent tyrosine residue facilitates long-range electronic coupling [49]. An analogous coplanar arrangement of the Fe-S<sub>γ</sub>-C<sub>β</sub>-C<sub>α</sub>-N unit that extends to the adjacent tyrosine is also evident in both 1Fe- and 2Fe-SORs [21, 22] and evidence for strong kinematic and electronic coupling within this extended Fe-S(Cys) unit is provided by the resonance Raman spectra of both *P. furiosus* 1Fe-SOR [27] and *D. vulgaris* 2Fe-SOR. This superexchange pathway for electron transfer contributes a high electronic coupling matrix element that is likely to facilitate tunneling over the 22-Å distance that separates Centers I and II. Small structural changes in the Fe-S<sub>γ</sub>-C<sub>β</sub>-C<sub>α</sub>-N unit of the coordinated cysteine in order to maximize electronic coupling would be expected to result in changes in the resonance Raman spectrum, as observed, and in the S(p<sub>π</sub>)-Fe(d<sub>π</sub>) interaction. The latter should be manifest by changes in the energy of the CysS<sup>-</sup>(p<sub>π</sub>) → Fe<sup>3+</sup>(d<sub>π</sub>) CT transition and the rhombicity of the *S* = 5/2 ground state, due to splitting of the two Fe d<sub>π</sub> orbitals. Hence the differences in the spectroscopic properties of oxidized SOR active sites in 1Fe- and 2Fe-SORs are readily rationalized in terms of

structural perturbations in the extended Fe-S(Cys) unit, and are likely to be important in understanding electron transfer from Center I to Center II in 2Fe-SORs.

**Acknowledgements** This work was supported by grants from the National Institutes of Health (GM60329 to MKJ and GM40388 to DMK) and a National Science Foundation Research Training Group Award to the Center for Metalloenzyme Studies (DBI9413236)

## References

1. McCord JM (2000) *Am J Med* 108:652-659.
2. Fridovich I (1998) *J Exp Biol* 201:1203-1209.
3. Liochev SI, Fridovich I (1997) *J Biol Chem* 272:25573-25575.
4. Jenney FE, Verhagen MFJM, Cui X, Adams MWW (1999) *Science* 286:306-309.
5. Lombard M, Fontecave M, Touati D, Nivière V. (2000) *J Biol Chem* 275:115-121.
6. Adams MWW, Jenney FE, Clay MD, Johnson MK (2002) *J Biol Inorg Chem* 7:647-652.
7. Coulter ED, Kurtz DM (2002) *J Biol Inorg Chem* 7:653-658.
8. Auchere F, Rusnak F (2002) *J Biol Inorg Chem* 7:664-667.
9. Imlay JA (2002) *J Biol Inorg Chem* 7:659-663.
10. Coulter ED, Shenvi NV, Kurtz DM (1999) *Biochem Biophys Res Commun* 255:317-323.
11. Coulter ED, Shenvi NV, Beharry ZM, Smith JJ, Prickril BC, Kurtz DM (2000) *Inorg Chim Acta* 297:231-241.
12. Jin S, Kurtz DM, Liu Z-J, Rose J, Wang B-C (2002) *J Am Chem Soc* 124:9845-9855.
13. Coulter ED, Kurtz DM (2001) *Arch Biochem Biophys* 394:76-86.
14. Emerson JP, Coulter ED, Cabelli DE, Phillips RS, Kurtz DM (2002) *Biochemistry* 41:4348-4357.
15. Coulter ED, Emerson JP, Kurtz DM, Cabelli DE (2000) *J Am Chem Soc* 122:11555-11556.

16. Abreu IA, Saraiva LM, Soares CM, Teixeira M, Cabelli DE (2001) *J Biol Chem* 276:38995-39001.
17. Lombard M, Houée-Levin C, Touati D, Fontecave M, Nivière V (2001) *Biochemistry* 40:5032-5040.
18. Ascenso C, Rusnak FM, Cabrito I, Lima MJ, Naylor S, Moura I, Moura JJG (2000) *J Biol Inorg Chem* 5:720-729.
19. Abreu IA, Saraiva LM, Carita J, Huber H, Stetter KO, Cabelli DE, Teixeira M. (2000) *Mol Microbiol* 38:322-334.
20. Nivière V, Lombard M, Fontecave M, Houée-Levin C (2001) *FEBS Lett* 497:171-173.
21. Yeh AP, Hu Y, Jenney FE, Adams MWW, Rees DC (2000) *Biochemistry* 39:2499-2508.
22. Coelho AV, Matias P, Fülöp V, Thompson A, Gonzalez A, Carrondo MA (1997) *J Biol Inorg Chem* 2:680-689.
23. Verhagen MFJM, Voorhorst WGB, Kolkman JA, Wolbert RBG, Hagen WR (1993) *FEBS Lett* 336:13-18.
24. Tavares P, Ravi N, Moura JJG, LeGall J, Huang Y-H, Crouse BR, Johnson MK, Huynh BH, Moura I (1994) *J Biol Chem* 269:10504-10510.
25. Moura I, Tavares P, Moura JJG, Ravi N, Huynh BH, Liu M-Y, LeGall J. (1990) *J Biol Chem* 265:21596-21602.
26. Clay MD, Jenney FE, Hagedoorn PL, George GN, Adams MWW, Johnson MK (2002) *J Am Chem Soc* 124:788-805.

27. Clay MD, Jenney FE, Noh HJ, Hagedoorn PL, Adams MWW, Johnson MK (2002) *Biochemistry* 41:9833-9841.
28. Berthomieu C, Dupeyrat F, Fontecave M, Verméglio A, Nivière V (2002) *Biochemistry* 41:10360-10368.
29. Mathé C, Mattioli TA, Horner O, Lombard M, Latour J-M, Fontecave M, Nivière V (2002) *J Am Chem Soc* 124:4966-4967.
30. Kurtz DM, Coulter ED (2001) *Chemtracts* 14:407-435.
31. Moura I, Huynh BH, Hausinger RP, LeGall J, Xavier AV, Munck E (1980) *J Biol Chem* 255:2493-2498.
32. Chen L, Sharma P, LeGall J, Mariano AM, Teixeira M, Xavier AV (1994) *Eur J Biochem* 226:613-618.
33. Drozdowski PM, Johnson MK (1988) *Appl Spectrosc* 42:1575-1577.
34. Shelnut JA, Rousseau DL, Dethemers JK, Margoliash E (1979) *Proc Natl Acad Sci USA* 76:3865-3871.
35. Johnson MK (1988) In: Que L (ed) *Metal Clusters in Proteins*. American Chemical Society, Washington, DC, pp 326-342.
36. Thomson AJ, Cheesman MR, George SJ (1993) *Meth Enzymol* 226:199-232.
37. Eaton WA, Lovenberg W (1973) In: Lovenberg W (ed) *Iron-Sulfur Proteins*. Academic Press: New York, pp 131-162.
38. Jovanović T, Ascenso C, Hazlett KRO, Sikkink R, Krebs C, Litwiller LM, Benson LM, Moura I, Moura JJG, Radolf JD, Huynh BH, Naylor S, Rusnak F (2000) *J Biol Chem* 275:28439-28448.

39. Solomon EI, Brunold TC, Davis MI, Kemsley JN, Lee S-K, Lehnert N, Neese F, Skulan AJ, Yang T-S, Zhou J (2000) *Chem Rev* 100:235-349.
40. Oganessian VS, George SJ, Cheesman MR, Thomson AJ (1999) *J Chem Phys* 110:762-777.
41. Gebhard MS, Koch SA, Millar MM, Devlin FJ, Stephens PJ, Solomon EI (1991) *J Am Chem Soc* 113:1640-1649.
42. Johnson MK, Robinson AE, Thomson AJ (1982) In: Spiro TG (ed) *Iron-Sulfur Proteins*. Wiley-Interscience: New York, pp 367-406.
43. Gebhard MS, Deaton JC, Koch SA, Millar MM, Solomon EI (1990) *J Am Chem Soc* 112:2217-2231.
44. Robin MB (1962) *Inorg Chem* 1:337-342.
45. Loehr TM (1992) *J Raman Spectrosc* 23:531-537.
46. Spiro TG, Czernuszewicz RS (1995) *Meth Enzymol* 246:416-460.
47. Andrew CR, Sanders-Loehr J (1996) *Acc Chem Res* 29:365-372.
48. Andrew CR, Han J, den Blaauwen T, van Pouderoyen G, Vijgenboom E, Canters GW, Loehr TM, Sanders-Loehr J (1997) *J Biol Inorg Chem* 2:98-107.
49. Dong S, Spiro TG (1998) *J Am Chem Soc* 120:10434-10440.
50. Li H, Wurrey CJ, Thomas GJ (1992) *J Am Chem Soc* 114:7463-7469.
51. Jarzecki AA, Spiro TG (2001) *J Raman Spectrosc* 32:599-605.
52. Brumlik MJ, Voordouw G (1989) *J Bacteriol* 171:4996-5004.
53. He S, Modi S, Bendall DS, Gray JC (1991) *EMBO J* 10:4011-4016.
54. Farver O, Pecht I (1981) *Proc Natl Acad Sci USA* 78:4190-4193.

Table 5.1 Assignment of the resonance Raman spectrum of oxidized C13S *D. vulgaris*

2Fe-SOR

Frequency, cm <sup>-1</sup>	<sup>NA</sup> S→ <sup>34</sup> S shift, <sup>a</sup> cm <sup>-1</sup>	<sup>NA</sup> N→ <sup>15</sup> N shift, <sup>a</sup> cm <sup>-1</sup>	Assignment <sup>b</sup>
210	0	-2	v(Fe-N(His))
241	0	-2	v(Fe-N(His))
299	-2.6	-3.0	v(Fe-S) + cysteine deformations
314	-1.4	-1.0	δ(S-C <sub>β</sub> -C <sub>α</sub> ) + v(Fe-S)
357	-2.0	-3.4	$\left. \begin{array}{l} \delta(\text{C}_\beta\text{-C}_\alpha\text{-C(O)}) + \\ \delta(\text{C}_\beta\text{-C}_\alpha\text{-N}) + \delta(\text{C(O)}\text{-C}_\alpha\text{-N}) \\ \delta(\text{C}_\alpha\text{-N-C(O)}) + \delta(\text{S-C}_\beta\text{-C}_\alpha) \\ \text{v(Fe-S)} \end{array} \right\}$
376	-1	-3	
404	-1	-2	
461	0	-3	
510	0	-1	
598	-5	-6	Overtone (2 × 299)
647	0	-6	Histidine (out-of-plane deform.)
659	0	-7	v(C <sub>α</sub> -N)
714	-4	-6	Overtone (2 × 357)
743	-4.1	-1.3	v(S-C <sub>β</sub> )
1005	nd	nd	Phenylalanine
1042	nd	nd	Tyrosine
1105	nd	nd	v(C <sub>β</sub> -C <sub>α</sub> )
1222	nd	nd	C <sub>β</sub> H <sub>2</sub> twisting
1300	nd	nd	Amide III
1433	nd	nd	C <sub>β</sub> H <sub>2</sub> scissoring
1566	nd	nd	Amide II
1668	nd	nd	Amide I

<sup>a</sup>Isotope shifts given to two significant figures have an estimated uncertainty of  $\pm 0.2$  cm<sup>-1</sup> and those given to one significant figure have an estimated uncertainty of  $\pm 1$  cm<sup>-1</sup>; nd, not-determined.

<sup>b</sup>Unless otherwise indicated, all assignments correspond to vibrational modes of Cys116 and indicate the major contributing modes.

Figure 5.1 X-band EPR spectra of *D. vulgaris* 2Fe-SOR: (A) Ascorbate-reduced wild-type; (B) Hexachloroiridate-oxidized wild-type; (C) Hexachloroiridate-oxidized C13S variant. All samples were 0.25 mM in 2Fe-SOR and were in 50 mM HEPES buffer at pH 7.5. All spectra were recorded at 9.60 GHz, using a modulation amplitude of 0.63 mT, a microwave power of 40 mW, and a temperature of 4.2 K. Selected g-values are indicated on each spectrum.

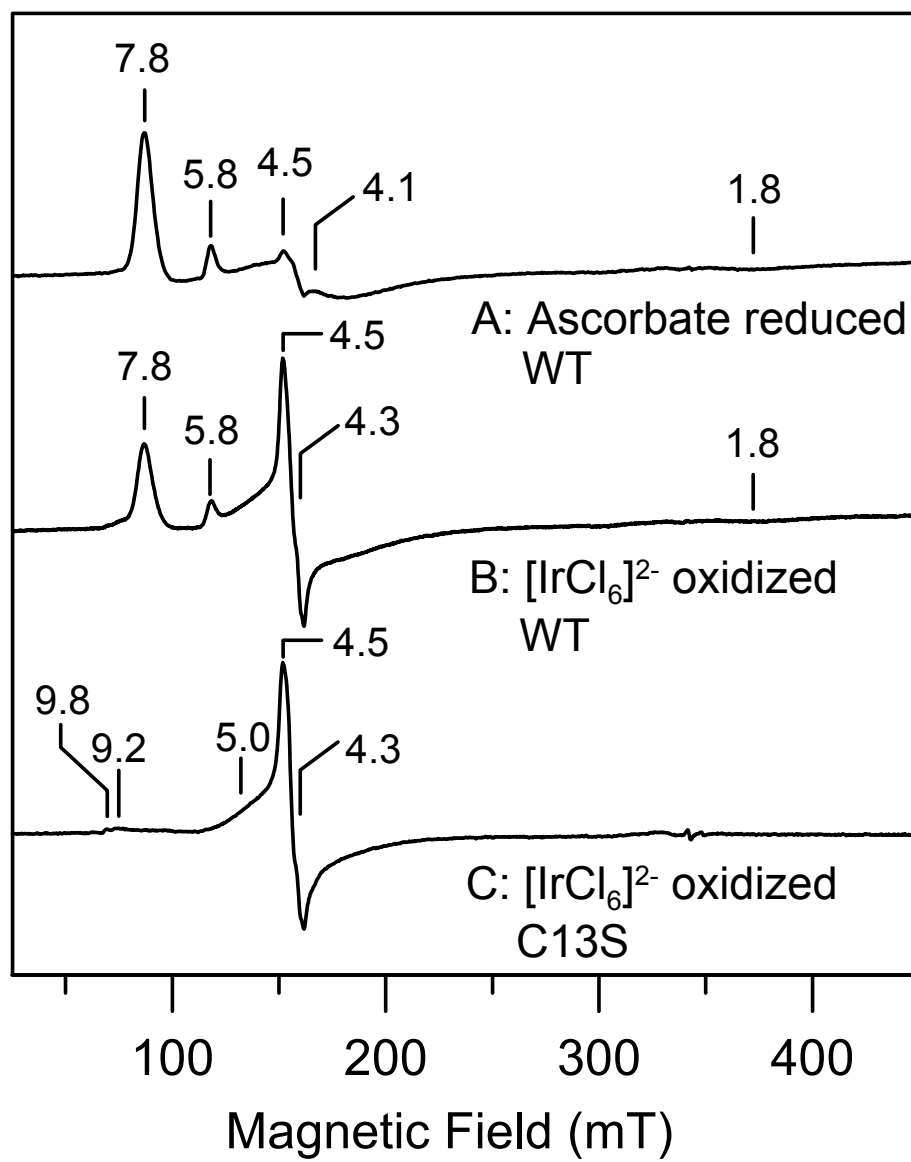


Figure 5.2 UV-visible absorption spectra of wild-type *D. vulgaris* 2Fe-SOR: (A) Hexachloroiridate-oxidized; (B) Ascorbate-reduced; (C) Dithionite-reduced; (D) A minus B subtraction. All samples were 0.35 mM in 2Fe-SOR and were in 50 mM HEPES buffer, pH 7.5. All oxidants and reductants were added in 5-fold excess and were removed by three 10-fold dilution/concentration cycles by Amicon ultrafiltration prior to data collection.

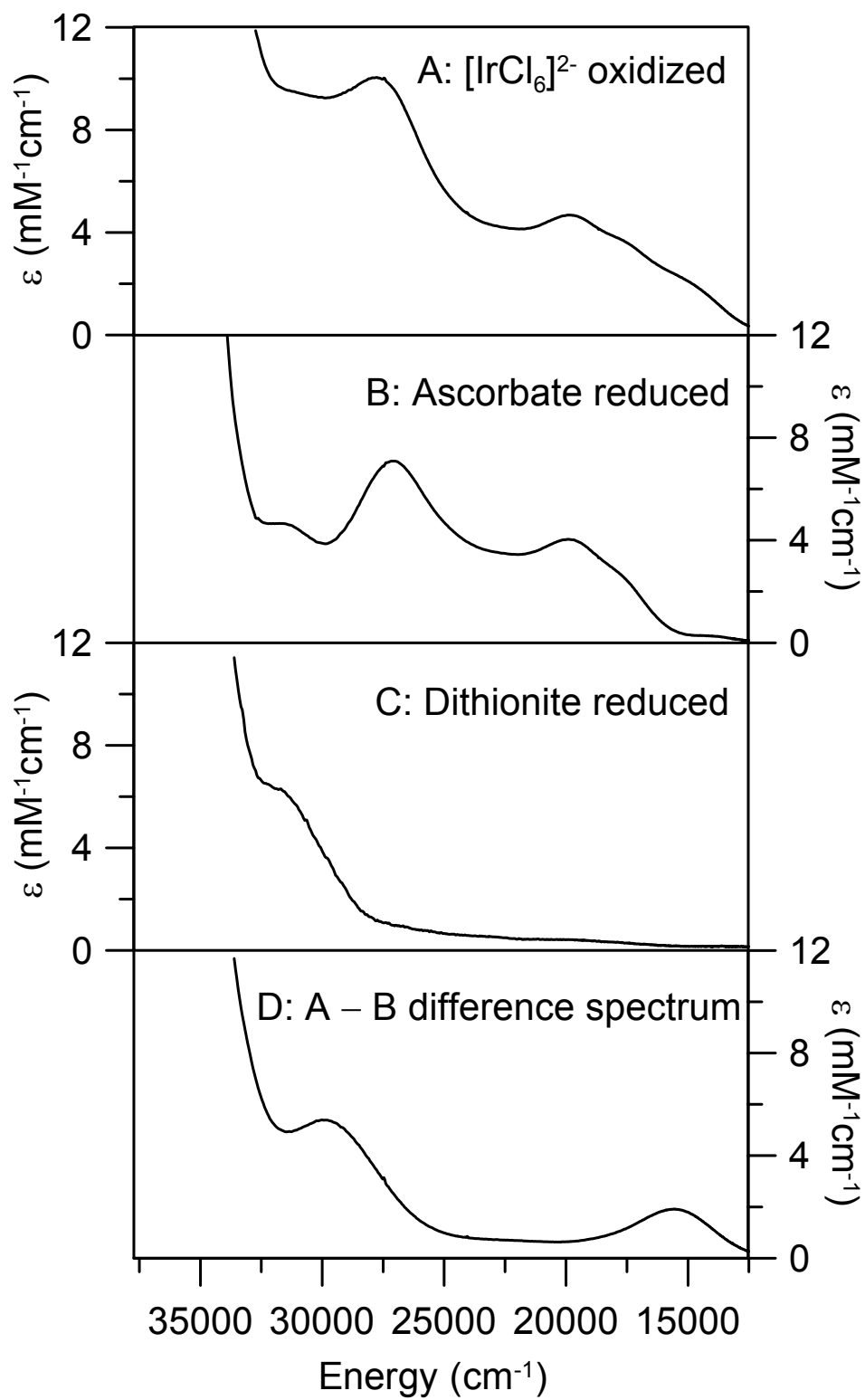


Figure 5.3 UV-visible VTMCD spectra of wild-type *D. vulgaris* 2Fe-SOR: (A) Hexachloroiridate-oxidized; (B) Ascorbate-reduced; (C) Dithionite-reduced. Samples are the same as those used in Figure 5.2 except for the addition of 55% (v/v) glycerol. Spectra were recorded in a 1-mm path length cell, with a magnetic field of 6 T at 1.79, 4.22, 10.6, 24.4, and 48.6 K. The MCD intensity for all bands increases with decreasing temperature.

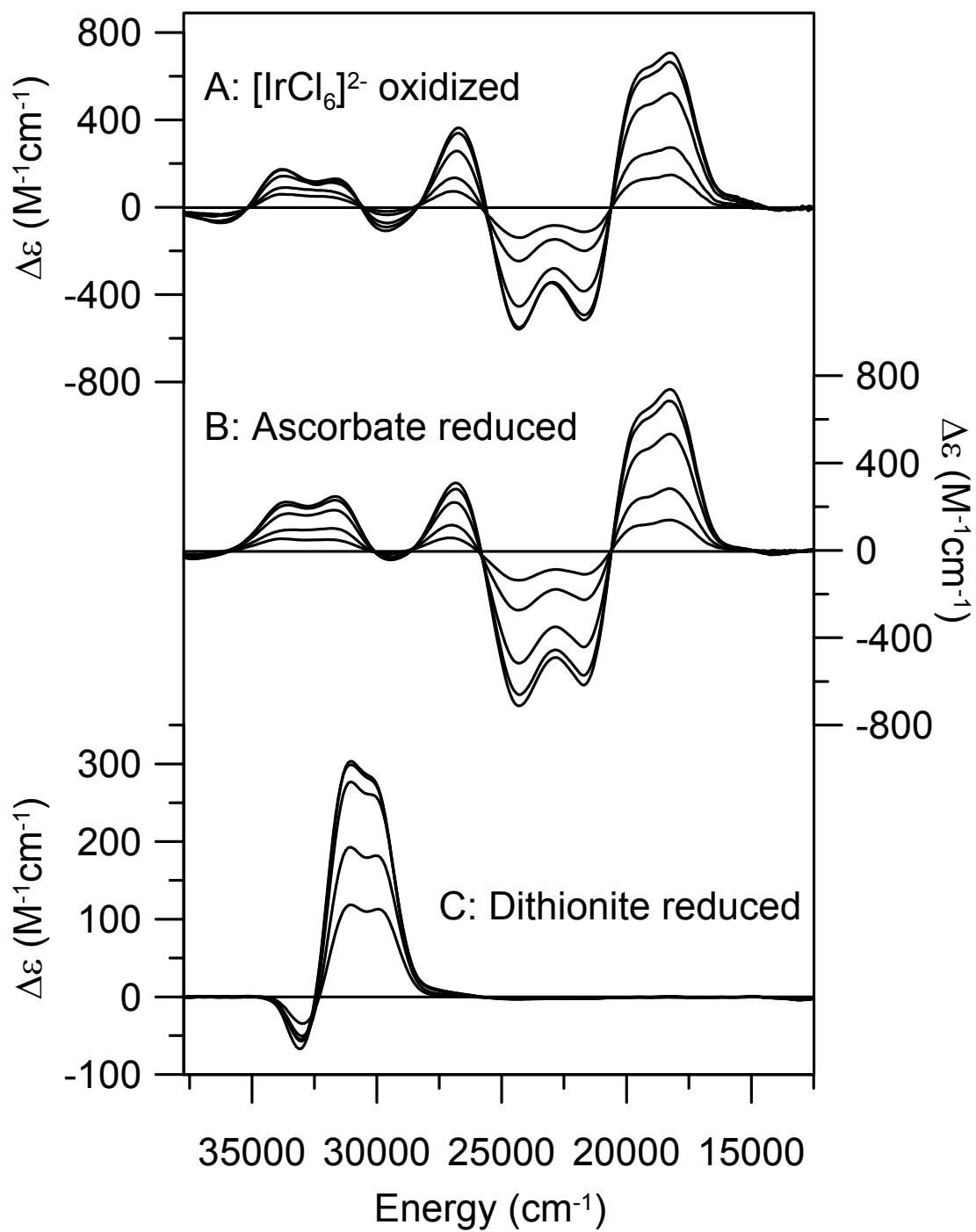


Figure 5.4 Near-IR VTMCD spectra of wild-type *D. vulgaris* 2Fe-SOR: (A) Hexachloroiridate-oxidized; (B) Ferricyanide-oxidized; (C) Ascorbate-reduced; (D) Dithionite-reduced. The sample preparation is the same as described in Figure 5.2, except each sample was 4.8 mM in 2Fe-SOR and was buffer exchanged into D<sub>2</sub>O 50 mM HEPES buffer, pD 7.5, by three 10-fold dilution/concentration cycles, followed by the addition of 55% (v/v) glycerol-*d*<sub>3</sub>. Spectra were recorded in a 1-mm path length cell, with a magnetic field of 6 T at 1.88, 4.22, 10.4, 24.5, and 50.8 K. The MCD intensity for all bands increases with decreasing temperature.

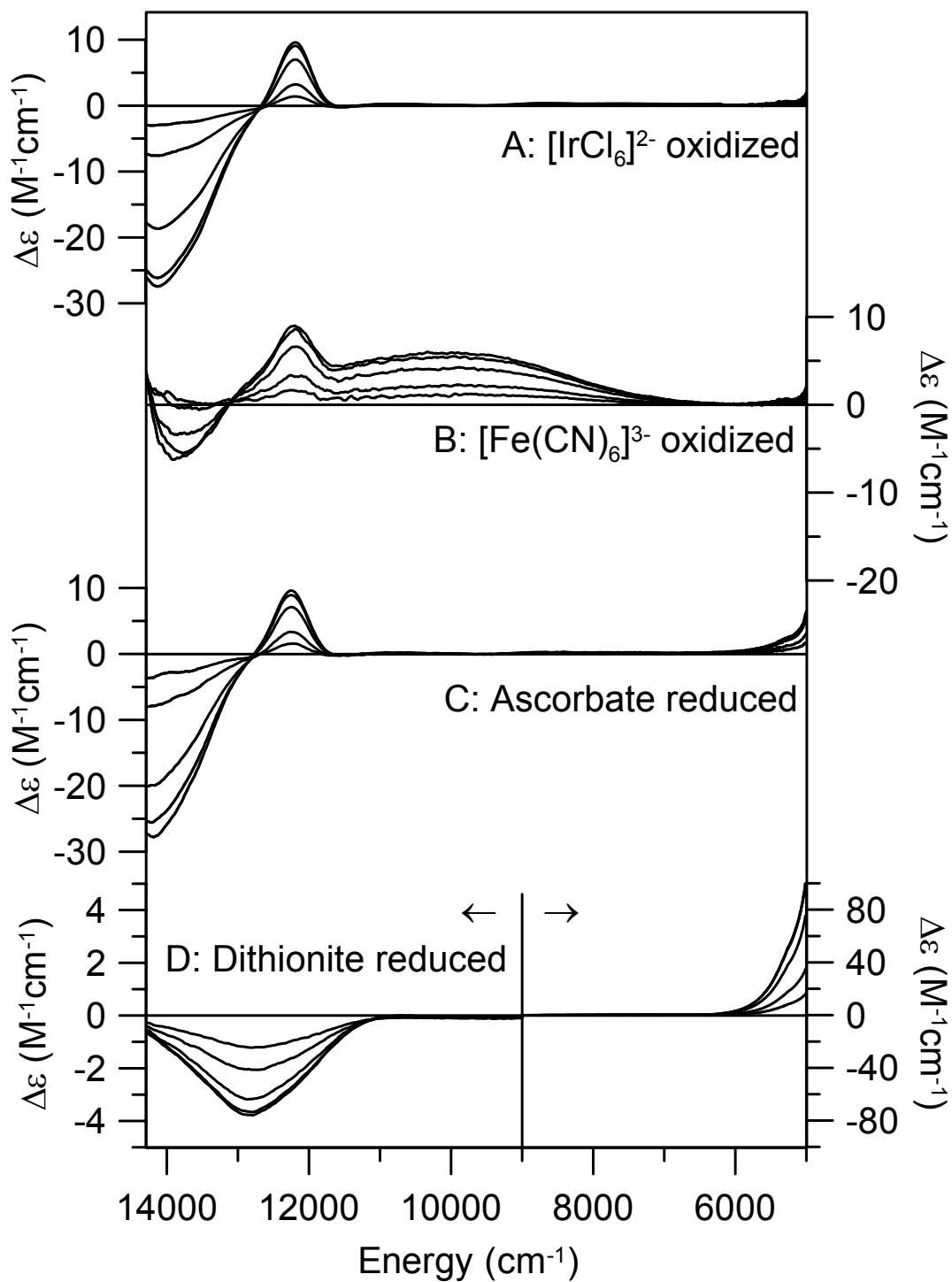


Figure 5.5 UV-visible absorption and VTMCD spectra of hexachloroiridate-oxidized C13S *D. vulgaris* 2Fe-SOR. The sample was 1.2 mM in 2Fe-SOR and was in 50 mM HEPES buffer, pH 7.5, with 55% (v/v) glycerol. Upper panel: room-temperature absorption spectrum in a 1-mm path length cell. Lower panel: VTMCD spectra recorded in a 1-mm path length cell at 1.85, 4.22, 10.8, 25.3, and 50.1 K with an applied magnetic field of 6 T. All MCD bands increase in intensity with decreasing temperature.

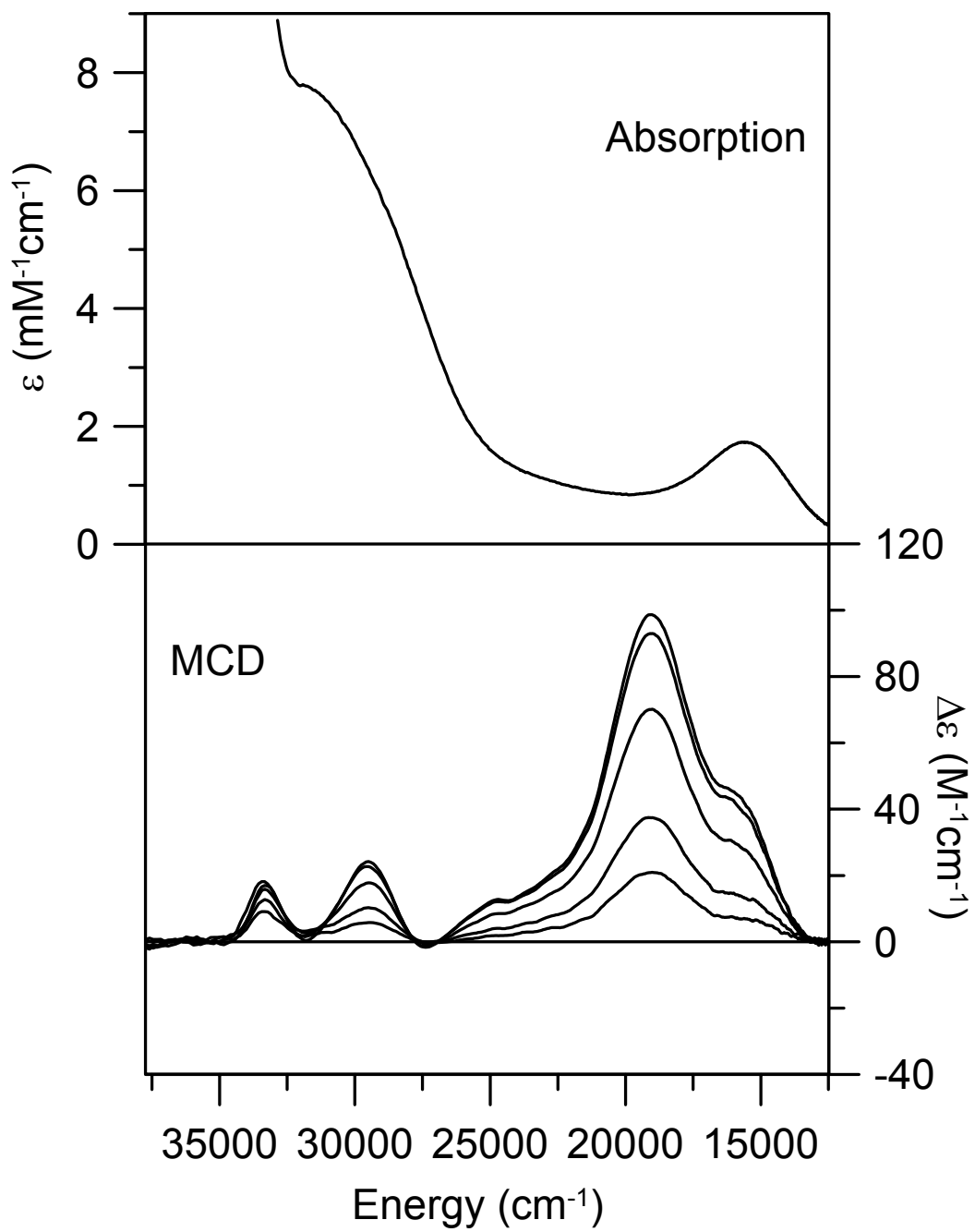


Figure 5.6 UV absorption and VTMCD spectra of ascorbate-reduced C13S *D. vulgaris* 2Fe-SOR. The sample was 0.4 mM in 2Fe-SOR and was in 50 mM HEPES buffer, pH 7.5, with 55% (v/v) glycerol. Upper panel: room-temperature absorption spectrum in a 1-mm path length cell. Lower panel: VTMCD spectra recorded in a 1-mm path length cell at 1.85, 4.22, 10.7, 24.0, and 50.6 K with an applied magnetic field of 6 T. All MCD bands increase in intensity with decreasing temperature.

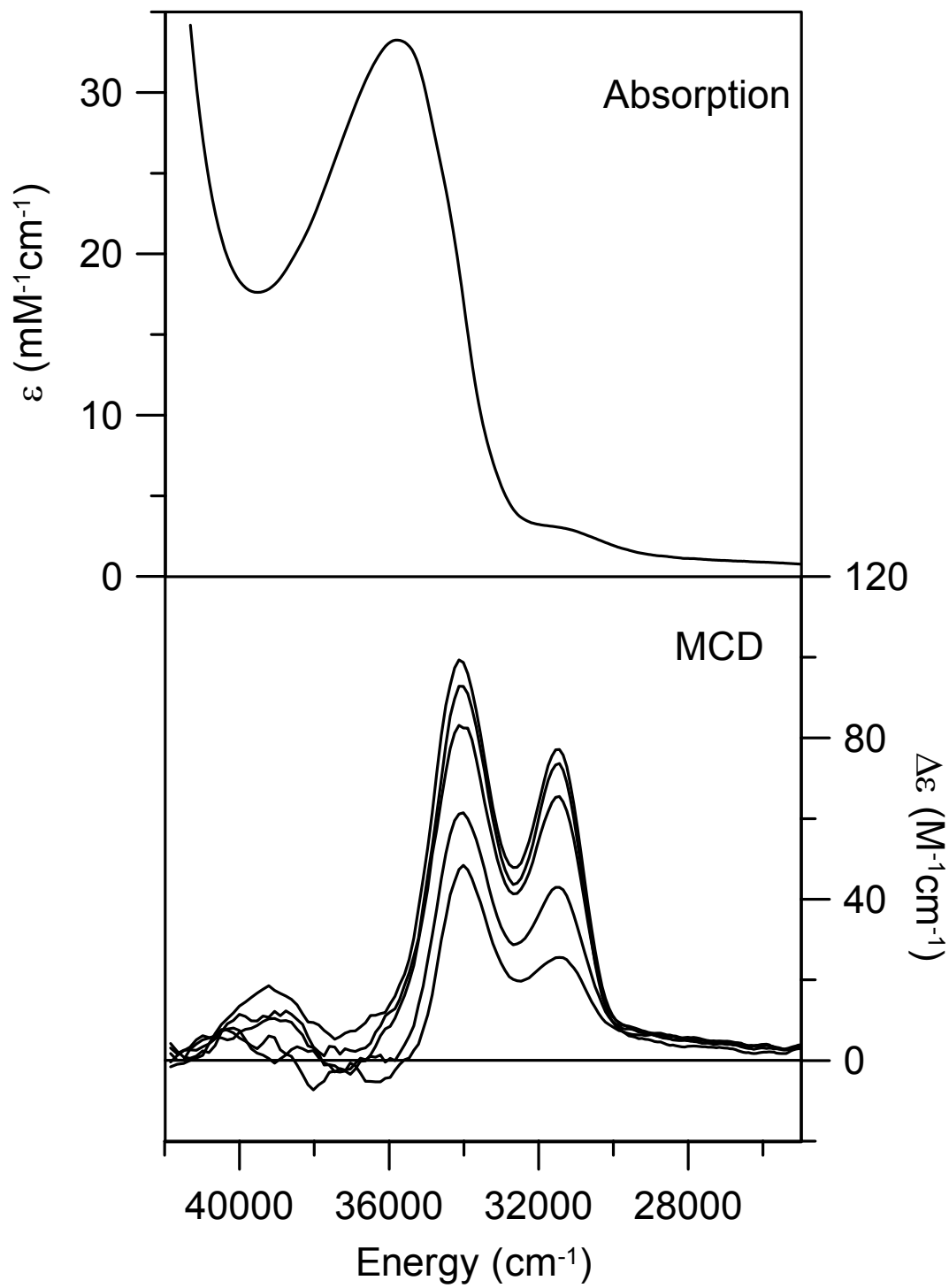


Figure 5.7 Near-IR absorption, CD, and VTMCD spectra of ascorbate-reduced C13S *D. vulgaris* 2Fe-SOR. The sample was 3.9 mM in 2Fe-SOR and was in 50 mM D<sub>2</sub>O HEPES buffer, pD 7.5, with 55% (v/v) glycerol-*d*<sub>3</sub>. Upper panel: room-temperature absorption spectrum in a 1-mm path length cell. Middle panel: room-temperature CD spectrum in a 1-mm path length cell. Lower panel: VTMCD spectra recorded in a 1-mm path length cell at 1.84, 4.22, 11.3, 25.0, and 50.8 K with an applied magnetic field of 6 T. All MCD bands increase in intensity with decreasing temperature.

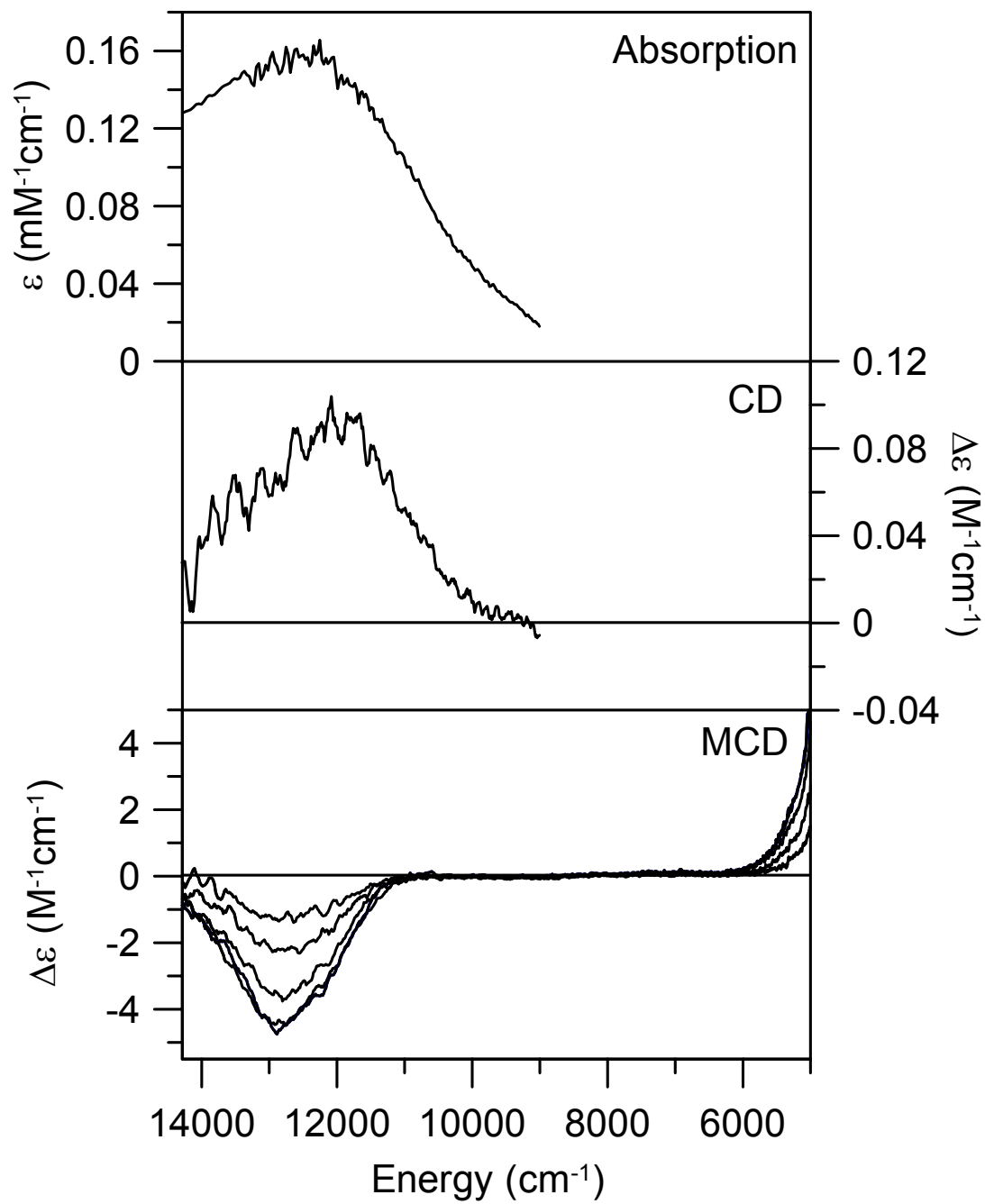


Figure 5.8 Resonance Raman spectra of oxidized C13S *D. vulgaris* 2Fe-SOR. Upper panel: natural abundance and  $^{34}\text{S}$  globally labeled samples with 647-nm excitation. Lower panel: natural abundance and  $^{15}\text{N}$  globally labeled samples with 647-nm excitation. All samples were  $\sim 5$  mM in 2Fe-SOR and were in 50 mM HEPES buffer (pH 7.5). The samples were frozen and maintained a temperature of 17 K. Spectra were recorded using  $6\text{ cm}^{-1}$  resolution by photon counting for 1 s every  $1\text{ cm}^{-1}$  and are the sum of 30 – 50 scans. The asterisks indicate lattice modes of ice.

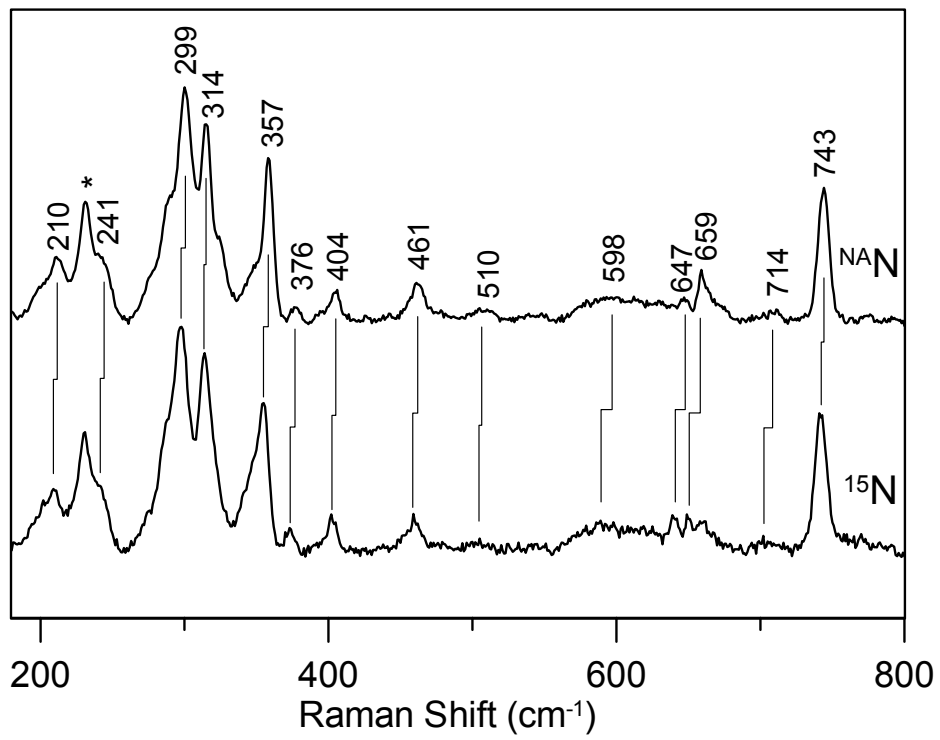
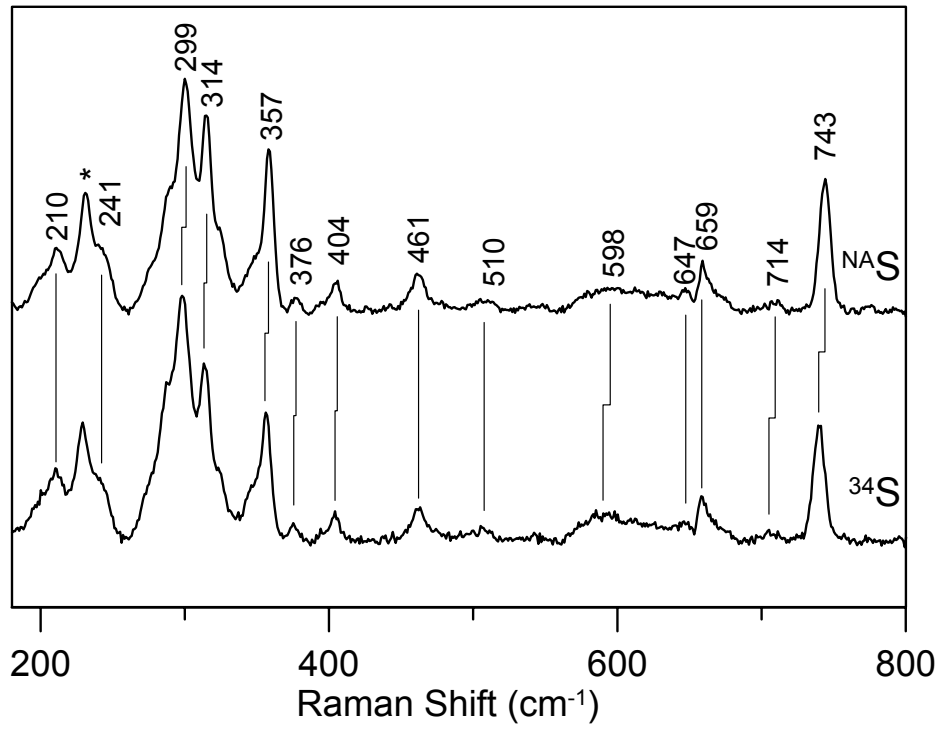


Figure 5.9 Resonance Raman spectrum of oxidized C13S *D. vulgaris* 2Fe-SOR with 647-nm excitation in the high-energy region, 800 – 2000  $\text{cm}^{-1}$ . The sample and measurement conditions are the same as those described in Figure 5.8.

